Author:
Samphire, Jenny L

Title:
Novel Synthetic Tools as Bacterial Diagnostics and Therapeutics

University of BRISTOL

Novel Synthetic Tools as Bacterial Diagnostics and Therapeutics

Jennifer Samphire

Supervisors: Professor M. Carmen Galan and Professor James Spencer

A dissertation submitted to the University of Bristol in accordance with the requirements for the award of the degree of Doctor of Philosophy in the Faculty of Science

School of Chemistry, 2021

Word count: 50,272

Abstract

The issue of antimicrobial resistance is of increasing concern and so is the ability to develop probes that can specifically recognise and target bacteria with alternative antibacterial mechanisms which will be of the utmost importance in countering its growth. The aim of this project is to develop a new class of diagnostic and antibiotic tools that can offer improvements on current protocols and alternative mechanisms of action. This thesis investigates the use of a bench stable, non-toxic, carbon-based nanomaterial, termed carbon dots (CDs), as bacterial labelling and antibacterial therapeutic tools. Previously reported green-fluorescent CDs (GCDs), synthesised via a three-minute microwave reaction, are shown to fluorescently label four different species of bacteria with incubation times as low as one minute. Also discussed is the antimicrobial effect exhibited by the GCDs in the presence of blue-LED irradiation, in both Gram-negative *Escherichia coli* and Gram-positive *Staphylococcus aureus.* Specific targeting of *E. coli* through the exploitation of the interaction between the membrane-bound carbohydrate binding protein (lectin) *FimH* and mannose is also targeted. Different nanoparticle platforms and a variety of mannose-derived ligands are also explored. A successful nanoprobe was developed, a blue fluorescent CD functionalised with a seven carbon mannoside ligand, which was seen to interact with *FimH* expressing *E. coli* in an agglutination-based assay.

Additionally, to the nanoparticle-based systems developed, a novel class of G4-binding antimicrobial compounds were investigated. G4s are nucleic acid secondary structures found in guanine rich sequences and have been identified in the genomes of multiple organisms, with particular research interest in their involvement cancer. However, little is known about their role and effect in bacteria. A variety of multidrug resistant, clinically relevant bacterial strains were screened against a previously synthesised library of G-quadruplex (G4) stabilising ligands. Several G4 stabilising ligands were found to exhibit antibacterial activity against the drug-resistant strains, one stiff-stilbene based ligand, **L6**, showing potency in both *E. coli* and *S. aureus* with minimum inhibitory concentrations as low as 1 μg/mL. An RNA G4 sequence from *E. coli* is also assessed and the stabilisation induced from G4 binding ligands measured with circular dichroism and FRET melting assays. The potent **L6** ligand exhibited better thermal stabilisation than the G4 benchmark ligands BRCO19 and TMPyP4. Nineteen compounds from the G4 ligand library were also shown to exert an antibacterial effect on *M. tuberculosis* model strain *M. smegmatis*. The results found in nanoparticle systems and G4 targeting ligands offer alternative strategies for bacterial identification and antibacterial therapeutics, where rapid diagnostics and novel antibiotic mechanisms are vital in the fight against antimicrobial resistance.

Author’s Declaration

I declare that the work in this dissertation was carried out in accordance with the requirements of the University's *Regulations and Code of Practice for Research Degree Programmes* and that it has not been submitted for any other academic award. Except where indicated by specific reference in the text, the work is the candidate's own work. Work done in collaboration with, or with the assistance of, others, is indicated as such. Any views expressed in the dissertation are those of the author.

SIGNED: .....  ..... DATE:....17/03/21.....

Acknowledgements

Firstly, I want to thank both my supervisors, Carmen Galan and Jim Spencer, for helping guide me through the worlds of both chemistry and microbiology. Thank you, Carmen, for your optimism and advice throughout my PhD and thank you Jim, for your patience and support in introducing me to an unfamiliar field. I am grateful that I was welcomed into two such friendly groups.

A big thank you is needed for Yuiko Takebayashi, my partner in microbiological crime. Thank you for teaching and guiding me in the ways of microbiology and for our long discussions anytime something unexpected happened…which was most of the time. I could have not undertaken this work without you.

Thank you to Stephen Hill, the carbon dot originator, for your guidance, assistance and company when I first joined the group. Thank you also to Michael O'Hagan, for being my G-quadruplex knight in shining armour and sharing some of your extensive knowledge with me, from quadruplexes to Grecian architecture. Thank you to Robin Jeanneret for proof-reading my thesis and disclosing some of your money-saving expertise, your insights into both invaluable. Thank you to all those, past and present, that made the office so fun and for the genuine friendships I have found. Thank you to my holiday partners Sadiyah Sheikh and Teo Garcia Millan for all the adventures, remember, what happens in Mexico stays in Mexico. Thanks to my duet partner Eliza Hunt, these chemistry degrees are only the start of our West End careers.

Thank you to the technicians and support staff working in the School of Chemistry and School of Cellular and Molecular Medicine for their important work in keeping everyone's research running. Thanks to all those working in each school's instrument services who have helped me run samples and collect the data so vital to my project, especially Dominic Alibhai, for teaching me on and trusting me with the fancy confocal.

I am also thankful to the Bristol Chemical Synthesis CDT team (Kevin Booker-Milburn, Emma Rose, Mar Ruiz-Molina and Laura Chavda), for giving me the opportunity to carry out this PhD and for their work and effort in arranging our training programme. Thank you for the 2016 cohort (e.g. the fun cohort), including honouree cohort member Dan Giernalczyk, for making settling into Bristol so easy and our first years so entertaining. Special thanks to cohort members Beth Donnelly and Debbie Nicol for agreeing to live with me for four whole years. I will treasure our times binge watching crime drama tv shows in our lovely flat.

I am also grateful for the support I received outside of Bristol. Thank you to my Dad, Peter, for always answering my calls within three rings and keeping me informed on all future weather fronts heading in my direction. Thank you to my Mum, Frances, for your belief in me and letting me occasionally bore you with science talk. Also thank you to my big sister, Rosie, who motivated me from early on and whose support I shall endeavour to repay in kind. Becoming an aunt will be much more exciting for me than becoming a doctor. Thank you also to my oldest friends, Sophia Panthaky and Elinor Day, for the pep-talks, the gossip and keeping me sane during lockdown.

Thank you to Sandwich Sandwich for your excellent southern fried chicken sandwich that helped me through thesis writing every Monday. And to all Bristol's excellent eateries that bought some joy to pandemic life.

A big un-thank you to corona.

Table of Contents

Abbreviations

AMR	Antimicrobial resistance
2,5-DOFR	2,5-Deoxyfructosazine
A	Adenine
Abs	Absorbance
Ac	Acetate
AEAPMS	*N*-(β-aminoethyl)-γ-aminopropyl methyl dimethoxy silane
AEEA	Aminoethylethanolamine
AFM	Atomic force microscopy
AGC	Automatic gain control
AIBN	Azobisisobutyronitrile
AMP	Ampicillin
AOBs	Acousto-optical beam splitter
Au-NP	Gold nanoparticle
Av	Antigenic variation
BCD	Blue fluorescent carbon dots
BCD	Blue-fluorescent CDs from glucosamine and TTDDA
BRACO-19	(9-[4-(N,N-dimethylamino)phenylamino]-3,6-bis(3-pyrrolodinopropionamido) acridine)
C	Cytosine
CA	Citric acid
CAMHB	Cation-adjusted Mueller Hinton broth
CD	Circular dichroism
CDI	Carbonyldiimidazole
CDs	Carbon Dots
CFU	Colony forming units
CGE	Cluster glycoside effect
CLSM	Confocal laser scanning microscopy
ConA	Concanavalin A
D	Translational diffusion coefficient
DABCO	1,4-Diazabicyclo(2.2.2)octane
DCM	Dichloromethane
DLS	Dynamic light scattering
DMAP	4-Dimethylaminopyridine
DMEM	Dulbecco's Modified Eagle medium
DMF	Dimethylformamide
dmol	Decimole
DMSO	Dimethyl sulfoxide
DNA	Deoxyribonucleic acid
DOPA	3,4-dihydroxyphenylalanine
DOSY	Diffusion-Ordered NMR Spectroscopy
DOX	Doxorubicin
EDA	2,2′-(Ethylenedioxy)bis(ethylamine)
EDA	Ethylenediamine
EDC	1-Ethyl-3-(3-dimethylaminopropyl)carbodiimide
EDC	Ethyl-3-(3-dimethylaminopropyl)carbodiimide

ELISA	Enzyme-linked immunosorbent assay
ELS	Evaporative light scattering
ESI	Electrospray ionisation
FAM	Fluorescein
FDR	False discovery rate
FITC	Fluorescein isothiocynanate
FRET	Förster resonance energy transfer
G	Guanine
G4	G-Quadruplex
GCD	Green fluorescent carbon dots derived from glucosamine and 1,3-phenylenediamine
GlcN	Glucosamine
GlycoNPs	Glyco-nanoparticles
HCD	High energy collision dissociation
HDF	Human Dermal Fibroblasts
HeLa	Cervical cancer cell line
HIV	Human immunodeficiency virus
HM	Heptyl α-d-mannoside
HMDS	Hexamethyldisilizane
HPLC	High-performance liquid chromatography
HPPT	4-Hydroxy-1H-pyrrolo[3,4- c]pyridine-1,3,6(2H,5H)-trione
HRTEM	High-resolution transmission electron microscopy
HR-TEM	High-resolution transmission electron microscopy
HSQC	Heteronuclear single quantum coherence
hv	Irradiation
IR	Infrared spectroscopy
k_B	Boltzmann constant
kV	Kilovolt
LB	Lysogeny broth
LC-MS	Liquid chromatography–mass spectrometry
LED	Light-emitting diode
LTR	Long terminal repeat
m/z	Mass-to-charge ratio
MALDI-TOF MS	Matrix assisted laser desorption ionization-time of flight mass spectrometry
MIC	Minimum inhibitory concentration
MIC_{50}	Minimum inhibitory concentration required to inhibit growth of 50% of organisms
MRI	Magnetic resonance imaging
MS/MS	Tandem mass spectrometry
MW	Microwave
MWCO	Molecular weight cut-off
nano-LC MSMS	Nanoscale liquid chromatography coupled to tandem mass spectrometry
NHS	Hydroxysuccinimide
NMM	N-methyl mesoporphyrin IX
NMR	Nuclear magnetic resonance
OD	Optical density
OD_{600}	Optical densitry read at 600 nm
PAβN	β-Naphthylamide

PBS	Phosphate-buffered saline
PCR	Polymerase chain reaction
PDT	Photodynamic therapy
PEG	Polyethylene glycol
PFA	Paraformaldehyde
ppm	Parts per million
PTT	Photothermal therapy
QD	Quantum Dots
qRT-PCR	Real-Time Quantitative Reverse polymerase chain reaction
QY	Quantum yield
R_H	Hydrodynamic radius
RNA	Ribonucleic acid
ROS	Reactive oxygen species
RP	Reverse phase
RPM	Revolutions per minute
SEC	Size exclusion chromatography
SEM	Scanning electron microscopy
SPS	Synchronous Precursor Selection
T	Thymine
TAMRA	Carboxytetramethylrhodamine
TB	Tuberculosis
TEM	Transmission electron microscopy
TEMPO	2,2,6,6-Tetramethyl-piperidinooxy
TGA	Thermogravametric analysis
Thr	Threonine
T_m	Melting temperature
TMPyP4	meso-5,10,15,20-Tetrakis-(N-methyl-4-pyridyl)porphine)
TMT	Tandem Mass Tag
TTDDA	4,7,10-trioxa-1,13-tridecanediamine
UPEC	Uropathogenic *E. coli*
UTI	Urinary tract infection
UV	Ultraviolet
XPS	X-ray photoelectron spectroscopy
YPD	Yeast peptone dextrose
δ	Chemical shift
ΔT_m	Change in melting temperature

1. INTRODUCTION

1.1 ANTIBIOTICS, THE DEVELOPMENT OF RESISTANCE

Since the discovery of Penicillin in 1928 by Alexander Fleming, the use of small-molecule antibiotics to treat bacterial infections has become common use. However, the 'golden era' of antibiotic development, from the 1930s to 1970s, ended when production of new antibiotics could not keep pace with the emergence of resistant pathogens.[1] Initially thought a 'magic bullet' solution, demand for antibiotics grew across many sectors leading to increases in production and allowed for cheaper and wider use. Despite Fleming cautioning against the dangers of antibiotic resistance in his 1945 Nobel Prize speech, warnings were not heeded and so the wide and irresponsible use of antibiotics has led to the point where there are many clinical isolates of pathogenic bacterial species, including *Mycobacterium tuberculosis, Escherichia coli, Klebsiella pneumoniae Staphylococcus aureus* and *Pseudomonas aeruginosa,* resistant to a vast majority of available antibiotics.[2] The ability of bacteria to quickly replicate allows for evolution of resistance which can be spread via numerous methods, such as plasmid transfer and transformation.[3] Factors contributing to the increases in antimicrobial resistance (AMR) have been attributed to general overuse, inappropriate prescribing and over-the-counter availability, extensive use in animal husbandry and agricultural, increased international travel and the limited availability of new antibiotics.[4] The British government issued a report in 2014 which found that, without intervention, worldwide deaths attributed to AMR would rise from 700,000 a year to 10 million by 2050 (Figure 1).[5]

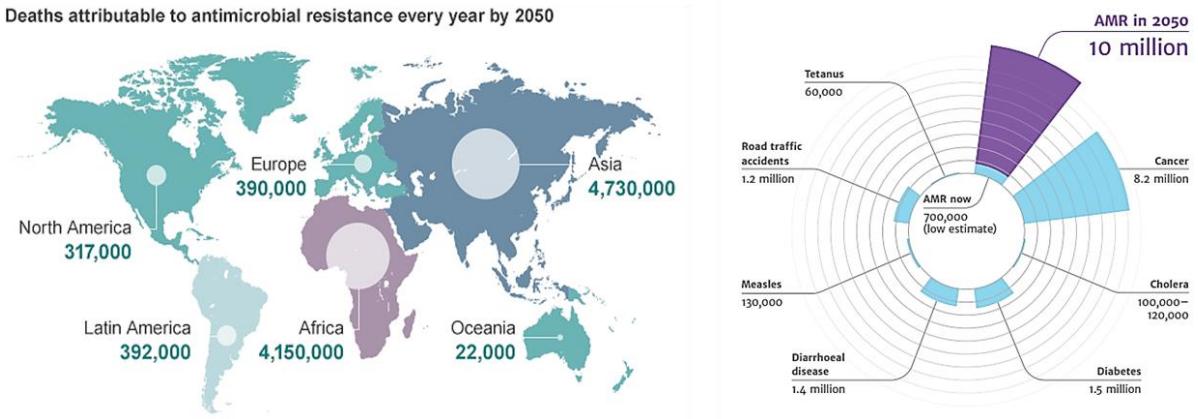

Figure 1 Projections from 2014 government-ordered review on AMR detailing the expected increase in AMR related deaths over the next 30 years (Diagram reproduced from 2014 report)[5].

Bacteria are usually split into two different classes: Gram-negative and Gram-positive. This is determined by a staining method which separates bacteria based on their cell wall constituents.[6] Gram-negative bacteria have a thin peptidoglycan layer sandwiched between two lipophilic membranes whereas Gram-positive bacteria have just one membrane surrounded by a thicker layer of peptidoglycan (Figure 2). Most antibiotics must pass through these cell walls to access their targets and passage through the outer membrane of Gram-negative bacteria can be particularly difficult. Two modes of access are diffusion pathways, exploited by hydrophobic drugs, and cross-membrane protein porins,

which molecules of a certain morphology and charge, such as β-lactams, can pass through.[7] Resistance can then be acquired through variations in membrane structure such as mutations in porins, mechanisms Gram-positive bacteria lack.[8] Therefore, due to their distinctive structure, Gram-negative microorganisms are inherently more resistant to many antibiotic treatments. There are some organisms that cannot be definitively classified the Gram staining technique. These organism's cell walls often have a higher level of structural complexity, such as Mycobacterium, whose multi-layered lipid-rich cell wall means it cannot be categorised as either Gram-negative or Gram-positive.[9]

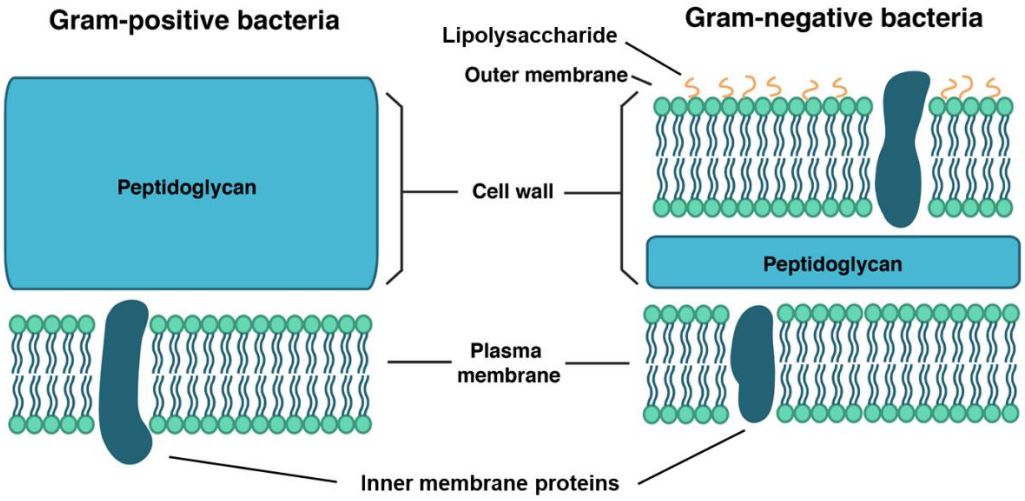

Figure 2 Difference in composition between Gram-positive and Gram-negative bacterial cell walls.

Another factor contributing to resistance is the ability of bacteria to produce protective films, termed biofilms. Bacteria can congregate in a self-produced matrix of extracellular polymeric substances which consist mainly of lipids, proteins and polysaccharides.[10] They can regularly form on indwelling medical devices which can cause recalcitrant, life-threatening infections.[11] Because of the encasing protective film, bacteria can avoid immunological response and are more resistant to high concentrations of antibiotics. Antimicrobials are unable to completely remove the infectious cells as even if the majority of pathogenic cells have been killed, anchored cells, called sessile cells, can re-establish infection and evolve resistant mechanisms.[12]

Developed resistance to common use antibiotics means patients often are put on a high-dose regimen that is sufficiently strong to inhibit bacteria that are both susceptible and resistant.[13] This has an associated risk, in that patients are likely to have longer hospital stays, experience toxic side effects and increased mortality.[12] Aggressive use of broad-spectrum agents can also disrupt the body's natural bacterial flora, which can increase risks of infection by organisms such as *Clostridium difficile*, which proliferates when normal intestinal microbiota is exposed to antibiotics.[14] Antibiotics are vital for modern medicine, procedures including organ transplantation, preterm baby care and cancer therapy are all dependent on them and so new approaches are needed to prevent the dawn of a post-antibiotic era.[15] Some societal changes highlighted as important in tackling AMR include government-initiated taskforces, monetary rewards for drug companies investing in financially high-risk antibiotic development programs and conservation through education and controlled access.[1]

The clinical life of antibiotics can be extended through mode-of-action-guided chemical alterations which can result in derivatives refractory to some known resistance mechanisms. Often the resistance mode of action however cannot be targeted completely without disrupting the molecule's antimicrobial activity.[16] Since there are multiple mechanisms of resistance for each class of antibiotic, eventual

resistance to derivatives is inevitable. Compounds targeting efflux of antibiotics, a common form of resistance in many classes, have been pursued but few effective inhibitors have been found.[17] Other tactics suggested include combining antibiotics with different modes of action, reducing selection pressures by 'cycling' antibiotics and antibiotics used in parallel with enzyme inhibitors targeting resistance mechanisms.[16,18–20] However, these methods usually just delay the onset of resistance. It is therefore important to find bactericidal agents that have a different mechanism of action to conventional antibiotics.

Alternatives to antibiotics have been developed, many not beyond the laboratory level. Examples include phage therapy, antimicrobial peptides and bacteriocins.[21] Antibodies are another strategy, they can exploit mechanisms distinct from the antibiotics and therefore avoid common resistance mechanisms. Antibodies can target the bacterial surface or act indirectly by targeting pathogenicity virulence factors such as bacterial toxins.[22,23] However, due to production cost and a short shelf-life they only have the potential to be a partial replacement of antibiotics. The use of probiotics is a treatment currently being used to treat gastrointestinal infections as antibiotic treatment disrupts the composition of gut microbiota and the non-pathogenic strains that are vital in gut health.[24] The governing ideology of probiotic treatment in bacterial infections is that restoring gut microbial flora balance allows for commensal bacteria to compete against and exclude pathogenic strains or by boosting the immune defence of the host.[25] Gastrointestinal infections including *Clostridium difficile*/*Helicobacter pylori* induced pseundomembranous colitis have been treated with probiotics.[26,27] Probiotics are cheap and easily available however are used mainly for intestinal infections only. The majority of alternative therapeutic strategies are species/strain-dependent and consequently different infections need to be identifiable before treatment with different therapeutics.[21]

Rapid diagnosis of bacterial infection is important in not only alternative therapeutics but also for allowing more targeted treatment by known antibiotics, limiting the use of broad range and unnecessary therapies. A prescription tailored to diagnosis is an important step in stopping inappropriate antibiotic prescription for those of unknown origin and viral infections. Development of new diagnostic tools allows for the tailoring of treatment to the susceptibilities of the pathogen.[1]

1.2 BACTERIA DIAGNOSIS

Bacterial detection and identification is crucial in healthcare but also veterinary, agricultural and food production sectors.[28,29] The techniques used for the diagnosis of infections range from accurate but time-consuming methods, usually involving culture growth, to quick yet inaccurate methods such as the urinary dipstick test. Generally, the more accurate the technique, the longer the timeframe, which could be critical in certain cases.

1.2.1 Culturing methods

Diagnostic approaches involving growth of bacterial cultures allow for identification by morphological examination as features such as size, shape and colour is specific to each species (Figure 3).[30] Pure cultures of microorganisms obtained through isolation can be grown on chromogenic media to identify phenotypic characteristics of specific species.[31] Other techniques that require overnight incubation include biochemical detection kits such as API 20E and the Vitek® system.[32,33] However, these traditional identification and susceptibility methods using pure cultures can take 36-48 hours, and can be longer dependent on microbial growth rates and the nature of resistance.[34] This time can be critical in infections, like sepsis, or for immune-compromised patients.[35] Techniques with shorter time-frames have been targeted and developed.

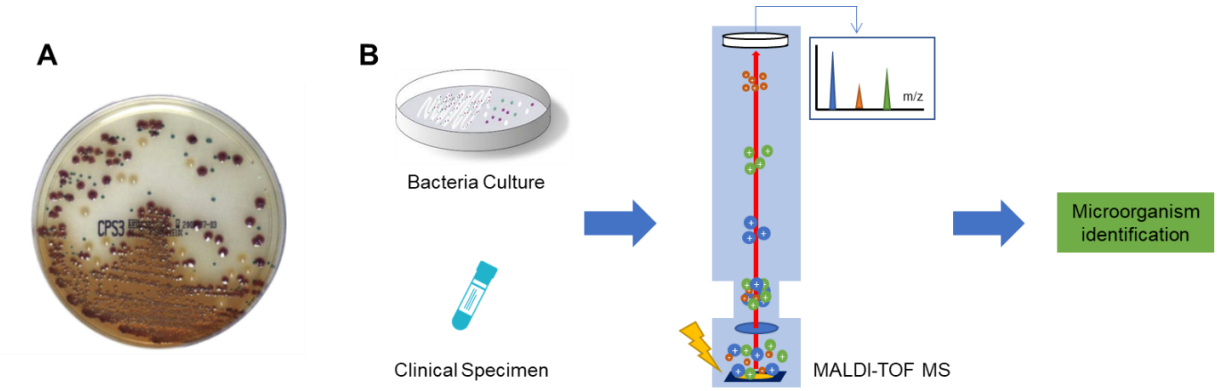

Figure 3 Bacterial identification techniques. A. Bacterial culture of *E. coli* (red) *P. mirabil*is (browm) and *E. faecalis* (green) using ChromID CPS medium for chromogenic identification.[30] B. Schematic representation of MALDI-TOF MS for bacterial diagnosis from bacteria cultures as well as clinical samples.[36]

1.2.2 DIRECT METHODS

Over the last decade, the use of matrix assisted laser desorption ionisation-time of flight mass spectrometry (MALDI-TOF MS) has become increasingly popular for bacterial identification (Figure 3). Bacterial cultures are usually first needed due to sensitivity but in some cases samples direct from the patient can be used. For example, the causative pathogen for the majority of urinary tract infections (UTIs) is *Escherichia coli*, which can be identified at 10^4-10^5 cfu (colony forming units)/mL[36,37]. Prescence of bacteria is confirmed by flow cytometry before centrifugation, initially at a low-speed to remove epithelial cells then at a higher-speed to collect bacteria. An ethanol-formic acid extraction method is used to isolate bacterial proteins to be identified by MALDI-TOF analysis.[36] Diagnosis has also been demonstrated as possible with positive blood cultures and cerebrospinal fluid for diagnosis of sepsis and bacterial meningitis respectively.[36] This allows for bacterial diagnosis in an hour, a vast improvement on the 24-48 hrs of previous culture methods. However, there are still some limitations within MALDI-TOF MS. Between commonly found organisms, identification between similar species is usually achievable. However, there are numerous exceptions to this where similar bacterial species cannot be distinguished, these include *E. coli* and *Shigella* and the *Mycobacterium tuberculosis* complex, *Mycobacterium abscessus* complex, and the *Mycobacterium avium* complex.[38–40] Also, as this identification procedure is dependent on a known database of microorganisms, errors in identification can occur due to a lack of sufficient spectra in the database.[40] Sometimes these misidentifications can have a detrimental clinical impact, for example, the inability to differentiate between three different sub-species of *Mycobacterium abscessus* is problematic as they vary in their resistance to antibacterial macrolides.[41] Other culture-independent techniques include immunoassays such as ELISA and molecular methods like PCR and DNA sequencing.[42] However, these can be laborious, expensive and require many reagents.[43–45]

A technique still in development is the use of fluorescence spectroscopy to identify, at genus and species level, bacteria through comparison of spectral fingerprints.[44] Giana *et al* demonstrated that the identification of three clinically significant bacterium, *Escherichia coli*, *Enterococcus faecalis* and *Staphylococcus aureus*, by distinctions in their autofluorescence spectrum.[46] High sensitivity of fluorescence spectroscopy allows for low detection limits and therefore could eliminate the need of an overnight culture. However, a limitation with this technique is the need for initial separation and purification of samples prior, as mixtures of many bacteria are difficult to separately identify and autofluorescence from host eukaryotic cells could also interfere.

The study of fluorescent nanoparticles is a recently developing field, that combines the sensitivity of fluorescence with the ability of chemical functionalisation to allow for specificity and selectivity in bioimaging.[42] Advantages of fluorescent nanoparticles over other nanomaterial-based biosensors, such as electrochemical systems, are the quick response times, reduced background effects, simple instrumentation and ability for multiplexed analysis.[42] Examples of nanoparticles used in bacteria sensing include gold nanoparticles (Au-NPs), quantum dots (QDs), dye-doped silica nanobeads and more recently carbon dots (CDs).[47–50] Saho *et al* reported a nanoparticle based system to detect bacteria.[51] A composite of a fluorescent paracetamol dimer with Au-NPs was shown to interact with bacterial cell walls and allowed for quantification of bacterial concentration and distinction between Gram-positive and Gram-negative species dependent on fluorescence quenching of the composite. Chemical functionalisation of nanoparticles can allow for specificity through exploitation of natural interactions with the bacterial cell surface. Studies from both Suherman *et al* and Chandra *et al* have demonstrated the use of CDs functionalised with the cyclic antibiotic colistin as a binding agent for Gram-negative bacteria.[52,53] Ionic charges in cell membrane phospholipids and lipopolysaccharides interact with the cationic region of colistin. Interaction between carbohydrates and surface-bound proteins, lectins, have also been exploited with nanoparticles. Gao *et al* developed a microarray with lectin-conjugated gold nanoparticles to capture microbes.[54] A major advantage of nanoparticle based systems in bioimaging and labelling is the power of multivalency, important when targeting singularly weak lectin-carbohydrate interactions.

1.3 LECTIN-CARBOYHYDRATE INTERACTIONS

1.3.1 LECTIN BINDING

A prerequisite for many bacterial infections is the adhesion of the micro-organism to the host tissues, preventing removal from natural cleansing mechanisms and facilitating transport of nutrients and toxins.[55] Carbohydrate-protein interactions are the most common method of attachment between the bacterium and host tissue.

Carbohydrates are complex, naturally occurring molecules that perform numerous roles in biological systems. Polysaccharides, such as chitin and cellulose, are some of the most abundant biopolymers in nature, and the monosaccharide deoxyribose forms a major component of DNA, the genetic code of life. One important role they play is in cellular communication between cells and tissues, carbohydrates decorating interfaces are the cell's first interaction with the external environment.[56] Carbohydrate-mediated processes include cell-cell recognition, cell adhesion, signalling and trafficking. These interactions are also crucial in the identification of glycans of pathogenic species by the host's immune response.[57] Although carbohydrate-protein interactions are the most common method of pathogenic adhesion they are less well understood than protein-protein interactions as the field is newer and there are implicit challenges with biomolecular characterisation of these complexes.[58] Lectins are the most common sugar-binding proteins, the structure of their binding pocket is vital in determining specificity of sugar binding.[59] To compensate for the individual interactions between proteins and carbohydrates being notably weak, many interactions are multivalent in nature.[60]

Bacteria present many lectins on their surface to interact with the tissue's multiple polymeric saccharides and the cumulative effect of these interactions allow for stronger adhesion. Cluster glycoside effect (CGE) is a term that has been used to illustrate these multiple binding events caused by an increased carbohydrate density (Figure 4).

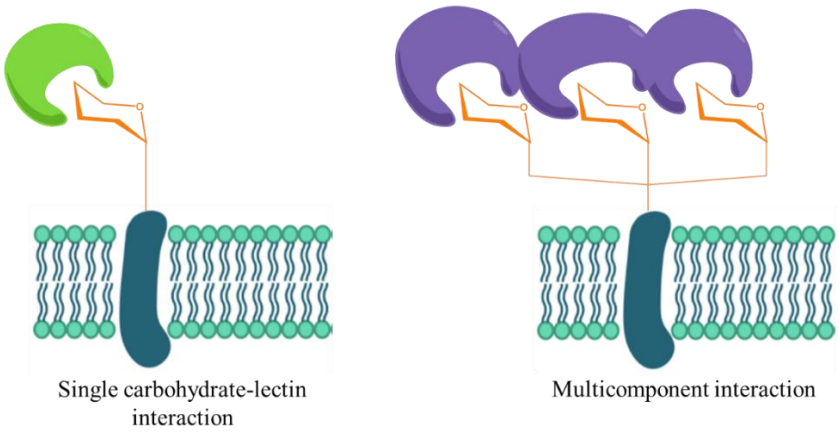

Figure 4 Diagrammatic representation of a weak, single carbohydrate interaction, green receptor, opposed to the CGE forming strong multivalent interactions, purple receptor.

A well-studied example of CGE can be found in the interaction of the homotetrameric lectin Concanavalin A (ConA) with clustered carbohydrates. Each ConA lectin has four carbohydrate domains and displays preferential binding to mannose, though weak avidity for glucose is also seen (Figure 5). This specificity highlights the effect structural differences impart on binding, the difference between mannose and glucose being the orientation of the hydroxy group at the secondary carbon.[61] The clustering of mannose increases the number of interactions and consequently ConA's binding avidity.[62]

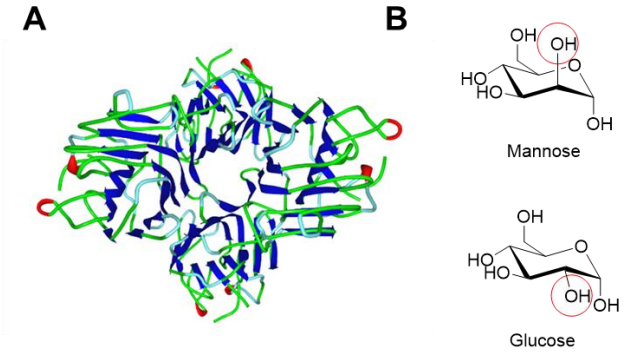

Figure 5 ConA lectin binding. A. Structure of ConA with the four mannose-binding sites highlighted (red) Reproduced from Matsumoto *et al.*[63] B. Structures of mannose, which is preferentially bound to ConA, and glucose with the change in position of the hydroxy group at the C-2 of the monosaccharide unit (circled).

1.3.2 *FIMH* STRUCTURE

FimH is another mannose-specific lectin and is found on *E. coli* type-1fimbriae. Uropathogenic *E. coli* (UPEC) are responsible for the majority of urinary tract infections (UTIs), a prevalent disease that affects 50% of women in their lifetime.[64,65] The main mechanism of infection is via type 1 fimbriae-dependent adhesion to mannosylated glycoproteins coating bladder epithelium cells.[66] The fimbriae are long, hair-like appendages that are highly expressed on UPEC surfaces. *FimH* is found at the distal tip on the fimbriae, which is also composed of a fimbrial base of repeating *FimA* subunits, which is connected to *FimH* by the subunits *FimF* and *FimG* (Figure 6).[66] Unlike mannose binding ConA, *FimH* displays preferential binding for a singular mannose unit and instead, weak binding is overcome by multiple fimbriae expressed on the surface of the bacterium.[67] *FimH* consists of two domains, the N-terminal, mannose-binding $FimH_L$ and C-terminal $FimH_P$ which is in association with the *FimG*

subunit.[68] The binding pocket of the *FimH*$_L$ has been closely studied as a potential drug target to prevent pathogenic adhesion.[69] Nathan Sharon in 1977 provided the first substantial work on the inhibition of mannose-facilitated adhesion of *E. coli* with epithelial cells using small molecules α-D-mannose and methyl α-D-mannopyranoside.[70] Subsequent work in the 80s and onwards probed further the understanding of *FimH* mannose binding and improved design of antagonists.[71–74]

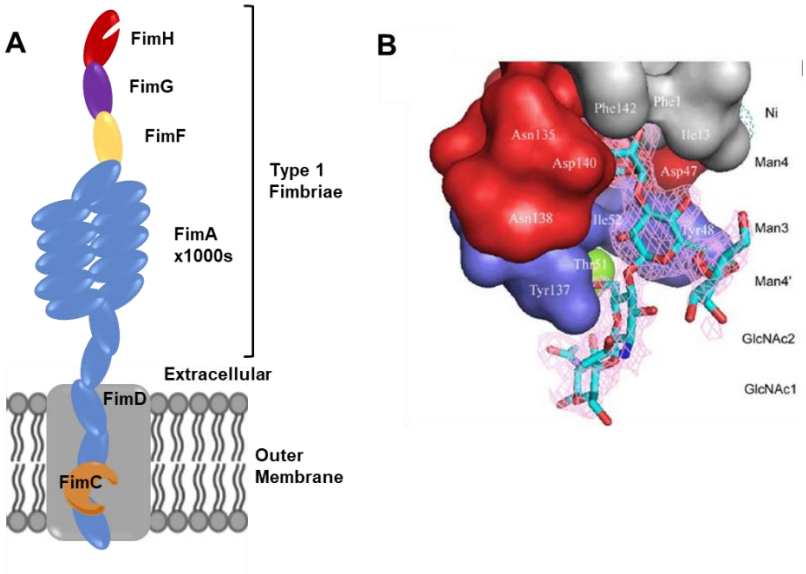

Figure 6 Structure of type 1 fimbriae and *FimH* binding site. A. Diagrammatic representation of the protein subunits on *E. coli* membranes that are capped with the *FimH* lectin. B. Model of oligomannose binding to *FimH* adapted from Wellens *et al (*2008).[69] Electron density map of *FimH* receptor binding site interacting with a bound oligomannose. Hydrophobic support region (grey), polar binding pocket (red), Thr51 side chain (green) and tyrosine gate (blue).

The mannose-binding region of the lectin is a tight polar pocket which is surrounded by a hydrophobic region subdivided into a threonine side chain (Thr51), a support platform and the tyrosine gate (Figure 6).[69] The mannose-binding pocket shows selectivity for α-D-mannose and binds to the sugar through a number of electrostatic and hydrogen bonding interactions.[75] The so-termed 'tyrosine gate' plays a vital role in forming molecular interactions with the aglycone of the binder.[76] Entry of the ligand into the binding pocket is somewhat guarded by these tyrosine residues lining the hydrophobic region, hence the term gate. Roos *et al* reported that binding avidity can be markedly affected by the orientation of the aglycone within the tyrosine gate, key factors in the ability to form van der Waals and π-stacking interactions.[77]

1.3.3 *FIMH* LIGANDS

Many different mannoside ligands have been developed and optimised over the last 40 years, a large section following the general structure of a hydrophobic linker conjugated to a mono-mannose ligand.[66] Some alternative structures include mannose dimers/trimers and also mannose terminated disaccharides (Figure 7).[78,79] Hydrophobic linker structures including simple aryl chains and biaryl linkers and *N*-. *O*-, *S*- or *C*- linked mannosides have been reported (**4**, **5**, **6),** each found to have its own benefits.[80–82] For example, *O*-linked ligands can improve solubility and for a *R*-hydroxymethylene linker, replacement of the anomeric oxygen with a C-linked linker increased binding potency.[80]

One simple but effective *FimH* antagonist is heptyl α-D-mannoside (HM) (**9**). When lectin affinity was compared with other alkyl and aryl mannosides, HM was found to have the lowest dissociation constant, K_d = 5 nM compared to K_d = 2.3 x10^3 nM of free mannose.[67] Wellens *et al* reported HM, **9**, to reduce adhesion and invasion of a pathogenic cystitis isolate in a mouse model. Biofilm formation was also

found to be inhibited at micromolar concentrations of HM.[69] A multivalent presentation of HM has also been reported to decrease inhibitory concentrations, in-line with CGE. Gouin *et al* recorded a 64-fold lower inhibitory concentration for a HM multimer in comparison with singular HM.[83] A set of multivalent HM ligands whose valency ranged from one to seven, labelled with a fluorescent probe, was designed by Almant *et al* (**11**).[84] A multivalency effect was observed, with the lowest inhibitory concentration for a UPEC *E. coli* strain found for heptavalent HM. Although *FimH* lectin binds monovalently, this effect was attributed to either indirect effects of multivalency, such as tethered HM ligands allowing subsequent binding and recapture of the lectin, or directly by binding multiple lectins simultaneously. Aggregation of bacteria was only observed with the trivalent ligand, a phenomenon not seen for monovalent ligands. Sivignon *et al* also observed increased *FimH* affinity and the ability for bacterial clustering with multivalent HM derivatives (**10**).[85]

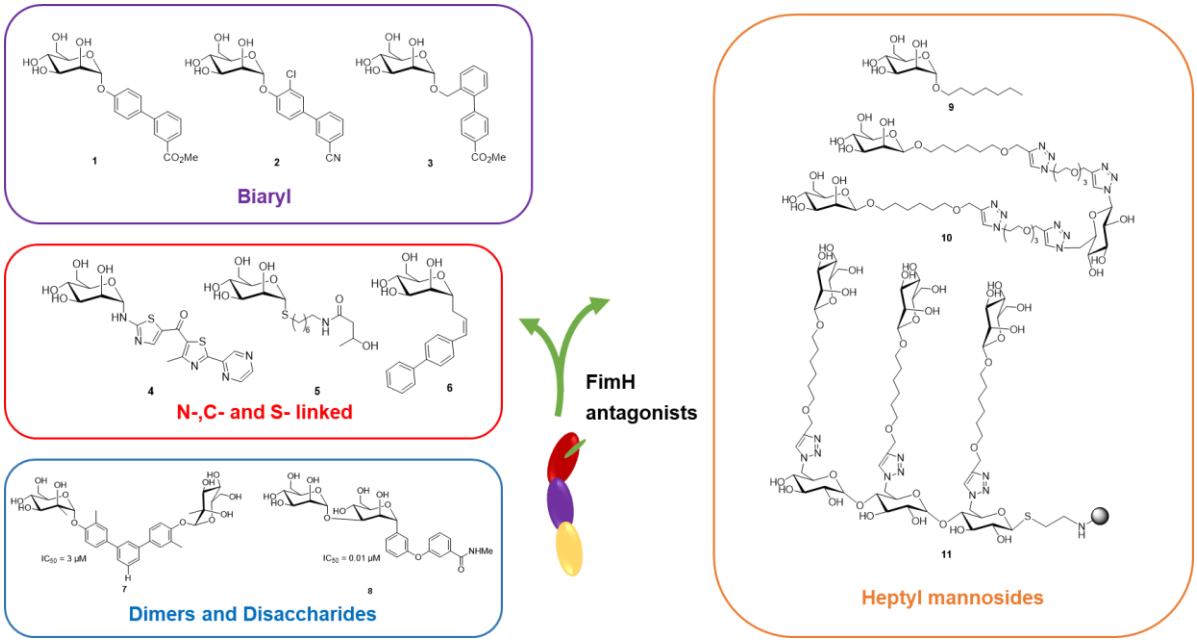

Figure 7 Examples of different classes of *FimH* ligands including multivalent heptyl mannoside derivatives.[66,83,84]

1.3.4 NANOPARTICLE TARGETING OF *FIMH*

The use of multivalency, so important in multiple interactions found in nature, has been incorporated into many biological techniques. Multivalent scaffolds incorporating sugars mimic cell surface interactions include glycoarrays, glycopolymers and glycodendrimers and have garnered interest for their use in diagnosis and therapy.[86] The use of nanoparticles allows for chemical manipulation at a nanometre level and allows for the glycocalyx of the cellular surface to be recreated. Glyco-nanoparticles (GlycoNPs) have the basic structure of an outer layer of glycans and an inner core that can confer its own properties such as magnetism or fluorescence.[87–91] For example, gold nanoparticles (AuNPs) decorated with an alkyl mannoside derivative were found to fluorescently label *E. coli*.[47] A thiopentyl mannosyl dimer was prepared before conjugation with AuNPs (Scheme 1).

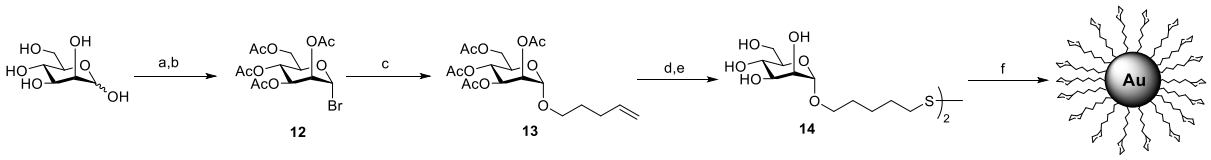

Scheme 1 Synthesis of mannosylated gold nanoparticles by Chun-Cheng *et al*.[47] Conditions: (a) Ac_2O, pyridine. DMAP (b) HBr/AcOH, 80% (c) 4-pentenyl alcohol, $Hg(CN)_2$ (d) AcSH, AIBN, dioxane (e) NaOMe (cat.), MeOH (f) $HAuCl_4$, $NaBH_4$.

The mannose-encapsulated AuNPs were incubated with two strains of *E. coli*, ORN178 which expresses wild-type type 1 fimbriae and ORN208 that lacks the *FimH* gene and binding accessed by transmission electron microscopy (TEM) (Figure 8). Selective labelling of only the ORN178 strain was observed in all conditions tested. A competitive binding study found that free mannose at concentrations of up to twenty-fold of the AuNPs concentration had little to no effect on nanoparticle fimbrial binding.

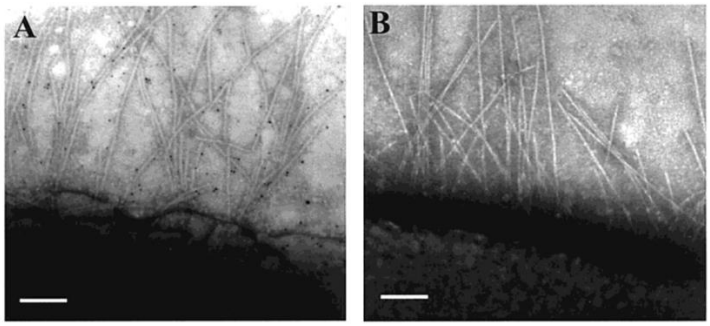

Figure 8 TEM images from Chun-Cheng *et al*'s paper on mannosylated AuNP *E. coli* ORN178 labelling.[47] A. Fimbriae labelled with AuNPs. B. Fimbriae without AuNP labelling. 100 nm scale bar.

1.4 NANOPARTICLES IN BIOIMAGING

Another fluorescent nanoparticle core that has been widely used for labelling and imaging techniques are semiconducting quantum dots (QDs). Composed of elements from groups II-VI, III-V or IV-VI, the diameter of QDs ranges from 2-20 nm.[42] Commonly included core elements include Zn, Cd, Se, Te or P.[92] The electronic properties of QDs can be modified through size and shape control. Because of their semi-conducting properties and size, the quantum confinement effect is implicated in the photoluminescence properties of QDs.[93] Decreasing the size of the QD increases the energy band gap and so a shorter wavelength emission is observed, consequently comparatively small QDs have a blue fluorescence emission, and increasing size red-shifts the emission. The size of QDs, and therefore the fluorescent wavelength emission, can be controlled during synthesis.

This tuneable emission is one of many advantageous properties of QDs, which also include high quantum yields of fluorescence (QY) and relatively high photostability. The surface of QDs can be modified through covalent linkage of surface-bound amine, thiol or carboxyl groups or through electrostatic interactions of the QD surface and an oppositely charged biomolecule or protein.[94] A variety of different functions have been reported for glycan-coated QDs. Guo *et al* reported QDs encapsulated with a dense array of mono-/disaccharides as probes for binding of lectins involved in HIV and Ebola viral entry.[95] The Galan group has synthesised a series of glycan-coated QDs to investigate the effect of glycan presentation in intracellular localisation in HeLa cells and found lactose could promote intracellular delivery of non-internalisable moieties.[96] In 2018, Yang *et al* reported an array technique for detecting *E. coli* and *E. faecium* based on glycosylated QDs and 4-

mercaptophenylboronic acid-functionalized MoS_2 nanosheets.[97] The fluorescence of a series of QDs, modified with a variety of mannose, glucose and galactose alkyl derivatives, is quenched when attached to the MoS_2 nanosheets. Introduction of a complementary lectin or bacterial species to the array displaces the QDs from the nanosheet surface, fluorescence is restored and therefore binding can be quantified.

The prospects of glycan functionalised QDs in bacterial detection are mainly limited to *in vitro* assays and techniques due to the inherent toxicity of the heavy metal cores. Cytotoxicity due to Cd^{2+} being released from the core was reported after processing such as UV and surface coatings.[98] To prevent leaching a biologically stable coating is required, however there are worries that oxidative procedures during cellular processes such as immunological responses could cause cytotoxicity.[99]

An alternative core, with the potential to overcome the cytotoxicity issues inherent with QDs, is provided by carbon-based nanoparticles termed carbon dots (CDs) or alternatively carbon quantum dots.

1.5 CARBON DOTS

Carbon dots were discovered in 2004 by Xu *et al* as an unknown fluorescent impurity in the electrophoretic purification of arc-synthesised single-walled carbon nanotubes.[100] The terminology of 'Carbon dots' (CDs) was not used until 2006 when Sun *et al.* looked further into the properties of the carbonaceous fluorescent material.[101] They found nanodots, 5 nm in diameter, whose photoluminescence increased upon surface passivation, attributed to surface energy traps, and fluorescence was stable with respect to prolonged photoirradiation.

1.5.1 SYNTHETIC ROUTES

Since the initial discovery of CDs, the field has grown dramatically with a wide number of reported synthetic routes, which can be classified as either top-down or bottom-up protocols (Figure 9). Top-down syntheses of carbon dots involves the breakdown of pre-existing carbon sources, for example, the oxidation of candle soot or laser fragmentation of graphene.[102,103] Generally, further surface passivation is usually required for stability and to improve fluorescent QY.[104] CDs formed from top-down techniques such as laser ablation are reproducible, with high QYs and a narrow size distribution.[105] However, for the most part, reported synthetic methodology requires high-energy processes, high-skill level techniques and is time consuming.[106] Bottom-up techniques build up CDs from carbon, oxygen and nitrogen-containing molecular precursors and usually do not involve as harsh or expensive conditions as top-down approaches. Precursors include amino acids, carbohydrates and ureas and use a variety of techniques such as thermal decomposition, acid treatment and microwave irradiation.[107–109] In comparison to many top-down methodologies, bottom up routes tend to be quicker, cheaper and simpler as can often be achieved in a 'one pot' reaction mixture.[110] Also, they allow for greater flexibility in morphology and composition through precursor selection and carbonisation conditions.[111] However, this flexibility is also one of the limitations of the technique. Reproducibility of CD morphology and size is difficult between and within batches due to the fact that small changes on reaction conditions (e.g. concentration, reaction time, reagent stoichiometry) within the synthetic protocol, often lead to fluorescent small-molecule side-products being generated.[111]

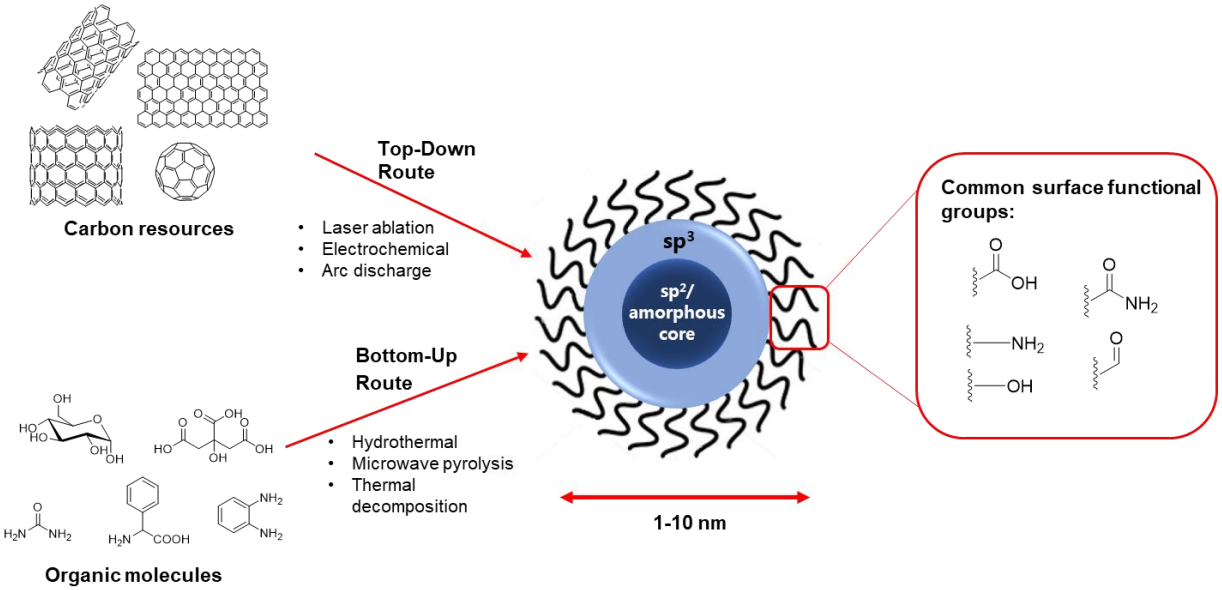

Figure 9 Overview of synthetic protocols to form CDs, highlighting possible synthetic routes, precursors and common surface functionality.

1.5.1.1 HYDROTHERMAL

Hydrothermal synthetic methodologies yield comparatively uniform, high QY CDs, and is one of the most popular synthetic routes for formation of CDs. First reported by Zhang *et al* in 2010, this technique has been widely used with precursors ranging from polymers, foods and waste microorganisms as well as small molecules.[106,112] Typically water is used as the solvent system, however alternative solvents are sometimes used to tune photoluminescence, for example Zhu *et al* used different solvent mixtures to yield blue, green and red emissive CDs.[113] Typically in a hydrothermal synthesis solvated precursors are heated in a Teflon-lined stainless steel autoclave where high temperatures and pressures initiate the formation of CD seeding cores.[105] Quantum yields of over 80%, comparable with fluorescent dyes, have been achieved with this method by Zhu *et al*.[114] Reaction time is typically around 4 hours and lower yields have been reported when in comparison to other bottom-up methodologies such as microwave and thermal decomposition.[115]

1.5.1.2 THERMAL DECOMPOSITION

A less popular technique, thermal decomposition, is where molecular precursors without solvation degrade under high heat conditions, generally in an endothermic manner. The thermal decomposition of citric acid (CA), a common CD precursor, was studied by Ludmerczki *et al*.[116] Within the temperature range of 180-200 °C, CA was dehydrated and reduced, forming fluorescent material, but the production of actual CDs was sensitive to reaction conditions and there was a potential to form a large variety of fluorescent side products.[116] One example of successful CD formation from CA thermal decomposition was reported by Wang *et al* in 2011.[117] The CD carbon sources were CA and the passivating agent, *N*-(β-aminoethyl)-γ-aminopropyl methyl dimethoxy silane (AEAPMS). CD formation was achieved after exposure to 240 °C for 1 minute and yielded 0.9 nm, highly fluorescent nanoparticles.

1.5.1.3 MICROWAVE

Microwave (MW) pyrolysis is one of the most popular routes for CD synthesis due to its ease of use, quick reaction times and low cost. The frequency of MW irradiation is not high enough to break chemical bonds and so cannot directly induce chemical reactions in the manner of higher energy electromagnetic radiation such as UV. MW irradiation produces an oscillating electric field to which molecules with dipoles or charges continuously align with, generating kinetic energy which is converted through collisions and molecular friction to heat.[118] The thermal energy generated is both simultaneous and homogenous throughout the reaction mixture which allows for fast reaction rates.[106,119] The first report of microwave-assisted CD synthesis was by Zhu *et al*. in 2009 using an aqueous solution of PEG-200 and a saccharide irradiated for 3 mins, yielding a CD with blue fluorescence emission.[120] A typical approach has the precursors, a carbon source and potentially additives and/or passivating agents, in an vessel or a closed hydrothermal setup. Either chemical MW reactors can be used, with control over temperature and pressure, or, for ease of use, a domestic microwave oven. The heating duration, usually 1-5 minutes, can vary between reactors depending on wattage and a visible colour change to dark yellow/brown is observed.[118] As with other bottom-up procedures, CDs are formed through the decomposition, dehydration and oligomerisation of the starting materials. The choice of solvent systems needs to take into account the solvent's ability to absorb microwave radiation, the majority of cases use water but ethanol, DMSO and methanol have also been used.[121] MW procedures have also been used to improve the fluorescence intensity of pre-existing CDs. Zhu *et al* prepared CDs through hydrothermal reaction of plant leaves followed by further irradiation increasing emission intensity without additional chemicals that could prevent biological applications.[118] The strong advantages of MW pyrolysis is the low cost and accessibility, for example, CDs made from a 3 minute procedure with common saccharides in a domestic MW can be cheaply made by non-experts, allowing synthesis within a biological lab setting for potential applications such as bio-imaging. This is an important advantage since commercial fluorescent labelling reagents normally cost in the hundreds of pounds for micromolar quantities. Limitations of MW reactions include the limited control over CD morphology, temperatures and pressures limited by solvent system and potential commercial scale-up.[121]

1.5.2 CD STRUCTURE AND PURIFICATION

Carbon dot morphology can be variable and difficult to analyse. Generally, CDs are quasi-spherical nanoparticles between 1 to 10 nm in diameter, composed of a primarily carbon-containing core that generally has sp^2 crystallinity but for some bottom-up processes can also have amorphous sp^3 character. The outer sp^3 shell also usually contains hydrogen, oxygen and nitrogen moieties, with functional groups decorating the surface than can act as "chemical handles" for surface modifications.[121] Reaction side-products are particularly prevalent during bottom-up routes, and can be fluorescent in nature, so purification of CDs is important. Common techniques include centrifugation, solvent extraction, dialysis and size exclusion chromatography.[122] Centrifugation can be used to pellet out large aggregates formed during a reaction, or centrifugal filters can be used to separate reaction products by size depending on membrane pore diameter for more precise separation. As CDs are soluble in aqueous, polar solvents, extraction systems can be used with immiscible organic solvents, such as dichloromethane, to dissolve contaminant small molecules. Dialysis is one of the most popular purification processes due to its simplicity and usually follows centrifugal separation. The principle behind dialysis is the diffusion of molecules from high concentration to low concentrations, where small molecule impurities cross a semipermeable membrane that is not permeable to larger nano-sized material (Figure 10).[122] The dialysis fluid is then changed multiple times until a pure sample is obtained. However, although widely used there is no standard for the molecular weight cut-off of the dialysis membrane or dialysis duration.[123]

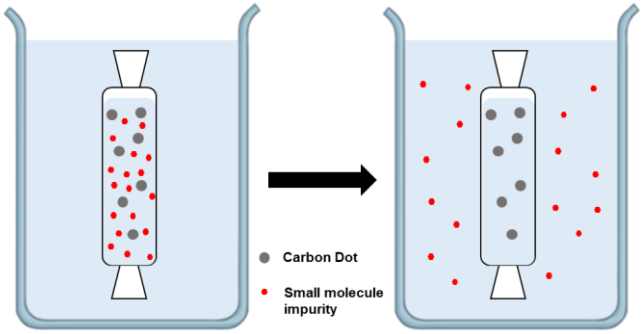

Figure 10 Diagrammatic representation of the purification of CDs by dialysis. Small molecule impurities diffuse through a semipermeable membrane to achieve purification of nanosized material.

1.5.3 FLUORESCENCE ORIGIN AND DOPING

The origin of fluorescence in CDs is widely researched and debated, and there is not one agreed explanation thus far. It is likely that the origin is different depending on the nature of the CDs, dependent on starting materials and reaction conditions. There are currently three main theories for the origin of CD fluorescence: (i) luminescence originating from the crystalline carbon core, (ii) surface energy traps created from non-perfect sp^2 domains and (iii) molecular fluorophores attached to the surface of the CDs.[119,124] Shi *et al* reported that the origin of fluorescence for many CA-based CDs, that was previously attributed to the carbonaceous core, is actually from organic fluorophores.[125] After analysis of literature-reported CDs, Essner *et al* clarified the importance of purification processes following the CD synthesis, since in many instances molecular fluorophores, and not the actual CD material, are the major contributor to fluorescence intensity.[126]

Initially, most examples of reported CDs described the fluorescence spectrum of CDs being centred mainly in the blue region, but now a whole spectrum of emission wavelengths has been accessed through multiple techniques such as heteroatom doping, graphitisation control and the use of different reaction solvents.[113,127,128] Carbon dot doping is the technique of introducing heteroatoms to confer and tune physicochemical and optical properties. The elements N, S and P are amongst those most common used.[129–131] The addition of atoms with different valences has a direct effect on the electronic states of the CD, consequently changing the width of the energy band gap and photoluminescence. Heteroatom doping can effect both intrinsic and surface electronic structures, therefore can manipulate the photoluminescence of CDs with fluorescence originating from both excited surface states and from the crystalline core.[106] Typically, introduction of heavier atoms red-shifts the fluorescence emission.[132] Bhattacharyya *et al* reported that increasing N content determined the size and position of sp^2 domains within the CDs, affecting photocatalytic and photoluminescent ability.[133] Red fluorescent carbon dots synthesised by sodium fluoride doping were reported by Yang *et al*.[134] Microwave synthesised CA/Urea CDs have a green fluorescent emission maxima which is red-shifted upon inclusion of fluoride ions in the reaction mixture.

The ability to generate CDs with a variety of emission wavelengths is important for applications such as biological imaging. Longer wavelengths are preferable in imaging of biological samples due to the presence of autofluorescence in the 350 to 500 nm range caused by endogenous fluorophores.[135] CDs with different functionalities and fluorescence emission allows for colocalisation and multiplexed images of biological samples, where multiple targets are imaged at once. CDs can be employed as orthogonal labels through the attachment of targeting groups to the nanoparticle surface.

1.5.4 CD FUNCTIONALISATION

As mentioned in Section 1.3.4, CDs can mimic multivalent biological surfaces through surface functionalisation (Figure 11). Functional groups on the surface can act as chemical handles for the attachment of biologically relevant molecules. The majority of functionalisation techniques use covalent attachment to the surface. Non-covalent methods such as electrostatic interactions and complexation have also been reported for the attachment of molecules to CDs that include fluorescein isothiocynanate (FITC) and a fluorescently labelled DNA strand.[136,137] Introducing new molecules around the CD increases the electron cloud density and so can often influence the fluorescence spectrum of the CDs.[138] Covalent techniques offer the greater flexibility, employing a variety of chemical strategies to attach a wide range of modifying agents. Azide-alkyne click chemistry was utilised by Gao *et al* to attach molecular beacon DNA and Li *et al* formed large molecular weight CDs through copolymerisation of hydroxy-CDs with glycidol.[139,140] The most common method for the covalent modification of carbon dots is via amide coupling. This is a reaction between an amino group and an acylating agent such as carboxylic acids. Both reacting functional groups are commonly found on the surface of CDs and so functionalisation is easily accessible. Coupling agents are used to activate carboxylic acids, the most common reaction conditions for CD amide coupling is 1-Ethyl-3-(3-dimethylaminopropyl)carbodiimide (EDC)/*N*-Hydroxysuccinimide (NHS) but carbonyldiimidazole (CDI) has also been reported.[138,141] Examples of carboxyl-terminated CD modification include Cu^{2+} sensor 1,4,8,11 tetraazacyclotetradecane cyclam, tyrosinase sensor DOPA and a *Salmonella eterica* sensing nucleic acid aptamer.[142–144] Zhong *et al* reported the conjugation of the glycopeptide antibiotic vancomycin to CA/urea CDs that labelled *S. aureus* and was employed to estimate bacterial concentration.[145]

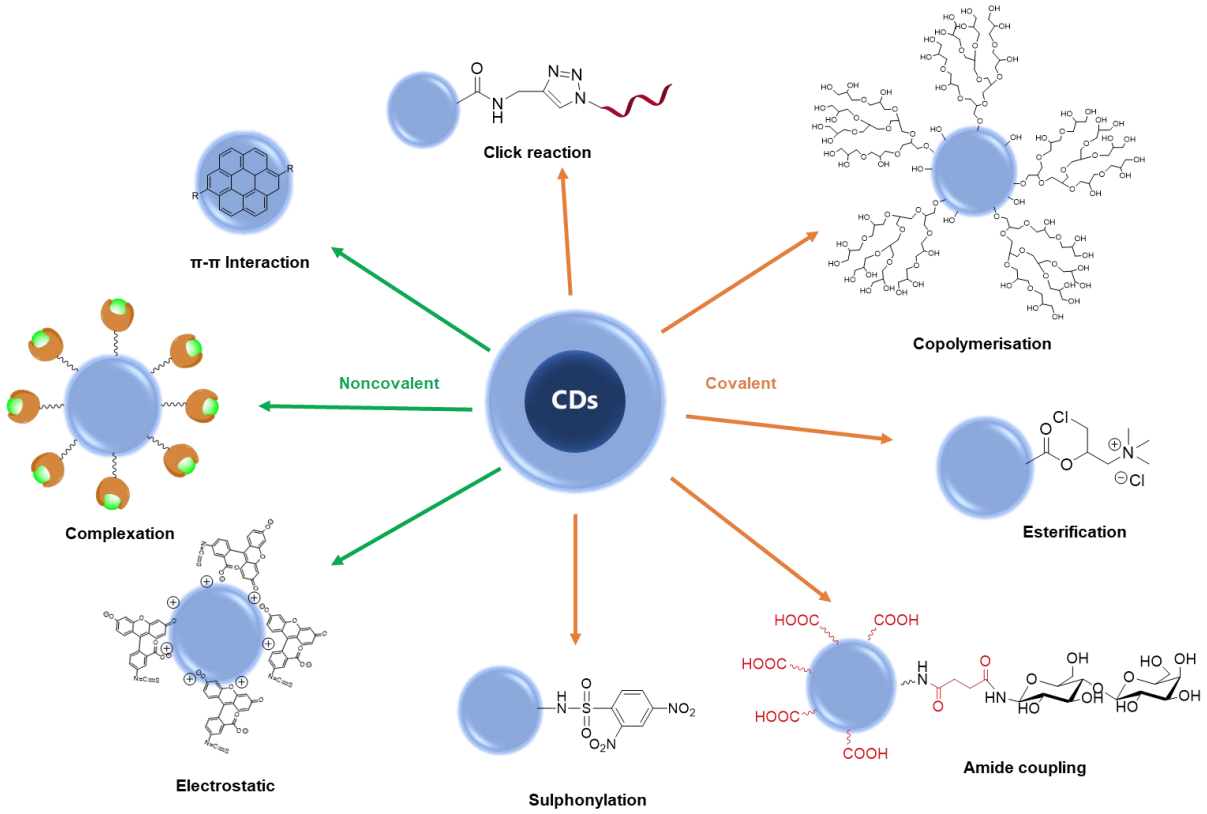

Figure 11 Summary of methods used for noncovalent and covalent surface modification of CD.[138]

1.5.4.1 GLYCAN MODIFICATION

Glycan conjugation to CDs has also been reported, Hill *et al* modified blue-fluorescent CDs (BCDs) via the conjugation of lactose for cancer cell labelling and Lu *et al* attached both glucose and 2,2,6,6-tetramethyl-piperidinooxy (TEMPO) to CDs for a dual modal MRI and optical cancer imaging agent.[141,146] Swift *et al* discovered that glucose-functionalisation of photosynthetic-enhancing CDs increases plant CD-uptake from soil.[147]

At the time of writing there appear to be no examples of covalently glycan-functionalised CDs for detection of bacteria. Instead of post-synthesis modification, Weng *et al* reported CDs synthesised with ammonium citrate and mannose, which selectively fluorescently labelled *E. coli* compared to CDs derived from ammonium citrate alone.[148] Blue fluorescent CDs were accessed through a 2 hour hydrothermal synthesis followed by treatment with sodium hydroxide with ammonium citrate in great excess (100 mg of ammonium citrate and 5 mg of mannose). A microplate spectrophotometer was used to detect labelled *E. coli* after a 1 hour incubation with CDs, this was also achieved in inoculated apple juice and human urine. Lai *et al* reported a synthetically similar mannose modification of hydrothermal ammonium citrate derived CDs that were able to label *E. coli*.[149] Following solid state CD synthesis, mannose was heated with the CDs for 2 hours at 200 °C for solid state dehydrative functionalisation. Microplate spectrophotometer analysis confirmed labelling of *E. coli* after incubation with CDs. Although, the mannose structure is not likely intact following the synthetic protocol, these reports demonstrate the ability of these mannose-derived materials to interact with *E. coli*.

Covalent modification of CDs would allow for flexible and designable post synthesis glycan modifications for target specificity and allow for orthogonal functionalisation for a potential theranostic approach. Theranostics is a rapidly growing field of research with the principle of combing imaging with therapy. Nanoparticles are ideal platforms for theranostic approaches as their surfaces are modifiable and allow for more specific delivery of therapy.[150] CDs are particularly suited due to their small size, large surface area, synthetic simplicity, low toxicity, aqueous solubility and biocompatibility.[151] Multiple nanotheranostic CDs have already been developed for cancer therapy with treatments including photodynamic therapy (PDT), photothermal therapy (PTT), gene delivery and targeted drug delivery.[152–155] For example, Tang *et al* designed a CD system with a FRET-based drug delivery system.[156] Cancer cells that overexpress folic acid receptors were targeted with CDs covalently modified with folic acid, the chemotherapy drug doxorubicin (DOX) was adsorbed to the CD surface through π-π interactions and acted as a FRET pair with the CD. Upon release of DOX into the cancer cell the CD fluorescence signal is recovered. PDT is the targeted killing of cells through reactive oxygen production initiated by light-induced excitation of photosensitisers.[157] Hua *et al* reported the synthesis of L-cysteine/*m*-phenylenediamine derived CDs conjugated with the protoporphyrin IX could target the nucleus of cancer cells and exhibited a PDT effect, through damage to genetic material, when irradiated with a 635 nm laser.[152] Another phototherapeutic technique, termed photothermal therapy (PTT), is possible when irradiated light is converted to heat which can cause localised thermal ablation of surrounding cells.[151] Sun *et al* developed red emissive CDs as multifunctional theranostic agents for nucleolar imaging, delivery of FITC into cells and as a PTT cancer agent with high photothermal conversion.[158]

As highlighted in Section 1.1, new, specific antibacterial therapeutics are needed to circumvent common resistance mechanisms, however examples of CDs acting as theranostic agents against bacteria are limited, with most work to date focused on cancer. CDs that were found to have broad-spectrum antibacterial activity and to fluorescently label cells were reported by Li *et al*. [159] Antimicrobial effects were found down to a concentration of 75 μg/mL however these CDs were found to degrade under visible light or at temperature of 37 °C, potentially limiting clinical applications. Mitra *et al* created dual purpose CDs by grafting sucrose derived CDs onto the surface of amine coated ZnO nanorods via

EDC/NHS coupling, combining the fluorescence labelling abilities of the CDs and the antibacterial effect of ZnO nanorods.[160] The minimum inhibitory concentrations (MICs) found were 144 µg/mL and 132 µg/mL for *E. coli* and *S. aureus* respectively. However, CD coating lowered the antibacterial efficacy of the ZnO nanorods, and the method of bacterial attachment/labelling and the specificity of the theranostic agent were not explored in the research. Many theranostic CDs reported involve the use of a secondary component such as ZnO nanorods, magnetic nanoparticles and titanium/hematite nanostructures.[161,162] Yang *et al* reported a theranostic system based on functionalised CDs alone.[163] Blue fluorescent aminoethylethanolamine(AEEA)-glycerol CDs were conjugated with lauryl betaine with EDC/NHS coupling, yielding CDs with multicolour emission. Selective labelling of Gram-positive bacteria was attributed to the surface presentation of hydrophobic carbon chains terminating in positively charged quaternary ammonium groups, with the MIC for *S. aureus* reported as 8 µg/mL. This system offers advantages of simplicity, specificity and higher efficacy. However, only Gram-positive species can be targeted using these CDs as there is no built-in tuneability to the system.

Carbon dots, combined with glycan modifications for tuneable specificity, have potential applications as a new theranostic therapy which could introduce alternative antibacterial methods of action for pathogens resistant to commonly used treatments.

1.6 ROLE OF G-QUADRUPLEXES IN BACTERIA

As outlined in Section 1.1, overcoming bacterial resistance requires novel approaches to combat the multiple known pathways to resistance development. A comparatively understudied field of research is bacterial G-quadruplex (G4) DNA, with the presence, location and functions of bacterial G4s relatively elusive in prokaryotic cellular processes.[164] However, scans of bacterial genomes have shown that G-quadruplex forming sequences may be widely distributed, and consequently they could have significant roles in gene regulation and other cellular processes.[165] Stabilisation of these G4 DNA structures could offer a potential new route to antibacterial activity through disruption to normal metabolic processes.

1.6.1 NUCLEIC ACIDS

Nucleic acids are formed of monomers, termed nucleotides, that consist of a ribose sugar conjugated to a nitrogenous base and a phosphate group.[166] DNA contains a deoxy ribose sugar and carries genetic information, whereas RNA has a hydroxyl group at the 2’ position on the sugar and is involved in the translation of information to function.[166] The sequence of nitrogenous bases in the DNA strand; adenine, thymine (uracil for RNA), cytosine and guanine, carries the genetic information encoding for proteins that are synthesised at the ribosome during translation (Figure 12). Both the bases and the conformation of the sugar ring can also influence the secondary structure of the nucleic acid.

For DNA, the most common secondary structure is the classic double helix, proposed by Watson and Crick in 1953 (Figure 12).[167] The complementary structure of the bases allows for hydrogen-bond engendered pairing between nucleotides which results in two strands associating and twisting into the right-handed double helix structure.[168]

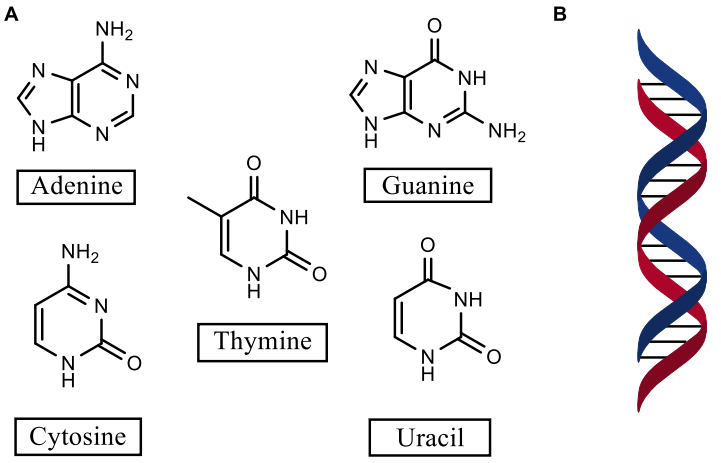

Figure 12 A. Five different nitrogenous bases. B. Representation of the double helix structure of DNA.

After this initial discovery, over ten different potential secondary structures have also been identified.[169] For example, Karst Hoogsteen reported in 1963 the presence of two hydrogen bonds between adenine and thymine, divergent from those reported by Watson Crick.[170] The combination of both types of hydrogen bonding allows for the formation of DNA triplexes, where a third strand of DNA can hybridise through Hoogsteen hydrogen bonds in the DNA major groove (Figure 13).[171]

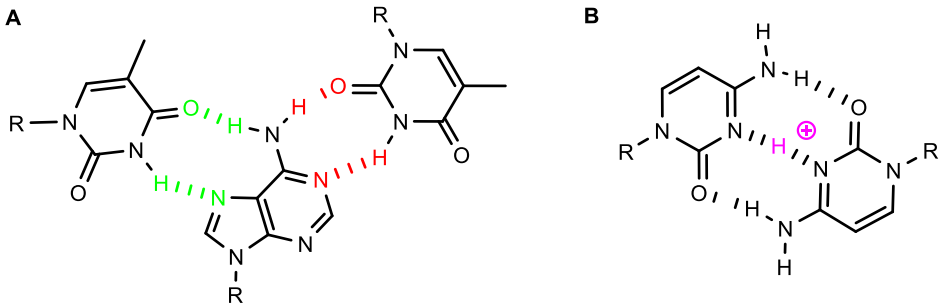

Figure 13 A. The triplex structure highlighting the Hoogsteen base pairing (green) and Watson-Crick pairing (red) between thymidine and adenosine. B. The i-motif structure between protonated cytosine bases.

There are two different four-stranded secondary structures identified, the i-motif and the G-quadruplex, both caused by the abundance of one type of nitrogenous base in a sequence.[172] The i-motif structure occurs in cytosine-rich nucleic acids and is stabilised in acidic conditions. The tetramer forms when two DNA duplexes are orientated antiparallel with respect to one another, stabilised by the intercalation of cytosine-cytosine$^+$ base pairs.[173]

1.6.2 G-QUADRUPLEXES

The first indication of the of a tetrad structure formed from guanine rich materials was reported by Gellert *et al.* in 1962 when studying gels formed by guanylic acid solutions, as first reported by Bang in 1910.[174,175] Aggregates were analysed and found to be ordered, four stranded structures. The first example identified in nucleic acids was by Henderson *et al* in 1987, by NMR analysis of eukaryotic telomeric regions of DNA.[176] After spontaneous formation of these tetrads by guanine-rich sequences in a salt buffer, Sen and Gilbert proposed that this must also occur *in vivo*.[177] This led in the early 1990s to a growing interest in further elucidation of these structures, using x-ray diffraction[178,179] and NMR techniques.[180,181]

1.6.2.1 G4 STRUCTURE AND TOPOLOGIES

A general rule of G4 formation is that it requires four consecutive runs of guanine in a sequence, containing at least 2-3 residues though there are exceptions to this rule (for example loop formation).[182] Guanine bases are arranged in a tetrad arrangement and at least two of these tetrads are stacked, stabilised by Hoogsteen and Watson-Crick hydrogen bonding.[183] A central monovalent cation (Na^+ or K^+ most common) stabilises the structure and is essential for G4 formation.[184] A representation of this structure is shown in Figure 14.

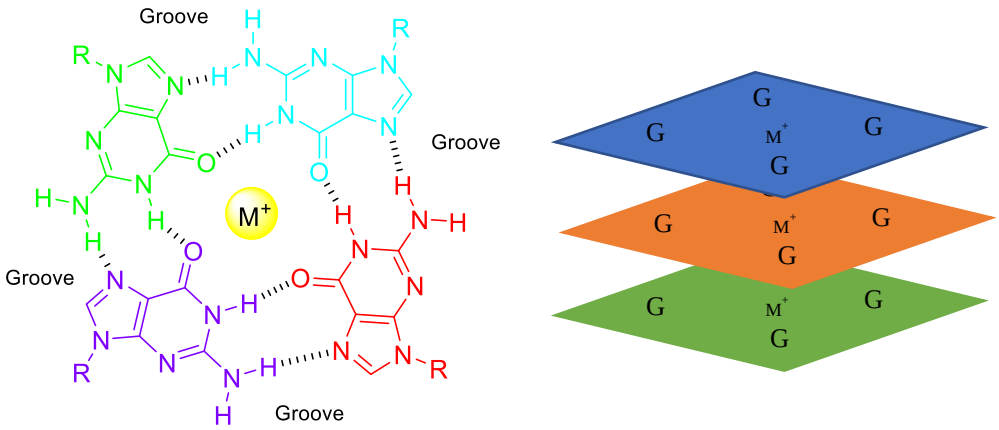

Figure 14 Left- molecular structure of G-tetrad. Right- systematic representation of a G-quadruplex.

G4 structures can be composed of 1-4 different nucleic acid strands and are found in both DNA and RNA. Dependent on the loops between the guanine runs, G-quadruplexes can form a variety of different topologies. A single G4-forming sequence potentially has the ability to fold into multiple different topologies, formed by either intra- or intermolecular folding. For example, tetramolecular G4s, formed from four different nucleic acid strands, can either be in parallel or anti-parallel alignment (Figure 15).

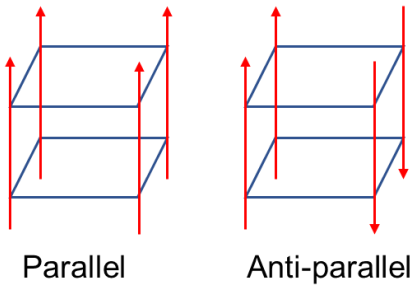

Figure 15 Representation of parallel and anti-parallel topologies of tetramolecular G-quadruplexes.

1.6.2.2 G-QUADRUPLEXES RELEVANCE

The discovery of G4 structures under physiological conditions precipitated a large increase in interest in this field of research over the past decade.[177] G-quadruplexes have been identified in multiple different organisms including protozoa,[185,186] plants,[187] viruses[188–190] and bacteria.[164,191] However, a large majority of the publications released in this field are concentrated on G-quadruplexes in the human genome. After high resolution sequencing, 716,310 G-quadruplex structures were identified in the

human genome and were notably found in oncogenes and sites of genomic instability.[192] Consequently, this has led to the identification of physiological G-quadruplex sequences as potential therapeutic targets. Although there are a range of conditions and diseases that have been identified as potentially associated with G4 sequences the majority of the research has been focused on cancer.

There have been many G4 sequences found, both DNA and RNA, in regions where modulation of gene expression may make it possible to cause an effect on the hallmarks of cancer.[193,194] One example is G-quadruplexes found in telomeric DNA.[195] In brief, G-quadruplex DNA was found to be particularly prevalent in telomeres, single-stranded guanine-rich DNA regions which protect the end of the chromosome.[196] In healthy cells, these ends shorten after each replication, leading to eventual cell apoptosis.[197] The enzyme telomerase, which reverses telomere degradation, has been found at significant concentrations in 80-85% of human cancers.[198] This upregulation prevents cellular senescence and therefore allows continual replication and uncontrolled proliferation. Zahler and co-workers found that when telomeric DNA was folded into a quadruplex, telomerase activity was inhibited.[199] However, without stabilisation the quadruplex unfolds due to protective proteins around the DNA within the cell. Therefore, stabilization of quadruplexes has been targeted as a potential cancer therapeutic target. Telomerase has been targeted previously by reverse transcriptase inhibitors and more successfully in the blocking of the template region of telomerase with complementary oligonucleotides.[200,201]

1.6.2.3 G-QUADRUPLEX LIGANDS

The stabilisation of G4 structures by exogenous ligands was first shown in 1997 by Hurley and Neidle who targeted the inhibition of telomerase.[202] The substituted anthraquinone derivative, **15**, (Figure 16) was only the first of many G-quadruplex ligands discovered, as the over the next 20 years the field has grown greatly.[203,204]

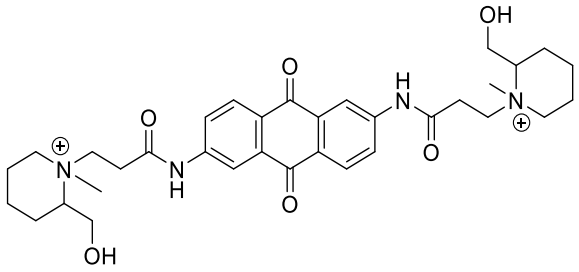

15

Figure 16 Anthraquinone derivative discovered by Neidle and Hurley to be the first G-quadruplex ligand.

G4 ligands have been designed with certain properties and functional groups to target different aspects of the G4 structures.[205] Rigid aromatic heterocyclic frameworks are employed to intercalate with the G-tetrads by π- π stacking interactions.[206] The grooves found in the intersection of the phosphate backbone of the quadruplex, or loops between the guanine runs, can also be targeted by functionalising side-chains.[188,207]

A number of small-molecules have already been reported and widely investigated for their stabilisation of G4s (Figure 17). The porphyrin derivative TMPyP4 was known initially as an DNA intercalator before its extensive use as a G quadruplex stabilising ligand [208,209]. Likely due to its high cationic charge, TMPyP4 is not selective between duplex and quadruplex DNA.[210] The molecule BRACO-19, a tri-substituted Acridine derivative, developed by Neidle *et al*, has also shown G-quadruplex binding

activity. Initially developed as a telomerase inhibitor, it has since been used as G4 ligand in multiple organisms targeting quadruplexes in regulatory regions of the genome.[211] For example, through stabilisation of G4 motifs in the long terminal repeat (LTR) region, BRACO-19 exhibited anti-HIV-1 activity.[188]

Pyridostatin is a quinoline-containing ligand discovered in 2008 by the Balasubramanian group as a candidate therapy targeting telomerase and is very selective for G4s.[212] It has also been shown to affect transcriptional regulations in neurons, and its potent interactions with G4s has led to its exploitation as a tool for G4 sequencing [192,213].

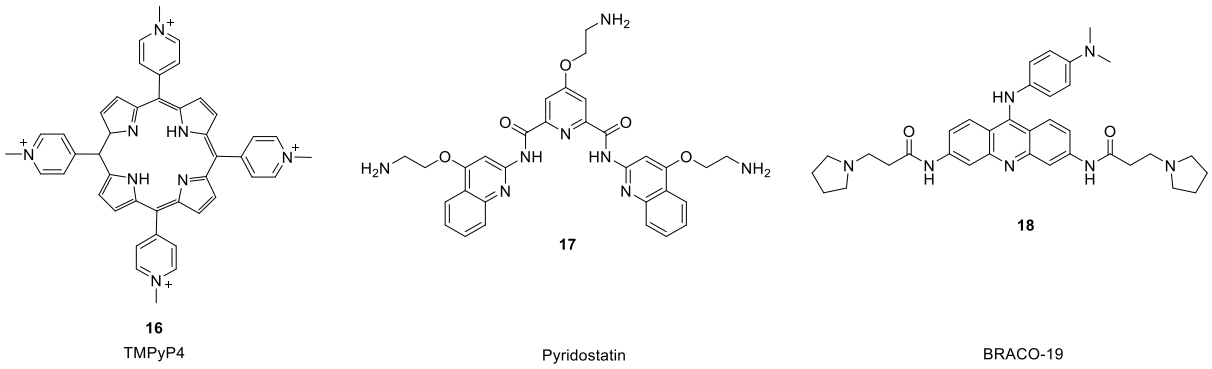

Figure 17 Known G-quadruplex ligands TMPyP4, pyridostatin and BRACO-19.

1.6.2.4 Analysis of G- quadruplexes

To ascertain the presence and strength of ligand binding by G-quadruplexes, a number of biophysical techniques can be used, including circular dichroism, FRET, NMR spectroscopy, molecular modelling and calorimetric titration experiments.[214–216]

Circular Dichroism Spectroscopy

Circular dichroism (CD) spectroscopy is a robust tool for characterising secondary structures of proteins and nucleic acids. CD is a form of light absorption spectroscopy, where a chiral sample differentially absorbs circularly polarised light to yield diagnostic spectral features. First a polarising filter creates linearly polarised light and then a quarter-wave plate causes the associated electromagnetic field to rotate about its direction of propagation while retaining a constant magnitude, therefore creating circularly polarised light (Figure 18).[217] A chiral sample will absorb the two directions of circularly polarized light by different amounts, the difference in this molar absorptivity a function of temperature, concentration and chemical environment.

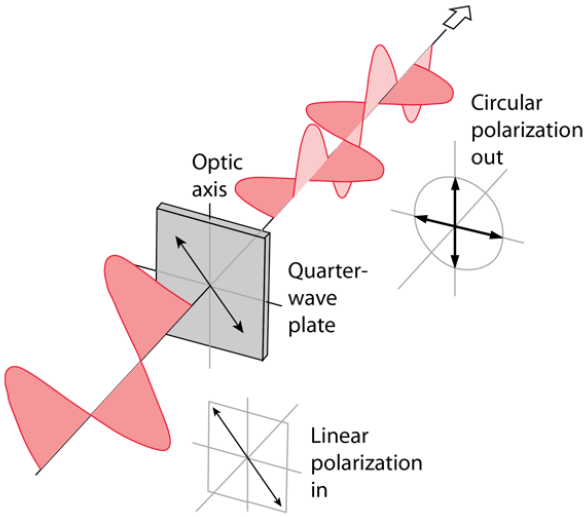

Figure 18 Diagrammatic representation of production of circularly-polarised light. Figure by Carl R. Nave.

As G-quadruplexes are polymorphic and can form multiple topologies, whose sequence of *syn* or *anti* glycosidic bond angles are different, they relate to different characteristic spectral features when observed by CD spectroscopy.[218] CD can be used to study the effects of ligand binding, and to confirm that the ordered nucleic acid sequence forms a G-quadruplex.

Förster Resonance Energy Transfer (FRET) Melting Assay

Förster Resonance Energy Transfer (FRET), also commonly termed fluorescence resonance energy transfer, is a distance-dependent phenomenon of non-radiative energy transfer between two chromophores. When the emission spectrum of the donor overlaps with the excitation profile of the acceptor molecule, energy is transferred through a intermolecular long-range dipole-dipole coupling interaction (Figure 19).[219] Because of the distance (r) dependence, which has an inverse r^6 relationship, molecular processes that cause a change in molecular proximity within a 1-10 nm range can be probed.[220,221]

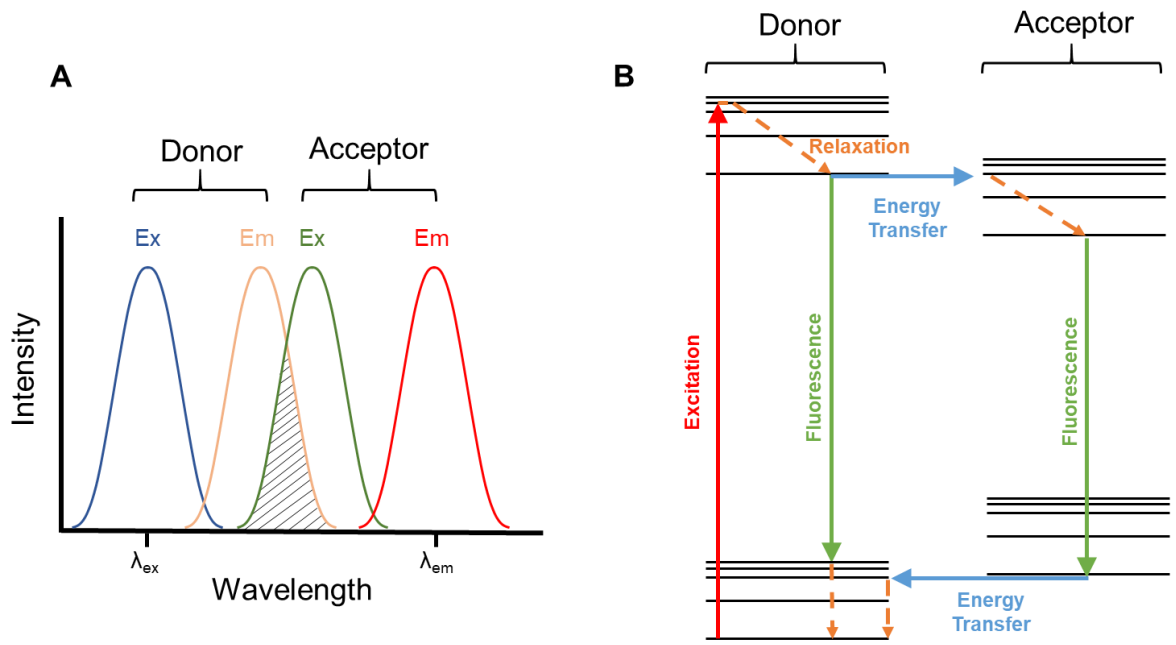

Figure 19 Representation of a FRET system. A. Fluorescence spectrum displaying the spectral overlap between donor emission and acceptor excitation. B. Jablonski diagram showing alternative energy transfer route to fluorescence. Solid lines representing a radiative process and dashed showing a non-radiative process.

FRET melting assays are commonly employed when investigating G4 ligand binding, and were first developed for this use in 2001 by Mergny *et al.*[222,223] Ligand-induced stabilisation increases the melting temperature (T_m) of a G-quadruplex and therefore can be used as an indication of the efficacy of G4 binding of the ligand, with ligand T_m showing good correlation with telomerase inhibition efficiency.[223] Generally, a nucleotide sequence is labelled with a FRET pair, commonly TAMRA and FAM, which are within close enough distance when the sequence is folded into a quadruplex for FRET to occur, but are not when the oligonucleotide is in the unfolded state. The fluorescence emission of the donor molecule, for FAM at a λ_{em} of 520 nm, is quenched when this is in close proximity to the acceptor, and so can be used to monitor folding (Figure 20).

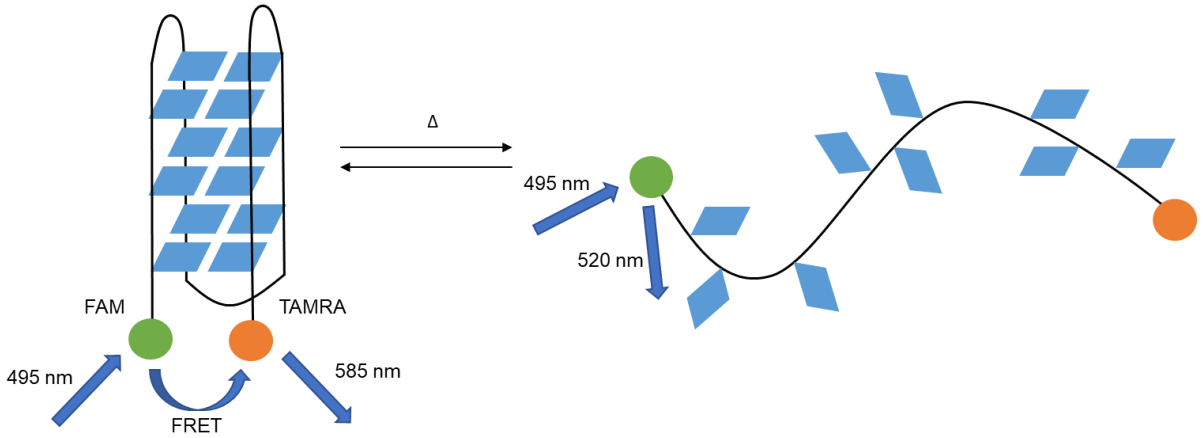

Figure 20 Pictorial representation of the FRET melting assay with FAM/TAMRA FRET pair. Heat catalyses the unfolding of the quadruplex and consequently leads to loss of the FRET interaction.

The melt temperature, T_m, is determined as when the fluorescence intensity of the donor is half of its maximum value. The introduction of a stabilising ligand increases the temperature of unfolding and can be compared to the T_m of the quadruplex in the absence of ligand to yield the ΔT_m, an indication of stabilisation when compared with different G4 ligands. This technique lends itself well to high-throughput screening as it can be set up in a 96-well plate and the high sensitivity of fluorescence detection means that minimal quantities of oligonucleotide are needed.

1.6.2.5 G-QUADRUPLEXES IN BACTERIA

The mammalian genome has been widely probed for the presence and function of G-quadruplexes and these sequences have been targeted for many potential therapeutic treatments.[182] In comparison, research into G4s in microbial systems is limited, and relatively little is known of the role they play in gene regulation and metabolism.

In the early 2000s, researchers first identified guanine-rich sequences in the genomes of multiple prokaryotes as well as eukaryotes and started to predict the formation of G-quadruplex structures, such as in the 2004 paper by Rawal *et al* predicting G4 DNA regulatory motifs in *E. coli*.[224] Interest in this field of work has grown since and, although still limited, more is now known about the role G4 structures play in bacterial cellular mechanisms. The regulatory regions of the genome of the extremophile *Deinococcus radiodurans* contain G-quadruplex motifs that have been shown to contribute to the species' radioresistance.[225] Also, G4 sequences in the genomes of the microbial pathogens *Treponema pallidum* and *Borrelia burgdorferi* act as activators in antigenic variation (Av), the process of altering proteins and carbohydrates presented on the bacterial surface to avoid immune detection.[226]

As more G4 sequences have been identified and isolated within bacteria, their involvement with gene expression and regulation has led to their targeting as a potential drug target. The use of stabilising G-quadruplex ligands as therapies would offer an innovative antibacterial mechanism. This is of particular interest as many G-rich sequences are conserved in drug-resistant strains, suggesting a potential effectiveness of G4 ligands for multi-drug resistant, as well as antibiotic-susceptible, bacterial strains.[226,227] Research with a variety bacterial species has demonstrated the potential of G4 ligands to affect regulatory mechanisms within the cell.

One example of a confirmed G4 structure *in vivo* was found by Cahoon and Seifert in *Neisseria gonorrhoeae,* and was linked with the microbe's resistance to immune detection.[228] Genetic screens were employed to identify a guanine-rich sequence near the antigenically variable pilin locus of pathogenic *Neisseria gonorrhoeae.* This sequence was confirmed to have a parallel G4 structure by CD spectroscopy and NMR. After discovering that mutations in the G4 sequence blocked pilin Av a G4-specfic ligand, N-methyl mesoporphyrin IX (NMM), was investigated. *N. gonorrhoeae* grown on a non-toxic concentration of NMM showed significantly decreased antigenic variation, consistent with the publication's conclusions on the importance of G4 structures to pilin Av.

The use of G4 ligands in nitrate assimilation control in the soil bacterium *Paracoccus denitrificans* has also been demonstrated by Waller *et al*.[229] After a genome-wide analysis identified 494 potential G-quadruplex forming sequences, one twenty-one nucleotide sequence containing four guanine runs was identified in the intergenic region of *nasT*. Gram-negative *P. denitrificans* displays a wide metabolic flexibility as it can support anabolic cellular processes with a range of different nitrogen sources, including nitrates. The *nasT* gene is an essential positive regulator for NO_3^- engendered growth and so the upstream G4 was targeted in order to induce changes in NO_3^- dependent growth. Two known G4 ligands, $TmPyP_4$ and a benzophenoxazine compound, were shown to stabilise the quadruplex *in vitro*

through CD, fluorescence titrations and FRET melting assays (a ΔT_m of 30 °C and 5 °C respectively). Studies *in vivo* demonstrated that bacterial growth in the presence of nitrates was sensitive to both ligands through inhibition of *nas* expression. This is one of the first demonstrations of quadruplex ligands being used to control microbial metabolic pathways.

A recent publication by Jain *et al*. reported an inhibitory effect of G4 ligands on quadruplex motifs found in the genome of *Salmonella enterica*.[226] Three guanine-rich nucleotide sequences were identified in the regulatory regions of the genes *mgtA*, *entA* and *malK/malE*, which control the homeostasis of essential nutrients magnesium, iron and maltose respectively. The morphology of these structures was confirmed with techniques including ^{1}HNMR and CD. The selective binding of the G4 ligands BRACO-19 and 9-Aminoacridine against the three G4 sequences was demonstrated by isothermal titration calorimetry and increased stabilisation of the quadruplexes shown by CD melting studies. After qRT-PCR in the presence of BRACO-19, *mgtA*, *entA* and *malK/malE* all displayed a greater than three-fold decrease in expression, which would likely affect survival of the bacterium within a host macrophage as without control of essential nutrients, mechanisms to respond to reactive oxygen/nitrogen stresses would be inhibited. This therefore highlighted a direct link between G4 stabilisation and pathogen inhibition. These G4 targets offer a potential alternative route to antibacterial therapy without risk of acquired resistance as they are highly conserved in both in drug-susceptible and drug resistance strains.

A potential G4 target has also been found in multi-drug resistant *K. pneumoniae*, a bacterial pathogen involved in many nosocomial infections, by Shankar *et al*.[227] After screening for evolutionarily conserved G4-forming sequences, six targets were identified in *K. pneumoniae* with potential biological relevance arising from positioning upstream of genes essential for bacterial metabolism and nutrient transport. CD melting assays confirmed G4 stabilisation with BRACO-19 and incubation of this ligand with the bacterium prevented growth, displaying a reduction in expression of genes downstream of the targeted G4s.

Potential G4-forming sequences have been identified in *E. coli*, some located in regulatory regions including transcription and signal transduction[191,230,231]. G4 ligands have been utilised to target helicases, DNA unwinding proteins, in *E. coli*, and shown to limit their activity.[232,233] Within *M. tuberculosis*, G-rich sequences have been found and linked to essential regulatory genes whose roles includes immune response and membrane formation.[234,235] Inhibition of *M. tuberculosis* growth was found by Perrone *et al* after incubation with the G4 ligands BRACO-19 and c-exNDI 2.[236] However, for many bacterial species, including clinically important pathogens such as *S. aureus*, little research has been undertaken into identifying and targeting G4s.

Based on results from all the publications detailed herein indicate that, although not extensively researched, G-quadruplex morphologies are present within bacteria, and some of these are located in regions of clinical interest i.e. where their targeting with and stabilising by small-molecule ligands has the potential to modify cell function and viability.

1.7 PROJECT AIM

The aim of this project is to investigate diagnostic and antibiotic tools that can offer improvements on current protocols and alternative mechanisms of action. Different fluorescent nanoparticle-based systems will be explored and developed for bacterial labelling and antibacterial therapeutics. Novel work will also be undertaken in the antibacterial activity of ligands designed to target nucleotide G-quadruplex structures.

Carbon-based nanoparticles, carbon dots (CDs), will be the main class of probe explored in this body of work. Previously reported green-fluorescent CDs (GCDs) offer many synthetic advantages and have potential as an accessible new tool for bacterial identification.[237] GCD internalisation and fluorescent labelling of clinically relevant bacterial species will be developed and optimised, focusing on an easily recreated, simple methodology to target a wide skill range. The effect of bacterial viability will also be explored in combination with low-energy LED irradiation, including attempts into elucidating the antibacterial method of action. The use of CDs will also be explored in targeting specific bacterial labelling through exploitation of natural lectin-carbohydrate interactions.

Nucleic acid secondary structures, G-quadruplexes (G4), are formed in guanine rich sequences and have been the focus of detailed research due to their implications in cancer resulting in G4 stabilising ligands being a popular therapeutic target. However, the presence and role of G4s in bacteria is an area of limited understanding. In this work, a library of previously synthesised G4 ligands will be screened against multiple drug resistant strains of clinically relevant bacteria to access their potential as antibiotic agents. The structure of an RNA G4 sequence from *E. coli* will also be assessed and stabilisation induced from G4 binding ligands measured.

2. GREEN FLUORESCENT CARBON DOTS AS BIOIMAGING AND ANTIBACTERIAL AGENTS

This chapter outlines new applications of a previously reported green fluorescent carbon dot (GCD) within a microbiological context. In this work, GCDs were initially used as general fluorescent labels for bacteria. The labelling process was optimised and quantified within different bacterial species. The potential antimicrobial activity of GCDs alone and also in combination with LED irradiation was also assessed. GCDs, synthesised from glucosamine hydrochloride and 1,3 phenylenediamine, have previously been shown to show labelling and toxicity in combination with LEDs in cancer cells. Also investigated were the potential causes of the antibacterial activity found, techniques include an intracellular ROS assay, the use of scanning electron microscopy (SEM) and proteomic analysis. The work discussed was conducted by myself with assistance for certain techniques, accordingly acknowledged. SEM and proteomics analysis was run by Yuiko Takebayashi and the relative imaging and proteomic facilities within the School of Cellular and Molecular Medicine.

2.1 SYNTHETIC OUTLINE

The carbon dots used in this work were synthesised following a procedure developed previously in the Galan group.[237] The first generation of carbon dots within the group, developed by Stephen Hill, were a blue-emitting nanoparticle synthesised from glucosamine hydrochloride and 4,7,10-trioxa-1,13-tridecanediamine (TTDDA) (BCDs). These water-soluble fluorescent nanoparticles emitted in the blue end of the visible spectrum (λ_{em} 350 nm , λ_{em} = 420 nm) and were used in live cell imaging.[141] However, as mentioned in Section 1.5.3, auto-fluorescence can cause complications with the fluorescent labelling imaging and so a new material, also developed by Stephen Hill, which would emit at a longer wavelength was pursued. This was achieved with a simple three-minute microwave synthesis with glucosamine hydrochloride and 1,3 phenylenediamine (Scheme 2).[237] These monodisperse, quasi-spherical green fluorescent CDs (GCDs) were purified by centrifugal filtration only. This purification technique uses a split-chambered centrifuge tube with a 10,000 Da molecular weight cut off (MWCO), the crude product transferred to the upper chamber and particles below the MWCO pass through upon application of centrifugal force. HR-TEM has shown the particles to have an average diameter of 2.42 ± 0.55 nm with an amorphous, carbonaceous core and a 33 % quantum yield. The ease of synthesis and purification is an advantage with regards to other strategies to access similar materials as it allows researchers from different fields (non-chemists) to recreate the synthesis of GCDs in their lab.

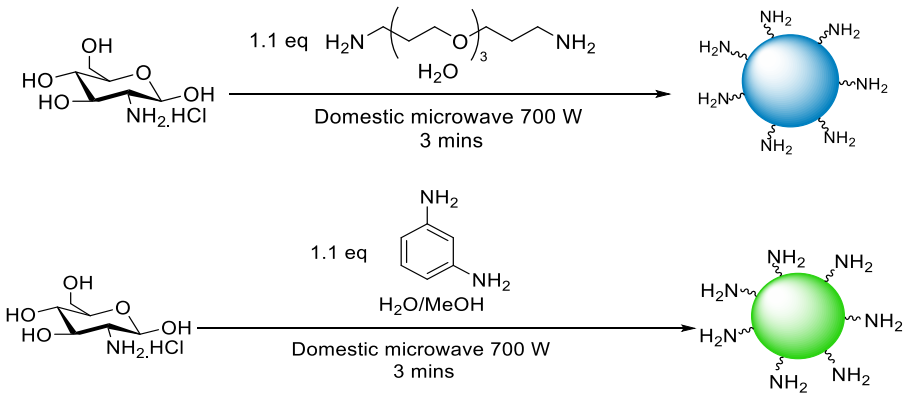

Scheme 2: Synthetic schemes for previously developed blue BCDs (top) and green GCDs (bottom).[237,238]

2.2 BACTERIAL LABELLING

Previous work from the Galan group demonstrated that GCD nanoparticles are passively internalised within human cell lines (HeLa and HDF), localising within the nucleus of the cell via DNA intercalation and easily visualised using confocal microscopy.[237] This posed the question whether bioimaging could also be feasible in bacteria. Initial GCD labelling was first performed on *Escherichia coli* (BW25113 strain), a Gram-negative bacterium and *Staphylococcus aureus* (Newman strain), a Gram-positive bacterium, before being tested on two further Gram-negative species, *Pseudomonas aeruginosa* (PA01 strain) and *Klebsiella pneumoniae* (NCTC 5055 strain). The strains of bacteria were chosen for their clinical relevancy and availability in the laboratory. A simple methodology for labelling was developed wherein a 10 x10^8 cfu/mL suspension of bacteria was incubated with GCDs. This is similar to methodologies in literature detailing nanoparticle bacterial labelling but offers advantages in photostability, synthetic simplicity and speed of labelling .[239–241] Initially laser confocal scanning microscopy (LCMS) confocal microscopy was used to confirm fluorescent labelling.

2.2.1 LABELING AND IMAGING OPTIMISATION PROTOCOLS FOR CONFOCAL MICROSCOPY

Initial attempts to image the bacterium that had been incubated with the GCDs were unsuccessful due to the movement of the cells across the microscope slide preventing attainment of clear images, especially composites formed from z-stacks. Therefore, a combination of paraformaldehyde (PFA) fixation and liquid mountant was employed to address this complication.

Biological fixation facilitates accurate observation of the morphology of the bacterial cell by terminating ongoing biochemical reactions and preserving the cell in a 'life-like' state.[242] The objective is to retain the bacterial cell's components in their native compartments, presenting a microscopical appearance.[243] The different fixation methodologies are split into two groups: additive and denaturing fixations. Paraformaldehyde (PFA) is an additive fixation method which causes covalent bonds to form between proteins, preserving protein structure.[244]

A mounting medium is used to prepare samples for confocal microscopy, embedding the sample under a coverslip. This protects the specimen from the external environment, binding the coverslip to the slide and sets the micro-organisms in place, allowing for imaging. The refractive index of the mountant can

affect the quality of imaging and so should be close to that of the glass slide and coverslip.[245] Initially ProLong™ Gold was used but mountants ProLong™ Diamond and ProLong™ Glass were also tested but were found to give near identical results to the gold. ProLong™ gold was used for all images reported in this work.

The optimised procedure allowed for imaging and identification of the GCD labelling (Figure 21). In brief, suspensions of bacteria grown overnight on agar were made to an optical density (OD) of 0.8-1.0 before incubation of GCDs (200 µg/mL for 30 mins). Samples were then centrifuged; the supernatant was removed and the pellet of bacteria resuspended in PBS. After fixation with 4% PFA for one hour and setting the sample with the mountant (cured for 24 – 48 hours) the sample could then be imaged using confocal microscopy. HyVolution software was also employed to deconvolute confocal images to produce higher-resolution images (Huygens HyVolution 2 software)[246]. This technique combines both optical, and computational, super-resolution to further resolve the fluorescence images.

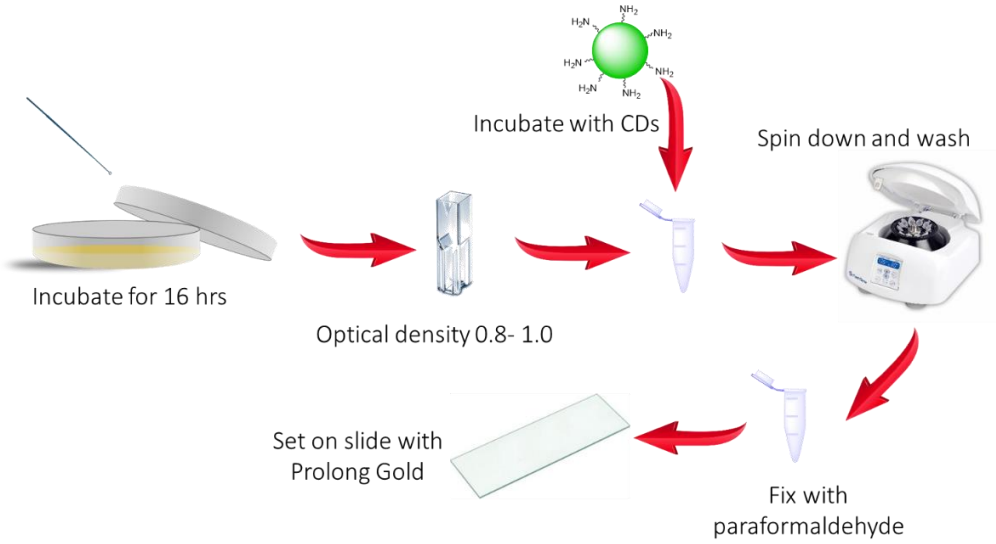

Figure 21 Pictorial diagram of GCD bacterial labelling methodlogy.

All bacterial species evaluated showed fluorescent labelling after incubation with GCDs (Figure 22). PBS was chosen as the media since it is isotonic which prevents osmotic stresses that could be introduced from suspending bacteria grown on media into water instead.[247] Aggregation of CDs can occur in PBS over longer durations due to the charged ions in the solution interacting with the surface charges on the GCD, however this effect was not observed during the labelling procedure.

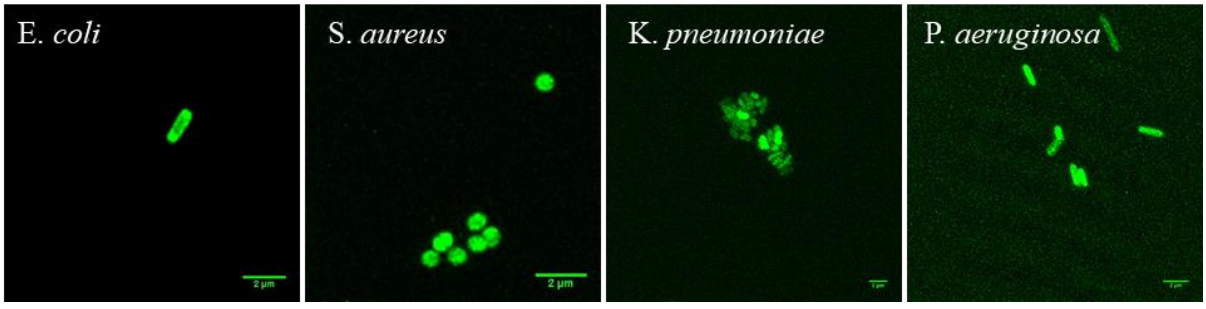

Figure 22 Hyvolution confocal microscopy z-stack max-projected images of GCD labelled (400 µg/mL) bacteria; *E. coli*, *S. aureus*, *K. pneumoniae and P. aeruginosa*.

A range of different GCD concentrations were trialed during extensive optimisation of the labelling procedure. Throughout out most of the bacterial labelling analyses, an overall concentration of 200 µg/mL GCDs was used for a better signal-to-noise ratio, however bacterial labelling was seen by confocal microscopy down to 20 µg/mL. As expected, the level of observed fluorescent labelling increased with increasing GCD concentration (Figure 23).

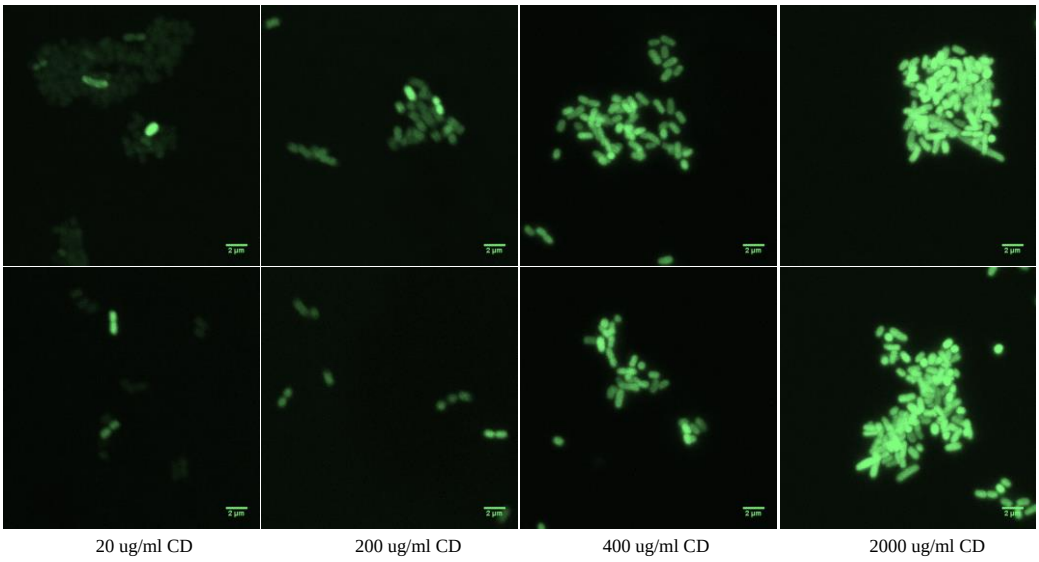

Figure 23 Effect of increasing GCD concentration in *E. coli* on labelling intensity.

2.2.2 QUANTIFYING BACTERIAL LABELLING FROM CONFOCAL IMAGES

Fiji software allows for the estimation of fluorescent labelling in comparison to a control.[248] The software can identify objects in images, create a 'mask' from the outline which is then consequently used to measure signal intensity within these areas. This generates a readout that can be compared to an autofluorescence control. Using this method initial estimations of the fluorescence labelling differences between bacterial species could be measured (Figure S 2). However, readouts generated varied significantly within each sample slide and gathering large number of images is very time-consuming and expensive, so datasets were limited. Therefore, a higher throughput method was sought for better quantitative measurements.

2.2.3 FLOW CYTOMETRY

Flow cytometry is a technique that uses lasers to produce scattering of light and fluorescent emission by a sample to measure characteristics of cell populations. This dual detection allows for the determination of fluorescent population concentrations in a mixed sample. In an effort to get higher throughput readings and therefore a more accurate determination on labelling, the use on flow cytometry was tested. However, issues arose when GCD labelling caused bacteria to aggregate, causing coincidence (coincident arrival of cells) in the data and giving false results (Figure S 3). Dilutions of the mixture were attempted but labelling was difficult to detect after. Bacterial samples could not be prepared at lower concentrations as pelleting would not be visible during PBS washes. The same issues

were also faced with samples prepared with a live/dead stain (Zombie Aqua) for assessment of toxicity. The departmental facilities had limited experience in flow cytometry for bacteria and so no immediate solutions were found to these specific difficulties in data collection and this approach was not pursued further.

2.2.4 FLUORESCENCE QUANTIFICATION WITH MICROTITER PLATE READER

Previous publications on fluorescent nanoparticle bacterial labelling have used a microplate reader to report labelling.[239] This simple method allows for a higher throughput technique. Instead of analysing singular bacterial cells, an average of each well is taken and multiple readings can then be repeated in biological replicates to achieve more reliable data. It also allows for comparative quantification of GCD labelling and also potentially quantification of bacterial concentration. Fluorescence intensity of bacterial cultures with known GCD concentrations was measured and plotted (Figure 24), allowing linear regression analysis to calculate a straight-line equation for estimation of bacterial concentration of labelling. Samples incubated with GCDs at identical bacterial concentrations, after subsequent PBS washes, can be measured in a microtiter plate, and the fluorescence intensity extrapolated to find the GCD concentration within the sample. Maintaining similar levels of bacterial concentrations is important as high concentrations of bacteria physically impede fluorescence and effect the intensity readout.

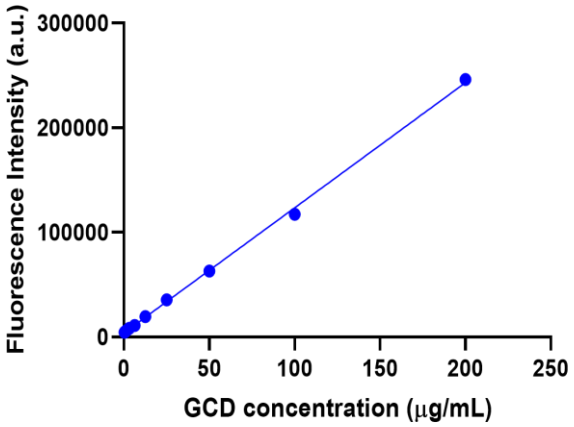

Figure 24 Calibration curve of known GCD concentrations in *E. coli* against fluorescence intensity. Linear regression analysis fit straight line with equation y=1195.2x+4042.

Different bacterial species were once again incubated with 200 μg/mL of GCDs and concentration of GCD uptake was calculated from the calibration curve (Figure 25). The labelling levels for the three Gram-negative species were notably higher than for the Gram-positive *S. aureus*.

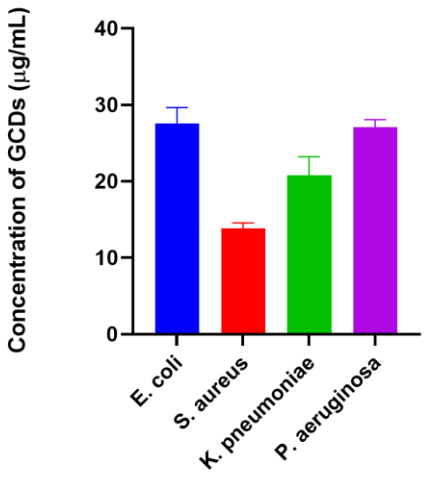

Figure 25 Quantification of GCD labelling for each bacteria species at a concentration of 1 x10^8 cfu/mL after 30 min incubation with 200 µg/mL of GCDs at room temperature. Repeated in triplicate.

The differential labelling observed between Gram-positive and Gram-negative bacteria could be linked to many factors such as bacteria cell wall composition and differences in cellular uptake mechanisms, but for more supported conclusions about levels of labelling and cell wall composition further testing with other Gram-positive species would be needed. In any case, the differences between species correlate with those calculated from the confocal microscopy images (Figure 26). This high-throughput method developed within this project allows for further optimisation of the labelling procedure.

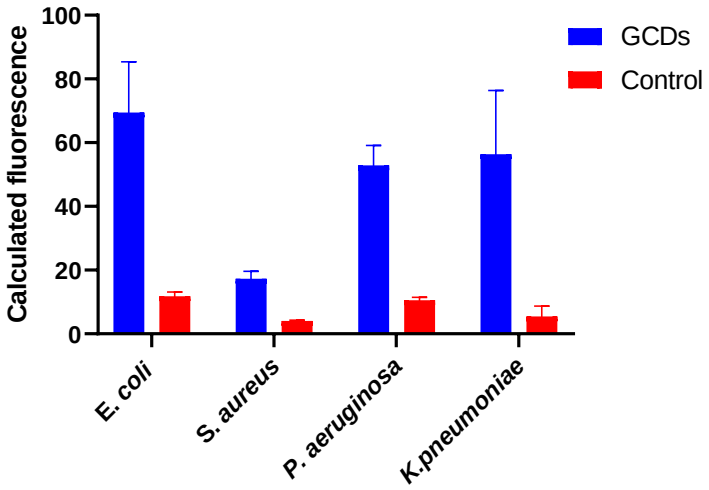

Figure 26 Fluorescence intensity data from confocal images, assigned by Fiji software. *E. coli*, *S. aureus*, *P. aeruginosa* and *K. pneumoniae* incubated with 200 µg/mL of GCDs for 30 minutes before confocal imaging.

Next, the difference between incubation times was investigated (Figure S 4). Incubation times between one minute to one hour were compared and levels of labelling were similar at each time point across all four bacterial species tested. This indicates that labelling is a very fast process. This same method of labelling quantification could then potentially be extrapolated to determining bacteria concentration. This could have a clinical application as patient samples could be quickly analysed for bacterial

concentration levels. Bacterial concentration opposed to GCD concentration would be varied. But as mentioned previously, the turbidity of bacterial concentrations impedes the fluorescence signal and gives a falsely low reading (Figure 27).

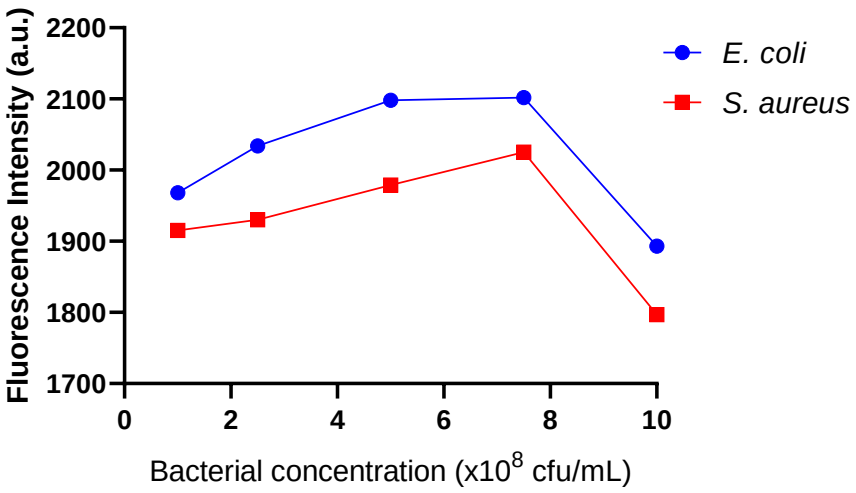

Figure 27 Fluorescence intensity of GCD labelling with increasing *E. coli and S. aureus* bacterial concentration after incubation with 200 µg/mL of GCDs for 30 mins. Contrary to expectations the highest bacterial concentration reads as the lowest fluorescence intensity of labelling as the increased turbidity of solution prevents fluorescence transmission.

This was overcome by doing calibration curves of GCDs at each bacterial concentration (Figure S 5). However, issues still occur at low concentrations of bacteria as, during sample preparation, the bacteria cannot visibly pellet out of solution. Also, due to the difference in labelling between bacterial species it could only be used to determine bacteria concentration of a singular species.

2.2.5 USE OF MEMBRANE DYE IN CONFOCAL MICROSCOPY

Work in human cell-lines had previously found that these GCDs were internalised within the cell and were shown to be highest within the cell's nucleus and most densely within the nucleolus.[237] Due to the location of the carbon dots within cell structures containing a high volume of nucleic acids an interaction between the GCDs and DNA/RNA was hypothesised. FRET was measured of the GCDs and DNA binder DRAQ5[249], a red fluorescent dye, in flow cytometry. A reduction in the GCD donor emission was observed and so was concluded that the GCDs do interact with DNA within the cells.

To determine whether the GCDs were internalised within bacteria fluorescent dyes were also used. However, a problem faced was that many fluorescent dyes used in confocal laser scanning microscopy (CLSM) are designed for use within eukaryotic cells and are not designed to penetrate the peptidoglycan wall in bacteria. DRAQ-5 was initially tested but the dye was not seen to be internalised within the bacteria. The membrane dye FM4-64FX (a fixable red fluorescent dye) however was found to label both the Gram-negative and Gram-positive bacterial species used. As it can be seen on the confocal images of bacteria incubated with FM4-64FX and GCDs (Figure 28), the membrane dye is shown in red, while the GCD are internalised (green) and yellow is shown for the overlap between GCD and dye. These images confirm that the carbon dots are internalised and not solely associated with the cell surface.

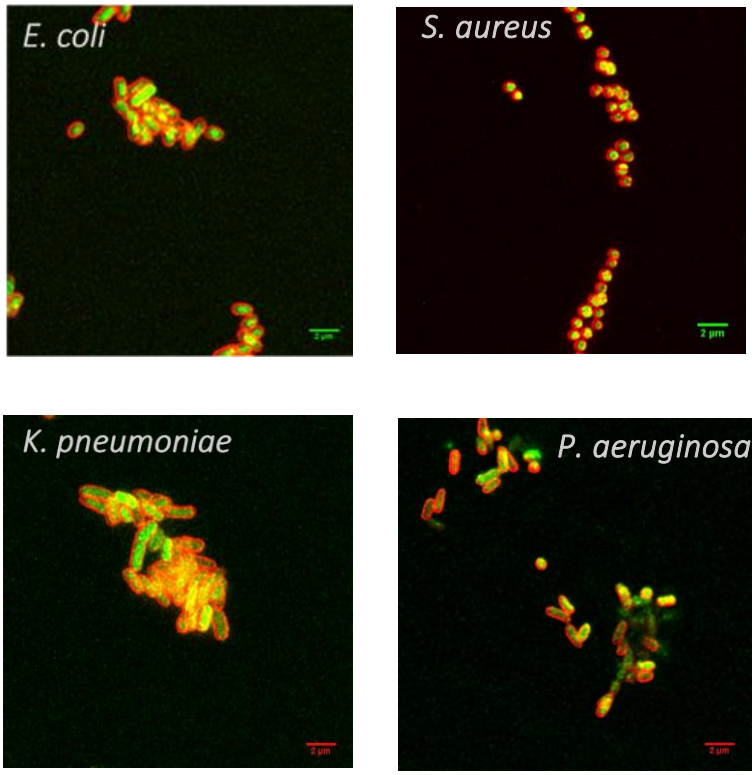

Figure 28 Confocal image of different bacterial species incubated with membrane dye FM 4-64 (red) and GCDs (green).

2.2.6 SURFACE-BOUND 2,5-DEOXYFRUCTOSAZINE A MAIN DRIVER BEHIND THE CELLULAR UPTAKE.

The initial experimental methodology developed by Stephen Hill, did not include further purification beyond centrifugal filtration but after the biological effects observed within cells and bacteria the surface composition of the carbon dot was investigated.[237] Purification through Sephadex G15 size exclusion chromatography (SEC) was done by David Benito-Alifonso to evaluate the homogeneity of the nanoparticles.[237] Previous work by *Ding et al* had shown that a single CD reaction mixture could be separated vis column chromatography to yield CDs with a gradient of spectral profiles dependent on their surface oxidation.[250] For GCDs, it was found that the CDs were separated into two main fractions, a blue-fluorescent carbon dot and a small molecule 2,5-deoxyfructosazine (2,5-DOFR) (Figure 29). This would indicate the GCD could be composed of a core carbon nanoparticle with an associated 2,5-DOFR layer on the surface. This core/corona model is supported by the thermogravametric analysis (TGA) data where 95% of the mass of GCD was retained while heating to 150 °C but heating to 650 °C saw a 65% mass loss which is indicative of loss of surface-adhered species.[237] The NMR DOSY experiments confirmed that the 2,5-DOFR was found to be loaded onto the GCD.[237]

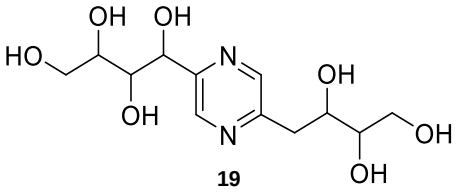

Figure 29 Structure of 2,5-deoxyfructosazine.[237]

The major precursor for the GCDs is glucosamine. The Maillard reaction describes the non-enzymatic process of condensation between the carbonyl group of reducing sugars and an amino group.[251] GlcN can undergo self-condensation at relatively low temperatures (37 °C – 70 °C) and form the advanced Malliard reaction products fructosazine and 2,5-DOFR. These polyhydroxyalkyl pyrazines are the main products that GlcN caramel solutions formed at low temperatures. Self-condensation of GlcN to form dihydrofructosazine, **20**, can then either be followed by dehydrogenation yielding fructosazine, **21**, or dehydration yielding 2,5-DOFR, **19**, (Scheme 3).[252]

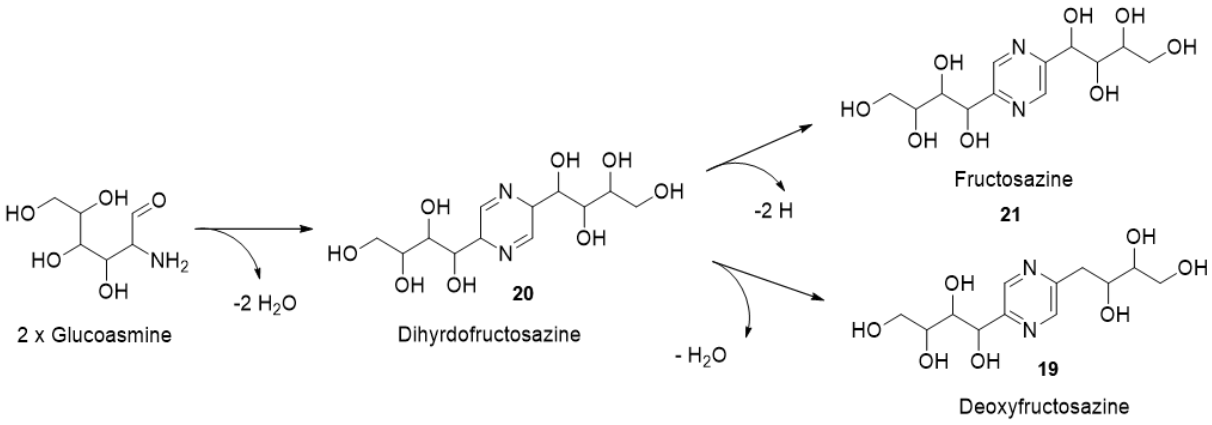

Scheme 3: Major compounds of GlcN degradation fructosazine and 2,5-DOFR formed by self-condensation of GlcN (*Hrynets*, 2016).[252]

Both fructosazine and 2,5-DOFR have been used as flavouring agents and have been identified in caramel, soy sauce, roasted peanuts and cigarettes.[253] The beer company Heineken have also patented the use of 2,5-DOFR as an additive that would act as a 'colourless caramel' that could stabilise beer against light-induced degradation as it can absorb UV light at 275 – 280 nm.[254]

Purified SEC products, the molecular fluorophore and internal core of the carbon dot, were then incubated with *E. coli* bacteria separately (Figure S 7). However, traces of carbon dot were still present in the 2,5-deoxyfructosazine sample and the core carbon dot could never be completely stripped of the fluorophore. Therefore, a commercial source of 2,5 deoxyfructosazine was used for comparison. This is a non-fluorescent molecule and did not show any labelling. The core carbon dots that had been stripped of some of the surface 2,5-deoxyfructosazine showed a large decrease in fluorescent labelling.

A sample of commercial 2,5-deoxyfructosazine allowed for the determination of the concentration non-covalently bound to the surface of GCDs through NMR. The distinctive pyrazine proton peak can easily be identified within the GCD ^{1}HNMR. The peak located at 8.73 ppm was used as a reference peak to compare 2,5-DOFR concentration in the GCD samples (Figure 30).

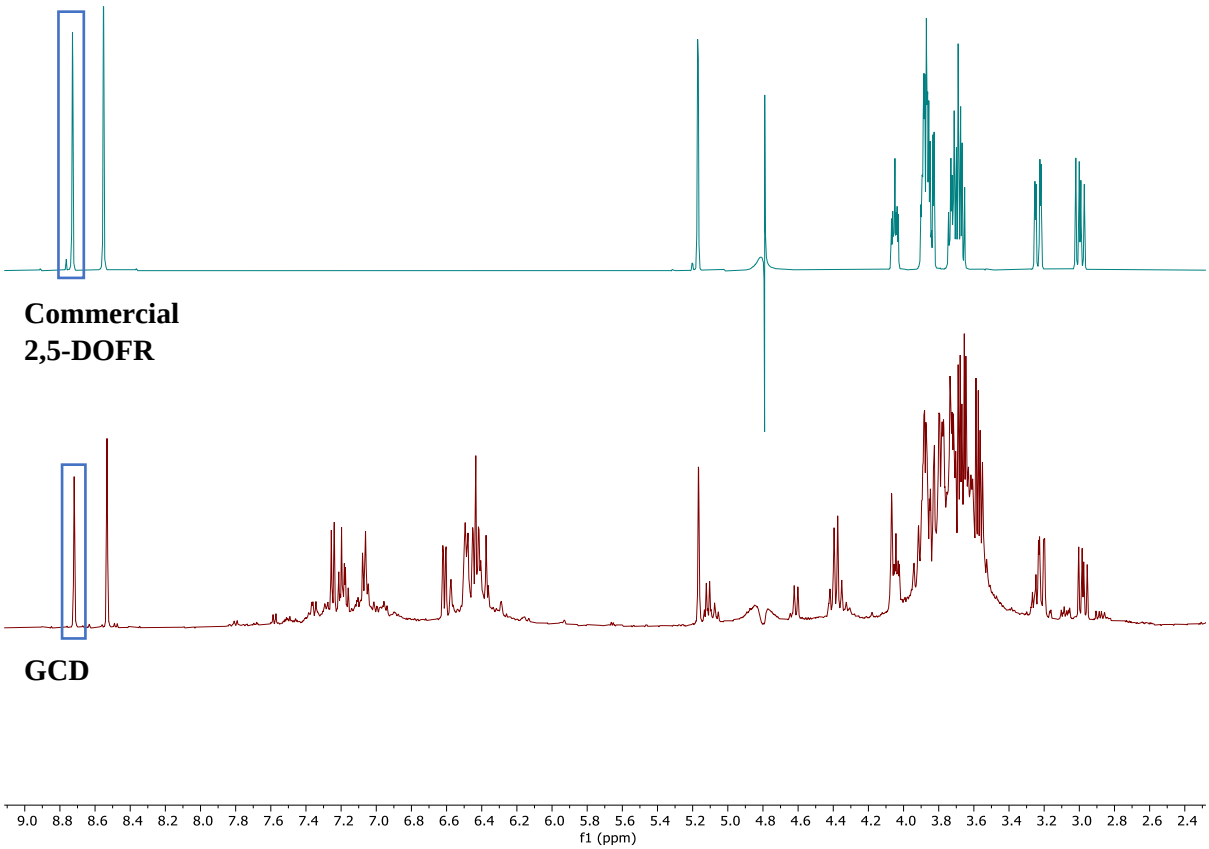

Figure 30 Stacked ^{1}HNMR of commercially purchased 2,5-deoxyfructosazine and GCDs. Pyrazine peak highlighted

It can therefore be concluded that the GCD fluorescent labelling observed is due to the GCDs as a whole, and not their individual components.

2.3 ANTIBACTERIAL STUDIES

Previously in the Galan group, photo-thermal therapies using GCDs had been explored by Hill *et al* and significant cellular ablation of HeLa cancer cells was induced by short GCD exposures followed by blue-light-emitting diode (LEDs, λ_{em} = 460 nm) illumination.[237] It was proposed that the same effect might also be seen within bacteria.

There have been a few examples in the literature of visible-light activated bactericidal functions of CDs. In 2016, Meziani *et al* reported CDs with photo-induced bactericidal functions against *E. coli*.[255] The CDs were synthesised after a 48 hour reflux reaction of carbon nanopowder and nitric acid followed by 2,2-(Ethylenedioxy)bis(ethylamine) (EDA) functionalisation. The CDs were then refluxed for 12 hours with thionyl chloride before being heated with EDA at 120 °C for 3 days and dialysis purification. *E. coli*, incubated with 500 μg/mL of EDA-CDs, was irradiated with an LED lamp for up to 6 hours before overnight incubation. A 10-fold decrease in bacterial colony formation was found in samples exposed to 6 hours of LED irradiation, but not complete killing was observed.

In 2018, Jijie *et al* reported ampicillin (AMP) functionalised CDs that had enhanced antibacterial properties upon visible light irradiation.[256] The core amine decorated CDs were synthesised hydrothermally. Both citric acid and ethylenediamine were heated in an autoclave at 250 °C for 5 hours before 3 days of dialysis purification. AMP was attached to the CDs through EDC/NHS coupling with the surface amines before further dialysis. Bactericidal effects were seen without visible light

illumination due to the attached antibiotic but potency was enhanced with light irradiation due to the generation of toxic singlet oxygen. At a CD incubation of 400 µg/mL and after 20 minutes of light irradiation *E. coli* a significant decrease in cell viability, $1x10^2$ cfu/mL of recovered growth compared to a control of $1x10^6$ cfu/mL.

Both literature CD/irradiation techniques have certain drawbacks as they involve functionalised CDs that are synthesised using comparatively harsh conditions with lengthy synthesises and antibacterial activity has only been demonstrated in *E. coli* and complete killing was not observed. The results observed with GCD are thus very promising since the synthesis and LED activation are mild and very straightforward and antibacterial activity was successfully demonstrated in four different bacterial species with the GCDs, which offer advantages to the reported protocols.

2.3.1 EFFECT OF GCD INCUBATION ON BACTERIAL VIABLE COUNT

The initial method used to explore the toxicity of GCDs alone on bacteria was a simple viable count. Suspensions of bacteria (OD_{600} 0.8 – 1.0) were incubated with GCDs for 30 mins before centrifugation to remove free GCDs from the supernatant. The subsequent pellet was resuspended and serially diluted in triplicate. The last three concentrations were then inoculated onto agar plates and grown overnight. Colonies could then be counted by hand and the cfu (colony forming units) per mL calculated. This was repeated with four bacterial species: *Escherichia coli* BW25113, *Staphylococcus aureus* Newman, *Pseudomonas aeruginosa* PA01 and *Klebsiella pneumoniae* NCTC 5055 (Figure 31).

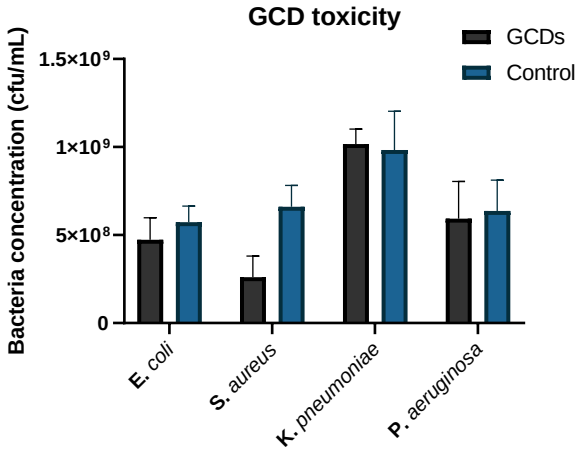

Figure 31 Viable count results detailing effect on viability of four bacterial species after 30 min incubation with 200 µg/mL of GCDs. Samples serially diluted in triplicate to $10x10^6$ before inoculation.

Only the growth of Gram-positive *S. aureus* is significantly affected by GCD incubation (30 mins, 200 µg/mL), with a 2.5 fold decrease in cell viability. Growth of Gram-negative *E. coli, K. pneumoniae* and *P. aeruginosa* is comparable to the controls. This higher level of stability in the presence of GCDs could be attributed to the double-cell wall, a feature of Gram-negative bacteria not found in Gram-positive species.[7]

Viable counts of bacteria suspensions exposed to GCDs and LEDs were subsequently performed. Samples were irradiated with the LEDs (λ_{em} = 460 nm) for either 30 mins, 60 mins and 90 mins. Three different control conditions (with GCDs alone, LED irradiation alone and with no external stimuli) were also conducted in parallel (Figure 32).

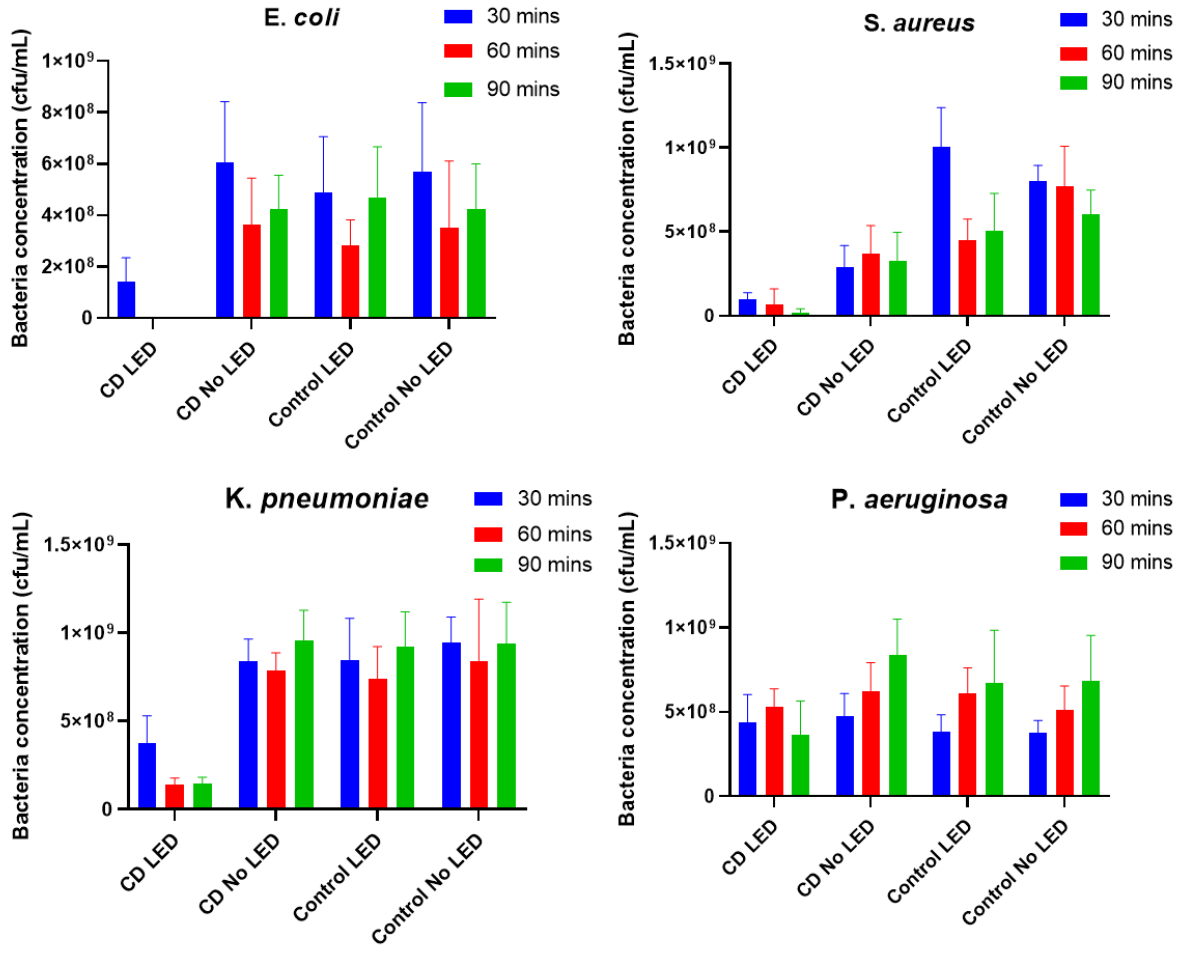

Figure 32 Viable count results for *E. coli*, *S. aureus*, *K. pneumoniae* and *P. aeruginosa*. Bacteria inoculated onto agar plates after four different conditions; incubated with 200 µg/mL of GCDs for 30 mins and then irradiated with LEDs, incubated with GCDs for 30 mins with no LED irradiation, no GCD incubation with LED irradiation and no GCD incubation and no LED irradiation as control. Samples irradiation with LED for either 30, 60 and 90 mins. Samples, in triplicate, were serially diluted to 10^6 before inoculation, repeated twice (three times for *P*. aeruginosa).

The three dilutions inoculated were $1x10^5$, $1x10^6$ and $1x10^7$. The results shown in Figure 32 are from $1x10^6$ as this was the highest dilution with a countable number of colonies. Each sample was grown in triplicate and repeated at least twice on different days. A disadvantage with this technique is the large variability between repeats as starting bacterial concentrations, determined from OD readings, could not be exactly recreated. However, the results do show the effect that the carbon dots, alone and when combined with LED irradiation, have on the viability of the four different species of bacteria.

Complete inhibition of growth was found for *E. coli* when incubated with 200 µg/mL of GCDs and irradiated for 60 and 90 mins. Viability of *S. aureus* and *K. pneumoniae* is also affected under GCD and LED conditions but complete inhibition is not shown. These three species also display decreasing viability in response to increasing LED irradiation. Little effect of GCD/LED conditions on viability is

observed in *P. aeruginosa*, a species with a known natural resistance to antibiotics and high adaptability to changes in environment.[257]

An important result is the lack of effect that LED irradiation alone has on bacterial viability. As mentioned previously, both UV-C and UV-B irradiation (200-315 nm) alone have antibacterial effects, with UV lights used widely for sanitisation.[258] The blue-emitting LEDs used (460 nm) are low-enough energy to not cause structural damage to the bacteria but at the right wavelength to overlap with the excitation peak of the GCDs (λ_{ex}= 450 nm). LED irradiation is preferrable in biological applications as alone it does not cause damage to healthy tissue while higher energy wavelengths such as UV-C and UV-B can.

2.3.2 EFFECT OF GCD/LED TREATMENT ON BACTERIAL GROWTH

An alternative method was undertaken to look further into the effect of GCD concentration on the GCD/LED antibacterial effects. Poor reproducibility as well as human error through the manual counting of colonies contributed to the relatively high standard deviation of the viable count results. Another disadvantage is the time required to plate out each sample, in triplicate, and to count the colonies of each triplicate, each at three different dilutions. For all four different species, this would be a total of 144 plates. In addition, to then also vary concentration would be very time consuming and impractical.

Initially, a standard minimum inhibitory concentration (MIC) test was trialled. A range of GCD concentrations from 0.5 to 1024 µg/mL were incubated with a $5x10^5$ cfu/mL of bacteria for 16 hours overnight after a ninety minute period of LED irradiation. Preliminary results were contradictory to expectations, as higher concentrations of GCDs promoted better growth. To investigate the discrepancies found, growth curves were set up, monitoring OD every ten minutes over a 16-hour period. Growth was seen to recover at a range of concentrations from 2 to 1024 µg/mL. As seen in the previous MIC results, higher concentrations were reading at an abnormally high OD_{600}, with concentrations above 128 µg/mL higher than the control (with no GCD present). An example with *E. coli* is shown (Figure 33). The stronger colour of the solution at higher concentration would contribute to the observed effect, but it is not solely responsible as the OD_{600} increases. Zeta potential of the 2,5-DOFR-containing GCDs has shown a cationic surface charge,[237] and due to this, GCDs aggregate in charged media. For both MIC's and growth curves, cation-adjusted Mueller Hinton broth (CAMHB) is used as the growth medium. Due to ions present in growing media, the GCDs are seen to visibly aggregate, leading to undulating and erroneous growth curves.

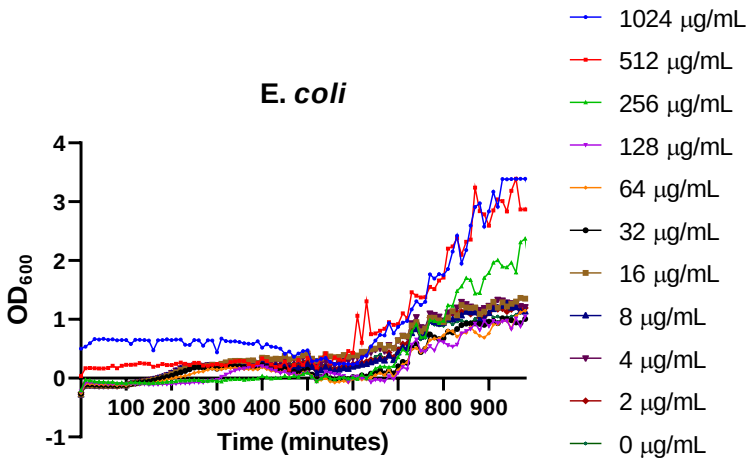

Figure 33 Growth curve of *E. coli* grown overnight with different concentrations of GCDs.

Due to the issues associated with the original protocol, the growth curve methodology needed to be updated and tailored to the materials being used. To prevent aggregation, high concentrations of GCDs in media (CAMHB was used for initial MIC experiments but aggregation was found in the majority of media used) for extended periods of time was avoided. GCD incubation and LED irradiation were therefore first conducted in PBS with a higher concentration of bacteria, before this was diluted into CAMHB for growth overnight (20 µL into 180 µL of broth). The resulting growth curves displayed a more accurate picture of toxicity, with higher concentrations of the GCDs and a longer LED irradiation period correlating to lower cell viability, as expected from our previous viable counts data. Complete killing of all species was reproducibly observed at 4 hours of irradiation and after treatment with over 32 µg/mL GCD (Figure 34), however killing could also sometimes be observed after just 90-minute LED irradiation.

Viable count results indicated *E. coli* to be the species most affected by the combination of GCDs and LED, however this was not observed in the growth curves. The MIC (of the GCD concentrations tested) was lower, 32 µg/mL, for both *S. aureus* and *P. aerguinosa* than *E. coli* and *K. pneumoniae*, 128 µg/mL.

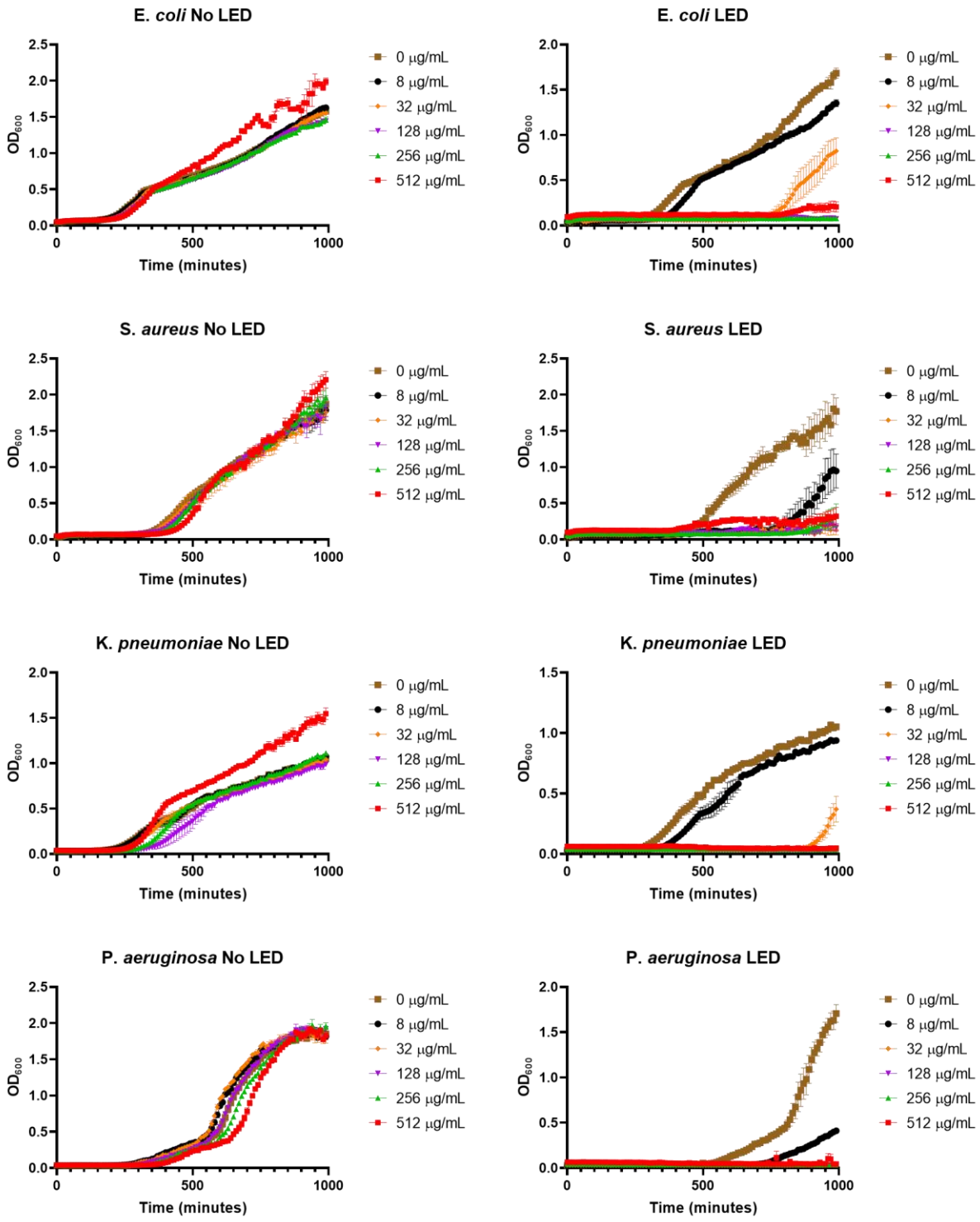

Figure 34 Growth curves of *E. coli*, *S. aureus*, K. pneumoniae and P. aeruginosa for the duration of 16 hours after treatment with varying concentrations of GCDs and 4 hours of LED irradiation. Experiment done in triplicate and error bars show standard deviation.

A normal bacterial growth curve is sectioned into an intial lag phase followed by exponential, stationary phase and finally a death/decline phase (Figure 35). The lag phase allows for bacteria to adapt to new environmental conditions.[259] The processes involved, hypothetically including syntheis of necessary cellular components and macro-molecular damage repair, is poorly understood and without known

physicological or biochemical critieria.[260] Fridman *et al* demonstrated bacteria's first response to antibiotic stresses in order to develop tolerance was a change in lag-time.[261] The exponetial phase is representative of rapid cell division and the stationary phase is the cessation of this rapid replication where rate of growth is equal to rate of death.

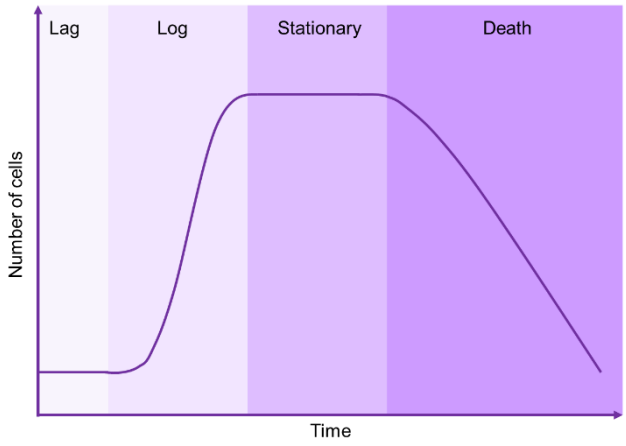

Figure 35 Typical bacterial growth curve.

Bacteria under 'no LED' conditions, (Figure 34) show little divergence from control, with only some aggregation at the highest concentration only. What is observed, particulary in *S. aureus* and *P. aeruginosa* is an extension in the lag phase. This indicates that the GCDs induces some stress which the bacteria takes longer to adapt to. For example, in the *S. aureus* a definite trend is seen between increasing GCD concentration and increasing delay before cell proliferation (Figure 36).

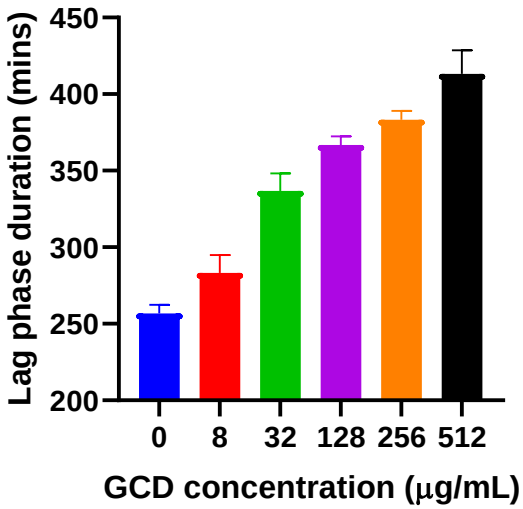

Figure 36 Difference in lag phase between the different concentrations of GCDs tested. Time taken to reach an OD_{600} of 0.1.

It can be seen from the growth curves that, although final bacterial concentrations are very similar with and without LED irradiation, there is a difference in lag times, a delay of approximately 100 min in each species. This suggests that LED irradiation alone does have a minor effect on bacterial processes, including the extending time needed to adapt. Combining LED with GCDs, at concentrations low

enough not to induce complete inhibiton of cell growth, show the greatest effect on lag times, for example *K. pneumoniae* growth only recovers after 15 hrs at 32 µg/mL of GCDs. Although some differences emerged with different bacterial viability monitoring techniques, a definite antibacterial effect of the GCD incubation combined with LED irradiation has been established.

2.3.3 EFFECT OF SURFACE 2,5-DEOXYFRUCTOSAZINE

The toxicity exhibited by the GCDs in the presence of LEDs is quite different from any activity reported for other CDs. For example, bacteria (*E. coli and S. aureus*) blue-fluorescent TTDDA/glucosamine derived carbon dots (BCDs) (Section 2.1) were irradiated with LED irradiation (λ=390 nm) that overlaps with the broad excitation peak of the BCDs (λ_{ex}=340 nm).[238] These CDs, also derived from glucosamine but without 2,5-deoxyfructosazine on the surface, displayed no toxicity in the absence or presence of LED irradiation (Figure S 16). A notable difference between the BCDs and the GCDs is the presence of 2,5-DOFR on the surface, this was consequently investigated for its role in the observed bacterial killing effect.

Outside of microbiology, 2,5- DOFR has been shown to be an active ingredient in the anti-diabetic phytodrug Madeglucyl®[253] and a potential immunomodulator, showing inhibitory activity against T-cell interleukin-2 production.[262] Toxicity of 2,5-DOFR has also been studied in the heat resistant *E. coli AW 1.7* isolated from beef carcass by Hrynets *et al.*[252] They reported the identification and quantification of 2,5-DOFR, along with fructosazine, as products of glucosamine browning and determined the MIC_{50} of each degradation product. Fructosazine, at a pH of 5, had a MIC_{50} of 3.6 mg/mL whereas 2,5-DOFR did not achieve an MIC_{50} at any pH value tested. Bhattacherjee *et al* further investigated fructosazine's antimicrobial mechanism of action in comparison to the photoseneitiser Riboflavin.[263] It was found that singlet oxygen, $^1O_2$, is generated by fructosazine and therefore has a similar antimicrobial mode of action as Riboflavin. The study concluded that permeabilisation of the cell membrane, damaging membrane integrity and the fragmentation of DNA by singlet oxygen was the cause of the antimicrobial effects of fructosazine.

It has been found that some of the hydroxyalkyl pyrazines Maillard products have shown photosensitising properties under UV light.[264–267] Bhattachererjee *et al*[254]. investigated antimicrobial effects of UV-B irradiation in combination with fructosazine, riboflavin and GlcN caramel. This combination of UV irradiation with photosensitising agents to produce phototoxic reactions is a form of photodynamic therapy. The Gram-positive bacterium *Staphylococcus aureus* is reportedly more susceptible to this kind of UV- initiated therapy than the Gram-negative *Pseudomonas aeruginosa* despite it possessing a thicker peptidoglycan cell wall.[268] They found that increased singlet oxygen generation from fructosazine correlated to increased UV-B irradiation and production was higher in the GlcN caramel. As previously reported, this $^1O_2$ release is then cause of the fragmentation of DNA in *Escherichia coli AW 1.7*. The release of singlet oxygen is potentiated by the UV-B irradiation. Since only fructosazine was seen to significantly effect bacterial viability, this suggests that 2,5-DOFR might not be the sole reason for the observed GCD/LED-engendered toxicity and that the while GCD complex is needed for activity. To demonstrate that the bactericidal effect was linked to the GCD/LED treatment and not due to 2,5-deoxyfructosazine/LED combination or 2,5-deoxyfructosazine alone, *E. coli* was treated with commercial 2,5-deoxyfructosazine at similar concentrations as those found on the GCDs, as estimated by NMR, and exposed to the same LED irradition conditions as previously used (Figure 37). Viable count of treated cells showed significant antibacterial effect only for GCD/LED exposures, with no effects observed for 2,5-DOFR treated cells, with or without LED, when compared to controls, demonstrated our proposed hypothesis.

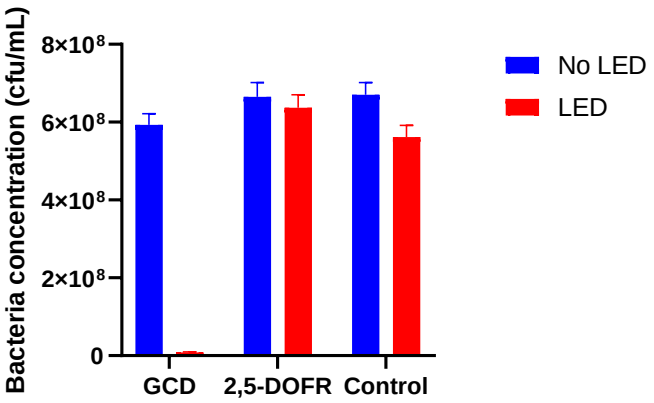

Figure 37 Viable count shown as CFU of *E. coli* treated cells with GCDS (200 µg/mL), commercial 2,5-DOFR (30 µg/mL) and control with and without LED irradiation for 90 mins.

GCDs that had been further purified by SEC, therefore reducing the concentration of 2,5-DOFR on the surface of the GCDs, were shown to have limited antibacterial effects with or without LED irradiation (Figure 38). Purified GCDs after LED irradiation had only a small impact on viability (28%) whereas intact GCDs showed a significant decrease (80%). It is also noted that although the majority of 2,5-DOFR had been removed from the surface, it was still present on the surface, the distinctive pyrazine peaks still shown in the NMR (Figure S 36).

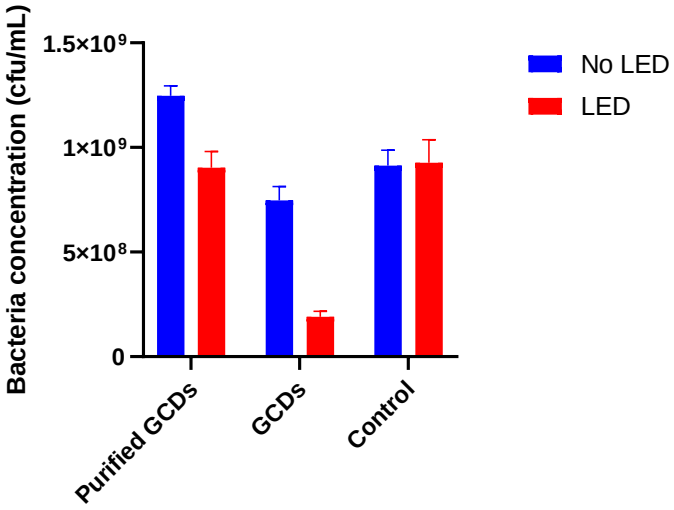

Figure 38 Viable count of comparing *E. coli* incubated with GCDs purified by SEC and GCDs without further purification (200 µg/mL) with and without LED irradiation for 90 mins.

2.3.4 SYTOX™ NUCLEIC ACID DYE TO DETERMINE MEMBRANE PERMEABILISATION

Both viable count and growth curve data indicate that *S. aureus* growth is most affected by the GCDs alone, without the LED irradiation. It was tentatively hypothesised that this difference originates in the differential cell wall structures. However, since only one Gram-positive species was investigated it should not be generalised to all species. As FM4-64FX was used to identify internalisation, the cell stain Sytox™ Red was used to identify cell-wall damage. *E. coli* were exposed to GCDs in combination with LED irradiation before a 15 min incubation of the dye (0.45 µM). Sytox™ Red is a red fluorescent nucleic acid stain that penetrates cell walls with compromised plasma membranes. Confocal microscopy was used to image the stained bacteria, the dye being shown as red and the GCDs as green (Figure 39). To verify the validity of the experiment, a molecule known to disrupt the cellular membrane was first tested. The efflux pump inhibitor phenylalanine-arginine β-naphthylamide (PAβN), **22**, structure shown in Figure 39, has been shown to permeabilize wild type *E. coli* at a concentration of 4 µg/mL.[269] This inhibitor was incubated with *E. coli* and exposed to the Sytox™ dye as a control system. Uptake of Sytox™ was observed when in the presence of the efflux pump inhibitor, the red dye shown within the cells in Figure 39, verifying that disruption to the cell wall causes the uptake of the dye.

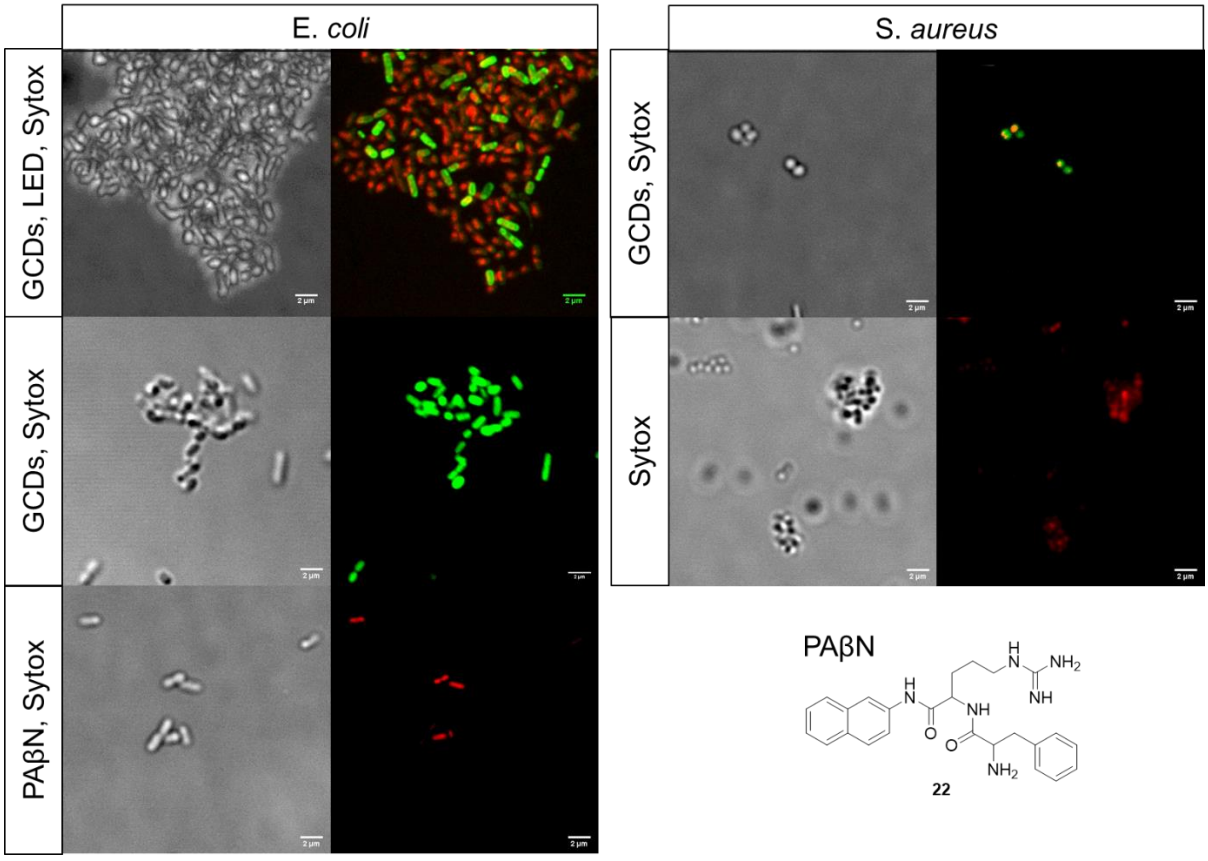

Figure 39 Confocal images of *E. coli* and *S. aureus* after treatment with different combinations of GCD (green) incubation, LED irradiation before 15 min incubation with nucleic acid dye sytox™-red (red). Efflux pump inhibitor PAβN structure shown.

After GCD incubation and LED irradiation, the Sytox™ red stain is internalised in the majority of *E. coli* cells. A small number of cells show no Sytox™ dye uptake and display a higher intensity of green GCD fluorescent labelling. It could therefore be concluded that the integrity of the cell wall is an important factor in GCD labelling. Also, after 200 µg/mL GCD incubation and 90 min LED illumination, not all bacteria cell walls were permeabilised. Without LED illumination Sytox™ is impermeant to *E. coli*, with GCD labelling seen only.

Sytox™ is marketed as a eukaryotic dead-cell indicator for use with flow cytometers and so this methodology had to be adapted for bacterial cells. It was also found that when incubated with the Gram-positive *S. aureus*, Sytox™ was permeant to cells without LED illumination or GCD incubation. Because of the differential cell wall compositions of the species studied, a different approach was needed to draw conclusions between species.

2.3.5 SCANNING ELECTRON MICROSCOPY OF BACTERIA INCUBATED WITH GCDS[1]

Effects of LED/GCD exposure was further studied by scanning electron microscopy (SEM). *E. coli* and *S. aureus* were both exposed to different combinations of GCDs (512 µg/mL) and LED irradiation. Analysis of SEM images allows for identification of cellular membrane damage, which can be seen as a protrusion of the cell wall, a phenomenon known as blebbing. The pockets on the outer membrane are formed naturally when the cell is producing vesicles but can also be triggered by disruption of the outer membrane, such as the introduction of intercalating molecules to the surface of the bacterium.[270] Lysis of the cell can also be identified, characterised by bacteria with ruptured membranes and cytoplasm leaking out of the cell.

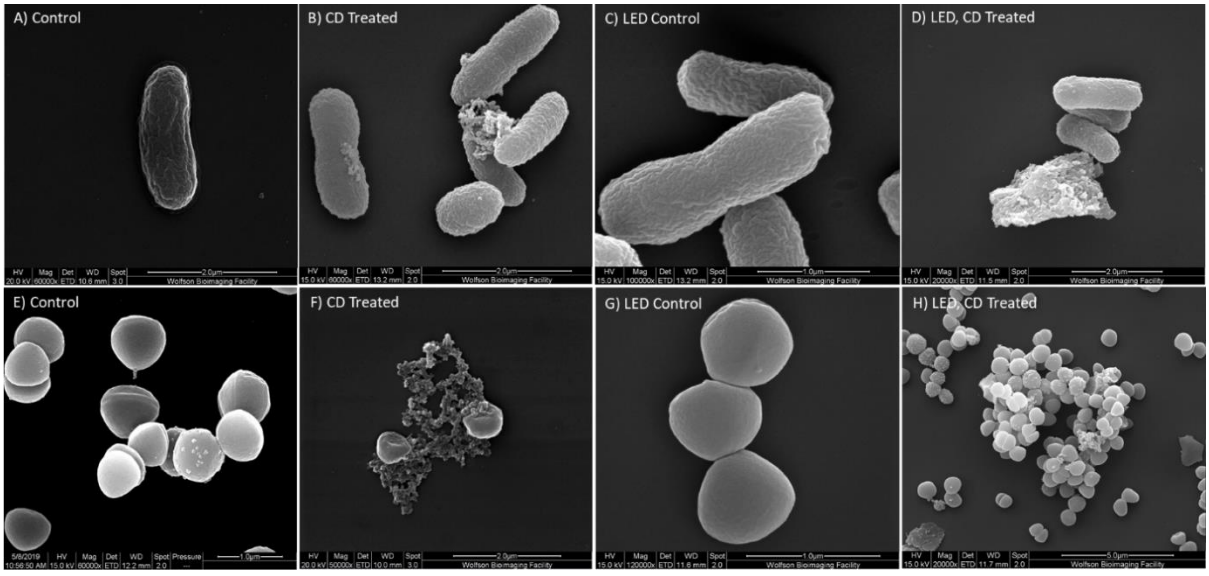

Figure 40 SEM images of *E. coli* (A-D) and *S. aureus* (E-F) in various treatments. Work completed by Yuiko Takebayashi.

[1] The work in this section was completed by Yuiko Takebayashi, Spencer Group, University of Bristol

Both conditions involving GCD incubation, with and without LED illumination, showed signs of envelope stress with increased membrane blebbing and lysis (Figure 40). As can be seen in the panel F, *S. aureus* and GCD treatment, complete cell lysis is seen, compared with panel B, *E. coli* and GCD treatment, where only one cell is lysed but blebbing can be seen on the surface of others. This indicates that the *S. aureus* is more affected by GCDs alone in comparison to *E. coli*, which has been seen with the toxicity studies also (Figure 31). Blebbing and lysis are also seen for both species when exposed to GCDs and LED irradiation, panels D and H. This indicates that the combination of GCD/LED exposure has a substantial effect on the integrity of the bacteria's cell wall and is likely one of the main contributors to the toxicity observed. LED irradiation alone did not induce these phenotypes, panels C and G, and were comparable to the control cells. This further highlights that exposure to LED irradiation alone does not affect the cell membrane.

2.3.6 VANCOMYCIN INTERNALISATION STUDY BEFORE AND AFTER GCD/LED TREATMENT

Vancomycin is a large-scaffold glycopeptide antibiotic that can be internalised in Gram-positive species such as *S. aureus* but exceeds the exclusion limit of the outer membrane β-barrel porins in *E. coli*.[271] Susceptibility of *E. coli* to vancomycin has previously been increased with small-molecules that can inhibit cell envelope biogenesis.[271,272] To further assess the effects on cell wall integrity by GCD/LED combination, it was hypothesised that Gram-negative *E. coli* could become more susceptible to antibiotics after treatment with GCD/LEDs. In triplicate, MICs were determined under GCD (200 µg/mL) and/or LED (90 mins) treatment and untreated control conditions. It was found that neither GCD and LED irradiation, separate or combined, exhibited an effect on *E. coli* vancomycin susceptibility, with an MIC of 128 µg/mL for all conditions tested. (Figure 41). The susceptibility of *S. aureus* was also investigated and no reduction in 1 µg/mL was found for the MIC.

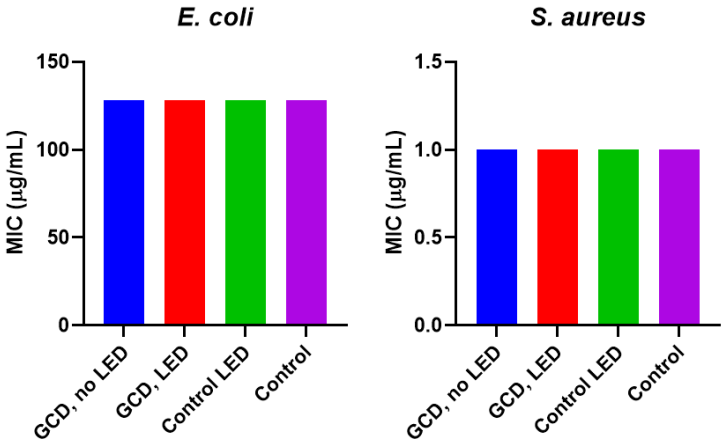

Figure 41 MIC values of antibiotic vancomycin. Graphs showing that GCD/LED treatment on *E. coli* and *S. aureus* has no effect on the MIC values of vancomycin.

2.4 MODE OF KILLING

After the initial Sytox™ stain investigations and vancomycin susceptibility studies gave limited, contrasting insights on the GCD/LED method of killing, further studies were pursued. When the GCD/LEDs system was analysed previously in mammalian cells, a photothermal effect was attributed to the selective killing observed. A temperature increase of 14 °C was measured after 90 min of illumination of a 500 µg/mL GCD solution in cell media in comparison to illumination of the cell media alone.[237]

2.4.1 TEMPERATURE PROBE

To assess if a temperature change is also observed in the presence of bacteria, a thermocouple was used to monitor temperature changes during LED irradiation. Intracellular temperature increases are impractical to measure and so local media temperature is used instead as indicator of the increase.[273] Similar to the growth curve methodology, bacterial suspensions in PBS were incubated and illuminated in a 96 -well plate in biological triplicate and the temperature recorded at 30 min intervals. After 30-minutes of LED illumination, 200 µg/mL and 800 µg/mL concentrations of GCD were found to be 2 °C and 4 °C higher respectively (Figure 42). The difference was similar at a longer illumination time (60 mins), 2 and 3 °C respective to 200 µg/mL and 800 µg/mL of GCDs.

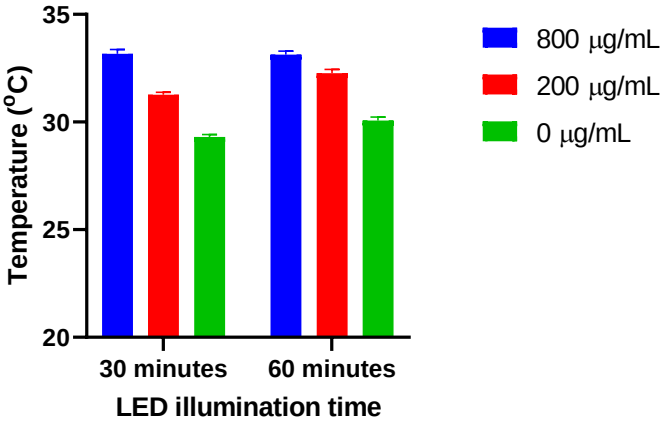

Figure 42 Temperature of GCD incubated (800 and 200 µg/mL) bacterial suspensions after 30 and 60 minutes of LED irradiation.

The conclusion of studies in mammalian cell lines was that GCDs act as a cancer-selective photothermal therapy (PTT). LED illumination at the excitation wavelength of GCDs is proposed to cause a localised heating effect, inducing cellular damage. However, the temperature difference found in bacteria was not as extensive as in mammalian cells. This could be attributed to the different conditions used, such as PBS instead of Dulbecco's Modified Eagle medium (DMEM) or could be due to levels of internalization and/or localization.

2.4.2 DETECTING THE PRESENCE OF REACTIVE OXYGEN SPECIES IN BACTERIA EXPOSED TO GCD/LEDS

To evaluate other potential toxicity mechanisms, the generation of reactive oxygen species (ROS) was measured. Moreover, proteomics analysis was also used to assess the effect on the cellular metabolism. ROS is a term to describe a number of highly reactive molecules and free radicals derived from molecular oxygen which includes hydroxyl radicals (HO•), hydrogen peroxide (H_2O_2) and superoxide anions (O_2^-). These species are known to exert an antimicrobial effect against a broad range of bacteria as they can react with multiple targets such as iron-sulphur cluster-containing proteins, that participate in many metabolic processes, and the cells genetic material.[274] If the GCD/LED system is found to generate ROS species in bacteria, oxidative damage could be a significant reason for the toxicity observed.

The superoxide indicator dihydroethidium[275] (DHE), **23**, was used to monitor the formation of reactive oxygen species (ROS) in LED and GCD treated bacteria. In the presence ROS, DHE undergoes conversion to ethidium, **24**, which emits at 605 nm (Scheme 4). A decrease in fluorescence emission (λ_{ex} 355 nm, λ_{em} 460 nm) indicates the production of ROS as the DHE is oxidised.

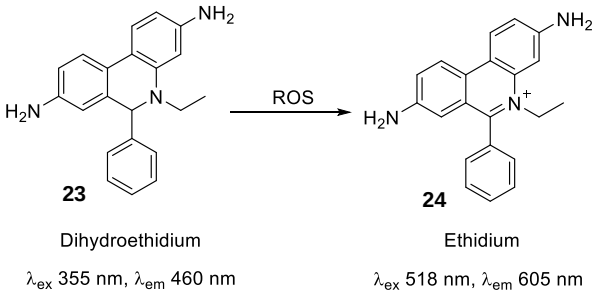

Scheme 4 ROS initiated conversion of dihydroethidium (DHE) to ethidium[275]

Bacteria, incubated with GCDs and illuminated with LEDs, were then treated with DHE and fluorescence was measured. Optimisation of the protocol was initially required as it was observed that when DHE was added to the solutions with or without bacteria, fluorescence reduction was observed regardless of the treatment as long as LED irradiation took place. For instance, 90 minutes of LED irradiation was seen to degrade DHE in just PBS alone (Figure S 8). Therefore, it was decided to add DHE after (LED, LED/GCD and GCD) treatment and control samples and directly measure fluorescence, to avoid this issue. (Figure 43).

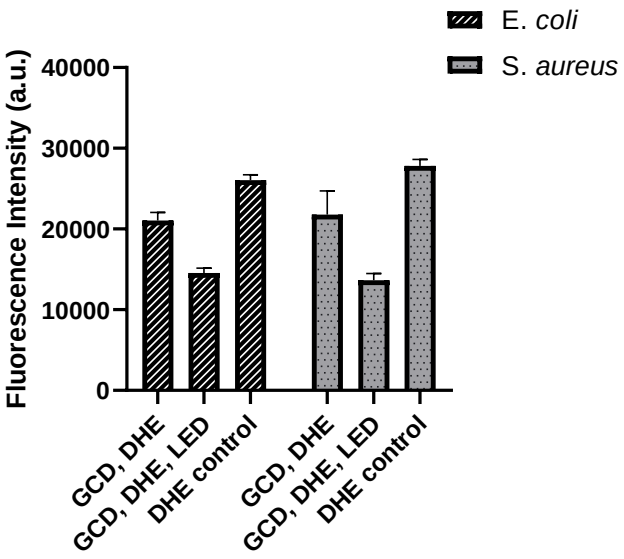

Figure 43 Chart showing the decrease in fluorescence intensity at λ_{em} 460 nm when incubated with 200 µg/mL CDs and illuminated with LEDs for 90 mins for *E. coli* and *S. aureus.*

A decrease in fluorescence intensity was observed in both GCD and GCD/LED conditions indicating the generation of ROS. The signal reduction for samples irradiated for 90 mins was significantly larger than those exposed to GCDs alone for 90 minutes, 55 % and 80 % of control respectively for *E. coli*. *S. aureus* displayed similar fluorescence depression, 49 % for GCD/LED and 78 % for GCD incubation alone. This suggests that GCDs can induce ROS production and that this it is increased with exposure of LEDs to the system. Stress factors such as ROS and temperature changes are likely pertinent to the LED/GCD-engendered toxicity.

2.4.3 PROTEOMICS[2]

To gain a more thorough understanding into the cellular stress responses, the protein expression levels of *E. coli* and *S. aureus* cultures grown in the presence or absence of GCDs (512 µg/mL) and LED irradiation were analysed by Tandem Mass Tag (TMT) proteomics. Changes in protein expression levels, compared to untreated samples, allowed insight into the cellular processes affected, determined by a volcano plot analysis (Figure 44). For *E. coli* a total of 2636 protein hits were found out of a possible 4469 sequences used for TMT analysis, which reflects approximately 59 % of predicted open reading frames.[276] For *S. aureus* 2581 total protein hits were found out of a possible 2583, near 100 %. Statistical significance, the p-value, was determined through a t-test in Microsoft Excel. Identification of proteins of interest among protein hits was performed using PantherDB. Only those with $p<0.05$ were included in volcano plot analysis, seen as the green number top right of the volcano plots (Figure 44).

[2] The work in this section was completed by Yuiko Takebayashi, Spencer Group, University of Bristol and the University of Bristol Proteomics Facility run by Kate Heesom

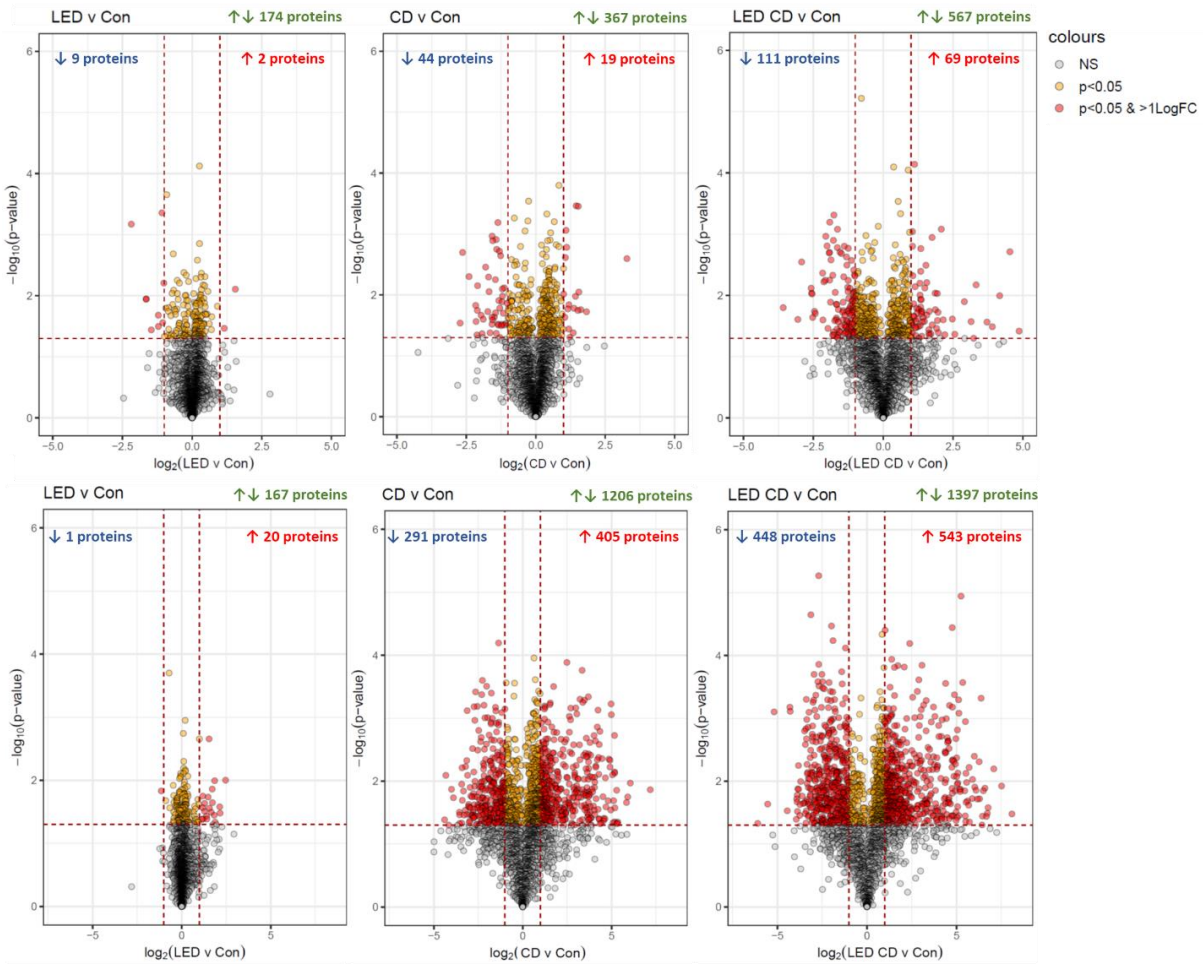

Figure 44 Volcano plots of (Top) *E. coli* and (Bottom) *S. aureus* treated with LED, GCD and LED-GCD. Overall number of proteins with changes in abundance levels indicated in green font. Grey circles represent proteins with differences in abundance levels (compared to control) that are not statistically significant, yellow circles represent those with statistical significance ($p<0.05$) and red circles represent those that are ≥ 2-fold different in abundance.

LED irradiation alone had little effect on protein expression levels with only 11, out of 174, and 21, out of 167, proteins showing over 2-fold changes for *E. coli* and *S. aureus* respectively. For GCD incubation alone, a 2-fold increase in protein expression is found in *E. coli* and a 7-fold increase in *S. aureus*. Proteins with increased expression levels for *E. coli* included those involved in cellular and metabolic processes, some of which were indicative of DNA damage (UvrA, RecN), cell envelope stress (YmgD, Spy) and toxic/chemical stimulus (FadA). Proteins downregulated included enzymes involved in biosynthesis of important precursors such as amino acids (AroF, AroG, MetR), carbohydrate metabolism (GatZ), ribosomal RNA transcription (Fis) and transport systems (CusF, DppF, YhjE). Notable proteins upregulated for *S. aureus* were involved in DNA/RNA repair (RecN, the most upregulated), ROS exposure (KatA, AphC), DNA damage (Rot, PcrA) and RNA repair (RnhB). Downregulated proteins included those also involved in DNA repair (RecO, RecG, RecF and MutL).

In terms of proteins involved in the response to cell envelope stress, various genome-wide transcriptional profiling studies of *S. aureus* treated with cell-wall-active antibiotics highlighted the upregulation of genes involved in cell envelope biogenesis.[277–280] Some of these corresponding proteins were also noted to be upregulated in the proteomics data, such as the glycine betaine transporter (OpuD), glycine-glycine endopeptidase (LytM), carboxyl-terminal processing proteinase (CtpA) and UDP-*N*-

acetylglucosamine 1-caryboxylvinyl transferase (MurZ). Similarly, expression of over 200 enzymes was downregulated, with notable changes in translational, metabolite interconversion and nucleic acid metabolism proteins, including those involved in DNA repair (RecO, RecG, RecF and MutL).

An increase differences in expression was found in bacterial cultures exposed to both GCDs and LED illumination with a further ~200 proteins affected. In *E. coli*, expression of multiple enzymes involved in DNA damage were upregulated compared to the GCD-only sample. Some of these (RecN, UvrA) were significantly upregulated on GCD exposure and further upregulated with LED irradiation; for others (RmuC, RecA) there was apparent upregulation on GCD exposure but the difference was not statistically significant without LED irradiation; and a third group (DinI, YebG, Cho) were little changed in the GCD-treated sample but showed significant upregulation with LED irradiation. Other proteins upregulated were those related to cellular responses to ROS (RclC), toxic/chemical stimulus (FadA), oxidative stress (KatG), osmotic stress (RstB) and starvation (YqjH). For *S. aureus*, all the proteins mentioned above (with the exception of Rot) were further upregulated and the additional proteins effected include those involved in cellular response to DNA damage (RecA, AddB) and also include multiple involved in metabolite interconversion, translation, transport and nucleic acid binding. Downregulation of DNA repair proteins was maintained with the addition of MutS and RadA.

The results of the proteomics analysis enabled a greater understanding behind the mechanism of GCD/LED-engendered killing. It has been shown that exposure of *E. coli* to GCDs alone is associated with induction of responses to both membrane and DNA damage. In the case of *S. aureus*, the effect of GCD exposure upon the proteome is more profound, but also includes proteins involved in the response to ROS exposure. However, when GCD treatment is augmented with LED irradiation, in both organisms proteomic signatures are consistent with a response to multiple stressors that include both membrane and DNA damage, as well as elevated ROS-levels. Membrane, DNA and ROS induced damage, have also been indicated by Sytox™ staining, SEM imaging and DHE oxidation.

2.5 EFFECT OF GCD EXPOSURE ON BACTERIA BIOFILM FORMATION

In response to extracellular stress factors bacteria can form a biofilm, a self-produced extracellular matrix protecting a collective of bacterial cells (Section 1.1).[281] Medically relevant, bacterial biofilms are estimated to be involved in two thirds of human bacterial infections.[282] The effect of GCD/LED exposure on the formation of biofilms with the was investigated in *E. coli*, *S. aureus*, *K. pneumoniae* and *P. aeruginosa.* Since we have demonstrated the toxcity of GCD/LED treatment with bacteria, we proposed that a potential application of the system we have developed within this programme is the prevention of biofilm growth.

A previously reported protocol for biofilm growth within a microtiter dish developed for *P. aeruginosa* was adapted for use in work with *E. coli, S. aureus* and *K. pneumoniae*.[283] The ubiquitous dye crystal violet, used commonly in Gram's method of classifying bacteria,[6] was used to determine the extent of biofilm formation. After optimisation of the procedure, it was found that minimal media and a 24-48 hour growth period was required for the formation of biofilms. In summary, bacterial cultures exposed to GCDs and/or LEDs were grown in 96-well microtiter plates before the supernatant was removed and a 0.1% solution of crystal violet was added for 15 mins of incubation. The stain was then removed by inversion of the plate, and biofilms were washed before the crystal violet was solubilised with 30% acetic acid and the absorbance of the solution subsequently measured.

P. aeruginosa and *E. coli* are both motile organisms and therefore form biofilms at the air-liquid interface, which leads to a distinctive ring around the well is formed from *P. aeruginosa* and *E. coli* when stained with crystal violet (Figure 45). On the other hand, *S. aureus* and *K. pneumoniae* are non-motile and therefore form biofilms at the bottom of the well.

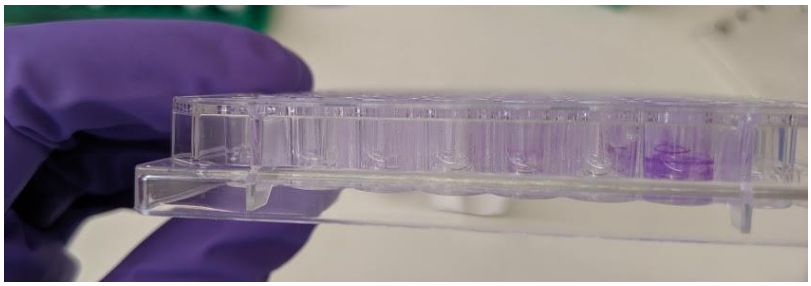

Figure 45 Image of biofilm formation, *P. aeruginosa* can be seen to form biofilm at liquid-air interface which is seen as a ring around the well after staining with crystal violet.

Contrary to what was expected, the GCD/LED combination treatment displayed no depletion in biofilm formation (Figure 46). Conversely, a slight increase in absorbance was seen for all bacterial species. Wells exposed to LED illumination alone had similar levels of absorbance as when LED illumination was in combination with GCDs, except for *P. aeruginosa* where a small decrease in biofilm formation was found.

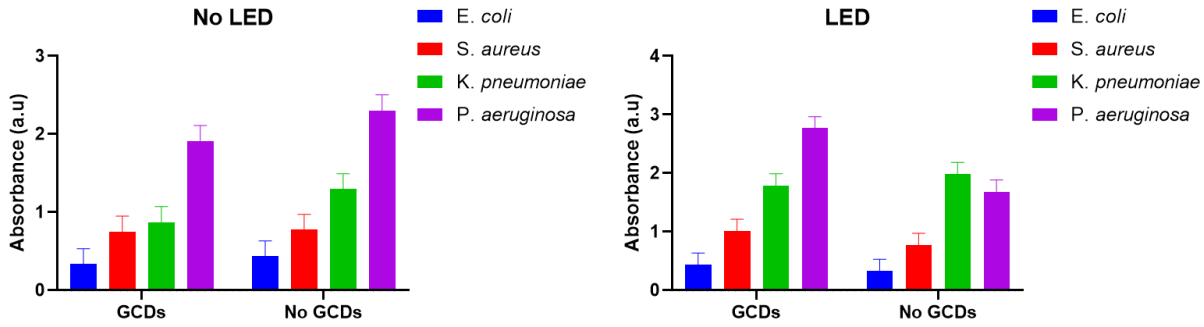

Figure 46 Absorbance at λ=550 nm of biofilms formed under a variety of conditions stained with crystal violet. Conditions include GCD incubation (200 µg/mL) and LED irradiation (90 mins), all grown for 24 hours.

Increased formation of biofilms could be indicative of the increased level of stress bacteria are exposed to, biofilm formation being a survival-driven response. Subsequently, all four species were also exposed to higher concentrations of GCDs, and bacteria biofilm formation evaluated after 48 hours (Figure 47). P. *aeruginosa* saw some irregularities between GCD concentrations but not an obvious trend, biofilm growth remaining at a relatively similar level. Increase in biofilm formation was seen in the other species tested, primarily in K. *pneumoniae*, where a significant increase in biofilm growth was found on increasing GCD concentration, between 200 and 400 µg/mL there was a 4-fold increase in absorbance. These data showcase that while GCD/LED exhibits a bactericidal effect, this is not an effective treatment to inhibit biofilm formation.

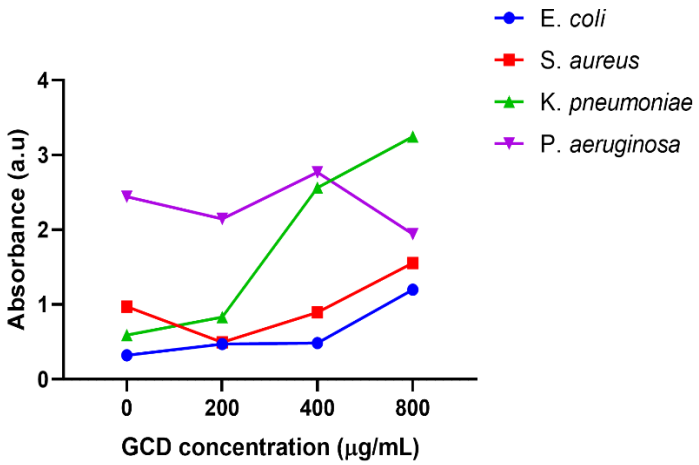

Figure 47 Absorbance at λ=550 nm of biofilms formed in bacterial cultures incubated with different concentrations of GCDs. Incubated for 48 hours.

2.6 CONCLUSIONS AND FUTURE WORK

The effect of previously developed green carbon dots (GCDs) in bacteria was investigated for the first time. After optimisation of the imaging methodology, GCDs were shown to uniformly label across four different bacterial species both Gram-negative and Gram-positive. Quantification of the bacterial labelling could be achieved with the use of a microtiter plate reader and differences observed in labelling intensity between bacterial species could be detected. GCDs are seen to be internalised inside bacterial cells when imaged with the surface specific FM4-64FX. In eukaryote research, the main mechanism of CD internalisation has been found to be endocytosis, a process where the cell membrane engulfs extracellular material which then breaks off into the cell.[284] However, this process has not been observed in bacteria and there has been little research into bacterial CD internalisation methods. The size and hydrophilicity of the GCDs would prevent passive diffusion through the hydrophobic membrane and so internalisation likely occurs through membrane proteins, porins. These proteins act as molecular filters for hydrophilic compounds, including bacterial nutrients. This includes the recognition of carbohydrates such as glucose. Because GCDs are obtained from glucosamine dehydration there is likely fragments of glucose-like structures on the GCD surface which could contribute to the recognition and internalisation of the nanoparticles.

GCDs incubation alone only affected bacterial growth at very high CD concentrations, with *S. aureus* being the most susceptible. When incubation was combined with LED irradiation, toxicity was found at lower concentrations. After 4 hours LED irradiation the MIC of GCDs is 32 µg/mL and 64 µg/mL and for *E. coli* and *K. pneumoniae.* The bactericidal mechanism was probed with multiple techniques including the red-fluorescent nucleic-acid stain (Sytox™), SEM, a molecular ROS indicator and proteomics. GCD incubation alone is seen to exhibit DNA damage on both *S. aureus* and *E. coli* but membrane-damage is found only with *E. coli* and a ROS respsonse only in *S. aureus*. When GCD incubation is combined with LED irradiation then DNA-, membrane- and ROS- damaging effects are observed. Researchers concluded from work with GCDs in cancer cell lines that GCDs formed intracellelular interactions with DNA[237] and this is a likely mechanism of action for the observed DNA damage. ROS formation could occur at the surface of the GCDs, through interaction with molecular

electron traps, or through the excitiation of the GCDs through exposure to LEDs. The proteomic results indicated that membrane damage was only found when combined with LED irradiaiton. Therefore the damage to the cell membrane is most likely caused through a PTT mechanism where excitation of the GCDs through LED irradiation causes localised heating. Overall, the observed toxcity can be reasonably presumed to be from multiple processes occurring at the same time, triggered by the combination GCD/LED exposure. The notable increase in the number of proteins with differences in expression with the GCD/LED combination is a strong indicator for the increase in toxicity.

The GCD surface-bound molecule, 2,5-deoxyfructosazine, was shown not to be solely responsible for either the labelling or antibacterial effects discovered. Instead, it was found that only when loaded on the surface of the GCD an effect was seen. This system offers advantages over other reported antibacterial CD/LED approaches as GCDs are easily accessible from cheap reagents and the synthetic protocol is simple and easily carried out by a non-specialist. Moreover, complete inhibition of growth has been demonstrated over four different bacterial species.

The differences found between Gram-negative and Gram-positive species were identified, such as a higher intensity of GCD fluorescent labelling in Gram-negative, but the differences in cell-wall structure could not be corroborated as the causative agent due to only one Gram-positive bacterium being tested. To investigate further the differences noted, future work should be undertaken using a larger range of Gram-positive species.

3. TARGETING SELECTIVE BACTERIA LABELLING VIA SUGAR - LECTIN INTERACTIONS

Discussed in this chapter is the work undertaken to functionalise CDs with saccharides for the specific labelling of bacteria. The microbial lectins (carbohydrate binding proteins) presented on the surface of a bacterium are dependent on the bacterial species and so can be exploited with targeted sugars. Initially, the attempts to functionalise the GCDs (synthesis covered in Section 2.1) in an effort to target specifically the labelling of different bacterial species, are detailed. In Chapter 2, it was shown that the 2,5-deoxyfructosazine coated GCDs fluorescently label all bacterial species tested and it was then hypothesised that specificity could be imparted through sugar functionalisation. As a proof of concept, the *E. coli* lectin *FimH* was targeted with mannose functionalised GCDs, this well-studied system was chosen based on previous reports into nanoparticle labelling.[47] Different nanoparticle cores are also explored, in this context a series of literature and novel carbon dots were synthesised and characterised with techniques including NMR, fluorimetry, IR, DLS and TEM. Disappointingly, the CDs produced from many of the literature procedures followed, did not match those reported and so a highly blue-fluorescent CD, developed in the Galan group, was chosen as the platform nanoparticle. An agglutination experiment, specific for testing binding of *E. coli FimH*, was employed to test specific binding of mannose-functionalised CDs.

3. 1 FUNCTIONALISATION OF GLUCOSAMINE-DERIVED GCDS

3.1.1 SELECTION OF LECTIN TARGET

Sugar-binding proteins, termed lectins, decorate the surface of the bacteria and are responsible for the recognition of specific glycolipids or glycoproteins from the host tissue, their importance is highlighted in Section 1.3.1. The presentation of oligosaccharides allows for more specific and selective binding.[285] Some of these carbohydrate targets in animal tissues have been identified and are shown in Table 1.

Table 1 Examples of identified carbohydrates that act as tissue attachment sites for pathogenic bacteria (Adapted from Carbohydrate Receptors of Bacterial Adhesins: Implications and Reflections[286]

Organism	**Target Tissue**	**Carbohydrate**
E. coli Type 1	Urinary	Man(α1-3)[Man(α1-3)] Man
E. coli K1	Endothelial	GlcNAc(β1-4)GlcNAc
E. coli S	Neural	NeuAc(α1-3)Gal(β1-3)GalNAc
P. aeruginosa	Respiratory	L-Fuc
K. pneumoniae	Respiratory	Man
N. gonorrhoea	Genital	Galβ4GlcNAc
C. jejuni	Intestinal	Fucα2GalβGlcNAc

By mimicking the presentation of target tissues, sugar-functionalised CDs have the potential for application as adhesion inhibitors, specific labelling agents or, by orthogonal functionalisation, targeted drug delivery agents. As a 'proof of concept' system the targeting of the well-studied lectin-carbohydrate pair, *FimH*-mannose, is explored in this chapter. The nature of the *FimH* binding pocket and preferred receptors are explored further in Section 1.3.2 and 1.3.3. This system offers many advantages because of the wide scope of research already reported for *FimH* and the ligand requirements.[66] Mannose specific binding has been shown with simple mannose derivatives, mannose itself is cheap and readily accessible, and numerous *FimH* inhibitors have been designed and tested. Also, within the laboratory I had access to a *FimA* deletion strain of *E. coli*, which lacks the gene encoding for fimbrial rod subunit *FimA* and so therefore also lacks fimbrial tip subunit *FimH* and the ability to bind mannose. This was used as a control system for labelling to differentiate from non-specific and mannose-specific binding.

In the majority of the experiments involving indiscriminate bacteria labelling and LED induced killing discussed in Chapter 2, the *E. coli* samples were grown from an agar plate overnight and suspended in PBS before incubation with the CD samples. However, it was suspected that this was not the optimum growth conditions for *FimH* expression as SEM images of *E. coli* grown on solid media found the absence of fimbriae, where the *FimH* lectin is located, on the cell surface (Figure 48). Expression of Type 1 fimbriae in *E. coli* can vary between strains and is dependent on growth conditions.[287] Abgottspon *et al* reported that statically grown *E. coli* had a 5-fold higher mannose-binding agglutination maximum in comparison to *E. coli* grown under shaking conditions.[288] When a similar aggregation assay was performed, detailed further in Section 3.4, overnight cultures and suspensions from overnight plates were compared and it was found that only *E. coli* grown static in liquid media for a minimum of 48 hours were shown to cause mannose-specific aggregation.

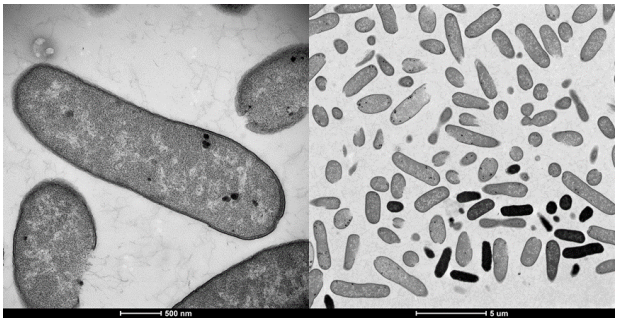

Figure 48 TEM images of *E. coli* grown overnight on solid-phase media. No fimbriae are expressed on the bacterial cell membrane. Bacteria prepared by Yuiko Takebayashi and images collected by Chris Neal from Wolfson Imaging Facility.

3.1.2 FUNCTIONALISATION OF GCDS

3.1.2.1 MANNOSE FUNCTIONALISATION

The functionalisation of blue-fluorescent glucosamine-derived CDs has already been published by the Galan group.[141] Glycosylamines, synthesised via a microwave-assisted Kotchevkov reaction, were coupled to the CD's surface carboxylic acid groups via amide coupling.[289] In this work, the synthesis was adapted to the GCDs with the addition of succinic anhydride to introduce carboxylic acid groups on the surface (Scheme 5).

Glycosylamines can be accessed via two synthetic pathways; (i) conversion of protected glycosyl azides that generally require at least five steps including protection and deprotection steps to synthesise or (ii) a one-step direct amination from the unprotected hemiacetal.[289] The original procedure for Kotchetkov amination involves stirred over 6-7 days with a fifty-fold excess of ammonium bicarbonate. Due to the long reaction times and large quantities of ammonium bicarbonate that need to be removed in subsequent purification steps, an optimised microwave synthesis was developed by Bejugman and Flitsch.[290] In this procedure, the sugar is MW irradiated with a 5 fold excess of ammonium carbonate in DMSO for 90 minutes at 40 °C, which yields the *β*-glycosylamine as the preferred product. Side products of this reaction include dimeric di-glycosylamines, glycosyl ammonium carbonate salts and glycosyl carbamates. [291] Coupling with carboxylic acids is still possible from these derivatives and size exclusion purification gives rise to the desired products.

Both 1'-carbonyldiimidazole (CDI) or ethyl-3-(3-dimethylaminopropyl)carbodiimide (EDC) were used for GCD coupling reactions. All reactions were purified with dialysis (500-1000 Da molecular-weight cut off) for a minimum of 24 hours to remove unconjugated saccharide, coupling reagents and sugar by-products. The use of CDI was preferred as EDC and the urea by-product were difficult to remove with dialysis purification, suggesting an association to the CD surface. A variety of mannose derivatives (described in the next section) were used to decorate the GCDs, the simplest being 1-aminomannose (Scheme 5). Sugar conjugation was confirmed through NMR studies based on methodology previously reported in the Galan group.[292] HSQC NMR was used to identify the presence of mannosyl residues on the CD's surface after dialysis purification by the identification of the distinctive anomeric proton peaks.

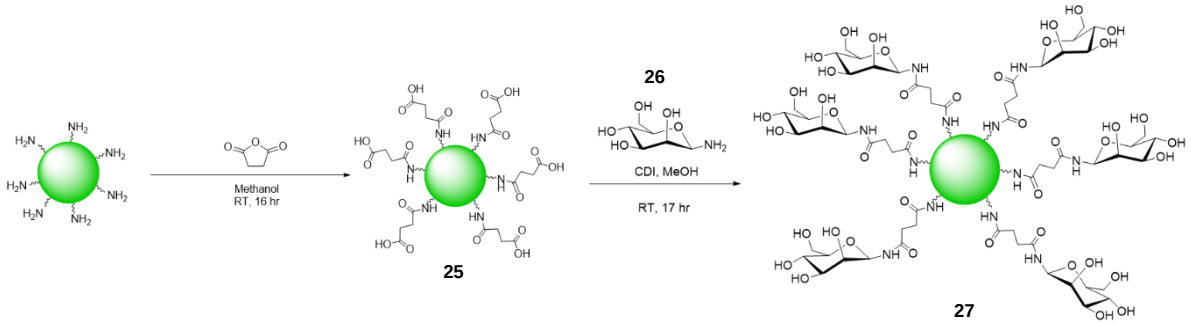

Scheme 5. Mannose functionalisation of GCDs.

3.1.2.2 Di- and tri-saccharides

Although many reported *FimH* ligands are monosaccharides, there have been previous examples of strong *FimH* binding with mannose disaccharides.[66] A mannose trisaccharide has also been identified as a lectin receptor, found on epithelium cells in the urinary tract, for *E. coli* adhesion (Table 1). To evaluate this with our probe, three different mannose derivatives (**28**, **29**, **30**) (Figure 49), aminated at the anomeric position, were prepared using the MW-assisted Kotchetkov amination procedure described before followed by CD conjugation by CDI mediated coupling.

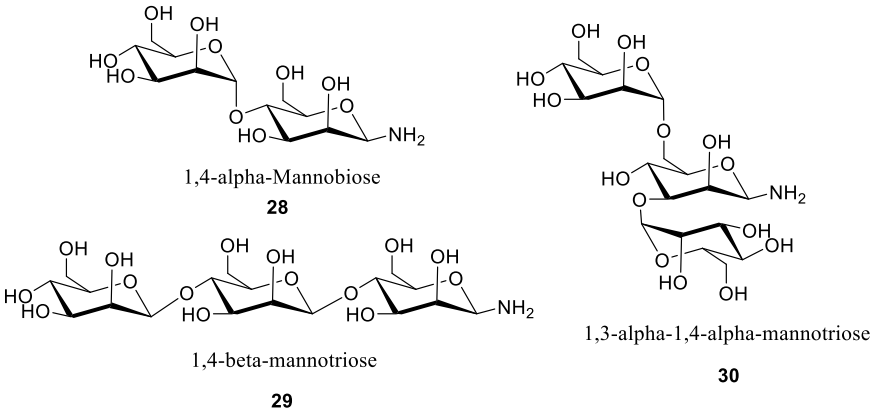

Figure 49. Three different mannose derivates **28**-**29**-**30**, that are used to functionalise GCDs.

3.1.2.3 TTDDA LINKER

To ensure the sugar attached to the CD surface can interact with the binding pocket a linker can be used to create distance from the surface of the nanoparticle. The binding pocket of *FimH* is found at the end of a large fimbrial protrusion and is shielded by both a hydrophobic and a 'tyrosine gate' region, shown in Section 1.3.2, which could cause steric hindrance to approaching nanosized particles. Therefore, a linker could facilitate carbohydrate accessibility of the binding pocket. Diamine 4,7,10-Trioxa-1,13-tridecanediamine (TTDDA) was employed to increase distance from the surface of the GCD from the binding mannose as functional groups too close to the surface could affect accessibility by the receptor. The importance of linker length for cellular targeting has been highlighted by multiple publications.[293–295] High-loading of nanoparticles can often engender instability and poly(ethylene glycol) (PEG) linkers have been previously reported to impart stability to the system.[295] TTDDA was chosen as a PEG-type linker that had shown biological compatibility as a component of cancer cell labelling blue-fluorescent CDs.[141] TTDDA was first reacted with succinic anhydride to form carboxylic acid **34** before CDI-conjugation to GCDs (**35)**, followed by mannose (**26**) attachment also CDI mediated (**36)** (Scheme 6).

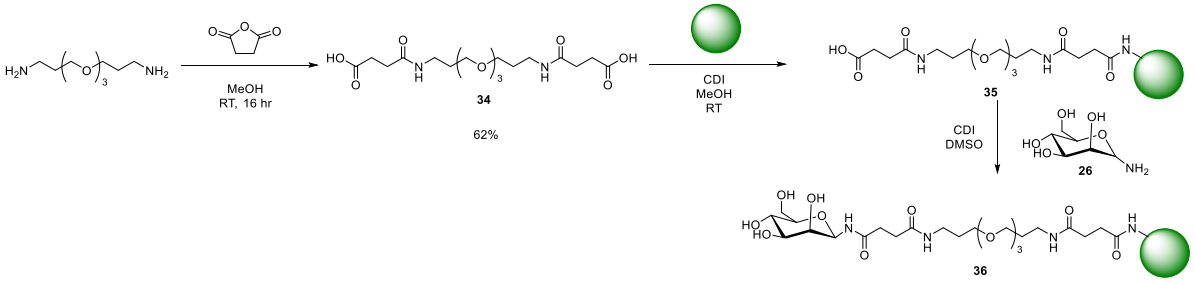

Scheme 6 Formation of carboxylic acid **34** and following attachment of linker to GCD and further functionalisation with mannose-NH_2 (**26**).

3.1.2.4 DENDRITIC LINKER

Different multivalent presentations of mannose for the targeting of *FimH* have been described in Section 1.3.3. Multivalency has been shown to increase ligand affinity in the *FimH* lectin despite being a monovalent receptor, this avidity has been linked to higher probability of binding and the simultaneous association of multiple lectins. Therefore, a dendritic linker was designed which would increase distance from the GCD surface and bind three mannose moieties per position, thus increasing the multivalent presentation of the sugar on the surface. Dendrimers are hyperbranched polymers, where monomeric units are highly ordered into tree-like branches from a central point to a high density of end groups.[296] A first-generation dendrimer was synthesised from an initial condensation of Tris base with *tert*-butyl acrylate (**37**) before deprotection with phosphoric acid (**38**) (Scheme 7). Acid functionalised CDs (25) were then activated with EDC. The excess EDC was quenched with mercaptoethanol, and then the acid-coated carbon dot was functionalised with the dendrimer via amide formation (**39**). Sugar conjugation was then performed as previously described, using the coupling reagent CDI (**40**).

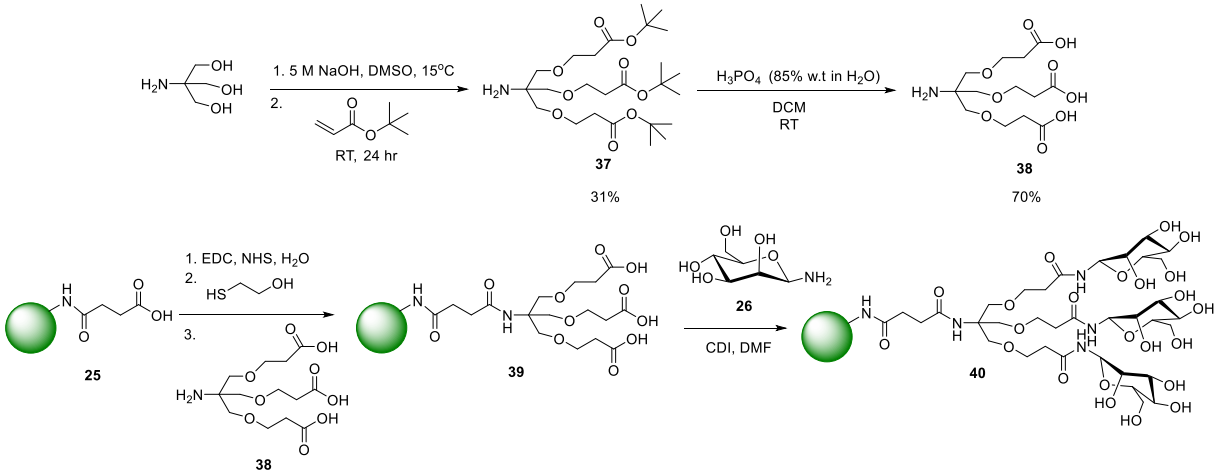

Scheme 7 Synthesis of dendrimer **38** and conjugation to acid-functionalised GCDs to form **40.**

3.1.3 IMAGING OF MANNOSE FUNCTIONALISED GCDS

Following the conjugation of different mannose derivatives to GCDs, functionalised GCDs were incubated with *E. coli* and imaged with confocal microscopy following similar protocol designed for unfunctionalized GCDs in Chapter 2. The *FimA* deletion strain of *E. coli* was employed as a control of mannose-specific binding.

Unfortunately, all mannose-functionalised carbon dots synthesised displayed no fluorescent labelling when incubated with *E. coli* or the *E. coli FimA* deletion. Only background fluorescence was seen in the confocal images of the bacteria incubated with mannose-functionalised dots indicating that the addition of the mannose had prevented the bacterial labelling (Figure 50). Not only was labelling specificity conferred through mannose conjugation but non-specific fluorescent labelling was also precluded.

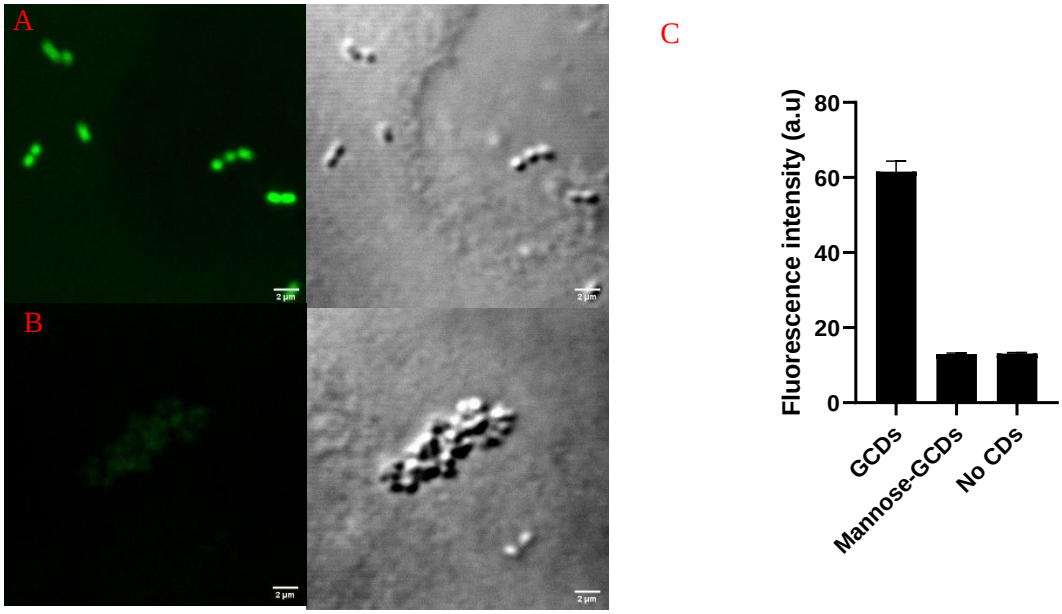

Figure 50. Labelling of *E. coli with mannose functionalised GCDs.* Confocal Microscopy images of (A) unfunctionalised GCDs fluorescent labelling in comparison to the (B) mannose-functionalised GCDS. (C) Graph showing the labelling fluorescence intensity calculated from confocal images (see Section 2.2.2) of GCDs and mannose-functionalised GCDs.

Although the functionalised GCDs were still fluorescent, a notable trend in the fluorescence spectra of GCDs was seen upon functionalisation and purification. For example, upon CDI-aided coupling of the dendrimer to the acid-functionalised GCD the 520 nm emission peak broadens and a new peak is seen at 450 nm. Further coupling of mannose strengthens the 450 nm peak and no 520 nm emission is detected (Figure 51). The intensity of the fluorescence is also reduced.

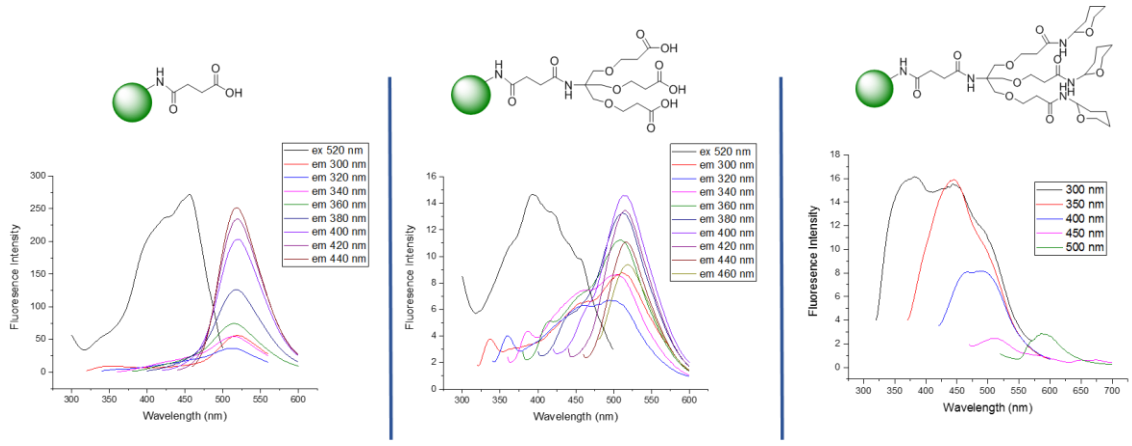

Figure 51 Fluorescence spectroscopy of each product during mannose-dendrimer functionalisation synthesis. Concentration of the samples were not the same so fluorescence intensity could not be directly compared.

The observed shift in fluorescence is likely due to the changing composition on the surface of the nanoparticle. As fluorescence intensity is linked to interactions with the 2,5-DOFR associated to the CD, displacement of this molecule through conjugation and repeated dialysis steps, and also the introduction of new electron environments is the probable cause of the variation in fluorescence spectrum.

The increased number of purification steps needed in the functionalisation of the GCDs were suspected of stripping the GCDs of the majority of 2,5-DOFR from the surface. Unfunctionalised GCDs were dialysed against deionised water for a week and fluorescence intensity was compared to GCDs which have not undergone further purification (Figure 52). Comparing both CD samples at a concentration of 133 µg/mL, it was observed that the intensity of the GCDs at λ_{em} = 520 nm after dialysis dropped dramatically. The forty-fold decrease detected between the samples demonstrated the importance of surface-bound 2,5-DOFR on the fluorescence of the CDs and indicates the core-CD independently has a low QY. The spectral profiles of both pre- and post-dialysis GCDs are similar, which supports the theory that some 2,5-DOFR is still attached to the core-CD. Consequently, any functionalisation attempt will likely strip most of the 2,5-DOFR from the surface of the GCD through the repeated purifications meaning fluorescence imaging will be ineffective.

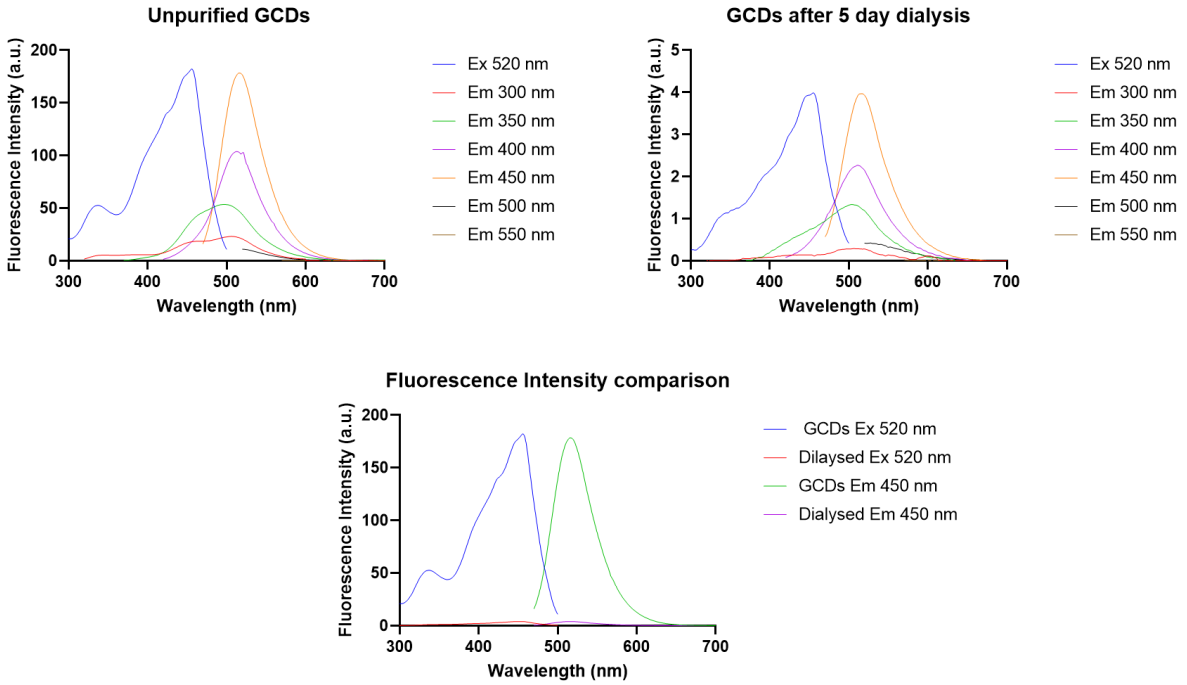

Figure 52 Fluorescence spectra of GCDs without further purification and GCDs dialysed against deionised water for 5 days, both at 133 µg/mL. Spectra below showing difference in fluorescence intensity at λ_{ex} 520 nm and λ_{em} 450 nm.

Due to the complications of non-covalently bound 2,5-DOFR that contributes to the GCDs green fluorescence emission, it was decided that the GCDs are not an ideal system for functionalisation. Therefore, a new nano-platform was needed.

3.2 QUANTUM DOTS

The first nanoparticles utilised within the Galan group for live cell labelling were CdSe-based quantum dots (QDs). Here, a series of glycan-coated QDs were investigated for their differential uptake and intracellular localisation in HeLa and SV40 epithelial cells, factors found to be dependent on the glycan surface presentation.[96] These nanoparticles were not initially considered for this research since as compared to CDs, QDs have higher toxicity, their synthesis is much more difficulty and the materials are more sensitive to photobleaching and degradation via oxidative processes. However, their use in bioimaging, including *FimH* targeted mannose labelling, has been well researched and reported, discussed in Section 1.4. Therefore, it was decided to evaluate their performance to establish the mannose-targeting of the *FimH E. coli* lectin, and validate the microbiological methodology used.

3.2.1 HEPTYL MANNOSIDE LIGAND[3]

As opposed to the previous mannose labelling strategies employed with the GCDs, a new, more targeted, approach was proposed. The binding pocket of the *FimH* lectin has been previously studied and ligands, optimised for their interactions with the fimbrial subunit, have been reported. A more detailed summary of different *FimH* ligands is discussed in Section 1.3.3. One popular ligand is the seven carbon alkyl chain mannoside, which is comparatively simple in structure yet found to have good affinity binding. First the N-linked heptyl mannoside (HM) ligand (**41**) was synthesised in a one-step reaction that required extensive HPLC purification and consequently was low yielding (Scheme 8).

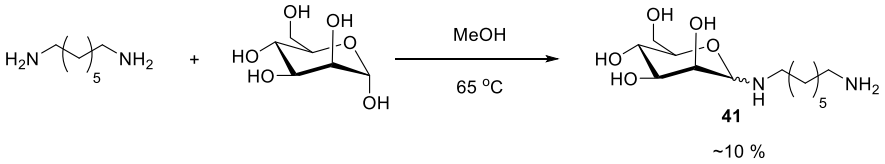

Scheme 8 One-step reaction to form N-linked C7 mannose linker.

Many difficulties arose in the purification of the ligand because of the hydrophobic nature of the seven carbon chain and the hydrophilic properties of the unprotected sugar. Therefore multiple HPLC runs were needed to obtain a pure product and therefore yield was very low. Green-fluorescent CdSe QDs synthesized following reported procedures with a passivating lipoic acid surface layer were functionalised with the N-linked HM ligand (prepared by David Benito-Alifonso) (Figure 53).[96]

3.2.2 CONFOCAL IMAGING OF LABELLING

The HM functionalised QDs (**45**) were incubated for 1 hour with *E. coli* and *FimA*-deletion *E. coli* strain and the labelling monitored by confocal spectroscopy (Figure 53).

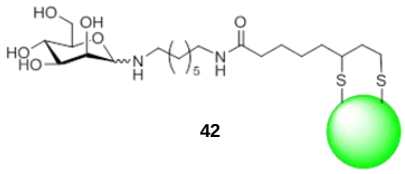

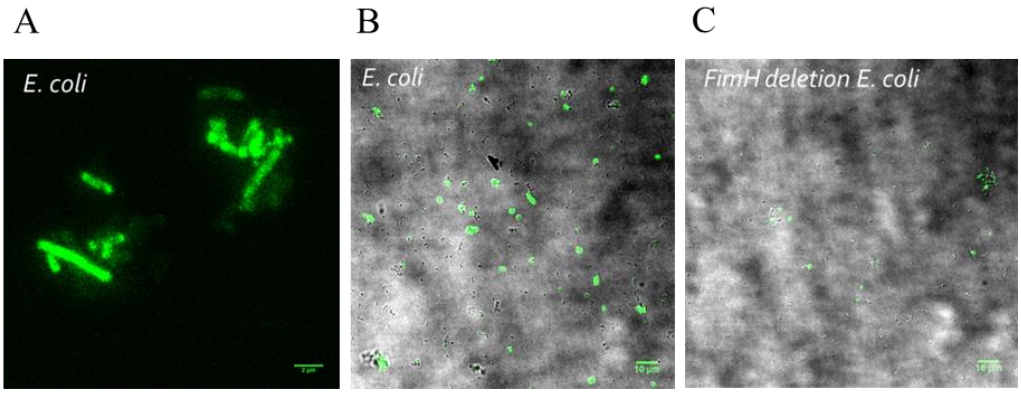

Figure 53. Labelling of *E. coli* by mannose functionalised green QDs (**43**). Above: Representation of the functionality at the surface of the QD. A-C Confocal images of Mannose-linker QD incubated with *E.coli* and *FimH* knockout for 1 hour before fixation. A. Fluorescence channel showing labelling of the *E.coli*. B-C. Overlay of fluorescence and bright field channels of *E. coli* (B) and Δ*FimA E. coli* (C).

[3] C7 mannose-functionalised QDs were prepared by David Benito-Alifonso

Green-fluorescent labelling was observed in *E. coli* but, as seen on the brightfield overlay, (Figure 53), the mannose-QDs did not universally label as some cells are unlabelled. The knockout *E. coli* strain, in comparison, exhibited little fluorescent labelling. However, some non-specific interactions were seen, and due to the qualitative nature of the technique the ratio between labelled and non-labelled bacteria could not be calculated and conclusions were only able to be drawn from qualitative observations.

3.2.3 LABELLING DIFFERENCES OF MANNOSE-QDS BETWEEN SPECIES

The mannose-specific binding of other bacterial species was also explored to ascertain whether *E. coli* could be specifically labelled and identified in a mixture. As in the previous chapter Gram-negative, *K. pneumoniae* and *P. aeruginosa* and Gram-positive *S. aureus* were tested (Figure 54).

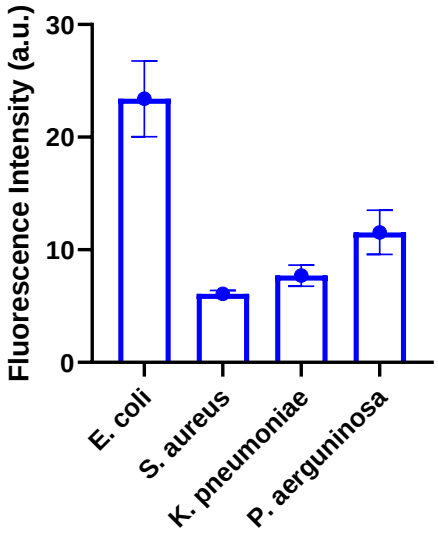

Figure 54 Graph of fluorescent labelling of different bacterial species by C_7-mannose functionalised QDs (**42**) after 1 hour incubation. Data from analysis of confocal images and adjusted for autofluorescence.

As with the *E. coli* knockout strain there was some background labelling of all strains incubated with the mannose-QDs (**42**). *S. aureus* has the lowest level of fluorescent labelling, similar to the non-specific interactions seen previously. This is expected as there are no reported mannose-specific lectins on the surface of *S. aureus*. *K. pneumoniae* does have a lectin with a *FimH* subunit. However, fine receptor-structural specificities of the protein can be substantially different between species.[297] It has been found that when compared to the monomannose specific binding of the *FimH* unit found on the surface of *E. coli*, *K. pneumoniae FimH* has an altered monomannose-binding pocket and so only very weakly binds *N*-linked terminally exposed mannose residues. However, it was shown to have preferential binding to trisaccharides with a terminal mannose.[297] This demonstrates the potential scope for using a trisaccharide linker to specifically label *K. pneumoniae* over *S. aureus.* Fluorescence labelling is also significantly lower in *P. aeruginosa* than *E. coli*. A mannose-specfic lectin has been identified on the surface of *P. aeruginosa* but it is a PA-II receptor opposed to *FimH*.[298] The linker structure is therefore unlikely to be complementary to the PA-II binding pocket, the structure of which being still relatively unknown in comparison to *FimH*.

This preliminary result using QDs were promising and were able to confirm the *FimH* ligand system was viable, but difficulties arose in the synthesis and solubility of the mannose functionalised QDs.

Reproducibility between batches of QDs can be hard to achieve as structure and fluorescence properties are very dependent on the reaction time before quenching.[96] The longer the reaction, the larger the QD and therefore the more red-shifted the fluorescence due to the quantum confinement effect. Unlike CDs, QD cores are not inherently soluble so water-solubility is achieved through surface functionalisation, although lipoic acid is an easily synthesised linker it does not impart good solubility. Also, confocal imaging with QDs is comparatively challenging when collecting multiple, high-resolution z-stacks of one area due to their tendency of photobleaching. It was therefore decided that further development of the system should use a different nanoparticle base.

Commercial polystyrene microspheres with an internal dye and carboxyl-functionalised surface were purchased as an alternative nanoparticle platform. The fluorescent carboxyl polystyrene microspheres purchased were the smallest available, at 50 nm in diameter, in efforts to replicate the proven QD system. Red fluorescent microspheres were chosen as this would not overlap with the autofluorescence spectral range. However, polystyrene microshperes are sensitive to freezing, drying and centrifuging, all which could cause irreversible aggregation. Therefore, in practical attempts to conjugate the HM ligand were virtually impossible without causing damage to the polystyrene core. Reaction mixtures that were consequently purified by small-scale dialysis or size-exclusion chromatography could not be concentrated, and therefore any products were too dilute for meaningful biological testing. Characterisation including NMR could also not be performed and so conjugation could not be verified.

3.3 ALTERNATIVE CARBON DOTS

Although the GCDs are not suitable cores for sugar engendered specific labelling, many alternative CDs have been reported in the literature, that do not have molecular species attached to the surface, that could be used as fluorescent conjugation platforms.

3.3.1 LITERATURE MANNOSE DERIVED CDS

Previously, the synthesis of CDs from ammonium citrate and mannose were reported by Weng *et al*.[239] The publication claimed a one-step synthesis of mannose-modified CDs that were shown to specifically label *E. coli* over CDs that did not possess mannose moieties. In order to compare the performance of our labelling strategy with Weng's report, a simple labelling-confirmation experiment was sought and so the mannose-derived CDs were synthesised. In brief, the ammonium citrate (in large excess) and mannose were heated at 180 °C for 2 hours before treatment with sodium hydroxide solution under sonication and finally dialysis purification lead to CDs which were blue-emitting fluorescent. The CDs were thus incubated with *E. coli* and *S. aureus* for 1 hour under gentle shaking at room temperature, before being centrifuged, bacteria pellet washed and fluorescence intensity recorded in a microplate spectrophotometer. The publication reported that CD fluorescent labelling of *E. coli* was seen using CDs with mannose precursor (**CD-1**) but not for CDs derived from solely ammonium carbonate (**CD-2**). The experiment was repeated as reported by Weng *et al*.[239], with the use of *E. coli* Δ*FimA* strain instead of *S. aureus* as the control, however the results were not in line with those reported in our hands (Figure 55). No labelling was seen for either strain or either CD incubated, with levels of fluorescence around that of the untreated control. The **CD-1** synthesis was repeated multiple times as was the incubation with bacteria, including incubation with *S. aureus* as well (Figure S 9). No labelling was seen at any attempt.

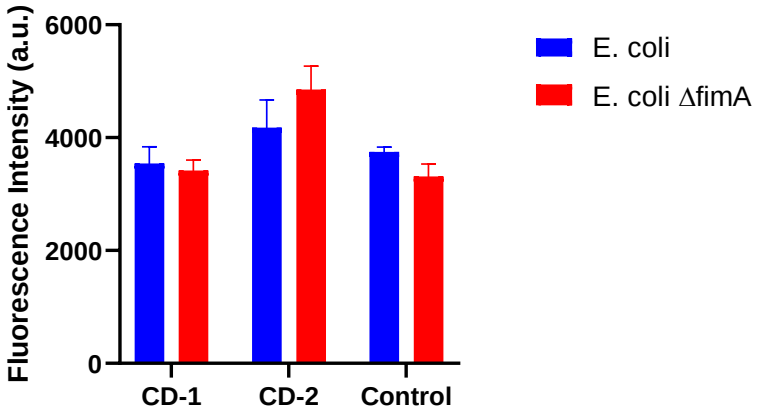

Figure 55 Fluorescence intensity readout of microplate spectrophotometer between samples *E. coli* samples with and without the fimbrial mannose receptor comparing labelling with CDs derived from mannose and ammonium carbonate (CD-1) and from ammonium carbonate solely (CD-2).

The reported fluorescence excitation and emission maxima were at λ_{ex} 365 nm and λ_{em} 450 nm respectively, however this differed from that found from those synthesised (Figure 56).[239] A small broad peak was observed around λ_{em} 590 nm from excitation at λ_{ex} 500 nm and the highest intensity fluorescence peak was found at λ_{em} 520 nm with excitation at λ_{ex} 460 nm.

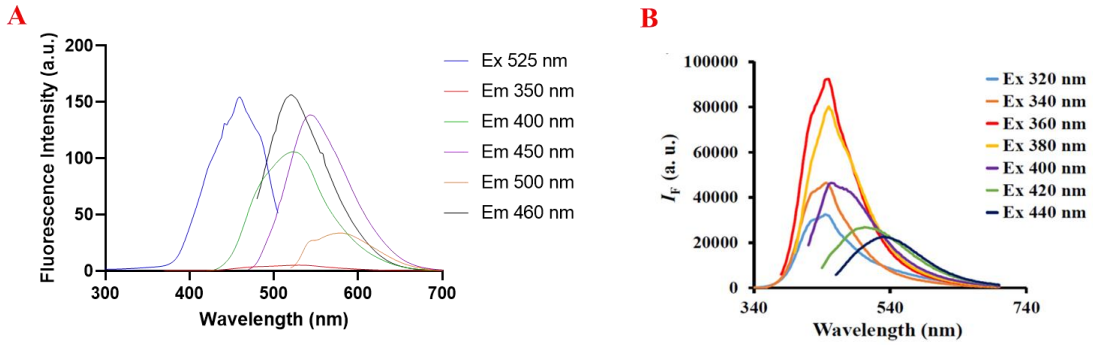

Figure 56 Fluorescence spectrum of CD-1. A. Spectrum measured for reproduced CDs; B. Spectrum published in Weng *et al* report.

3.3.2 LITERATURE CD SYNTHESIS SCREEN

This led to speculation over the reported CDs synthesis reproducibility. There seems to be an issue with data published for CD methodology that is not always reliable, as highlighted by Essner *et al*, who found the presence of small fluorophores as the source of fluorescence in many reported CDs and claimed inconsistencies and errors were widespread in CD publications. Therefore, before further functionalisation and labelling attempts, a selection of published CDs synthesis were attempted and characterised to evaluate if the materials obtained matched that reported in the literature. The most reports used commonly reported and easily accessible CD precursors such as citric acid (CA), urea and ethylenediamine. A summary of the synthesised CDs is found below in Table 2.

Table 2 Summary of literature CDs synthesised.

Name	Authors	Starting reagents	Reaction conditions	Reported fluorescence emission	Fluorescence emission measured
CD-3	Yang *et al*[134]	Citric Acid, Urea and NaF	Domestic MW	510 nm	600 nm
CD-4	Qu *et al*[299]	Citric Acid and Urea	Domestic MW	540 nm	520 nm
CD-5	Khun *et al*[300]	Diammonium hydrogen citrate and Urea	Hydrothermal	537 nm	450 nm & 510 nm
CD-6	Yu *et al*[301]	Phthalic acid and DABCO	Domestic MW	Broad 480 - 510 nm	Broad 480 - 510 nm
CD-7	Liu *et al*[302]	Citric acid, cysteine and dextrin CDs	Domestic MW	495 nm	430 nm
CD-8	Jiao *et al*[303]	1,4-Phenylenediamine and HCl	Hydrothermal	590 nm	350 nm
CD-9	Wu *et al*[304]	Dicyandiamide and citric acid	Hydrothermal	452 nm	430 nm and 505 nm

3.3.2.1 CD-3: CITRIC ACID, UREA AND SODIUM FLUORIDE CDS

Yang *et al* reported the microwave synthesis of red fluorescent fluorine-doped CDs in 2018 (**CD-3**).[134] This synthesis was chosen as it was reported as a simple, MW reaction that produced CDs with a desirable red fluorescence from readily available starting materials. In brief, citric acid, urea and sodium fluoride in water are irradiated in a domestic MW for 5 mins before filtration and dialysis purification. The authors reported that on excitation with λ_{ex} 530 nm wavelength the fluorescent emission wavelength was λ_{em} 600 nm, however this did not correlate with our own characterisation of the synthesised material. No red fluorescence was found but instead a green fluorescence maxima at λ_{em} 510 nm was found with excitation with λ_{ex} 400 nm (Figure 57). This is similar to other reported CDs synthesised from CA and urea, and suggests the fluorine has not be incorporated into the CD structure.[305] The synthesis was repeated multiple times, but the same green fluorescent material was recovered. The differences in the integral fluorescent properties of the resulting **CD-3s** indicates that the product is a different core than reported.

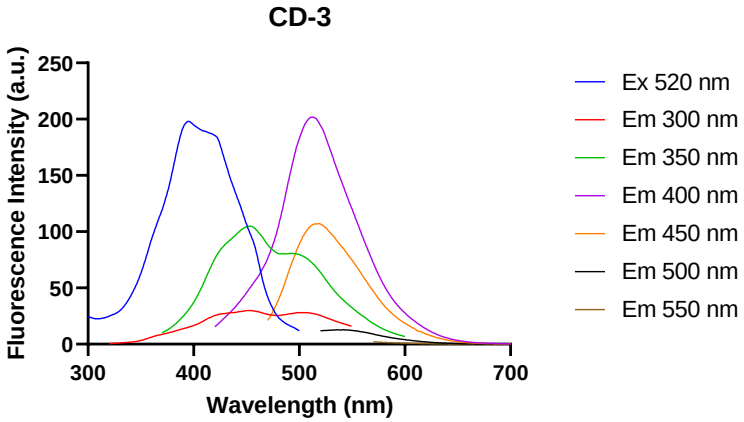

Figure 57 Fluorescence spectrum of CD-3 CDs showing a prominent blue/green fluorescence.

3.3.2.2 CD-4: CITRIC ACID AND UREA CDS

There are many examples of citric acid as a precursor in CD synthesis which are commonly used as starting materials in combination with urea. One study by Sendão *et al* analysed six CA-based CDs, two of which included urea in the reaction mixture, with different bottom-up synthetic methodologies.[306] The highest quantum yield (QY) was found for both CA containing CDs QY = 51.98 % for a five minute microwave synthesis and QY = 49.01% for a 2 hour hydrothermal synthesis. Without CA the highest QY reported was 8.37% for a hydrothermal synthesis. CA CDs were also shown to have a blue fluorescent emission however the addition of urea introduces *N*-doping and fluorescent emission was seen to be red-shifted.

Another publication, from Qu *et al*, also examined the effect of urea *N*-doping on fluorescent emission.[299] They reported the modulation of CD optical properties through modification of the CD reagent ratio alone. Two CA/urea CDs were reported, both synthesised from identical experimental methodology, a four minute domestic MW synthesis, but the ratio of reagents altered. It was found that the CDs formed with the low urea mass ratio (0.2:1) exhibited a blue emission (λ_{em} 440 nm) and a QY of 15 %. Conversely, CDs with a high urea mass ratio (2:1) resulted in a green emissive nanoparticle (λ_{em} 540 nm) and a QY of 36%.

The reported Qu *et al* four minute MW synthesis of the high urea mass ratio CDs was thus repeated at a scaled down volume (but keeping the same reagent concentration) (**CD-4**). The fluorescence emission reported was reported as λ_{em} 540 nm but the synthesised material was found to have an emission λ_{em} 520 nm, which although similar, highlights again possible changes to the reported structure (Figure 58). Also, of note is during the dialysis step of purification a large reduction of mass was found, from over 1 gram of starting material to 189 mg of recovered purified product. The low conversion to **CD-4** could be explained by molecular by-product synthesis as the dialysate was deeply coloured during purification.

Kasprzyk *et al* studied the molecular origin of green fluorescence from CA/urea MW synthesised CDs and found the molecule 4-hydroxy-1H-pyrrolo[3,4- c]pyridine-1,3,6(2H,5H)-trione (HPPT), through purification, isolation and detailed NMR characterisation, as the main contributor to the CDs high QY's.[307] The corresponding ^{1}HNMR of the pre and post dialysis product of **CD-4** shows a considerable decrease and loss of multiple peaks indicating the loss of small particles (Figure S 37).

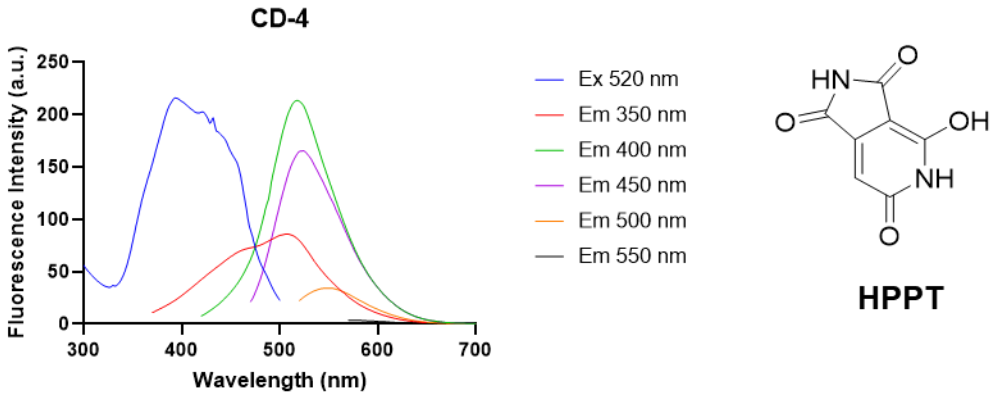

Figure 58 Fluorescence spectrum of CD-4 and structure of proposed molecule fluorophore 4-hydroxy-1H-pyrrolo[3,4- c]pyridine-1,3,6(2H,5H)-trione (HPPT).

3.3.2.3 CD-5: Diammonium hydrogen citrate and Urea CDs

An alternative to the use of CA/urea dots was reported by Khan *et al* where diammonium hydrogen citrate is used in the place of CA (**CD-5**)[300] The **CD-5s** were reproduced following reported procedures, heating of 180 °C for 1 hour followed by centrifugation and filtration. The fluorescence emission was reported λ_{em} 537 nm, but again was different to the spectra measured for the ones made in our lab (Figure 59). Instead, double maxima were found, at λ_{em} 450 nm and 520 nm.

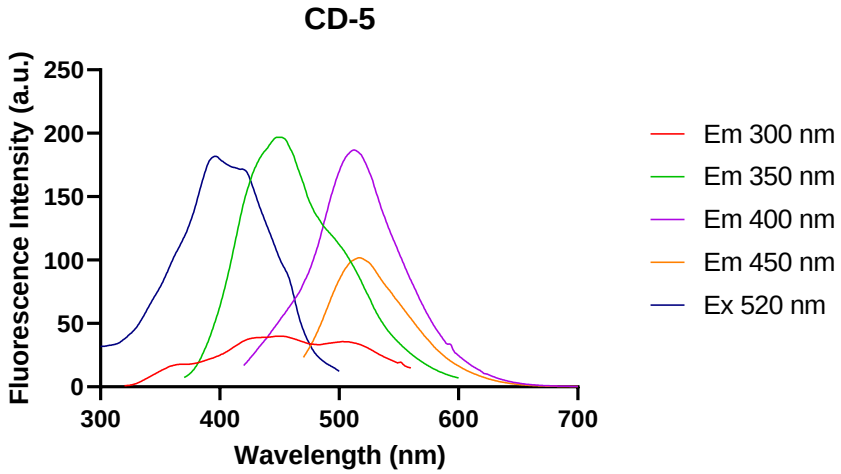

Figure 59 Fluorescence spectrum of **CD-5.**

Another issue with the synthesised **CD-5s** was that they displayed slight fluorescence labelling of bacteria without further purification (Figure 60). This is not an ideal core property for a system designed to label through specific carbohydrate-lectin interactions only, as was found for the GCDs.

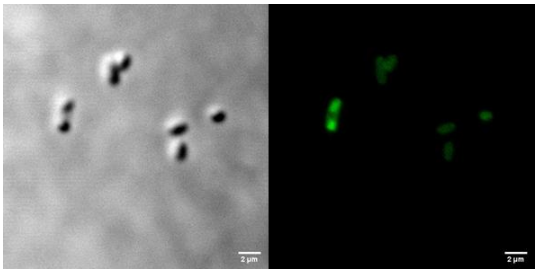

Figure 60 Confocal microscopy image of unfunctionalised CD-5 with *E. coli* after incubation for 1 hour.

3.3.2.5 CD-6: PHTHALIC ACID AND DABCO CDS

Due to the difficulties experienced with CA/urea reported systems, a literature synthesis was chosen that had less common starting materials. Yu *et al.* reported that phthalic acid and 1,4-diazabicyclo(2.2.2)octane (DABCO) yielded green fluorescent CDs from a simple 1 minute domestic microwave reaction (**CD-6**)[301] Upon repeating this synthesis, the resulting fluorescence profile of **CD-6** was characterised. A broad fluorescence maxima was found at λ_{em} 500 nm and the fluorescence spectrum recorded matched that which had been reported in the publication (Figure 61).

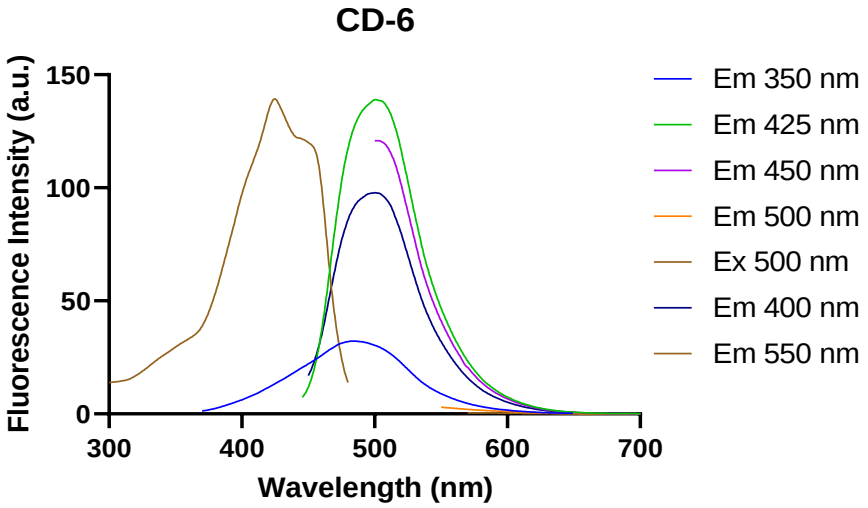

Figure 61 Fluorescence spectrum of **CD-6.**

However, one major issue with this synthesis is the loss of product during the purification stages. Originally the mass of starting materials was over 3 grams, but the material recovered after centrifugation filtration and dialysis was 15 mg, indicating poor conversion to CD and the majority of the product being large aggregates or small molecules. To use a core with such a significantly low yield, 0.4 %, for bioimaging would be wasteful and impractical.

3.3.2.6 FURTHER LITERATURE CD SYNTHESIS

Multiple other literature CDs were also synthesised from a variety of starting materials including CA/cysteine/dextrin CDs (**CD-7**), 1,4-phenylenediamine/HCl CDs (**CD-8**) and dicyandiamide/CA (**CD-9**).[302–304] Unfortunately, as with previous attempts reproducibility issues were encountered as fluorescence characterisation of the materials did not match that reported in the literature (Figure S 12, Figure S 13, Figure S 14 respectively).

Many of the synthesised CDs saw a large decrease in mass during purification processes, likely due to the formation of either large, insoluble carbonaceous material or small molecule by-products. To confirm that the resulting purified products are actually nanoparticular products and not molecular aggregates further characterisation was also needed. Techniques including dynamic light scattering (DLS) and transmission electron microscopy (TEM) allow for nanoparticle determination and estimation of size.

3.3.3 DLS CD CHARACTERISATION

Dynamic light scattering (DLS) is a common analytical technique for finding the approximate size distribution of CDs in solution hydrodynamic radii.[308] This technique is based on the Brownian motion of the dispersed nanoparticles where smaller molecules move at higher speeds. The diffusion coefficient of particles is determined by the scattering of light through the sample which is detected as a function of time. The input of experimental variables and computational decoding against model systems allows for the calculation of population size distribution. DLS data was collected for some of the literature CDs synthesised to ascertain whether carbon nanoparticles had been formed as reported fluorescence profiles were not reproduced (Figure 62). Nanosized particles were found with a mean diameter between 0.4 nm – 2.1 nm. However, for all reported CDs synthesised, the size of the nanoparticles was determined to be over 2 nm (2.3- 10 nm). For example, CA/urea/NaF **CD-3** had a mean diameter of 2.1 nm whereas Yang *et al* reported a mean of 10 nm, a significantly larger particle size, from transmission electron microscopy (TEM) analysis.[134]

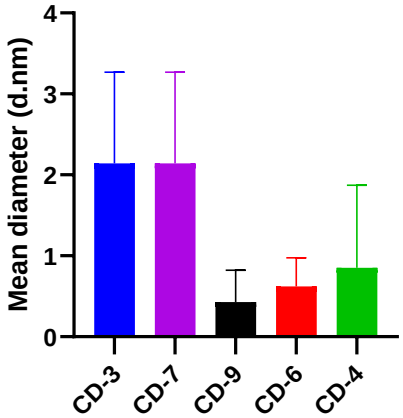

Figure 62 DLS diameter calculations for synthesised literature CDs in H_2O.

The lack of correlation between DLS results measured and those reported is likely linked to the lack of reproducibility in methodology, but also in the chosen analytical technique, many using TEM. DLS is a relatively common method for nanoparticle analysis however, it is not widely used for CD analysis. Commonly, bottom-up synthesised CDs have a large population size distribution which can contribute to high standard deviations, as can be seen with the CD measurements (Figure 62). Because of the heterogeneity issues encountered with CD size measurement with DLS, it is recommended to use HRTEM and AFM for diameter estimation.

3.3.4 NEW CD CORE WITH IMPROVED QUANTUM YIELD [4]

Due to the unreliability of reported CD literature procedures, CDs that had been developed and characterised in the Galan group were chosen as more reliable CD dots for functionalisation. The **CD-10s** are synthesised from citric acid and ethylenediamine (EDA) in a ten minute domestic MW reaction (Scheme 9). The **CD-10**s fluorescence maxima is λ_{em}= 450 nm with a calculated QY of 48% (Figure 63).[309]

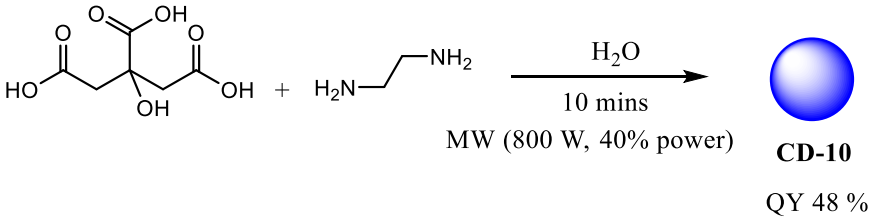

Scheme 9 Synthesis of **CD-10s** from citric acid and EDA.

TEM analysis was used to access particle size and core composition. This microscopy technique allows imaging of nanosized material by passing an electron beam through the sample and allows for greater image resolution than provided by light microscopy techniques.[310] The higher the electron density of the sample, the better the contrast produced so heavier atom materials such as Au nanoparticles have good size resolution. CDs can be harder to view due to their carbonaceous character, but this technique does allow for the characterisation of sp^2 regions which can be visualised as distinct lines in the centre of the CDs. TEM imaging of the **CD-10** showed distinct, nanoparticle structures at an average size of 4 nm, and distinct lines are seen indicating sp^2 character.

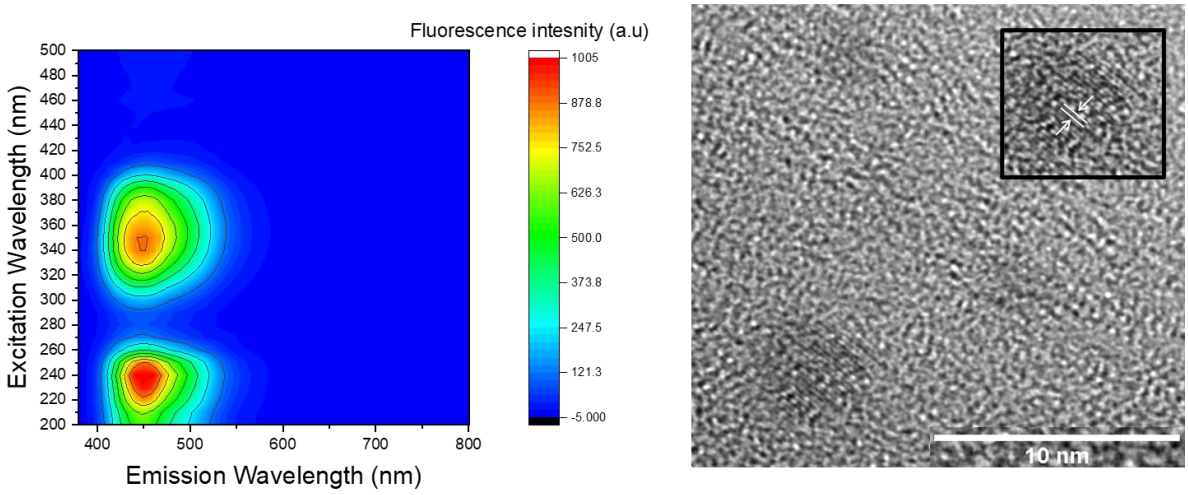

Figure 63 2D fluorescence spectra of **CD-10** and HRTEM.

X-ray photoelectron spectroscopy (XPS) was used to assess the surface functionality of the CDs. In brief, an X-ray beam is focused on the sample which ejects surface electrons which are consequently registered by a detector at a pre-set angle. The binding energy of the recorded electrons is distinct and

[4] The synthesis and characterisation of blue, fluorescent **CD-10** was performed by Teodoro Garcia Millan, Galan group and the synthesis and conjugation of ligand **44** completed by Francisco Javier Ramos Soriano, Galan group.

specific to it's orbital residence and frequency of electrons allows for calculation of the proportion of each element. For **CD-10s**, the oxygen content was found to be higher (23.6%) than of nitrogen (13.5%). Infrared spectroscopy (IR) displayed distinctive carbonyl peaks that indicate the presence of carboxylic acid groups on the surface, common for CA derived CDs. These can act as functionalisation handles for conjugated of sugar moieties.

Francisco Javier Ramos Soriano designed and undertook the synthesis of the α-*O*-linked heptyl mannoside **44** and subsequent conjugation to **CD-10**. The azido compound, **43**, was synthesised according to the methodology reported by Kalograiaki *et al.*[311] Reduction to amine (**44**) was followed by HATU/DIPEA coupling with surface carboxylic acids (**45**) (Scheme 10).[312]

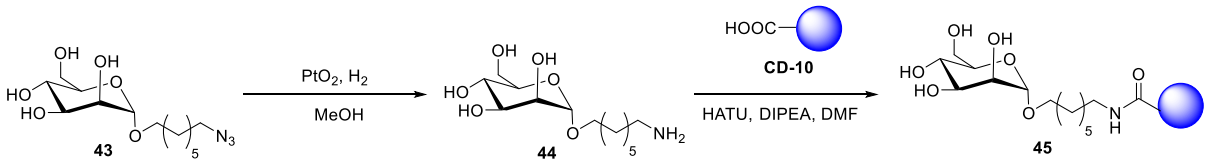

Scheme 10 Synthesis of *O*-conjugated heptyl mannoside (**44**) and functionalisation of CD-10 by Francisco Javier Ramos Soriano.

3.4 AGGLUTINATION ASSAY

Due to the difficulties arising in viewing potential blue-fluorescent labelling from functionalised CDs emission a new, non-fluorescent based technique based on an aggregation-based assay was implemented to quickly evaluate the ability of the probes to bind to *E. coli*. This strategy, which is a long-established technique in evaluating the activity of *FimH* antagonists, exploits the aggregation of *Saccharomyces cerevisiae* (yeast) in the presence of *E. coli*, instigated by the presence of mannan in *S. cerevisiae* cell walls. Mannan is a mannose polysaccharide consisting of backbone of α-(1-6) and α-(1-2) linked mannose with α-(1-3) linked side chains.[313] This simple technique gives either a positive or negative result to evaluate mannose binding with no regard to potency of the lectin antagonist.

Previously reported methodology measured aggregation using an aggregometer, however this was not available in our experiments so a visual determination of aggregation was initially used.[74] Optimisation of the system was needed as initial attempts resulted in no aggregation. A suspension of approx. of $2x10^8$ cfu of *E. coli* was added to a droplet of *S. cerevisiae* in a 1:2.5 ratio (50 µL to 125 µL). The system was found to be sensitive to different conditions with any mixing of bacterial solutions preventing aggregation. After 15 minutes, slight agitation was needed to form the aggregates.

As highlighted in Section 3.1.2, the conditions of *E. coli* growth are important in the expression of fimbriae, and consequently *FimH*, on the surface of bacteria. The agglutination assay could be used to test that *E. coli* growth conditions were the optimum for fimbrial expression. Liquid overnights and suspensions from agar plates were compared in the aggregation assay and it was found that only *E. coli* grown static in liquid media for a minimum of 48 hours were shown to cause aggregation in *S. cerevisiae*. Those samples that had been incubated with shaking were shown not to cause aggregation and so were used as controls in the experiment. SEM also confirmed that *E. coli* grown overnight on agar did not have surface pili, where the *FimH* lectin is found. Clouding is observed in the sample without pili showing settlement of the *S. cerevisiae*, distinguishable from the aggregation of the *E. coli* with pili where the solution clears and distinct white clumps form (Figure 64).

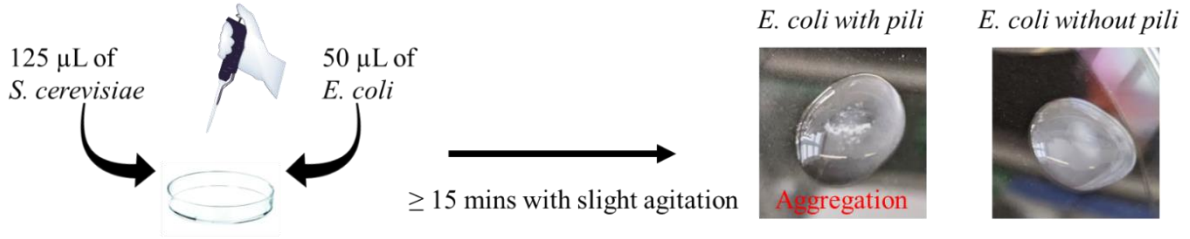

Figure 64 Schematic of simple agglutination process with *E. coli* grown without shaking (with pili) and with shaking (without pili).

3.4.1 AGGLUTINATION ASSAY WITH FREE SUGARS

After optimisation of the agglutination methodology a library of free sugars were tested (Figure 65). As expected, all free sugars containing mannose bound competitively to the *FimH* lectin, therefore preventing aggregation of the *S. cerevisiae*. Glucose and galactose, used as controls, did not prevent aggregation, consequently proving the mannose specificity of this system.

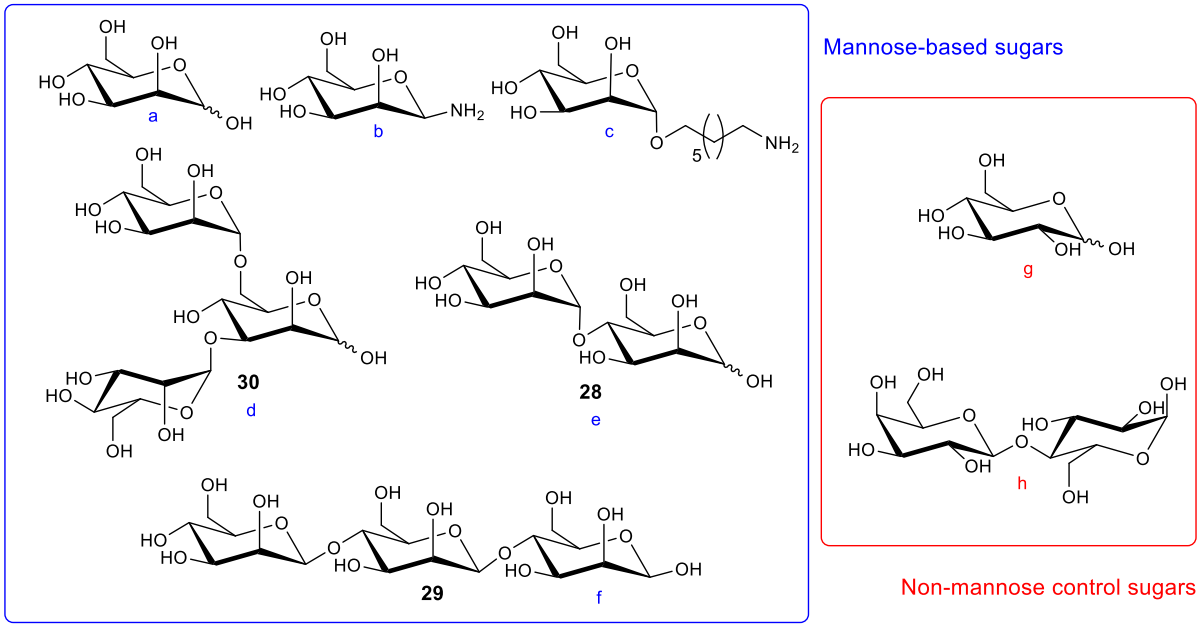

Figure 65 Library of free sugars used in initial agglutination studies. a; Mannose b; Mannose-NH_2 c; C_7-linker Mannose; d; 1,3-α-1,6-α-D-Mannotriose (**30**) e; 4-o-(α-D-Mannopyranosyl)-D-mannose (**28**) f; 1,4-β-D-Mannotriose (**29**) g; Glucose h; Lactose.

3.4.2 AGGLUTINATION WITH MANNOSE FUNCTIONALISED CDS (45)

Once specificity for mannose had been demonstrated with the library of free sugars, CDs functionalised with the heptyl mannoside, **45**, were then evaluated in this system. **CD-10**s were functionalised by Javi Ramos Soriano with two different linker variants. CDs were conjugated with the C_7 linker with both mannose (**45**) and a galactose (**46**) terminal sugar as well as a C_3 mannose ligand (**47**). Distinctive aggregation of the *S. cerevisiae* was found only with the galactose-functionalised CD (**46**) (Figure 66).

This is expected as galactose does not bind *FimH*, and therefore would not displace the mannan-containing yeast, allowing for aggregation. Both mannose-functionalised CDs, **45** and **47**, displayed no aggregation, only slight settlement of cells was observed. This indicates that the mannose ligands compete with the yeast, and are preferential in binding to the *FimH* lectin, and so the yeast cells do not aggregate. This is seen in both the seven and the three carbon mannosyl ligands showing both linker lengths are effective in targeting the *FimH* binding pocket.

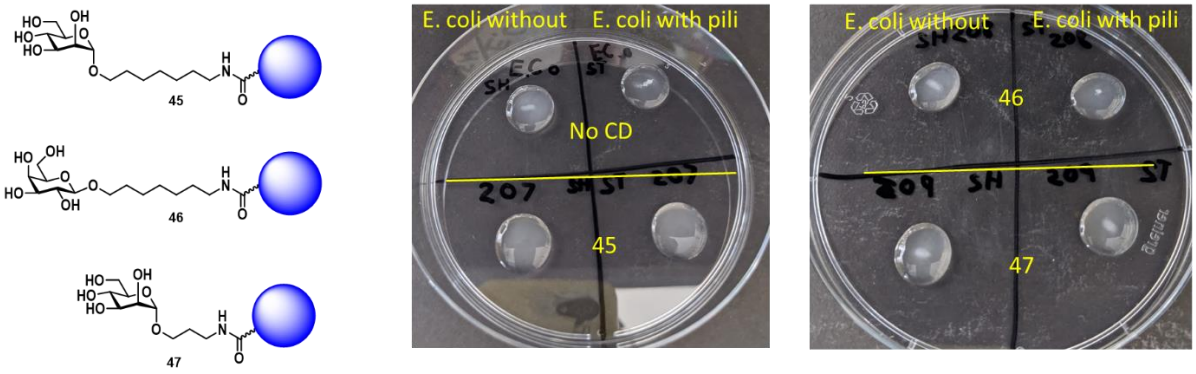

Figure 66 Agglutination results from **CD-10s** functionalised a C7 mannose ligand (**45**), a C7 galactose ligand (**46**) and a C3 mannose ligand (**47**).

3.5 CONCLUSION AND FUTURE WORK

In conclusion, specific targeting of *E. coli* was achieved through the use of mannose functionalised **CD-10s**, exploiting the specific interaction between the carbohydrate mannose and fimbrial lectin *FimH*. GCDs, shown previously to exhibit universal bacterial labelling and antibacterial effects, were found to be unsuitable to chemical functionalisation due to the non-covalently bound 2,5-DOFR displacement which led to lose of fluorescence. Quantum dots were proposed as an alternative fluorescent probe and were conjugated with a heptyl mannoside ligand, **42**, which is known for its affinity to the *E. coli FimH* lectin. Higher levels of fluorescent labelling were observed in bacteria that expressed the *FimH* lectin over a control deletion strain that did not. Differences in labelling observed between bacterial species correlated with that expected from the mannose-binding capabilities of each species. However, difficulties in the synthesis of this materials and concerns with stability led to the search for alternative carbon-based platforms.

A new CD platform was then targeted and several literature CD syntheses attempted. However, none could be replicated. One explanation for the lack of reproducibility could be that many of the CD procedures use a domestic MW oven, which means exact conditions are difficult to perfectly reproduce as power levels can vary between models. Also, we have found that small changes in reaction conditions in general e.g. reagent ratios and/or concentrations have an effect on final CD materials formed. Therefore, a CD developed in the Galan group was utilised as the functionalisation platform in the end, **CD-10**, which was shown to have a good QY with carboxylic acid on the surface that can act as conjugation handles. The **CD-10** was functionalised with mannose and galactose and its ability to interact with bacteria evaluated.

An agglutination assay was employed to test mannose specific binding. This technique is based on the aggregation seen in yeast cells, whose cell wall composition includes mannan (a mannose-polymer), when *FimH*-expressing *E. coli* is introduced to the system. Mannose conjugated **CD-10s** displace mannan binding and so no aggregation is observed. For future exploration of this system, a more quantitative measurement could be developed using an aggregometer or through optical density measurements to access sample aggregation. Fluorescent labelling could also be examined with the use of a microtiter spectrometer. More quantitative mechanisms would allow for differentiation between binding affinity and therefore the optimisation of the mannose ligand, and strategies such as a dendrimer presentation system could be compared.

Ideally, this system could be developed to have a range of sugar functionalised CDs, all targeting distinct bacterial species. This could offer potential applications in the quick identification and diagnosis of bacterial infections. The orthogonal attachment of antibiotics to sugar-conjugated CDs could also offer potential theranostic applications. CDs are generally non-toxic to human cells so have prospective use as targeted drug delivery systems, allowing antibiotic delivery direct to the bacterial cell surface which could prevent unwanted side effects caused by off-target interactions.

4. DISCOVERY OF NOVEL ANTIMICROBIAL DRUG TARGETS

In the previous chapters, the work described has been focused on the use of nanoparticle systems, carbon dots in particular, as bacterial diagnostic and therapeutic tools. The development of novel approaches to bacterial infection treatment is vital to slowing the impending growth of antimicrobial resistance, highlighted in Section 1.1. Therefore, research into areas that are under researched could potentially help a new therapeutic target be identified. One field of research that is poorly understood is the role G-quadruplexes have in bacteria metabolism and viability.

G-quadruplexes (G4s) are nucleic acid secondary structures that form in sequences rich in guanine residues and are found in both DNA and RNA.[314] The formation of G4 structures traditionally require four consecutive runs of guanine which form into a tetrad arrangement that can form a variety of different topologies, discussed further in Section 1.6.2.1. They have been identified in the genome of multiple organisms including parasites, viruses and plants. [187,189,315] Their role in cell function within eukaryotes had been widely studied, especially their involvement in cancer. Ligand-induced stabilisation of G4s has been investigated as a potential cancer therapy with a large variety of G4 ligands developed and assessed for stabilising potency and activity in cellular and animal models.

Meanwhile, relatively little is known about the role of G4s in prokaryotic organisms, such as bacteria, although some studies have employed bioinformatics approaches to analyse genomes for potential G4 forming sequences.[230] Some examples of G4 stabilising ligands targeting G4s upstream of important metabolic genes have been reported in the literature, enabling control over specific metabolic pathways (Section 1.6.2.5). Outlined in this chapter is initial investigations of the effect of a library of G4 ligands on bacterial viability and metabolism. Ligands, initially synthesised within the Galan group[5] as potential cancer treatments, were screened for antibacterial activity against resistant strains of clinically relevant bacteria, *E. coli* and *S. aureus.* As a first step towards investigating the possibility that the observed antibacterial activity may be mediated by G4 binding, the ability of the ligands to stabilise an RNA G4 identified in *E. coli* was examined by the FRET melting assay introduced previously (Section 1.6.2.4). Work is currently ongoing into the mechanism of action for the observed antibacterial effects and whether this is linked to the ability of the ligands to stabilise G4 structures. The effect of the G4 ligands is also explored in the *M. tuberculosis* model strain, *M. smegmatis*.

4.1 ZONE OF INHIBITION TEST

Within the Galan group, twenty-six G4 ligands had been developed previously, using different scaffolds such as stiff-stilbene, dithienylethene and azobenzenes (Figure 67) with some being isomeric analogues (see Appendix 1 for the full list of ligands included in this screening programme). The ligands display binding to the human telomeric G4 and other related G4 sequences. For example, bis-pyridinium stiff stilbene compound **L5** displays a ΔT_m value for telomeric G4 of 15 °C at 1 μM ligand concentration (Figure 67) whilst not affecting the stability of duplex DNA ($\Delta T_m = 0$ °C), demonstrating selectivity for G4s.[316]

[5] G-quadruplex ligands were synthesised by Michael O'Hagan and Francisco Javier Ramos Soriano, Galan group

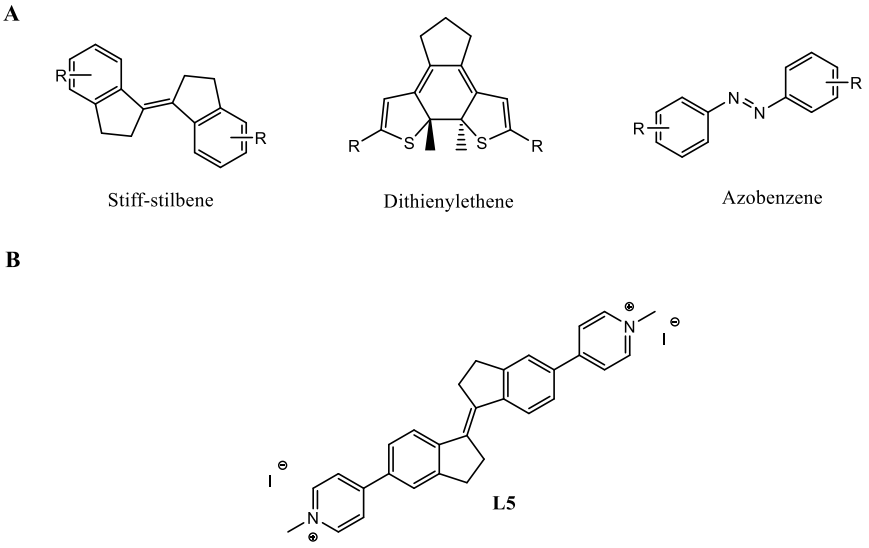

Figure 67 A. General structures G-quadruplex ligand scaffolds included in the ligand library B. Structure of a lead compound previously identified in Galan group screening studies, **L5.**

In the first instance, to examine the potential antimicrobial effects of the ligands, a zone of inhibition test was used. Also known as a Kirby-Bauer Test, it is a standard qualitative technique to test the ability of substances to inhibit microbial growth first developed in the 1950s, refined by W. Kirby and A. Bauer and standardised in 1961 by the World Health Organization.[317–320] In brief, the bacteria is grown on Mueller-Hinton agar in the presence of filter paper disks, impregnated with the chosen antibacterial agent. The antibacterial then diffuses into the surrounding agar, with concentration of the agent decreasing the further the distance from the disk. After incubation overnight, the point of critical mass, when bacterial growth overpowers the inhibitory effects of the compound, is seen as a distinct circle around the disk (Figure 68). The size of the zones can then be compared among different agents and species to indicate comparative antibacterial strength. One caveat of this test is that the diffusion of the antibacterial compound through the agar is proportional to the molecular weight and solubility in the agar. Therefore, comparative conclusions can only be drawn between molecules with similar sizes and functional groups. The majority of the G4 ligands tested in this work have similar molecular weights and share similar molecular scaffolds and motifs, thus qualitative comparisons could be in principle be made.

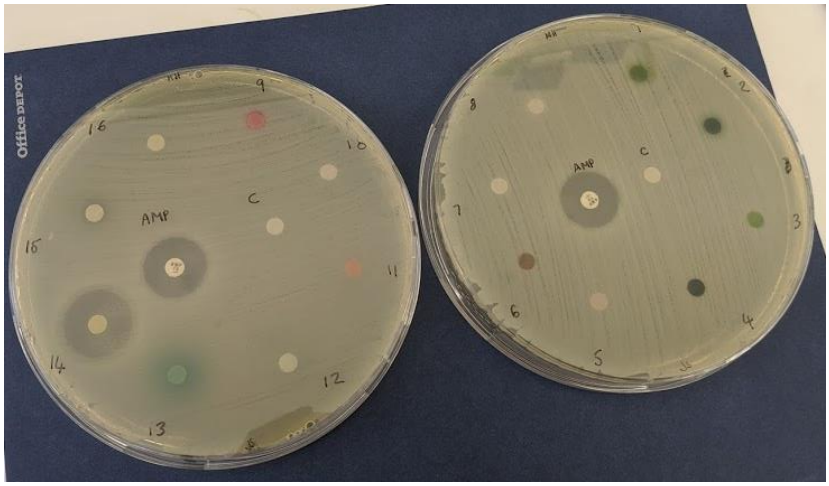

Figure 68 Example of zone of inhibition test to screen multiple G4 ligands. Ampicillin (AMP) and dimethyl sulfoxide (DMSO) [labelled as C] as control conditions.

Both *Escherichia coli* (ATCC 25922) and *Staphylococcus aureus* (Newman strain) were initially tested against the twenty-six G4 ligands library mentioned above (Appendix 1), as well as three benchmark G4 ligands known for the high affinity for G4 DNA; TMPyP4, BRACO-19 and pyridostatin (detailed in Section 1.6.2.4). Any G4 ligands found to have antibacterial effect in each species were then further evaluated with other, multi-drug resistant strains. Each disk was loaded with 25 µg of compound, since concentrations above this amount will have little clinical relevancy. The ligands that displayed antibacterial properties are shown in Figure 69.

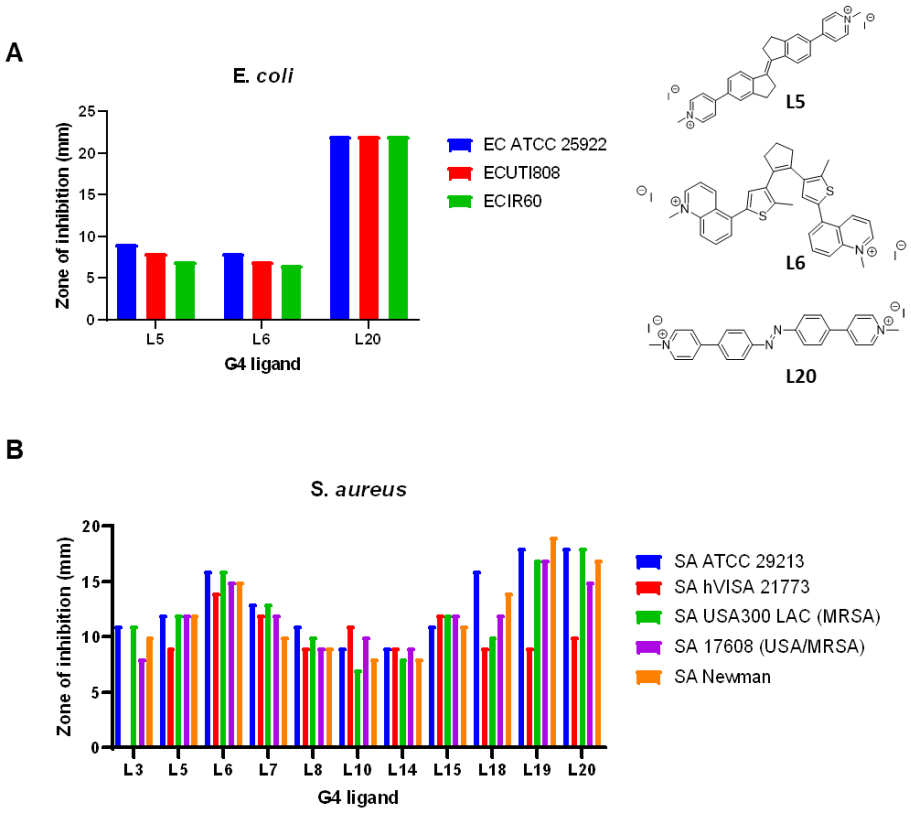

Figure 69 Zone of inhibition (mm) for G4-ligands (25 µg) against different *E. coli* (A) and *S. aureus* (B) strains. Disks used were 5 mm in diameter.

For *E. coli*, three G4 ligands were found to induce a zone of inhibition, with toxicity similar across all three species. Where the zone for ligands **L5** and **L6** was just above the size of the disk, 5 mm, **L20** displayed significant inhibition at over 20 mm for each species. In contrast, eleven compounds displayed activity against the *S. aureus* strains and showed more divergence across the different strains. As in *E. coli* the ligands, **L6**, **L5** and **L20** all displayed significant inhibition. At the concentration tested, 25 µg, no benchmark G4 ligand exhibited any antibacterial behaviour. This perhaps suggests that mechanisms of activity other than G4 binding are operating as known binders are seen to exhibit no antibacterial effects. However, this could also be due to differential uptake of ligands with these compounds not being able to enter the bacterium.

4.2 MIC EXPERIMENTS

Once the 26 ligands were screened and hits identified, the minimum inhibitory concentration (MIC) of each active compound was determined. In brief, the ligands were incubated with bacteria in varying concentrations between 64 to 0.0625 µg/mL over a 16-hour period, the growth of bacteria was measured through optical density measurements in a microtiter plate spectrophotometer. The lowest concentration of ligand that inhibited bacterial growth was recorded (Table 3). The G4 ligand **L5** was determined as the most potent for *S. aureus* with an MIC of 0.25 µg/mL whereas across all *E. coli* species **L20** was found to have lower MIC values (2-4 µg/mL). Notable difference between the Gram-positive *S. aureus* and Gram-negative *E. coli* is seen in the difference in potency of ligand **L6**, 1 µg/mL and 16 µg/mL respectively.

Table 3 MIC values (µg/mL) for G4 ligands against *S. aureus* and *E. coli*.

G4 ligand label	**MIC (µg/mL)**			
	S. aureus	***E. coli***		
	S. aureus Newman	*E. coli* ATCC 25922	*E. coli* UTI 808	*E. coli* IR 60
L3	8	-	-	-
L5	0.25	4	4	32
L6	1	16	16	16
L7	2	-	-	-
L8	4	-	-	-
L10	4	-	-	-
L14	4	-	-	-
L15	4	-	-	-
L18	8	-	-	-
L19	8	-	-	-
L20	4	4	4	2

In both the zone of inhibition and MIC measurements *S. aureus* has a generally higher susceptibility to G4 ligands with a greater number of ligands displaying antibacterial activity and lower MIC concentrations recorded. This could because of the differences in membrane composition, especially if internalisation of the ligand is critical for antibacterial activity. The potent **L5** ligand has a green fluorescence emission, allowing for confocal imaging of bacteria incubated with the ligand for determination of internalisation (Figure 70). Strong green fluorescence was shown in both *E. coli* and *S. aureus* indicating that the ligand is internalised.

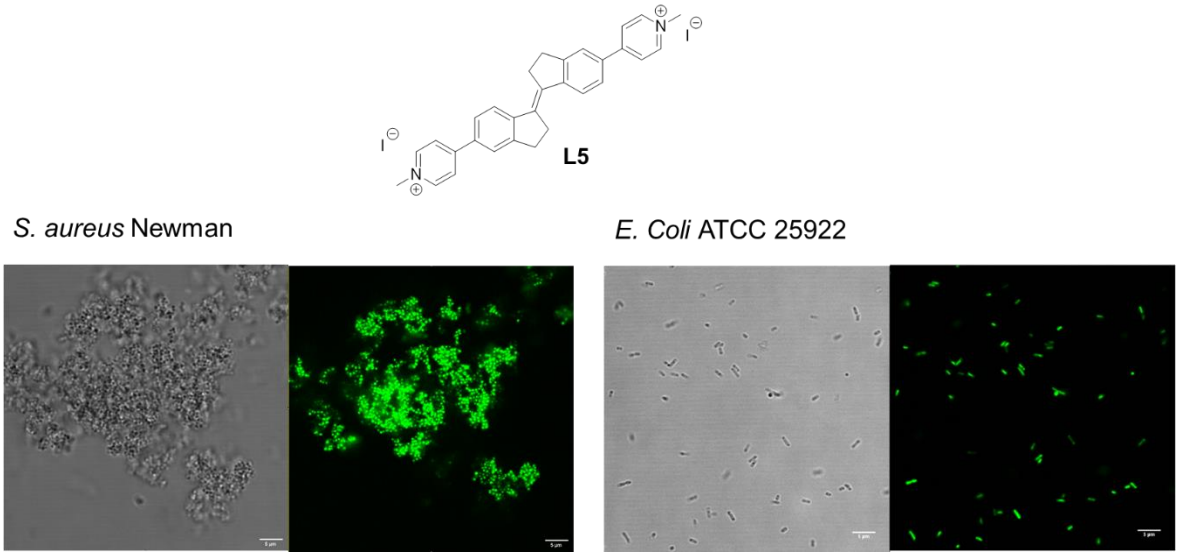

Figure 70 Bright-field and confocal images of *S. aureus* and *E. coli* incubated with G4 ligand L5, structure shown, after 1 hour incubation.

Multiple G4 ligands had core scaffolds, analogous to each other, with varying pendant functional groups. A set of three ligands, **L20, L21** and **L22**, have similar structures apart from the position of methylpyridinium substitution of the outer ring, but the three compounds showed significant differences in their antibacterial effects (Figure 71). Both **L21** and **L22** exhibited no toxicity in the zone of inhibition screening whereas **L20** was the most potent for *E. coli* with the lowest MIC. This indicates that the pyridinium group is crucial for antibacterial activity.

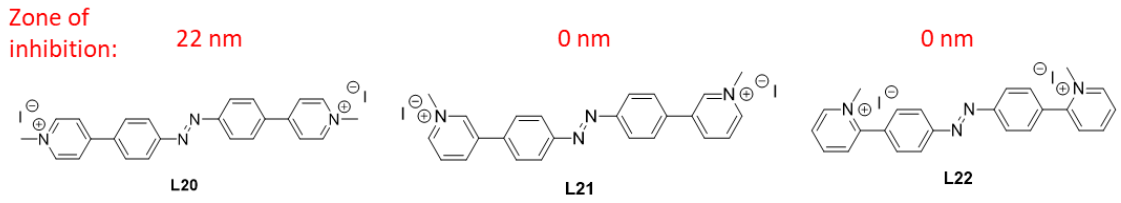

Figure 71 Structure of three different G4 ligands that differ only in the position of the pyridinium substitution with their comparative inhibition zones found from *E. coli* grown in the presence of a 25 µg loaded disk

To investigate further the causes of the observed antibacterial activity in the G4 ligands three different techniques were employed. To probe whether the toxicity may be due to the binding of the ligands to G4 structures, and consequently interrupting metabolic cell processes, circular dichroism (CD) spectroscopy and FRET melting assays were used to investigate the binding of the ligands to suspected G4 forming nucleic acid sequences found in *E. coli*.[223] Proteomic analysis was also conducted by Yukio Takebayashi, probing upregulated and downregulated proteins of *E. coli* ATCC 25922 incubated with **L20** and the benchmark ligand pyridostatin.

4.3 HEML RNA G-QUADRUPLEX

To analyse the binding of the ligand library with bacterial G4 sequences the first bacterial nucleic acid sequence tested in this work was hemL, an *E. coli* mRNA sequence reported by Shao *et al* in 2020.[164] In this publication they identified RNA G4s as an abundant secondary structure in wide range of bacterial species.[164] One species, *E. coli*¸ was investigated further with high-throughput sequencing which identified 168 *in vitro* RNA G4 sites. One G4-enriched mRNA site was identified as *hemL*, a gene encoding glutamate-1-semialdehyde aminotransferase, an enzyme important in cell metabolism. A 21-base pair sequence from the RNA G4 region of *hemL* coding sequence was selected and the quadruplex structure confirmed with CD spectroscopy which displayed a negative peak at λ 240 nm and a positive peak at λ 263 nm, indicating the formation of a parallel topology. The authors used real-time quantitative PCR and Western blot analysis which indicated the RNA G4-dependent regulation of the *hemL* regions in *E. coli*. The *hemL* sequence identified in this research was obtained tagged with the FAM/TAMRA fluorophore pair, and the library of G4 ligands screened for their ability to stabilize this structure.

4.3.1 CIRCULAR DICHROISM SPECTROSCOPY

Circular dichroism (CD) spectroscopy was used to verify the folding of the hemL RNA sequence into a G-quadruplex structure as reported by Shao *et al*.[164] A CD spectra of hemL nucleic acid, without FRET fluorescent labels, was first obtained in 100 mM K^+ buffer to confirm the parallel folding that was previously reported (Figure 72). Parallel quadruplex structures have characteristic CD peaks, a positive peak at ~260 nm and a negative minimum at ~240 nm.[321] These characteristic parallel sequence peaks were reported by Shao *et al* in the presence of monovalent potassium and also included a negative peak at ~290 nm. The reproduced CD spectra matched those peaks reported indicating the formation of a parallel G-quadruplex structure under the relevant experimental conditions (Figure 72).

For the FRET melting assay, a potassium-containing buffer was used to mimic physiological conditions. Generally, higher concentrations of potassium ions lead to an equilibrium shift to the folded structure as the quadruplex structure is stabilised by the presence of the monovalent metal ions. The concentration of potassium in the buffer needs to be high enough for G4 folding but still allow G4 unfolding upon heating. Additionally, the nucleic sequence used in FRET measurements is labelled on each end with a fluorophore, which could potentially affect the folding topology and so the CD spectra were recorded with the labelled hemL sequence with a variety of KCl concentrations. It was found that all conditions yielded qualitatively similar CD spectra to the unlabelled hemL sequence, indicating folding at all concentrations of K^+ tested, including solutions with no K^+ ions present (Figure 72), and that the presence of the fluorophores in the labelled sequence do not significantly affect folding topology. The normal physiological concentration of K^+ in the cytoplasm of *E. coli* is approximately 250 mM and so a higher concentration of K^+ is preferable in the FRET assay. Therefore, a trial FRET melting assay was run to ascertain if hemL would unfold upon heating at this K^+ concentration.[322]

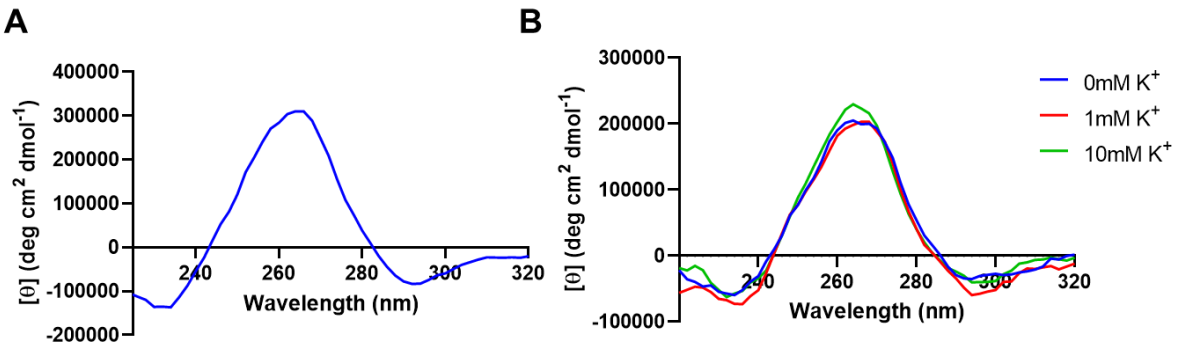

Figure 72 CD spectra of hemL RNA sequence. A. Parallel G4 complex formed by unlabelled hemL in the presence of K^+ ions (100 mM KCl) B. Difference in folding between FRET labelled hemL RNA sequence in the presence of increasing concentration of K^+.

4.3.2 FRET MELTING ASSAY RESULTS

A FRET melting assay was used to determine the stability of the hemL G-quadruplex structure. As detailed in Section 1.6.2.4**,** a FRET melting assay employs a nucleic acid sequence labelled with fluorescent dyes at opposing ends allowing the unfolding of the secondary structure upon heating to be monitored by measuring the change in FRET efficiency (observed as an increase in donor emission) during the melting process. Normalisation of the resulting curves allows for the determination of the melting temperature, T_m, of the G4 structure, when observed normalised fluorescence is 50%.

Following initial optimization of conditions, a FRET melting assay was used to examine the thermal stability of hemL, labelled with FRET donor/acceptor pair FAM/TAMRA, at three different KCl concentrations (Figure 73). The folded hemL G4 sequence displayed similar melting temperatures, between 65-67 °C, across all concentrations of potassium tested. Because the highest concentration of KCl, 10 mM, gave a reasonable melting curve as the hemL quadruplex unfolded, T_m of 66 °C, this concentration was selected to assess the stabilisation of the G4 by the ligand library.

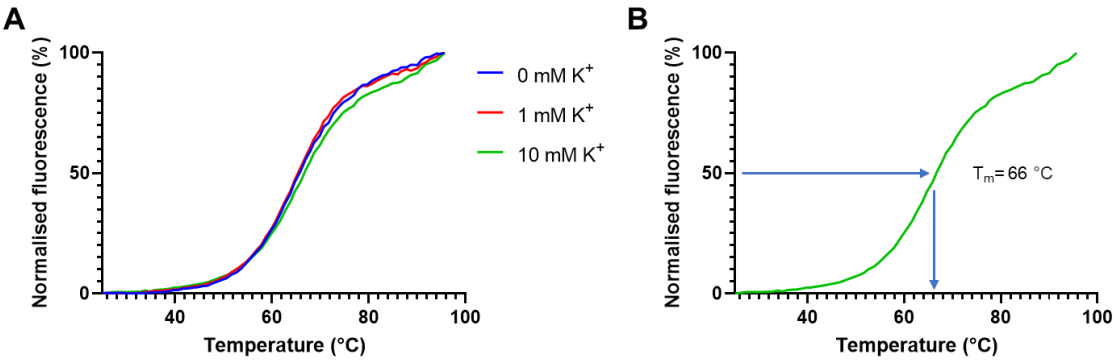

Figure 73 Normalised FRET melt curves of hemL in 10 mM LiCacodylate buffer at pH 7.2 plus KCl (blue 0 mM, red 1 mM and green 10 mM), 90 mM LiCl. B. 10 mM KCl melt curve with a T_m of 66 °C.

The compounds were screened at ligand concentrations 1 µM, 2 µM, 5 µM and 10 µM (Figure 74). Stabilisation at ligand concentrations above this is not considered comparatively effective and errors can also be seen for particularly strong binding ligands that prevent unfolding (the reason why the values for TMPyP4 are not reported above 2 µM).

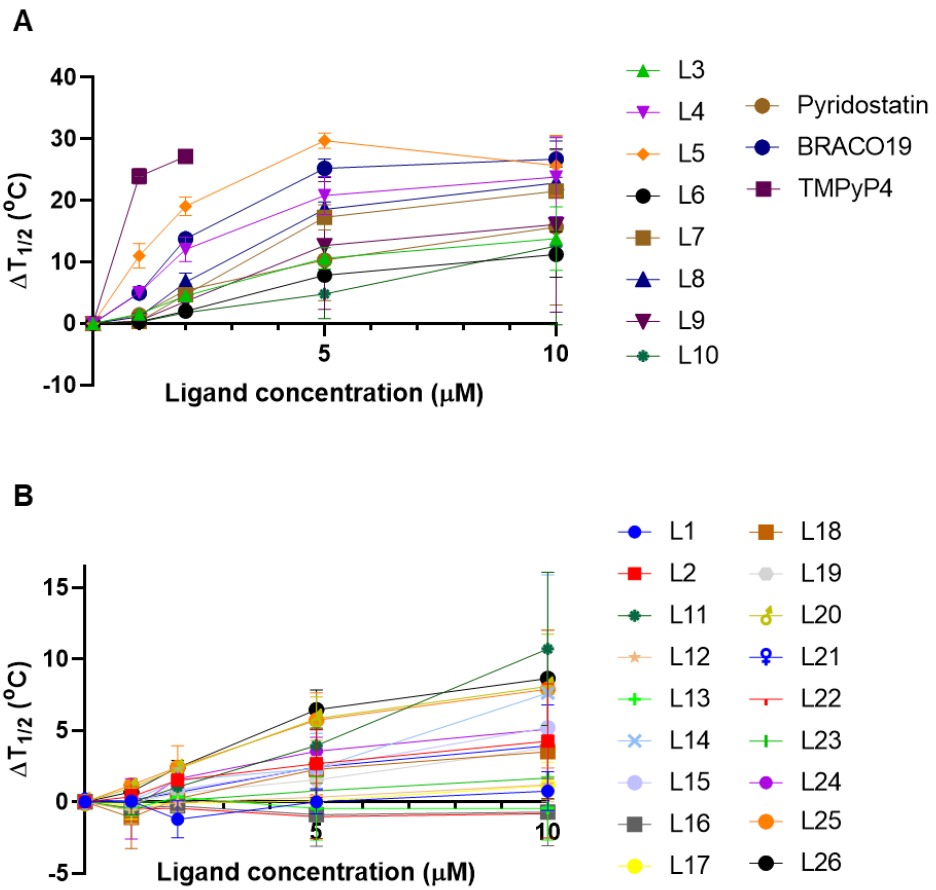

Figure 74 FRET thermal stabilisation values induced by ligands L1-L26 (see Appendix 1) and benchmark ligands pyridostatin, BRACO19 and TMPyP4. A. Ligands with higher thermal stabilities and B. less effective ligands.

Pleasingly, thermal stabilisation was observed for many of the screened library of ligands. TMPyP4 was shown to be the best stabiliser with a ΔT_m of 27 °C at 2 µM ligand concentration. Encouragingly, the next best stabiliser was not one of the benchmark ligands but **L5**, which was previously shown to have significant toxicity in both *E. coli* and *S. aureus*, (Section 4.2). However, the thermal stabilisation was not as significant for the other antibacterial ligands, where **L5** had a ΔT_m of 30 °C at 5 µM ligand concentration, **L6** and **L20** had a ΔT_m of 8 °C and 6 °C respectively at 5 µM. This suggests that the anti-bacterial toxicity mechanism of these ligands is unlikely solely through stabilisation of the hemL forming G-quadruplex. Also, the ligands that show highest ability to stabilise the hemL G4 the best, do not exhibit high *E. coli* toxicity *in vitro*. In addition, despite TMPyP4 being the best binder, no antibacterial activity was observed for this ligand. **L4** had a reasonable thermal stabilisation temperature of 21 °C at 5 µM ligand concentration although no toxicity was observed. **L4** and **L5** are configurational isomers of each other, (Figure 75), which could explain their relative similarity in binding stabilisation. **L3** is another configurational isomer but displays poorer binding, its ΔT_m being 11 °C at 5 µM ligand concentration, showing a decrease in stability of ~10 °C for each isomer (Figure 75). Despite the similarities in structure, **L3** and **L4** display no antibacterial activity in either *E. coli* or *S. aureus* whereas **L5**, possessing a more linear and rod-like geometry, displayed significant toxicity, especially in *S. aureus*.

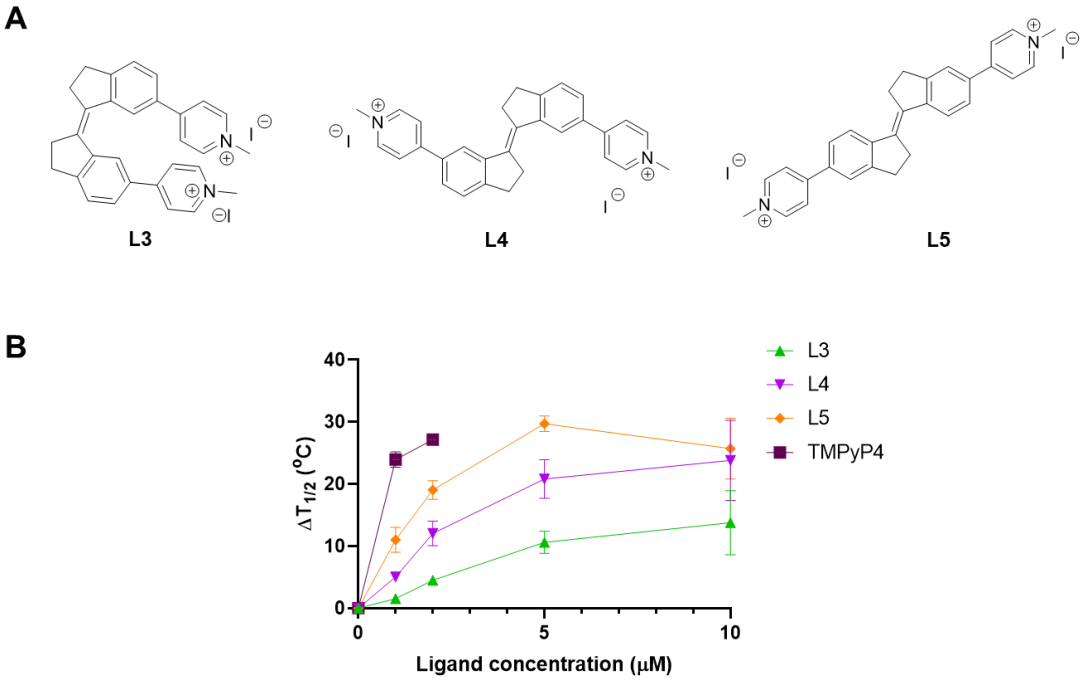

Figure 75 A. Molecular structure of G4 ligands **L3**, **L4** and **L5**. B. FRET thermal stabilisation values induced by ligands L3-5 for hemL RNA sequence.

FRET thermal stabilisation assays alone cannot demonstrate a link between G4 binding and antibacterial toxicity. The further experimental investigation of these compounds and their effects on bacteria and bacterial G4 sequences is currently being undertaken by the Galan group. A recent proteomic study[6] of the **L20** in *E. coli* highlighted an upregulation of efflux mechanisms, a common response seen in bacteria to combat antibiotic induced stress. The proteomic analysis of **L20** in *E. coli* was also used, in combination with a publication by the Balasubramanian group that had mapped the genome of *E. coli*, to identify potential G4-containing genes whose expression has been affected by incubation with **L20**.[191] Six further G-quadruplex forming nucleic acids were selected and ordered for analysis with CD and FRET in combination with the library of ligands. Although work has only just started, preliminary analysis indicates that the antibacterial activity seen by **L20** in *E. coli* is not caused by G4 stabilisation, as suggested by the results with hemL.

4.4 TUBERCULOSIS MODEL BACTERIAL LIGAND SUSCEPTIBILITY

Initial experiments investigating the effect of the G4 ligand library on *M. tuberculosis* model species *Mycobacterium smegmatis* were also conducted. *Mycobacterium tuberculosis* is a pathogenic bacteria which is the causative agent of tuberculosis, a disease that is reported to kill over a million people each year, with infants the most at risk.[323] *Mycobacterium smegmatis* is used as a *M. tuberculosis* model as it can be grown faster in the laboratory at a lower biosafety level. The library of compounds was screened against *M. smegmatis* as ligand concentrations varying between 64 to 0.0625 μg/mL (Table 4).

[6] Proteomic study prepared by Yuiko Takebayashi, Spencer group

The compound **L5** was found to be significantly active against *M. smegmatis*, its toxicity already been demonstrated in both *E. coli* and *S. aureus*, with an MIC of 0.5 µg/mL. However, the ligand **L7** also had an MIC of 0.5 µg/mL, a compound that had previously shown no antibacterial activity in *E. coli* and *S. aureus*. Also of note, in comparison to the previous toxicity tests, was the higher number of ligands that displayed antibacterial activity and an increased potency, with ten of the hit ligands exhibiting an MIC of 2 µg/mL or under. These initial investigations into the effects of the G4 ligands on *M. smegmatis* found potentially exciting results that could be explored further in future work.

Table 4 MIC values for G4 ligands against *M. smegmatis*.

G4 ligand label	MIC (µg/mL)
L1	64
L3	8
L4	2
L5	0.5
L6	2
L7	0.5
L8	1
L9	2
L11	8
L13	2
L14	2
L15	2
L16	4
L17	64
L18	8
L19	16
L20	1
L25	64
L26	4

4.5 CONCLUSIONS AND FURTHER WORK

Discussed in this chapter are initial investigations into the effects of G4 stabilisation on bacterial viability. A library of 26 different G4-targeting ligands were screened against resistant clinical strains of *E. coli* and *S. aureus* and against model *M. tuberculosis* strain *M. smegmatis*. Fortunately, hit compounds were identified for all three bacterial species tested. Further investigations were conducted with the bacterial RNA G4-forming sequence hemL, a nucleic acid sequence whose stabilisation by ligands has not been previously reported. CD spectroscopy confirmed a parallel quadruplex structure and FRET melting assays were used to ascertain the stabilisation properties of the ligands. The ligand **L5** was found to have a higher thermal stabilisation temperature than two different benchmark G4 ligands, BRACO-19 and pyridostatin. **L5** is composed of a stiff-stilbene scaffold with two methylpyridinium side groups. A common method of stabilisation for G4 ligands with an aromatic core and ionic side chains is a stacking interaction between the core and external tetrads with the basic side chains residing in the G4 grooves. However, it has been found that stiff-stilbenes are comparatively ineffective at this binding mode and that the high stabilisation achieved is from alternative binding modes, such as groove binding rather than end-stacking.[316]

The ligand found to be most potent against *E. coli*, **L20**, was not found to have a significant stabilisation effect on the hemL G4 sequence. This does not rule out that the toxicity found is not through G4 stabilisation as hemL is only one sequence, however, it could indicate that the toxicity observed from this molecule is through a separate mechanism. What has been shown to be key in the structure-activity relationship for **L20** is the positioning of the methylpyridinium substitution on the outer ring as molecules analogous in structure but with meta and ortho substitution instead of para, **L21** and **L22**¸ displayed no antibacterial activity. This suggests that the toxicity is not derived from destabilisation from the ionic charge alone as the structure is important to the molecules activity, potentially indicating that the molecule is interacting with cellular pathways, with the methylpyridinium being vital for recognition and binding. Further techniques included proteomic analysis and FRET melting assays with another six G4 sequences within the Galan and Spencer groups, performed by Yuiko Takebayashi and Francisco Javier Ramos Soriano, respectively are under investigation. However, concrete evidence to link the antibacterial activity found for **L20** with G4 stabilisation has not been demonstrated, although there are potentially more G4 forming sequences in the *E. coli* genome that **L20** could be targeting. Since the area is not widely researched, the number of true G4-forming sequences in *E. coli* is not known, nor is the differences in expression of these sequences between bacterial strains. Therefore, the work in this area, is novel in nature and is part of the exploration of the role of G4 stabilisation in bacterial cell viability.

Future work could be done to access the mechanism of **L5**, a ligand that demonstrated potent antibacterial activity and strong stabilisation of the *E. coli* RNA G4 sequence. Proteomic analysis of both *E. coli* and *S. aureus* incubated with **L5** could help identify if there is a common mechanism of action, and if this is related to the modulation of genes related to G4s. Another potential factor that could be explored in future studies is the uptake and internalisation of the ligands by bacteria. Being fluorescent in nature, **L5** was shown to be internalised within both *S. aureus* and *E. coli* (Section 4.2). To assess other, non-fluorescent ligands, bacteria that have been incubated with the compound could be lysed and the contents analysed by high throughput ligand chromatography (HPLC) or LC-MS. Characteristic ligand peaks could potentially then be identified and compared between the cell medium and lysate to determine the levels of ligand internalisation within the bacteria. Differences in internalisation could help in elucidating the differences in observed bacterial toxicity.

Despite uncertainty with regards to the mechanism of action, the novel antibacterial ligands discussed in this chapter represent a potential new class of antibiotics, which exhibit activity against bacterial strains that are already resistant to commonly used antibacterials.

5. CONCLUSIONS AND FUTURE WORK

In conclusion, work has been performed over multiple disciplines in a multipronged effort to develop new bacterial diagnostic and antibacterial tools. Several of the aims set out for the project have been met and the work has opened up opportunities for future projects to further understand and improve some of the systems developed and investigated within this research.

Commercial dyes that label bacteria are very expensive, easily photo-bleach and sometimes are only effective with one class of bacteria. Promising results were found with fluorescent bacterial labelling using cheaply synthesised green fluorescent carbon dots (GCDs). The labelling methodology was optimised and GCDs were found to uniformly label across different four different bacterial species that include both Gram-positive and Gram-negative organisms without photo-bleaching (Figure 76). Confocal imaging was used initially to assess labelling intensity, but a more quantitative process was developed employing a microtiter plate reader and so fluorescent levels between species could also be assessed.

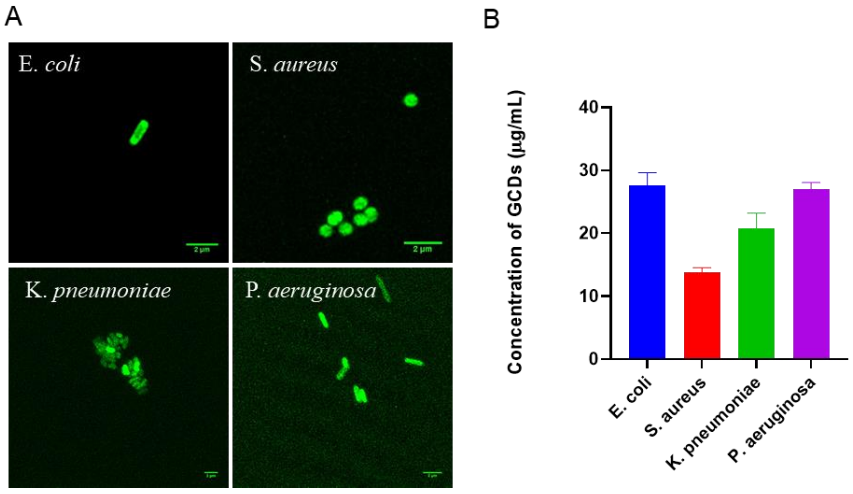

Figure 76 A. Confocal images showing GCD fluorescent labelling of four bacterial species. B. Differences of GCD labelling concentration levels between bacterial species measured on plate reader.

In order to evaluate whether the GCDs had been internalised or just were just interacting with the bacteria surface, the membrane imaging dye FM4-64X was used and this allowed for the visualisation of GCD internalisation. Bacterial membrane porins are likely to be involved in the transport of the nanoparticles into the cell, possibly mediated by glucose-like moieties on the surface of the GCDs. The effect of GCDs on the bacterial viability was also investigated (Figure 77). Only at particular high concentrations (>1 mg/mL) were any significant effects of GCDs on toxicity. However, when GCD incubation was combined with LED irradiation growth inhibition was found at lower GCD concentrations such as 32 µg/mL for *E. coli*. There are very few examples of CD photothermal activation in antimicrobial PTT and most materials contain transition metals which can be activated with NIR light or other sensitizers for photodynamic therapy applications.[324,325] Those that do not include metals require lengthy synthesises and report only decreases in cell viability at concentrations no lower than 400 µg/mL.[255,256] The GCD system developed displays complete growth inhibition at much small concentrations of material and therefore a significant improvement on past published materials.

Microbial techniques including nucleic acid staining, SEM, a molecular ROS indicator and proteomics were used to probe the mechanism of antibacterial activity. Our proteomic experiments suggested some DNA damage in both *E. coli* and *S. aureus* was found upon incubation with GCDs alone. However, on the introduction of LED irradiation, a notable increase in proteins with differences in expression levels was found and DNA-, membrane- and ROS- damaging effects are generally observed. It is proposed DNA damage is caused through associated of DNA to the GCDs, likely through charge interactions, and that ROS are generated through the excitation of the GCDs with LED illumination. Membrane damage can be attributed to a localised heating effect upon GCD irradiation. All three mechanisms contribute to the observed toxicity effects within bacteria.

A non-fluorescent molecule, 2,5-dexofructosazine (2,5-DOFR), which is generated during the synthesis of the GCDs and is present on the surface of the GCDs, was found to be integral to fluorescent labelling of bacteria by the probes. During our investigations, it was found that surface bound fluorophores and 2,5-DOFR (which is not fluorescent) could be removed through purification processes such as SEC and dialysis. Further experiments with just 2,5-DOFR alone was shown to have no labelling or antibacterial effect on bacteria, demonstrating that the intact GCD was required for any observable activity. The accessibility and simplicity of this GCD system is advantageous over other reported antibacterial CD/LED approaches. For example, complete inhibition of growth was achieved in four different bacterial species whereas, to my knowledge, only a reduction in bacterial viability have been reported for other published CD/LED systems.

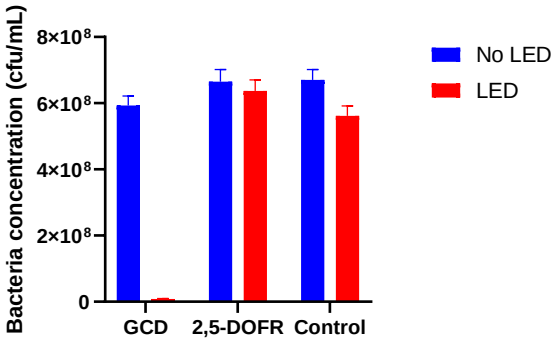

Figure 77 Difference in *E. coli* growth recovery after exposure to various external stimuli. LED alone and 2,5-DOFR are shown not to affect cell viability whereas the GCD/LED combination has a dramatic effect on growth.

Carbohydrate functionalisation of this GCD system was also investigated in an attempt to convey bacterial specificity, however issues were encountered due to surface-bound 2,5-DOFR and so were deemed an unsuitable platform. The lectin *FimH*, a mannose specific protein found on the fimbrial tip of *E. coli*, was targeted due to its clinical relevance in infections such as UTIs. Previously reported research has shown gold particles functionalised with the *FimH* targeting heptyl mannoside ligand to label the fimbriae of *E. coli*. In this work, quantum dots (QDs) functionalised with a heptyl mannoside ligand were shown to have higher levels of fluorescent labelling in *FimH*-expressing *E. coli* strains. However, due to the toxicity, synthetic difficulty and instability of QDs, new CD systems were investigated. Seven different literature CD protocols were undertaken but results reported could not be recreated. This could be due to slight changes in methodology, such as the domestic microwave used, and inaccuracies in reported protocols. Therefore, a CD developed in the Galan group, Section 3.3.4, was employed as the functionalisation platform, **CD-10**, which offered an advantageously high QY and surface carboxylic acid conjugation handles. An agglutination assay, based on the aggregation of yeast in the presence of *E. coli*, was optimised and allowed for the demonstration of heptyl mannoside functionalised **CD-10** specifically labelling *E. coli* through the displacement of the yeast (Figure 78). However, fluorescent detection of this probe was not possible since the emission profile clashed with

bacteria autofluorescence. Previously reported CD systems that label bacteria have either used antibiotic functionalisation or use glycans within the synthesis of the CDs themselves to confer labelling.[239,326] Using post synthesis glycan modification gives the potential for a more flexible system where labelling could be tuned through the use of alternative carbohydrates.

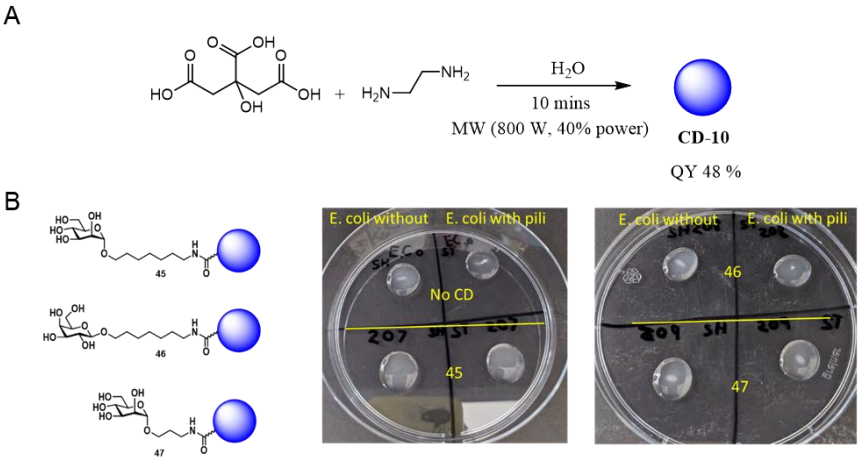

Figure 78 A. Synthesis of CD core **CD-10** developed within the Galan group. B. Sugar functionalised **CD-10s** tested for *E. coli* binding with an agglutination assay where only mannose-functionalised **CD-10s** were seen to disrupt aggregation.

A different approach to alternative antibacterial therapeutics was also explored in the investigations into the effect of G4 stabilisation on bacterial viability. G4 ligand-induced stabilisation has been well studied in telomeres as a potential anti-cancer therapeutic however little research had been reported on the role of G4s in bacterial metabolism. However, there have been a few promising reports where stabilisation of G4 nucleic sequences has affected corresponding gene expression.[228,229] Preliminary research has identified a few G4-forming sequences in *E. coli* but so far no research has been published on the potential effects of ligand stabilisation. [191,230,231]

In this work a library of twenty-six G4-stabilising ligands were screened against resistant clinical strains of *E. coli* and *S. aureus* and against model *M. tuberculosis* strain *M. smegmatis*. Ligands that conveyed antibacterial activity were identified for all three bacterial species tested (Figure 79).

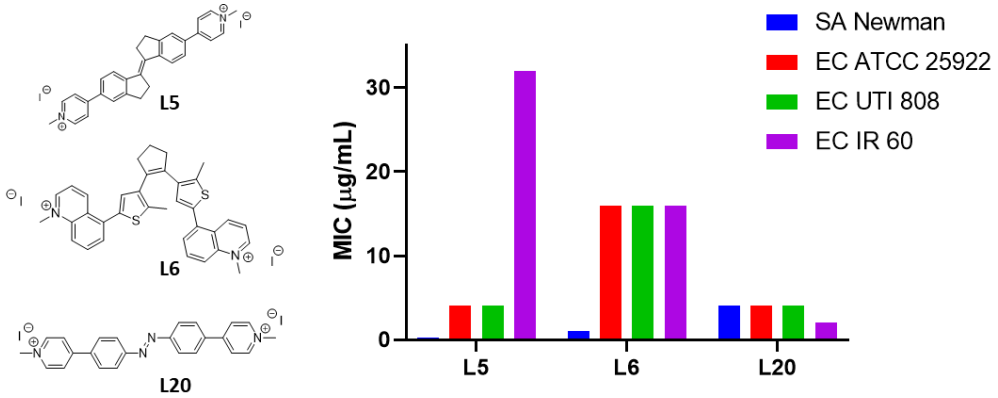

Figure 79 Three G4 ligands, **L5**, **L6** and **L20**, were found to antibacterial effects in all bacterial species tested. The minimum inhibitory concentrations (MIC) show the variation in toxicity across different species and strains. Promising levels of antibacterial activity were found, for example, **L5** has an MIC of 0.25 µg/mL for *S. aureus* Newman and **L20** has an MIC of 2 µg/mL for multiresistant clinical isolate *E. coli* IR 60.

In efforts to elucidate the role of G4 stabilisation has in the ligands antimicrobial activity a bacterial RNA G4-forming sequence hemL was studied. The formation of a parallel G4 quadruplex structure was confirmed through circular dichroism spectroscopy and FRET melting assays were used to ascertain the stabilisation properties of the ligands. Stabilisation of the hemL nucleic acid sequence has not previously been reported but many of the library of G4 ligands displayed thermal stabilisation. Ligand **L5** was found to have a higher thermal stabilisation temperature than two different benchmark G4 ligands, BRACO-19 and pyridostatin. **L5** was shown to have significant antibacterial activity in both *S. aureus* and *E. coli*. However, ligand, **L20**, that was found to be most potent in *E. coli* did not display a significant stabilisation effect on the hemL G4 sequence. This could indicate that the antibacterial activity is not related to G4 stabilisation, however there are also many potential G4 forming sequences in the *E. coli* genome that **L20** could be targeting. As this particular area is not well-researched, the true number of G4-forming sequences is not known. It was found that the position of the outer methylpyrinium group for **L20** had to be para for effective toxicity, and so therefore is likely vital to the method of action, whether G4 mediated or not.

The work reported herein offers many potential routes for future research exploration. Specific labelling was demonstrated in one system which could be expanded further. A more quantitative agglutination assay could be developed to allow for the optimisation of the mannoside ligand and ideally work would be performed in expanding to fluorescent based labelling as well. Functionalisation of **CD-10** offers a CD system with a high quantum yield and a more suitable emission profile, and the hope would be to have a range of sugar functionalised CDs that could target distinct bacterial species and therefore offer applications in rapid infection diagnosis. The sugars chosen for functionalisation would be carbohydrates already identified to be targeted by specific pathogenic bacteria, for example those shown in Figure 80. Through the orthogonal attachment of antibiotics to sugar-conjugated CDs potential theranostic applications could also be investigated. CDs have the capability to be targeted drug delivery systems as they are generally non-toxic to human cells. This would allow antibiotic delivery directly to the bacterial cell surface which could prevent unwanted side effects caused by off-target interactions.

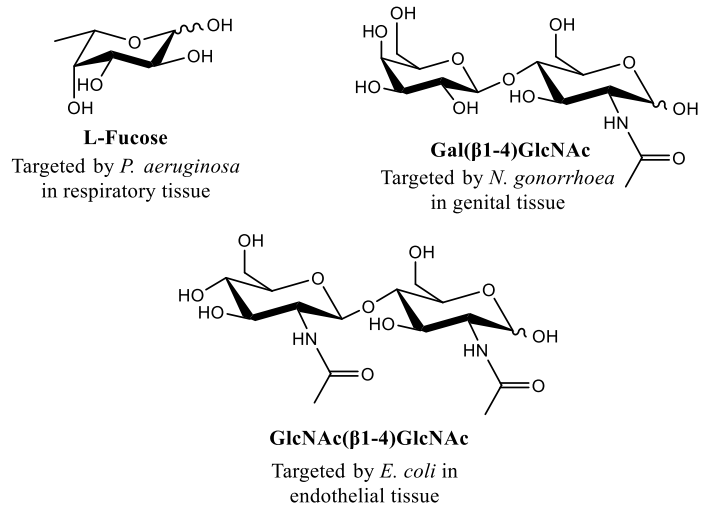

Figure 80 Structures of carbohydrates that have been identified as attachment sites for pathogenic bacteria.[286]

Another area with great potential for future development is G4 stabilising ligands as novel antibiotic targets. This thesis details preliminary investigations into the effect of these ligands in bacteria, with promising and exciting results found. In the continuation of these studies further FRET melting assays are being performed on other bacterial G4-forming sequences. The comparison of stabilisation results from the ligand library could offer interesting findings and potentially allow for further elucidation of the system. Proteomic analysis is currently being undertaken on the effect of **L20** on *E. coli* protein

expression which could give indications as to whether the antibacterial effect is G4 mediated, but also suggest other processes that could be at play. Proteomics could also offer insights into the effect of **L5** in *E. coli* and *S. aureus* as antibacterial effects were found for both and **L5** was also seen to be the most potent G4 stabilising ligand in hemL. Although still in the preliminary stages of research, this project not only offers exciting potential for the development of a novel class on antibiotics, but also in efforts for the general elucidation and clarification of the role of G4s in bacteria.

6. EXPERIMENTAL

6.1 SYNTHETIC GENERAL EXPERIMENTAL

Chemicals were purchased and used without further purification. Reactions requiring anhydrous conditions were performed under N_2; glassware and needles were either flame dried immediately prior to use, or placed in an oven (150 °C) for at least 2 h and allowed to cool in desiccators or under concentrated pressure. Liquid reagents, solutions or solvents were added via syringe through rubber septa; solid reagents were added via Schlenk type adapters. Reactions were monitored by TLC on Kieselgel 60 F254 (Merck). Detection was by examination under UV light (254 nm) and either by charring with 10% sulphuric acid in ethanol (if carbohydrate is present), ninhydrin or potassium permanganate. Flash chromatography was performed using silica gel [Merck, 230−400 mesh (40−63 μm)], the crude material was applied to the column by pre-adsorption onto silica, where appropriate. Extracts were concentrated under concentrated pressure using both a Büchi rotary evaporator at a pressure of either 15 mmHg (diaphragm pump) and 0.1 mmHg (oil pump), as appropriate, and a high vacuum line at room temperature. Preparative HPLC was performed on an automated Grace Reveleris Prep purification system with UV and ELS detectors. ^{1}H NMR and ^{13}C NMR spectra were measured at 25°C in the solvent specified with Varian spectrometers operating at field strengths listed. Chemical shifts are quoted in parts per million with spectra referenced to the residual solvent peaks ^{1}H and ^{13}C NMR chemical shifts are quoted in parts per million (ppm) and referenced to the residual solvent peak ($CDCl_3$: 1 H = 7.26 ppm and ^{13}C = 77.2 ppm, D_2O: 1 H = 4.79 ppm) and coupling constants (J) given in Hertz. Multiplicities are abbreviated as: br (broad), s (singlet), d (doublet), t (triplet), q (quartet), p (pentet) and m (multiplet) or combinations thereof. Fluorescence measurements were made and conducted on a Perkin-Elmer LS45 in quartz cuvettes (ThorLabs). The domestic microwave (MW) used for carbon dot synthesis was a 800 W 20 L MW purchased from Wilko. GE Healthcare Life Sciences VIVASPIN 20 centrifugal concentrators were used with a molecular-weight cut off of 10,000 Da. Dialysis membranes were purchased from Sigma-Aldrich, with a 500-1000 Da molecular-weight cut off. Kotchetkov's animation of mannose was performed using a Biotage Initiator+ microwave reactor. Dynamic Light Scattering (DLS) analysis was performed with a Malvern Instruments Nano-S90 ZEN1690.

6.2 CARBON DOT SYNTHESIS

6.2.1 BCD

BCD were prepared following the procedure reported by Hill *et al*.[238] Glucosamine hydrochloride (1.00 g, 4.63 mmol) and 4,7,10-trioxa-1,13-tridecanediamine (TTDDA) (1.11 mL, 5.09 mmol) were dissolved in distilled H_2O (20 mL) before heating for 3 mins in a domestic MW (800W, 70% power). The resultant brown residue was dissolved in 10 mL of distilled water, centrifuged through 10000 Da concentrator (8500 rpm, 40 mins) before lyophilisation to yield desired BCD product (~2 g). Characterization data in agreement with reported literature.[238] Fluorescence spectrum (Figure S 10) λ_{ex} = 340 nm λ_{em} = 420 nm [literature: λ_{ex} = 340 nm λ_{em} = 420 nm]. Characteristic peaks in ^{1}HNMR (D_2O, 500 MHz): δ 3.4-3.6, 3.0 and 1.8 (TTDDA linker) match those reported in literature.

6.2.2 GCD

Prepared according to the procedure reported by Hill *et al*.[237] Glucosamine hydrochloride (1.00g, 5.58 mmol) was dissolved in deionised water (20 mL). 1,3-phenylenediamine (0.55 g, 5.10 mmol) in methanol (10 mL) was then added to the sugar solution and the mixture was heated in a domestic microwave (800 W, 80% power) for 3 min. The obtained CDs were re-dispersed in water (10 mL) and centrifuged through a 10,000 MWCO filter (8500 rpm, 40 mins). The bulk solution was then lyophilised to yield a brown solid, 1-1.5 g. Characterization data in agreement with reported literature.[237] Fluorescence spectrum (Figure S 11) λ_{ex} = 460 nm λ_{em} = 520 nm [literature: λ_{ex} = 460 nm λ_{em} = 520 nm]. Characteristic peaks in ^{1}HNMR (D_2O, 500 MHz): δ 8.6, 8.5 (pyrazine signals) and 2.9, 3.1, 3.4-4.3 (polyhydroxylated architectures) as reported in literature.

6.2.3 CD-1/CD-2: MANNOSE-CD LITERATURE CDS

Prepared according to the procedure reported by Weng *et al*.[239] Ammonium citrate (100 mg, 0.48 mmol) with mannose (5 mg, 0.028 mmol) (**CD-1**), or not (**CD-2**), was heated in at 180 °C for 2 hours before cooling to room temperature. The black reaction residue was dissolved in a 100 mM sodium hydroxide solution (10 mL) and sonicated for 1 hour. The resulting mixture was purified by centrifugation through a 10,000 MWCO (8500 rpm, 30 mins) before dialysis against deionised water overnight (48 mg **CD-1**, 59 mg **CD-2**). Fluorescence spectrum (Figure 56Figure S 11) λ_{ex} = 460 nm λ_{em} = 520 nm [literature: λ_{ex} = 365 nm λ_{em} = 450 nm][148]. Fluorescence spectra did not match that reported so material not taken any further.

6.2.4 CD-3: CITRIC ACID, UREA AND SODIUM FLUORIDE CDS

Prepared according to the procedure reported by Yang *et al*.[134] Citric acid (180 mg, 0.94 mmol), urea (540 mg, 9.00 mmol) and sodium fluoride (100 mg, 2.38 mmol) were dissolved in 10 mL of deionised water. After sonication for 10 mins the and the mixture was heated in a domestic MW (800 W, 80% power) for 5 mins. The obtained CDs were re-dispersed in water and purified by syringe filter (0.22 µm) before dialysis against deionised water for 24 hrs before lyophilisation to yield a yellow/brown solid (586 mg). Fluorescence spectrum (Figure 57) λ_{ex} = 400 nm λ_{em} = 510 nm [literature: λ_{ex} = 530 nm λ_{em} = 600 nm][134]. Fluorescence spectra did not match that reported so material not taken any further.

6.2.5 CD-4: CITRIC ACID AND UREA CDS

Preparation adapted from the procedure reported by Qu *et al*.[299] Citric acid (384 mg, 2.0 mmol) and urea (960 mg, 16 mmol) was dissolved in 20 mL of deionised water, heated for 4 minutes in a domestic MW (800 W, 80% power). The resulting brown residue was then heated at 60 °C under vacuum for 1 hour. The solid CD product was then dissolved in 10 mL of water before purification through centrifugation through 10,000 MWCO (8500 rpm, 30 mins) before dialysis against deionised water overnight and lyophilisation (183 mg). Fluorescence spectrum (Figure 58) λ_{ex} = 400 nm λ_{em} = 520 nm [literature: λ_{ex} = 420 nm λ_{em} = 540 nm][299]. Fluorescence spectra did not match that reported so material not taken any further.

6.2.6 CD-5: DIAMMONIUM HYDROGEN CITRATE AND UREA CDS

Prepared according to the procedure reported by Khan *et al*.[327] Diammonium hydrogen citrate (200 mg, 0.88 mmol) and urea (200 mg, 3.33 mmol) were ground together in a pestle mortar to form a homogenous powder which was heated for 180 °C for 1 hour, The resulting black residue was dissolved in 10 mL of water and centrifuged (8500 rpm, 30 mins), the supernatant removed and filtered through a syringe filter (0.22 µm). The resulting solution was lyophilised to yield a black/brown **CD-5** product (102 mg). Fluorescence spectrum (Figure 59Figure S 11) λ_{ex} = 400 nm λ_{em} = 450 and 510 nm [literature: λ_{ex} = 420 nm λ_{em} = 537 nm][327]. Fluorescence spectra did not match that reported so material not taken any further.

6.2.7 CD-6: PHTHALIC ACID AND DABCO CDS

Prepared according to the procedure reported by Yu *et al*.[301] Phthalic acid (2 g, 12.0 mmol) and triethylenediamine hexahydrate (DABCO) (1.35 mg, 12.0 mmol) were partially dissolved in 3 mL of deionised water and heated in a domestic MW (800 W, 80% power) for 1 minute. The obtained CDs were re-dispersed in water and purified by syringe filter (0.22 µm) before dialysis against deionised water 500-1000 MWCO dialysis membrane for 24 hrs before lyophilisation to yield a yellow/brown solid (14.8 mg). Fluorescence spectrum (Figure 61) λ_{ex} = 425 nm λ_{em} = 500 nm (broad) [literature: λ_{ex} = 454 nm λ_{em} = 500 (broad) nm][301]. Product recovery was so poor that the material was not taken any further.

6.2.8 CD-7: CITRIC ACID, L-CYSTEINE AND DEXTRIN CDS

Prepared according to the procedure reported by Liu *et al.*[302] Citric acid (190 mg, 1.00 mmol), L-cysteine (110 mg, 0.91 mmol) and dextrin (300 mg, 0.60 mmol) were partially dissolved in 15 mL of deionised water before being heated in a domestic MW (800W, 80% power) for 3 minutes. The resulting residue was re-dispersed in 5 mL of water, filtered through centrifugation and dialysed for 24 hours before lyophilisation (188 mg). Fluorescence spectrum (Figure S 12) λ_{ex} = 350 nm λ_{em} = 430 and 510 nm [literature: λ_{ex} = 420 nm λ_{em} = 495 nm][302]. Fluorescence spectra did not match that reported so material not taken any further.

6.2.9 CD-8: 1,4-PHENYLENEDIAMINE CDS

Prepared according to the procedure reported by Jiao *et al*.[303] 1,4-Phenylenediamine (216 mg, 2.00 mmol) was dissolved in 20 mL of water before the addition of 300 µL of HCl. The mixture was transferred to a Teflon-lined autoclave and heated at 200 °C for 8 hrs. The resulting residue is centrifuged at 8500 rpm for 30 mins, the supernatant was removed and dialysed against deionised water over 3 days. The CDs were then lyophilised to yield a brown powder (168 mg). Fluorescence spectrum (Figure S 13) λ_{ex} = 345 nm λ_{em} = 460 nm [literature: λ_{ex} = 365 nm λ_{em} = 590 nm].[303] Fluorescence spectra did not match that reported so material not taken any further.

6.2.10 CD-9: CITRIC ACID AND DICYANDIAMIDE CDS

Preparation adapted from the procedure reported by Wu *et al*.[304] Citric acid (900 mg, 4.68 mmol) and dicyandiamide (250 mg, 2.97 mmol) were dissolved in 20 mL water and 10 mL methanol before being heated in a domestic MW (800W, 80% power) for 4 minutes. The resulting product was redissolved in 10 mL of water and purified through 10,000 MWCO centrifugation filtration (8500 rpm, 30 mins) before dialysis against deionised water overnight and lyophilisation (170 mg). Fluorescence spectrum (Figure S 14) λ_{ex} = 360 nm λ_{em} = 430 and 505 nm [literature: λ_{ex} = 370 nm λ_{em} = 452 nm].[304] Fluorescence spectra did not match that reported so material not taken any further.

6.2.11 CD-10: CITRIC ACID AND ETHYLENEDIAMINE CDS

Material was synthesised by Teodoro Garcia Millan. Citric acid (1.00 g, 5.2 mmol) was dissolved in distilled H_2O (10 mL) in a 250 mL conical flask. Ethylenediamine (384 µl, 5.72 mmol) was then added to the solution and stirred for 30 min to ensure homogeneity. The conical flask was then heated in a domestic microwave (800 W, 40% power) for 10 min. A viscous amber residue was obtained which was washed with a solution MeOH:Acetone 1:1 (four times). The precipitate was then phase separated by centrifugation and re-dissolved in 15 ml of distilled H_2O. The solution was then purified via centrifuge filtration (MWCO of 10 kDa, 8500 rpm, 30 min). The supernatant was lyophilised to yield an amber powder (1-1.1 g). Fluorescence spectrum (Figure 63) λ_{ex} = 350 nm λ_{em} = 450 nm. TEM analysis estimated diameter at 4 nm.

6.3 LINKER AND LIGAND SYNTHESIS FOR CD FUNCTIONALISATION

6.3.1 ACID FUNCTIONALISATION OF GREEN CARBON DOTS (25)

Prepared according to the procedure reported by Stephen Hill.[328] GCD (20 mg) and succinic anhydride (40 mg, 0.40 mmol) were dissolved in deionised water (5 mL). The solution was sonicated for 5 mins before stirring for 17 hrs. The resulting product was then concentrated *in vacuo.* Diethyl ether (50 mL) is added to the resulting residue and sonicated for 10 mins before removing supernatant (repeated at least three times with fresh solvent). Resulting product dissolved in water (5 mL) and lyophilised to yield a brown solid **25** (15-20 mg). Desymmetrisation of succinic anhydride peaks (2.4-2.6 ppm) are observed in the ^{1}HNMR (Figure S 19). Characterization data in agreement with reported.

6.3.2 KOTCHEVKOV AMINATION OF MANNOSE –1-AMINO-1-DEOXY-D-MANNOSE **(26)**

Originally reported by Bejugman and Flitsch and adapted by Stephen Hill..[290,329] Oven-heated microwave vial was cooled under N_2. Mannose (0.25 g, 1.39 mmol), ammonium carbonate (1.25 g, 13.0 mmol) and anhydrous DMSO (0.8 mL) was added under nitrogen. The tube was sealed and placed in an automated microwave at 40 °C for 90 mins. Water (10 mL) was then added to the solution and the mixture was lyophilised to afford the β-mannosyl amine as a white solid **26** (0.1 g, 0. 56 mmol, 40 %). ^{1}HNMR (D_2O, 400 MHz) : β-D-mannose: δ 4.8 (d, 1H, *J*= 1.1 Hz). α-D-mannose δ = 5.16 (d, 1H, *J*=1.9 Hz). 1-amino-1-deoxy-β-D-mannose δ = 4.32 (d, 1H, *J*=1.1 Hz) 3.93 (dd, 1H, *J* = 1.1 Hz), 3.40 (d, 1H, *J* = 2.2 Hz).

6.3.3 GENERAL METHOD FOR GLYCO-FUNCTIONALISATION OF GCDS

Prepared according to the procedure reported by Stephen Hill.[328] Acid-functionalised CDs **25** (10 mg) were dissolved in deionised water (1 mL) before addition of 1,1′-Carbonyldiimidazole (CDI) (40 mg, 0.25 mmol). The mixture was sonicated for 15 mins and then a solution of the aminated sugar (2 mL, 10 mg/mL in H_2O) was added and stirred for 17 hrs. The resulting product was purified by the dialysis against ultrapure water using a 500-1000 MWCO dialysis membrane for 24 hrs before lyophilisation to yield a brown solid, 25-30 mg.

6.3.3.1 CONJUGATION OF 1,4-MANNOBIOSE TO GREEN CDS (**28**)

A scaled down microwave-assisted Kochevkov methodology was used first to generate the aminated sugar. 1,4-α-mannobiose (20 mg, 0.06 mmol), ammonium carbonate (58 mg, 0.60 mmol) and anhydrous DMSO (0.4 mL) was added under nitrogen. The tube was sealed and placed in an automated microwave at 40 °C for 90 mins. Water (5 mL) was then added to the solution and the mixture was lyophilised to afford a white solid that was added to a 1 mL solution of **25** (10 mg) that had been sonication with CDI (40 mg, 0.25 mmol) for 15 mins. The solution was then stirred for 17 hrs before dialysis purification over 24 hrs and lyophilisation to yield the functionalised GCDs, **28** (18 mg).

6.3.3.2 CONJUGATION OF 1,4-MANNOTRIOSE TO GREEN CDS (**29**)

A scaled down microwave-assisted Kochevkov methodology was used first to generate the aminated sugar. 1,4-β-mannotriose (26 mg, 0.05 mmol), ammonium carbonate (48 mg, 0.50 mmol) and anhydrous DMSO (0.4 mL) was added under nitrogen. The tube was sealed and placed in an automated microwave at 40 °C for 90 mins. Water (5 mL) was then added to the solution and the mixture was lyophilised to afford a white solid that was added to a 1 mL solution of **25** (10 mg) that had been sonication with CDI (40 mg, 0.25 mmol) for 15 mins. The solution was then stirred for 17 hrs before dialysis purification over 24 hrs and lyophilisation to yield the functionalised GCDs, **29** (21 mg).

6.3.3.3 CONJUGATION OF 1,4-MANNOBIOSE TO GREEN CDS (**30**)

A scaled down microwave-assisted Kochevkov methodology was used first to generate the aminated sugar. 1,4-α-mannobiose (19 mg, 0.04 mmol), ammonium carbonate (38 mg, 0.40 mmol) and anhydrous DMSO (0.4 mL) was added under nitrogen. The tube was sealed and placed in an automated microwave at 40 °C for 90 mins. Water (5 mL) was then added to the solution and the mixture was lyophilised to afford a white solid that was added to a 1 mL solution of **25** (10 mg) that had been sonication with CDI (40 mg, 0.25 mmol) for 15 mins. The solution was then stirred for 17 hrs before dialysis purification over 24 hrs and lyophilisation to yield the functionalised GCDs, **30** (15 mg).

6.3.4 TTDDA LINKER SYNTHESIS

6.3.4.1 4,20-DIOXO-9,12,15-TRIOXA-5,19-DIAZATRICOSANEDIOIC ACID (**34**)

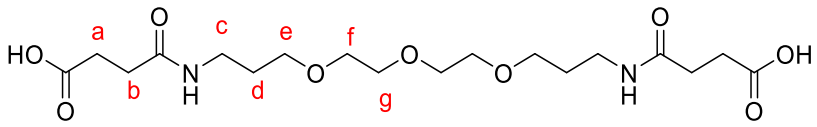

4,7,10-Trioxa-1,13-tridecanediamine (TTDDA) (1.00 g, 4.54 mmol) was dissolved in methanol (40 mL) and succinic anhydride (1.34 g, 11.35 mmol) was added. The reaction was stirred for 20 hrs and then concentrated *in vacuo*. Purification by flash column chromatography (DCM/MeOH, 80:20) yielded the desired product **34** as a colourless oil (1.18 g, mmol, 62%). ^{1}HNMR (D_2O, 400 MHz): δ 1.61 (p, *J*= 6.6Hz, d); 2.35 (t, *J*= 6.6 Hz, a); 2.49 (t, *J*= 6.8 Hz, b); 3.09 (t, *J*=6.6 Hz, c); 3.40 (t, *J*= 6.3 Hz, e); 3.49 (s, f/g); 3.51 (s, f/g). HRMS-ESI of $C_{18}H_{32}N_2O_9$ calc: 420.21 found 421.2504 [$M+H^+$].

6.3.4.2 CONJUGATION OF LINKER TO GREEN CDS (**35**)

4,20-dioxo-9,12,15-trioxa-5,19-diazatricosanedioic acid **34** (34 mg, 0.08 mmol) and 1,1′-Carbonyldiimidazole (CDI) (13 mg, 0.08 mmol) in methanol (1.34 mL) was sonicated for 15 mins. Green CDs (20 mg) were then added to the solution and stirred for 17 hrs. The resulting product was dialysed against deionised water using a 500-1000 MWCO dialysis membrane for 24 hrs before lyophilisation to yield a brown solid **35** (46 mg).

6.3.4.3 CONJUGATION OF MANNOSE TO LINKER-GCDS (**36**)

35 (4 mg) and CDI (10 mg, 0.06 mmol) were dissolved in DMSO (1 mL) and sonicated for 15 mins. Aminated mannose (**26**) (10 mg, 0.06 mmol) was added and the mixture was stirred for 18 hrs. 2 mL of H_2O was added to the reaction and lyophilised to remove solvents. The resulting brown solid was dialysed against 36 hrs before lyophilisation to yield a brown solid **36** (13.7 mg).

6.3.5 DENDRIMER SYNTHESIS

6.3.5.1 TRIS{[2-(TERT-BUTOXYCARBONYL)ETHOXY]METHYL}METHYLAMINE (**37**)

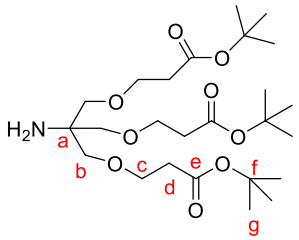

Tris(hydroxymethyl)aminomethane (Tris base) (1.21 g, 10 mmol) was dissolved in DMSO (2 mL) and cooled to 15 °C under N_2. Whilst stirring 6 M NaOH (0.16 mL, 10 mmol) was added, followed by the dropwise addition of *tert*-butyl acrylate (5.0 mL, 34 mmol). The reaction mixture was allowed to reach room temperature and left stirring for 24 hr. The product was then lyophilised and purified by flash column chromatography (DCM/MeOH 90:10) to yield a colourless oil **37** (1.55 g, mmol, 31%).^{1}HNMR ($CDCl_3$, 400 MHz) : δ 1.33 (s, 27H, g); 2.33 (t, *J* = 6.3 Hz, 6H, d); 3.20 (s, 6H, b); 3.53 (t, *J*= 6.3 Hz, 6H, c). ^{13}CNMR (CDCl3, 101 MHz): δ 28.0 (g); 36.2 (d); 55.9 (a); 67.0 (c); 72.61 (b); 80.3 (f); 170.8 (e). Data was in agreement with previously reported synthesis.[330]

6.3.5.2 TRIS{[2-CARBOXYETHOXY]METHYL}METHYLAMINE (**38**)

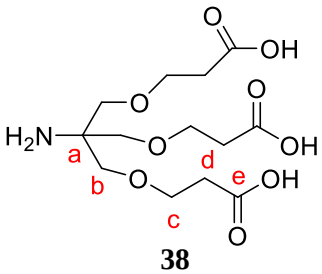

38

Tris{[2-(tert-butoxycarbonyl)ethoxy]methyl}methylamine **37** (95 mg, 0.19 mmol) was dissolved in DCM (0.5 mL). Phosphoric acid (85% wrt to water, 50 μL) was added and the mixture stirred for 16 hrs. Deionised water (2 mL) was then added and product extracted with ethyl acetate before reduction *in vacuo* to yield the product **38** as a colourless oil (45 mg, mmol, 70 %). ^{1}HNMR (D_2O, 400 MHz) : δ 2.53 (6H, t, *J* = 5.8 Hz, d); 3.51 (6H, s, b); 3.64 (6H, t, *J* = 5.8, c) ^{13}CNMR (D_2O, 101 MHz) : δ 34.2 (d); 59.4 (a); 66.8 (c); 67.9 (b); 176.3 (e). HRMS-ESI of $C_{13}H_{23}NO_9$ calc: 337.14 found 338.1410 [M+H$^+$].

6.3.5.3 CONJUGATION OF TRIS{[2-CARBOXYETHOXY]METHYL}METHYLAMINE AND GREEN CDS (**39**)

Acid-functionalised CDs **25** (10 mg) were dissolved in deionised water before the addition of N-(3-Dimethylaminopropyl)-N′-ethylcarbodiimide hydrochloride (EDC) (44 mg, 0.23 mmol) and N-Hydroxysuccinimide (NHS) (20 mg, 0.17 mmol). The solution was stirred for 25 mins and then quenched with 2-Mercaptoethanol (18 mg, 0.23 mmol) and stirred for a further 10 mins. **38** (78 mg, 0.23 mmol) was then added and then the mixture was stirred for 17 hrs. The resulting product was dialysed against ultrapure water using a 500-1000 MWCO dialysis membrane for 24 hrs before lyophilisation to yield a brown solid **39** (70 mg).

6.3.5.4 CONJUGATION OF TRIS{[2-CARBOXYETHOXY]METHYL}METHYLAMINE AND GREEN CDS (**40**)

39 (3.4 mg) and CDI (30 mg, 0.18 mmol) were dissolved in DMF (1 mL) and sonicated for 15 mins. Aminated mannose (**26**) (30 mg, 0.17 mmol) was added and the mixture was stirred for 16 hrs. DMF was removed under vacuum and the resulting brown solid was dialysed against 36 hrs before lyophilisation to yield a brown solid **40** (8.3 mg).

6.3.6 1-(1,7-DIAMINOHEPTANE)-α/β-D-MANNOPYRANOSE (41)

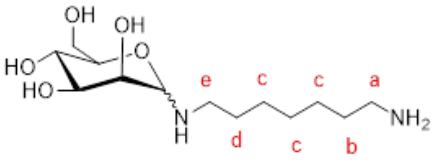

41

1,7-Diaminoheptane (0.5 g, 3.84 mmol) and mannose (0.69 g, 3.84 mmol) in 5 mL of methanol were stirred at 60 °C for 2 hours. The solution was concentrated under vacuum before being purified with reverse-phase preparative HPLC (5% to 95% MeOH w/0.05% formic acid in H_2O w/0.05% formic acid) to give the product **41** as a slightly yellow oil (60 mg, mmol, 5%). ^{1}H NMR ($CDCl_3$, 400 MHz) : δ 1.29 (s, 6H, c); 1.56 (m, 2H, d); 1.62 (m, 2H, b); 2.89 (t, *J*= 7.6 Hz, 2H, a); 3.01 (t, *J*= 6.85 Hz, 2H, e); 3.42-4.10 (m, 7H, sugar protons including anomeric). ^{13}CNMR (CDCl3, 101 MHz): δ 25.8, 26.3, 28.1, 28.5, 30.5, 40.2, 44.5, 61.1, 67.2, 71.1, 73.8, 77.2, 86.5. HRMS-ESI of $C_{13}H_{28}N_2O_5$ calc: 292.20 found 293.2102 [M+H$^+$].

6.4 2,5-DEOXYFRUCTOSAZINE CONCENTRATION ESTIMATION ON GCDS

The distinctive pyrazine proton peaks can easily be identified within the GCD ^{1}H NMR. The peak that is located between 8.70- 8.740 ppm was used as a reference peak to compare 2,5-DOFR concentration in the GCD samples.

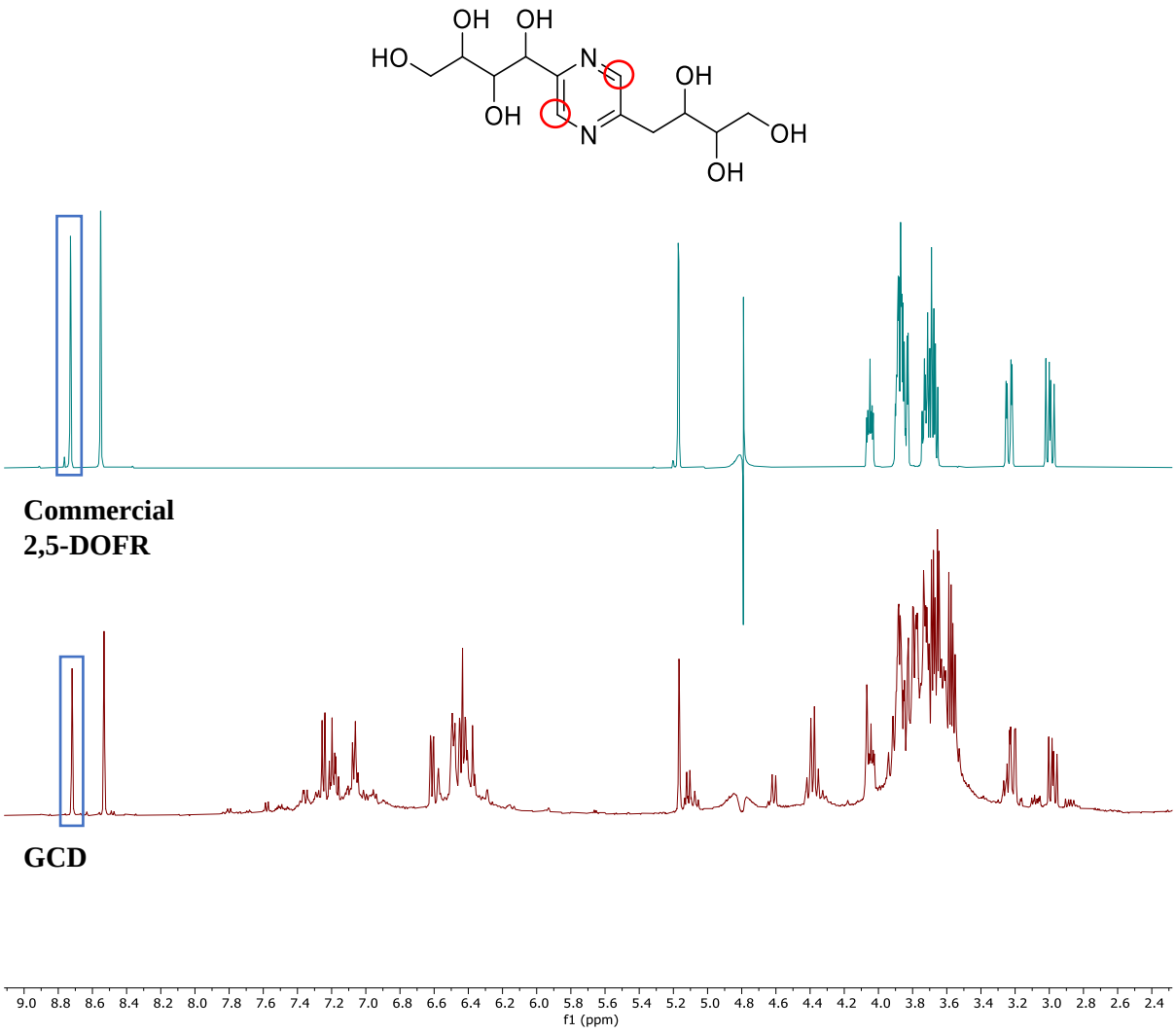

Figure S 1 Stacked ^{1}HNMR of commercially purchased 2,5-deoxyfructosazine and GCDs. Pyrazine peak highlighted

6.5 DLS MEASUREMENTS

Dynamic light scattering (DLS) is a measurement technique for the analysis of particle size in the nanometer range. This method is based on the principle of Brownian motion when particles move in random directions when dispersed in a liquid and constantly colliding with solvent molecules. Smaller molecules will move at higher speed, a factor that can be measured with irradiation by a laser (633 nm) and detection of the resulting backscatter from particles. Speed of particles can be related to hydrodynamic size through the Stokes-Einstein equation:

$$D = \frac{k_B T}{3 \pi \eta R_H}$$

Where D = Translational diffusion coefficient (m^2/s) ('speed of particle'), k_B = Boltzmann constant (m^2kg/Ks^2), T = Temperature (K), η = viscosity (Pa.s.), R_H = Hydrodynamic radius

DLS can give information of size distribution, number, intensity and volume of the sample. In the results presented in Section 3.3.3 the number-based distribution is used.
Synthesised CDs were dispersed in 1 mL of HPLC-grade water at a concentration of 1 mg/mL and vortexed for 15 seconds. Plastic 70 µL cuvettes were used for measurement in the instrument. All experiments were performed with a Malvern Instruments Nano-S90 ZEN1690.

6.6 GENERAL BACTERIAL CULTURE EXPERIMENTAL

Eleven different bacterial strains were used, detailed in Table S1.

Table S 1: Suppliers and strains of the five bacterial strains used

Species	Supplier
***Escherichia coli* (BW25113)**	*E. coli* genetic stock centre at Yale University
***Escherichia coli* [BW25113 (*ΔFimA*)]**	*E. coli* genetic stock centre at Yale University
***Escherichia coli* (ATCC 25922)**	American Type Culture Collection
***Escherichia coli* (UTI 808)**	Gift from Dr Jacqueline Findlay
***Escherichia coli* (IR 60)**	Multiresistant clinical isolate originally from Prof. Tim Walsh (Oxford University)
***Pseudomonas aeruginosa* (PA01)**	Pseudomonas genetic stock centre at East Carolina University
***Klebsiella pneumoniae* (NCTC 5055)**	Gift from Prof Matthew Avison
***Staphylococcus aureus* (Newman)**	Gift from Dr Angela Nobbs
***Staphylococcus aureus* (hVISA 21773)**	Gift from Prof A MacGowan at Southmead hospital, Bristol
***Staphylococcus aureus* [USA300 LAC (MRSA)]**	Community-acquired MRSA strain from Dr Angela Nobbs
***Staphylococcus aureus* [17608 (USA/MRSA)]**	Gift from Prof A MacGowan at Southmead hospital, Bristol
***Mycobacterium smegmatis* (ATCC 607)**	Purchased from LGC Standards
***Saccharomyces cerevisiae* (BY4741 YSD83)**	Gift from Dr Stephanie Diezmann

For labelling and LED toxicity experiments with GCD, bacterial inoculations used were sourced from glycerol stocks stored at -80 °C and either streaked onto Nutrient agar and incubated at 37 ˚C for 18-24 hours. Following incubation, and immediately prior to use, colonies were resuspended in PBS. To generate the desired concentration, a 1 mL sample from this solution was sampled and absorbance photometry was then conducted at 600 nm using an Ultrospec Spectrophotometer (Amersham Biosciences) calibrated to a control of 1mL of PBS alone. The solution was diluted to achieve an absorbance of 0.1 to 0.08 (equating to 0.5 McFarland standard of approximately 1 to 2 x 10^8 colony forming units (cfu) per mL). LED-irradiated samples were exposed to blue-LED strip lights (purchased from LightingEVER via Amazon.co.uk, Voltage: 12V, Wattage: 24W and mounted on a black foamboard support, λ_{em}= 460 nm) for durations specified below. For *FimH* specific targeting, *E. coli* were grown statically for 36-48 hours in lysogeny broth (LB) media before dilution to the appropriate concentration, determined through absorbance as above. For growth curves and MIC experiments optical density was measured using PolarStar Omega plate reader (BMG labtech) at 600nm.

6.6.1 GENERAL SAMPLE PREPARATION FOR CONFOCAL IMAGING

960 µL of bacterial suspension at a concentration of 1 x10^8 cfu/ml was prepared. 40 µL of a 5 mg/mL solution of carbon dots (CDs) was added to give a final concentration of 200 µg/mL. The suspension was exposed to the CDs for 30 mins while rotating at room temperature. The samples were then centrifuged at 2500 xg for 10 mins and the cell pellet washed with PBS solution and centrifuged again. The supernatants were removed and the cell pellets re-suspended in 50 µl 2% paraformaldehyde (PFA). The cells were left to fix for 1 h at room temperature before transferring 5 µl into 15 µl ProLongTM Gold Antifade mountant (ThermoFisher). The samples were mounted on glass slides with coverslips and left to set at room temperature for at least 12 h.

6.6.2 HYVOLUTION CONFOCAL MICROSCOPY

Images were acquired on a Leica TCS SP8 system attached to a Leica DMi8 inverted microscope (Leica Microsystems) using a 100x HC PL APO CS2 oil immersion objective. The GCD-treated samples were excited using a white light laser and an acousto-optical beam splitter (AOBs) set at 405 nm. For labelling with GCD, fluorescence was detected using a hybrid detector operating over an emission range of 480-550 nm and images acquired at 512 x 512 pixels and 4096 time bins. FM™ 4-64FX (ThermoFisher)-treated samples were excited at 561 nm and fluorescence detected over an emission range of 700-770 nm.

6.6.3 AGGLUTINATION ASSAY

Methodology was adapted from that reported by Abgottspon *et al*.[288] *S. cerevisiae* is grown at 30 °C for 48 hours in Yeast peptone dextrose (YPD) broth and *E. coli* BW25113 is grown at 37 °C in LB broth for 48 hours either statically (for *FimH* expression) of shaking (as a Δ*FimH* control). The bacterial concentration for both was adjusted to OD_{600} , approximately 2 x10^8 cfu/mL of *S. cerevisiae* and 9.6x10^7 cfu/mL of *E. coli* before centrifugation at 6000 xg for 1 min and resuspended in PBS. 125 µL of *S. cerevisiae* was spotted on a sterile plate and overlayed with 50 µL of *E. coli*. After 20 mins the plate was gently agitated, and the presence of aggregation noted. For CD and free saccharide screening 0.7 µL of 50 mg/mL of CD stock or 8.75 µL of 1M saccharide stock respectively were added to the 50 µL *E. coli* suspension before drop casting.

6.7 TECHNIQUES TO ASSESS LABELLING AND ANTIBACTERIAL ACTIVITY OF GCDS

6.7.1 BACTERIAL DYE PROCEDURES

6.7.1.1 FM™ 4-64FX

240 μL of bacterial suspension at a concentration of 1 x10^8 cfu/ml was prepared. 20 μL of a 10 mg/mL solution of GCDs was added to give a final concentration of 40 μg/mL. The suspension was exposed to the CDs for 30 mins while rotating at room temperature. The samples were then centrifuged at 2500 xg for 10 mins and the cell pellet washed with PBS solution and centrifuged again. The pellet was then resuspended in 25 μL of 100 μg/mL of FM™ 4-64FX (ThermoFischer Scientific) and shaken at 37 ˚C for 30 mins before the addition of 10 μL PFA. After fixing the cells for 1 hr the samples were prepared for confocal microscopy as above.

6.7.1.2 SYTOX™ RED CELL STAIN

Sample preparation was the same as labelling and after a 30 min exposure to GCDs the samples were irradiated with the LED lights for 90 mins. The samples were then centrifuged at 2500 xg for 10 mins and the cell pellet washed with PBS solution and centrifuged again. The pellet was then resuspended in 500 μL PBS and 250 μL of this was disposed. The remaining 250 μL was diluted with another 250 μL of PBS before the addition of 50 μL of a 5 μM solution of Sytox™ red stain (ThermoFisher Scientific) andncubated for 15 mins in the dark while turning. 7 μL of each sample was then added to 15 μL of confocal mountant with no fixation and loaded onto the microscope slide.

6.7.2 FLOW CYTOMETRY

GCD labelled *E. coli* was prepared as above for confocal imaging but at bacteria concentration of 2.5 x10^7 cfu/mL and a 30 min incubation of GCD. A control of *E. coli* without GCD incubation was also prepared. Flow cytometry data was acquired using a Novocyte 3000 flow cytometer (ACEA Biosciences, San Diego, CA, USA). A 405 nm solid laser was used to excite GCD and the emission was measured in the BL1-A band pass (488 nm). A minimum of 30,000 cells was measured for each sample.

6.7.3 ESTIMATION OF SURFACE GCD CONCENTRATION

A calibration curve was first created by measuring the fluorescence of known concentrations of GCD in a 96 well microtiter plate (in PBS inoculated with the same bacterial concentration as that of the desired sample to match turbidity). This allowed the generation of a linear equation which could be used to estimate the concentration of GCD bacterial labelling by entering the fluorescence units of bacteria incubated with GCD.

6.7.4 VIABLE CELL COUNTING

Sample preparation was as described for confocal imaging above. After 30 min exposure to GCD, samples were irradiated with LED lights for 30, 60 or 90 mins. The samples were then centrifuged at 2500 xg for 10 mins and the cell pellet resuspended in 1 mL of PBS. 25 µL of this suspension was taken and diluted in ten-fold serial dilutions up to 10^{-7}. 100 µL of the last three dilutions were plated on to agar plates and incubated overnight. Cell colonies were then counted to determine viable cell counts.

6.7.5 GENERAL SAMPLE PREPARATION FOR GROWTH CURVES

5 mL overnight bacterial cultures were centrifuged at 2,900 xg for 10 min at room temperature and washed twice in PBS. Serial dilutions of GCD in water were prepared in flat-bottom 96-well plates (Corning), inoculated with 10 µL of 1 x 10^8 cfu/ml of washed cells and continuously shaken on a rotating platform with or without blue-LED exposure for up to 4 h. The samples were then further diluted 10-fold in Mueller Hinton broth 2 (Sigma-Aldrich) and placed in a plate reader (BMG Omega) for absorbance readings at 600 nm every 10 min for 16.5 h at 37°C.

6.7.6 TEMPERATURE MEASUREMENTS

In a flat-bottom 96-well plate (Corning), 240 µL of bacterial suspensions were mixed with either 10 µL (800 µg/mL final concentration) or 2 µL (200 µg/mL) of 20 mg/mL GCD. Control wells contained PBS only. Wells were either irradiated with LED or kept in the dark and the temperature was recorded at regular 30 min intervals. A Thermocouple (type K from Fisher Scientific) was used to record temperature to 1 decimal place.

6.7.7 DIHYDROETHIDIUM ROS DETERMINATION

192 µL of bacterial suspensions were added to wells of 2 flat-bottom 96 well plates. 8 µL of either GCD (10 mg/mL) or sterile water was incubated for 1 hour. One plate was then irradiated with LED lights for 90 mins whilst the other was kept in the dark. 10 µL dihydroethidium (DHE) (1 mg/mL) was then added to each well and fluorescence measured at λ_{ex} = 355 nm and λ_{em} = 460 nm (BMG PolarStar Omega plate reader).

6.7.8 SCANNING ELECTRON MICROSCOPY (SEM)[7]

1 mL bacterial overnight cultures were centrifuged at 13,000 xg for 5 min and the pellets washed once in PBS. GCDs were added to yield a final concentration of 512 µg/mL and incubated for 30 min with rotation. After 30 min, the blue-LED board was placed in front of the rotator and samples not requiring LED-treatment were covered with foil. The samples were rotated for another 30 min before centrifuging at 8,000 xg for 5 min and washing twice in PBS. On the last wash, 50 µl of sample was removed,

[7] The work in this section was completed by Yuiko Takebayashi, Spencer Group, University of Bristol and Chris Neal and Judith Mantell of the Wolfson Bioimaging facility

centrifuged and the pellet re-suspended in 50 µl of PBS. Samples were fixed on poly-L-lysine (0.1% w/v in water) treated glass coverslips in 2.5% glutaraldehyde overnight at 4°C. The samples were dehydrated in a series of ethanol solutions from 20, 50, 70, 90 and 100% and chemically dried with hexamethyldisilizane (HMDS) before being mounted on metal stubs and gold sputter coated (Emitech). The samples were imaged at magnifications of 20,000-120,000x on the FEI Quanta 200 FEG-SEM with a working distance of 10-13 mm, chamber pressure of $<10^{-5}$ Pa in high vacuum mode and an accelerating voltage of 15-10 kV.

6.7.9 VANCOMYCIN MINIMUM INHIBITORY CONCENTRATION (MIC) STUDIES

Bacterial suspensions of $1x10^8$ cfu/mL in PBS are made from overnight plates and diluted 1:20. A 200 µg/mL stock solution of GCD Muller Hinton broth is prepared. Serial dilutions of vancomycin in the GCD broth were prepared in flat-bottom 96-well plates, to a volume of 90 µL , before they were inoculated with 90 µL of GCD broth is then added and 20 µL of the bacterial suspensions. Vancomycin concentrations of 128 µg/mL to 0.125 µg/mL were tested and each condition repeated in triplicate. After incubation for 30 mins the plates were exposed to LED irradiation for 90 mins. The plates were then incubated at 37 °C for 16-20 hours and absorbance readings at 600 nm were measured in a plate reader (BMG Omega).

6.7.10 PROTEOMICS SAMPLE PREPARATION AND ANALYSIS[8]

6.7.10.1 TANDEM MASS TAG LABELLING AND HIGH PH REVERSED-PHASE CHROMATOGRAPHY

Whole cell lysates were obtained from *E. coli* and *S. aureus* cultures grown in M9 minimal media in duplicate for 6 and 3 h respectively, with or without 512 µg/mL GCD and continuous LED irradiation. Aliquots of 50 µg of each sample were digested with trypsin (2.5 µg trypsin per 100 µg protein; 37°C, overnight), labelled with Tandem Mass Tag (TMT) ten plex reagents according to the manufacturer's protocol (Thermo Fisher Scientific) and the labelled samples pooled.

The pooled sample was evaporated to dryness, resuspended in 5% formic acid and then desalted using a SepPak cartridge according to the manufacturer's instructions (Waters, Milford, Massachusetts, USA). Eluate from the SepPak cartridge was again evaporated to dryness and resuspended in buffer A (20 mM ammonium hydroxide, pH 10) prior to fractionation by high pH reversed-phase chromatography using an Ultimate 3000 liquid chromatography system (Thermo Scientific). In brief, the sample was loaded onto an XBridge BEH C18 Column (130Å, 3.5 µm, 2.1 mm X 150 mm, Waters, UK) in buffer A and peptides eluted with an increasing gradient of buffer B (20 mM Ammonium Hydroxide in acetonitrile, pH 10) from 0-95% over 60 minutes. The resulting fractions were evaporated to dryness and resuspended in 1% formic acid prior to analysis by nano-LC MSMS using an Orbitrap Fusion Lumos mass spectrometer (Thermo Scientific).

[8] All the work towards proteomic preparation, measurements and data analysis was completed by Yuiko Takebayashi, Spencer Group and by the University of Bristol Proteomics Facility run by Kate Heesom

6.7.10.2 NANO-LC MASS SPECTROMETRY

High pH RP fractions were further fractionated using an Ultimate 3000 nano-LC system in line with an Orbitrap Fusion Lumos mass spectrometer (Thermo Scientific). In brief, peptides in 1% (vol/vol) formic acid were injected onto an Acclaim PepMap C18 nano-trap column (Thermo Scientific). After washing with 0.5% (vol/vol) acetonitrile 0.1% (vol/vol) formic acid peptides were resolved on a 250 mm × 75 μm Acclaim PepMap C18 reverse phase analytical column (Thermo Scientific) over a 150 min acetonitrile gradient, divided into 7 gradient segments (1-6% solvent B over 1 min., 6 - 15% B over 58 min., 15 - 32% B over 58 min., 32 - 40% B over 5 min., 40 - 90% B over 1 min., held at 90% B for 6 min and then concentrated to 1% B over 1 min.) with a flow rate of 300 nl min^{-1}. Solvent A was 0.1% formic acid and Solvent B was aqueous 80% acetonitrile in 0.1% formic acid. Peptides were ionized by nano-electrospray ionization at 2.0kV using a stainless steel emitter with an internal diameter of 30 μm (Thermo Scientific) and a capillary temperature of 275°C.

All spectra were acquired using an Orbitrap Fusion Lumos mass spectrometer controlled by Xcalibur 4.1 software (Thermo Scientific) and operated in data-dependent acquisition mode using an SPS-MS3 workflow. FTMS1 spectra were collected at a resolution of 120 000, with an automatic gain control (AGC) target of 200 000 and a max injection time of 50ms. Precursors were filtered with an intensity threshold of 5000, according to charge state (to include charge states 2-7) and with monoisotopic peak determination set to Peptide. Previously interrogated precursors were excluded using a dynamic window (60 s +/- 10 ppm). The MS2 precursors were isolated with a quadrupole isolation window of 0.7m/z. ITMS2 spectra were collected with an AGC target of 10 000, max injection time of 70ms and CID collision energy of 35%.

For FTMS3 analysis, the Orbitrap was operated at 50 000 resolution with an AGC target of 50 000 and a max injection time of 105 ms. Precursors were fragmented by high energy collision dissociation (HCD) at a normalised collision energy of 60% to ensure maximal TMT reporter ion yield. Synchronous Precursor Selection (SPS) was enabled to include up to 5 MS2 fragment ions in the FTMS3 scan.

6.7.10.3 DATA ANALYSIS

The raw data files were processed and quantified using Proteome Discoverer software v2.1 (Thermo Scientific) and searched against the UniProt Human database (downloaded September 2018: 152927 entries) using the SEQUEST algorithm. Peptide precursor mass tolerance was set at 1ppm, and MS/MS tolerance was set at 0.Da. Search criteria included oxidation of methionine (+15.9949) as a variable modification and carbamidomethylation of cysteine (+57.0214) and the addition of the TMT mass tag (+229.163) to peptide N-termini and lysine as fixed modifications. Searches were performed with full tryptic digestion and a maximum of 2 missed cleavages were allowed. The reverse database search option was enabled and all data were filtered to satisfy a false discovery rate (FDR) of 5%.

Volcano plots were plotted to visualise statistical significance (p-value) versus fold change using R studio.[331] PantherDB was used for geneontology analysis.[332]

6.7.11 PROCEDURE FOR BIOFILM GROWTH AND ANALYSIS

Adapted from the methodology reported by O'Toole.[283] Bacterial strains were grown overnight in LB broth. The overnight cultures were diluted 1:100 in minimal M9 media supplemented as below:

For every 1 L of M9 media
2 ml 1M $MgS0_4.7H_20$
10 ml 40% glucose
33.3 ul 3M $CaCl_2$
1 ml 0.2% Thiamine

100 µL of diluted bacterial culture was added to the well of a 96-well plate, for each sample condition four replicates were grown. For GCD experiments, each well had a final GCD concentration of 200 µg/mL and was incubated for 30 mins before being exposed to LED irradiation for 90 mins. The plate was incubated for 24 hours at 37 °C. After incubation the wells were emptied and washed gently with water before the addition of 125 µL of a 0.1% aqueous solution of crystal violet dye and incubated for 15 mins. The plate was then rinsed,washed and left to dry. Once dry, 125 µL of 30% acetic acid was added to each well and left to solubilise over 10 mins. The contents of the plate were then transferred to a new 96 well microtiter plate and absorbance read at 550 nm.

6.8 TECHNIQUES TO ACCESS ANTIBACTERIAL ACTIVITY OF G4 LIGANDS

6.8.1 ZONE OF INHIBITION ASSAY

In PBS, 1 x 10^8 cfu/mL bacterial suspensions were spread evenly over 50 mL Mueller Hinton agar plates. 25 µg of G4 ligands (dissolved in DMSO) were loaded onto 5 mm disks of filter paper and placed on the surface of the inoculated agar, including a control 10 µg ampicillin susceptibility disk (Oxoid). The plates were incubated at 37 °C for 16-20 hours and any zones of inhibition were recorded in millimetre.

6.8.2 MINIMUM INHIBITORY CONCENTRATION METHODOLOGY

Bacterial suspensions of 1 x 10^8 cfu/mL in PBS were made from overnight plates and further diluted 100-fold. Serial dilutions of 75 µL of G4 ligands in Mueller Hinton cation-adjusted broth were prepared in flat-bottom 96-well plates and inoculated with 75 µL of the 1:100 diluted bacterial suspensionfor a final bacterial concentration of 5 x 10^5 cfu/mL. The plates were incubated at 37 °C for 16-20 hours and absorbance readings at 600 nm were measured in a plate reader (BMG Omega). For *M. smegmatis*, liquid cultures were grown over three days at 30 °C in LB broth supplemented with 0.05% TWEEN80, 0.2% glucose and 0.2% glycerol. The plates were prepared as described above but to a total volume of 200 µL and the antibiotic cefoxitin used as a control. Plates were wrapped in Parafilm and grown over 3 days at 37 °C.

6.9 TECHNIQUES FOR ACCESSING G-QUADRUPLEX LIGAND AFFINITY

6.9.1 OLIGONUCLEOTIDE SEQUENCE

The hemL RNA sequence was purchased from Eurogentec (Belgium), purified by HPLC and delivered dry. The FRET active sequence was labelled with FAM, 6-carboxyfluorescein, at the 5' end and TAMRA, 6-carboxy-tetramethylrhodamine, at the 3' end. Stock solutions of hemL were prepared in HPLC-grade H_2O and stored at -20 °C. Before measurements hemL stock were diluted to the correct concentration in the appropriate buffer and annealed through heating at 90 °C for 2 mins and then placed in ice for 10 mins.

	Sequence
hemL	5'-FAM-GGU-CCG-GUC-UAU-CAG-GCG-GGU-TAMRA-3'

6.9.2 CIRCULAR DICHROISM SPECTROSCOPY

Circular dichroism (CD) spectroscopy measurements were acquired with a Jasco J-810 spectrometer fitted with a Peltier temperature control. A 200 μM stock solution of RNA was made in the appropriate buffer (10% DMSO). Initially CD measurements were run in 10 mM TrisHCl buffer at pH 7.4 to verify that reported by Shao *et al*.[164] Following this measurements for the FRET-active sequence were completed in a 10 mM lithium cacodylate buffer (pH 7.2) with varying concentrations of potassium chloride. Measurements were taken at 20 °C in a quartz cuvette with apath length of 5 mm, at a 100 nm / min scanning speed at 1 nm intervals. The CD spectra were recorded between 800 and 200 nm, and baseline corrected for the buffer used. The ligand was added for an overall concentration of 5 μM in 1 mL of buffer. The average of three scans for each sample was reported. The observed ellipticities (θ = mdeg) reported from the CD spectrometer were converted to molar ellipticity ($[\theta]$ = deg cm^2 $dmol^{-1}$).

6.9.3 FRET THERMAL MELTING ASSAYS

Fluorescence resonance energy transfer (FRET) melting assays were performed according to the reported procedure by De Cian *et al*.[333] The assay was performed using a 96 well plate in a Stratagene Mx3005P qPCR instrument. The final volume in each well was 25 μL, 20 μL of hemL (200 nM) in 10 mM lithium cacodylate and 10 mM of KCl buffer (pH 7.2) and 5 μL of the desired ligand. G4 ligands were prepared from an intermediate stock of 50 μM in HPLC-grade H_2O for final ligand concentrations of 1 μM, 2 μM, 5 μM and 10 μM. Each well was repeated in duplicate on the same plate and each plate repeated in duplicate. Suitable control conditions were also run in parallel to allow for the calculation of ΔT_m. Samples were heated in 1 °C increments, allowing 1 min for equilibration at each temperature before the FAM fluorescence, λ_{ex} = 492 nm, λ_e= 516 nm, is measured. T_m was determined as the value where fluorescence is half its maxima from the normalised curves.

6.10 FIGURES

6.10.1 QUANTIFICATION OF BACTERIAL LABELLING FROM CONFOCAL IMAGES

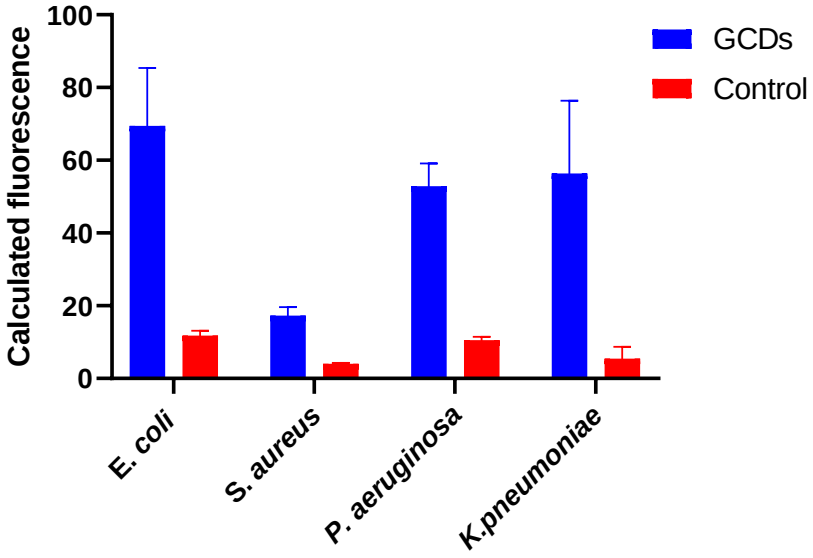

Figure S 2 Fluorescence intensity data from confocal images, assigned by Fiji software. *E. coli*, *S. aureus*, *P. aeruginosa* and *K. pneumoniae* incubated with 200 µg/mL of GCDs for 30 minutes before confocal imaging

6.10.2 PRELIMINARY FLOW CYTOMETRY RESULTS

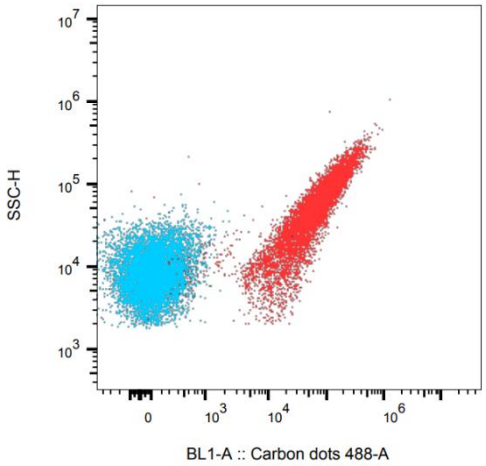

Figure S 3 Flow cytometry plot of side scatter vs GCD fluorescence at 488 nm. Blue patch indicates unlabelled *E. coli* and red those labelled with GCDs but size increases with fluorescence indicating aggregation of *E. coli* cells

6.10.3 DIFFERENCES IN LABELLING CONCENTRATION OVER INCREASING INCUBATION TIMES

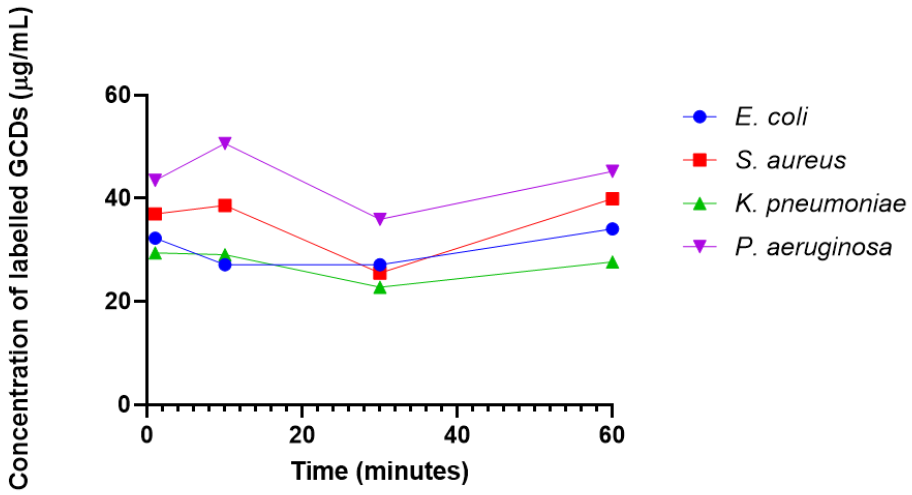

Figure S 4 Calculated bacterial labelling concentration of GCDs in four different species of bacteria over 1, 10, 30 and 60 minutes of incubation with 200 µg/mL of GCDs

6.10.4 EFFECT OF TURBIDITY ON FLUORESCENCE INTENSITY OF GCD LABELLING

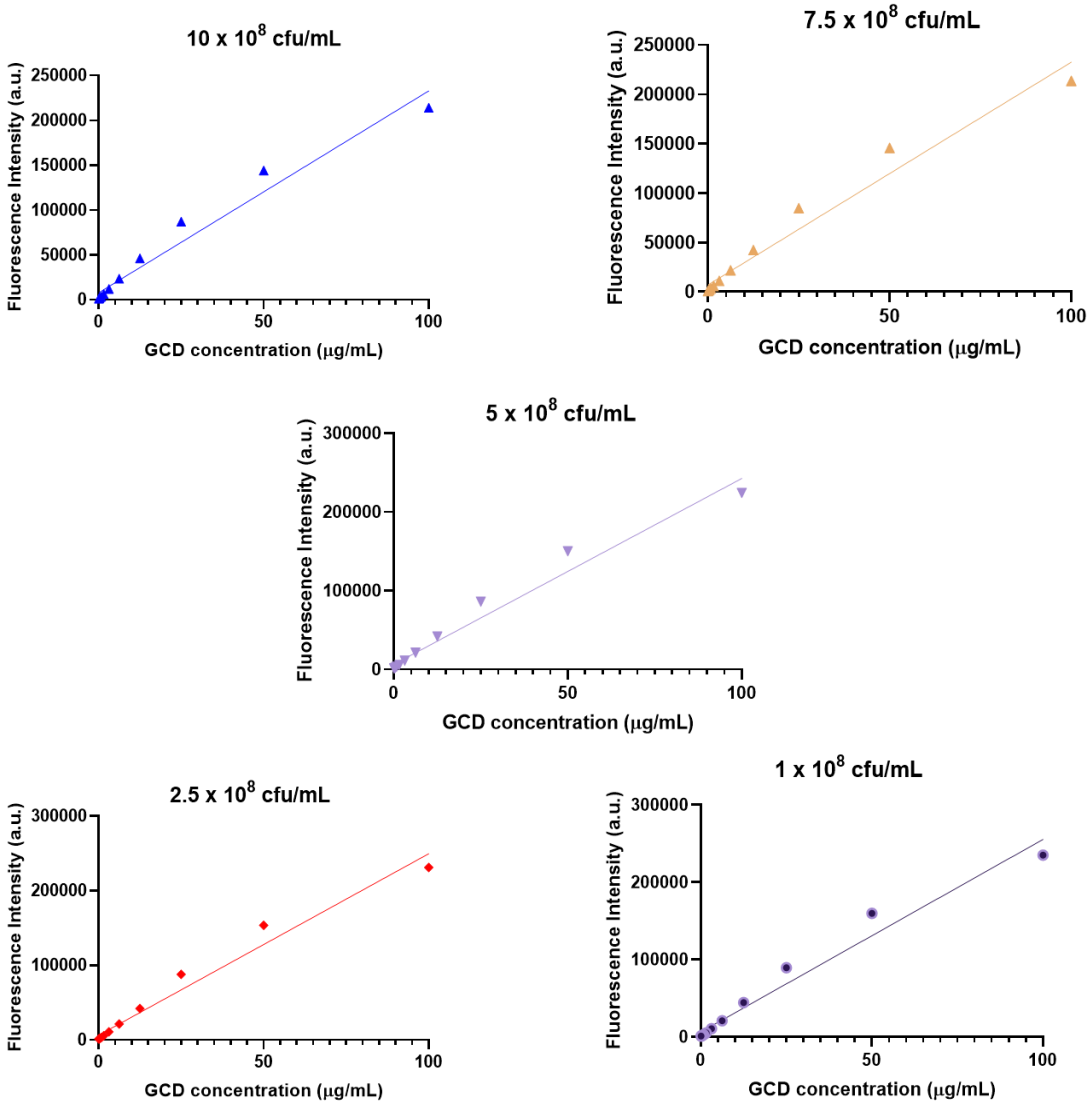

Figure S 5 Calibration curves at different concentrations of bacteria to overcome the issue of turbidity affecting fluorescence transmission

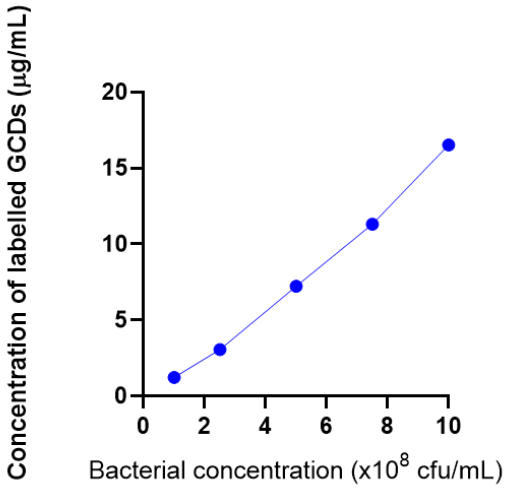

Figure S 6 Concentration of GCD labelling at different bacterial concentrations. Calculated labelling concentration taken from calibration curves at each bacteria concentration

6.10.5 COMPARISON OF CORE-GCDS AND GCDS

Labelling of GCDs without further purification compared with dialysed GCDs, the majority of 2,5-deoxyfructosazine (2,5-DOFR) stripped from the surface, and mostly purified 2,5-DOFR (some GCD-core remaining). Fluorescence intensity calculated from confocal images.

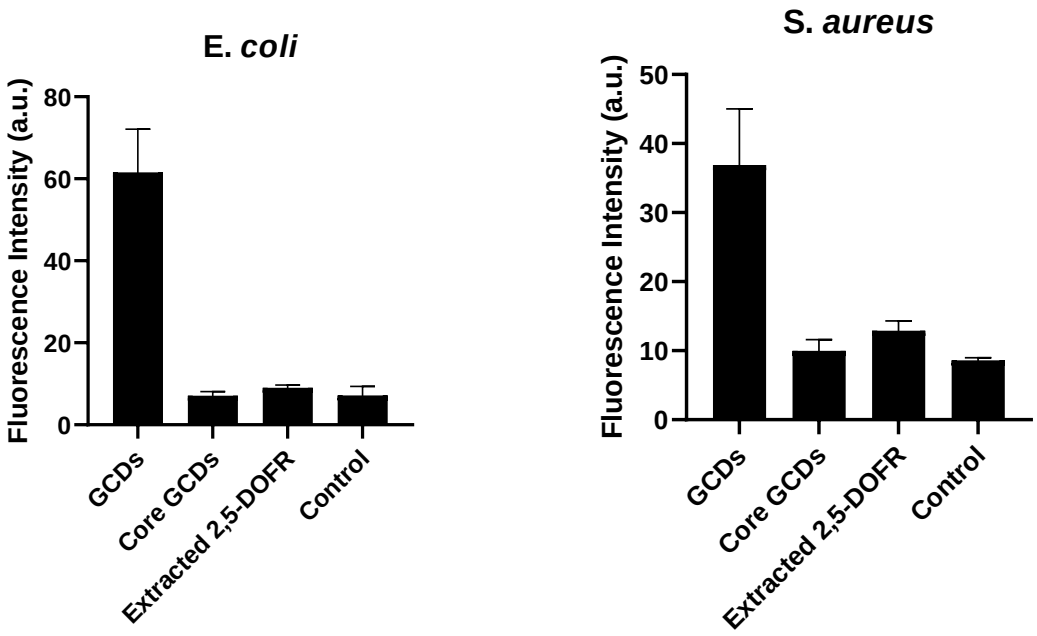

Figure S 7 Fluorescent labelling of *E. coli* and *S. aureus* by GCDs, core GCDs (stripped of 2,5-deoxyfructosazine) and 2,5-DOFR extracted from GCDs. Bacterial control to autofluorescence level. Values calculated from confocal images

6.10.6 DEGRADATION OF SUPEROXIDE INDICATOR DIHYDROETHIDIUM (DHE)

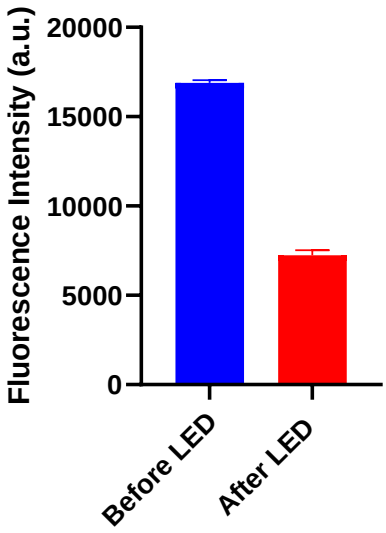

Figure S 8 DHE fluorescence intensity measured at λ_{ex} = 355 nm and λ_{em} = 460 nm of PBS with 5 ng/mL of DHE in PBS before and after 90 mins of LED irradiation

6.10.7 CD-1/CD-2 LABELLING: LITERATURE MANNOSE DERIVED CDS

Repetition of labelling experiment detailed in Section 3.3.1 (Figure 55) with *S. aureus* as control condition as reported in literature.[148]

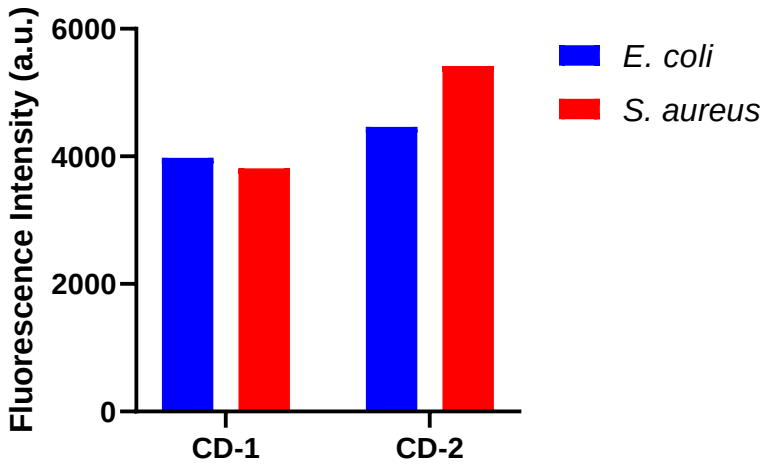

Figure S 9 Fluorescence intensity (λ_{ex} = 355 nm and λ_{em} = 450 nm) of *E. coli* and *S. aureus* comparing labelling with CDs derived from mannose and ammonium carbonate (**CD-1**) and from ammonium carbonate solely (**CD-2**)

6.10.8 FLUORESCENCE SPECTRA OF RECREATED LITERATURE CDS

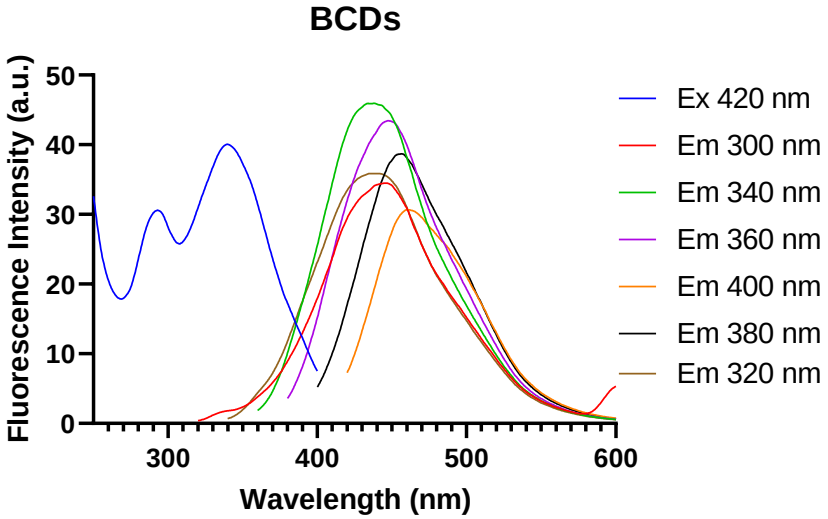

Figure S 10 Fluorescence spectrum of BCDs. Spectra matches that reported by Hill *et al.*[238]

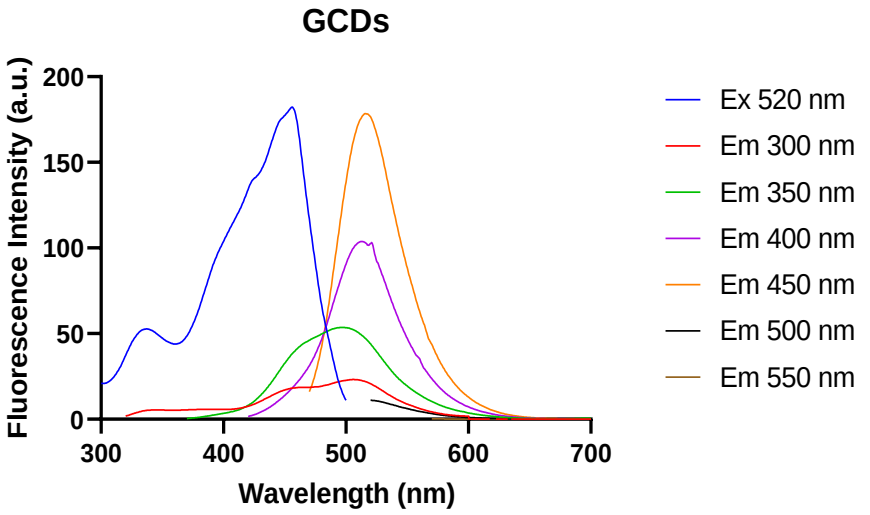

Figure S 11 Fluorescence spectrum of BCDs. Spectra matches that reported by Hill *et al*.[237]

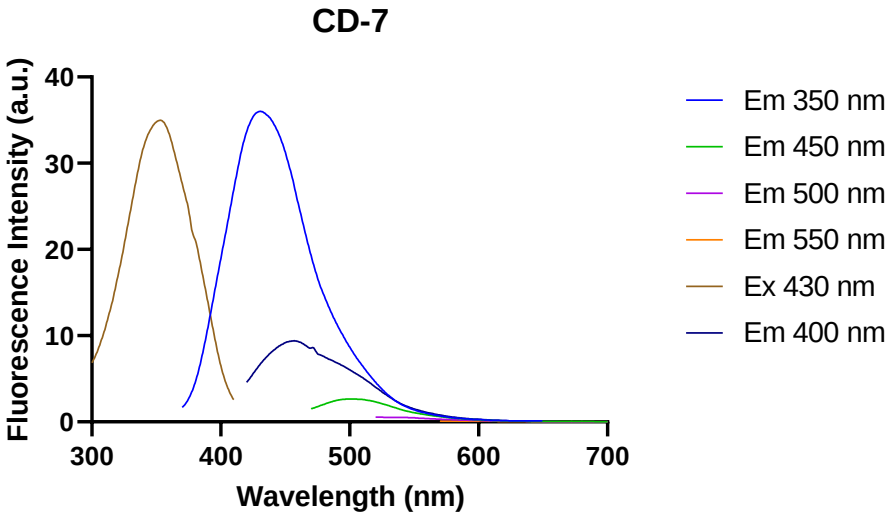

Figure S 12 Fluorescence spectrum of **CD-7**

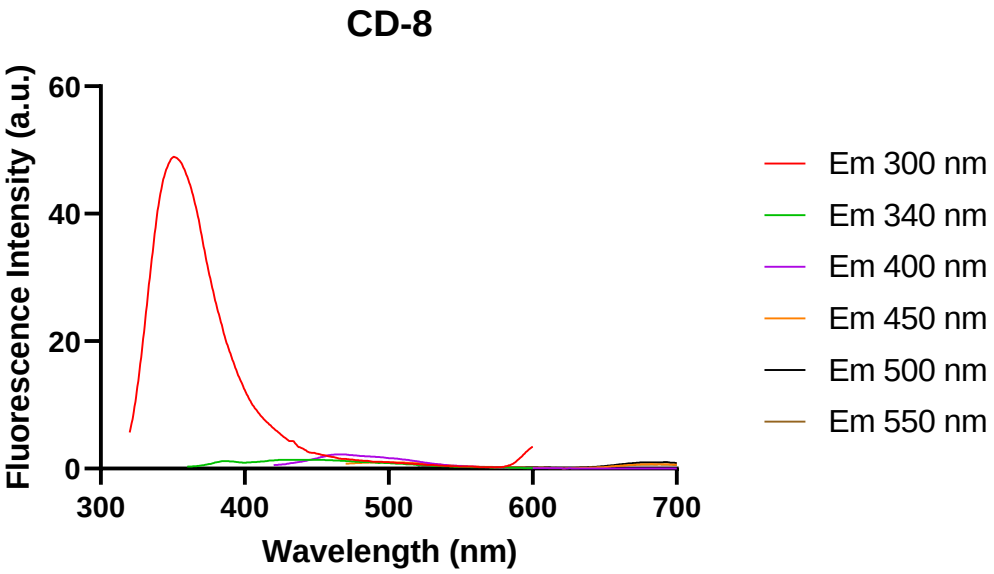

Figure S 13 Fluorescence spectrum of **CD-8**

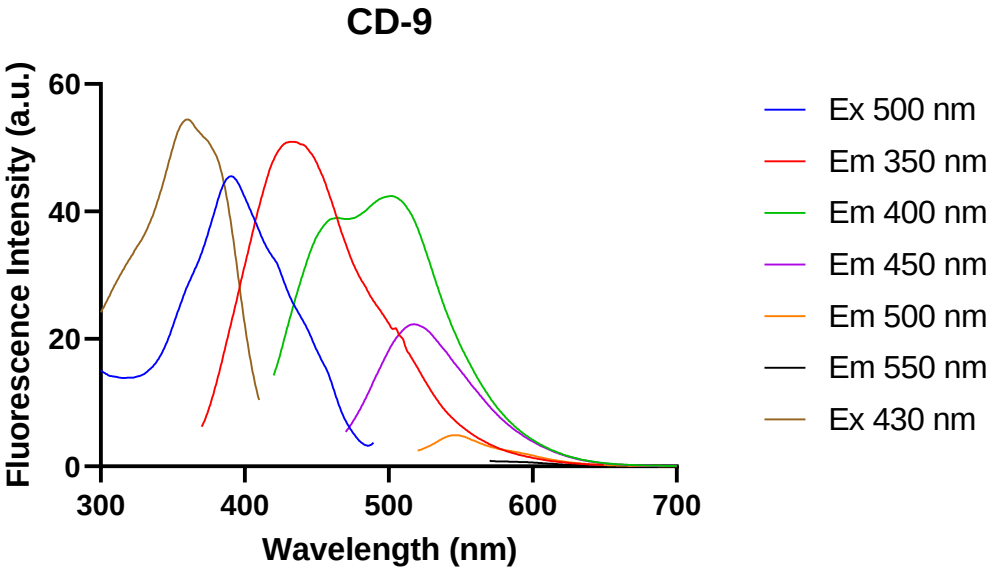

Figure S 14 Fluorescence spectrum of **CD-9**

6.10.9 SUMMARY OF ZONE OF INHIBITION RESULTS FOR ALL G4 LIGANDS SCREENED

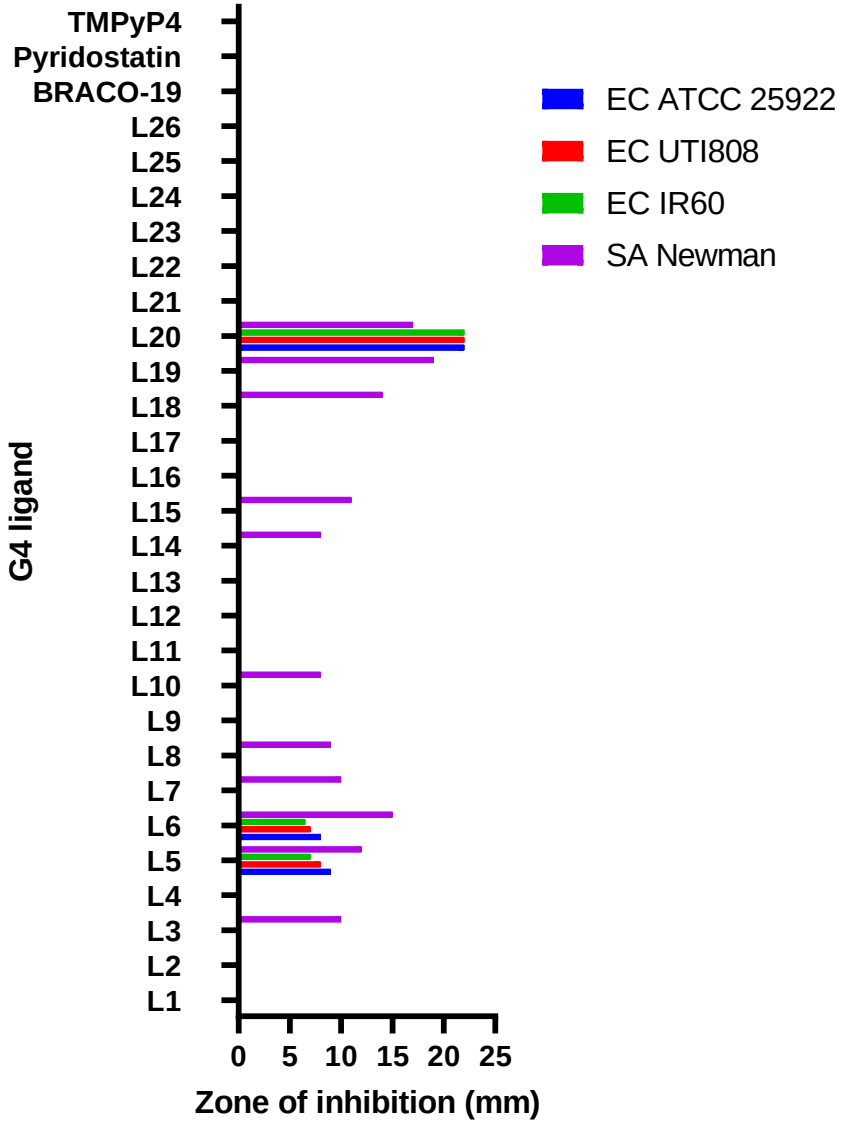

Figure S 15 Summary of zone of inhibition for all G4 ligands screened on three *E. coli* strains and *S. aureus* Newman. 25 µg of ligand loaded onto each disk and plate incubated at 37 °C for 16-20 hours

6.10.10 EFFECT OF BCD INCUBATION WITH LED IRRADIATION

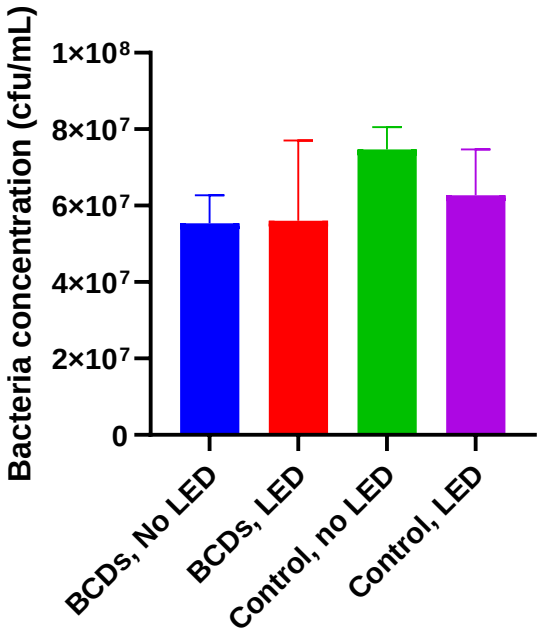

Figure S 16 Results from a viable count studying the effect of TTDDA/glucosamine derived carbon dots (BCDs) incubation in combination with LED irradiation λ=390 nm (in the region of the broad excitation peak of the BCDs) on *E. coli* viability. The methodology was the same as the GCD viability counts. These CDs, also derived from glucosamine but without 2,5-deoxyfructosazine on the surface, displayed no toxicity in the absence or presence of LED irradiation

6.11 NMR SPECTRA OF SYNTHESISED MOLECULES AND FUNCTIONALISED CDS

6.11.1 BCDS

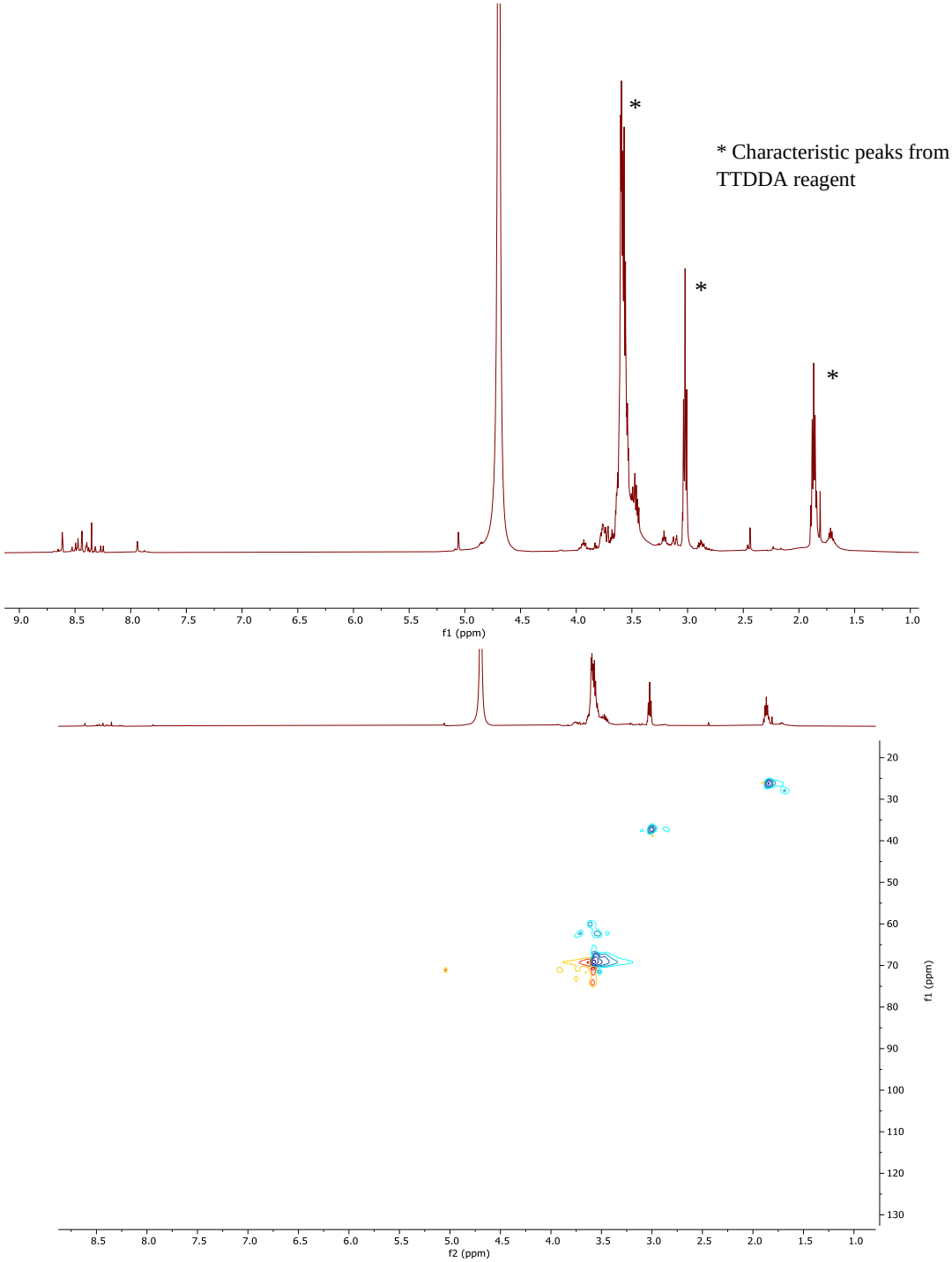

Figure S 17 HNMR and HSQC in D_2O of BCDs functionalised with succinic anhydride. In agreement with characterisation reported by Hill *et al.*[238]

6.11.1 GCDS

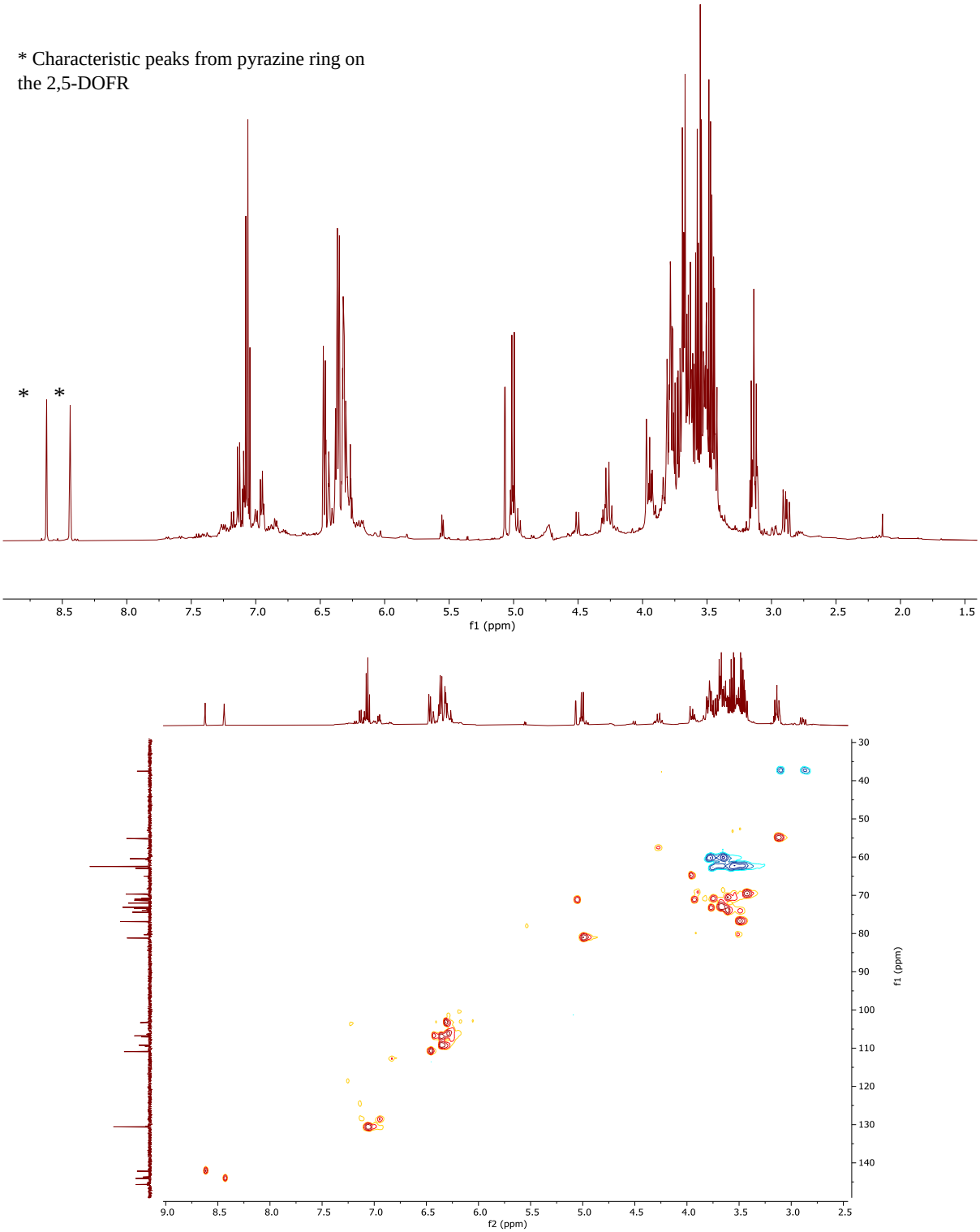

Figure S 18 ^{1}HNMR and HSQC in D_2O of GCDs functionalised with succinic anhydride. Previously reported.[237]

6.11.2 ACID FUNCTIONALISED GCDS (25)

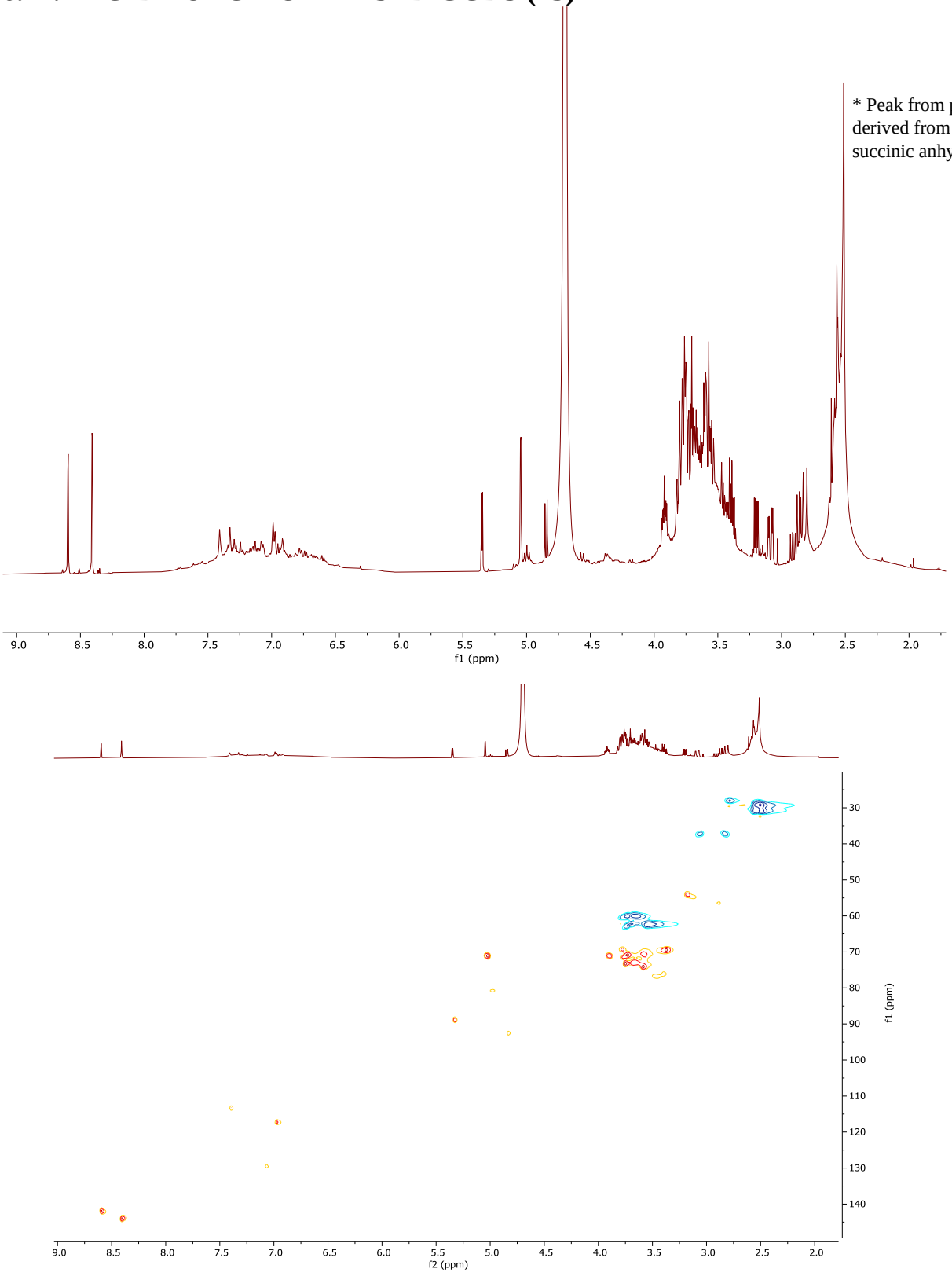

Figure S 19 ^{1}HNMR and HSQC in D_2O of GCDs functionalised with succinic anhydride **25**. As reported in Stephen A. Hill PhD thesis[328]

6.11.3 KOCHETKOV AMINATION OF MANNOSE (26)

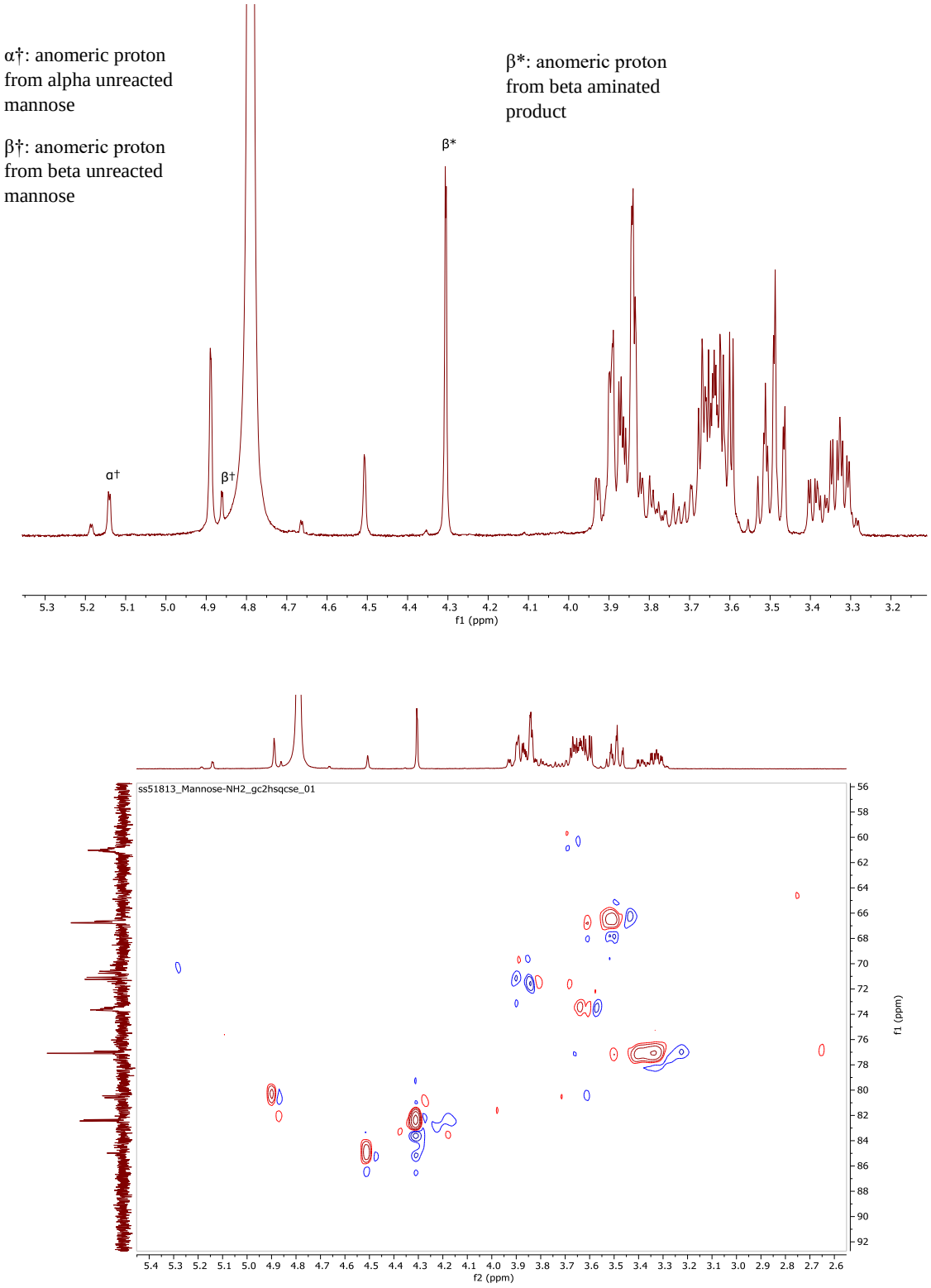

Figure S 20 ^{1}HNMR and HSQC in D_2O of the product of Kochetkov amination of mannose **26**. As reported in Stephen A. Hill PhD thesis[328]

6.11.4 MANNOSE-GCD (27)

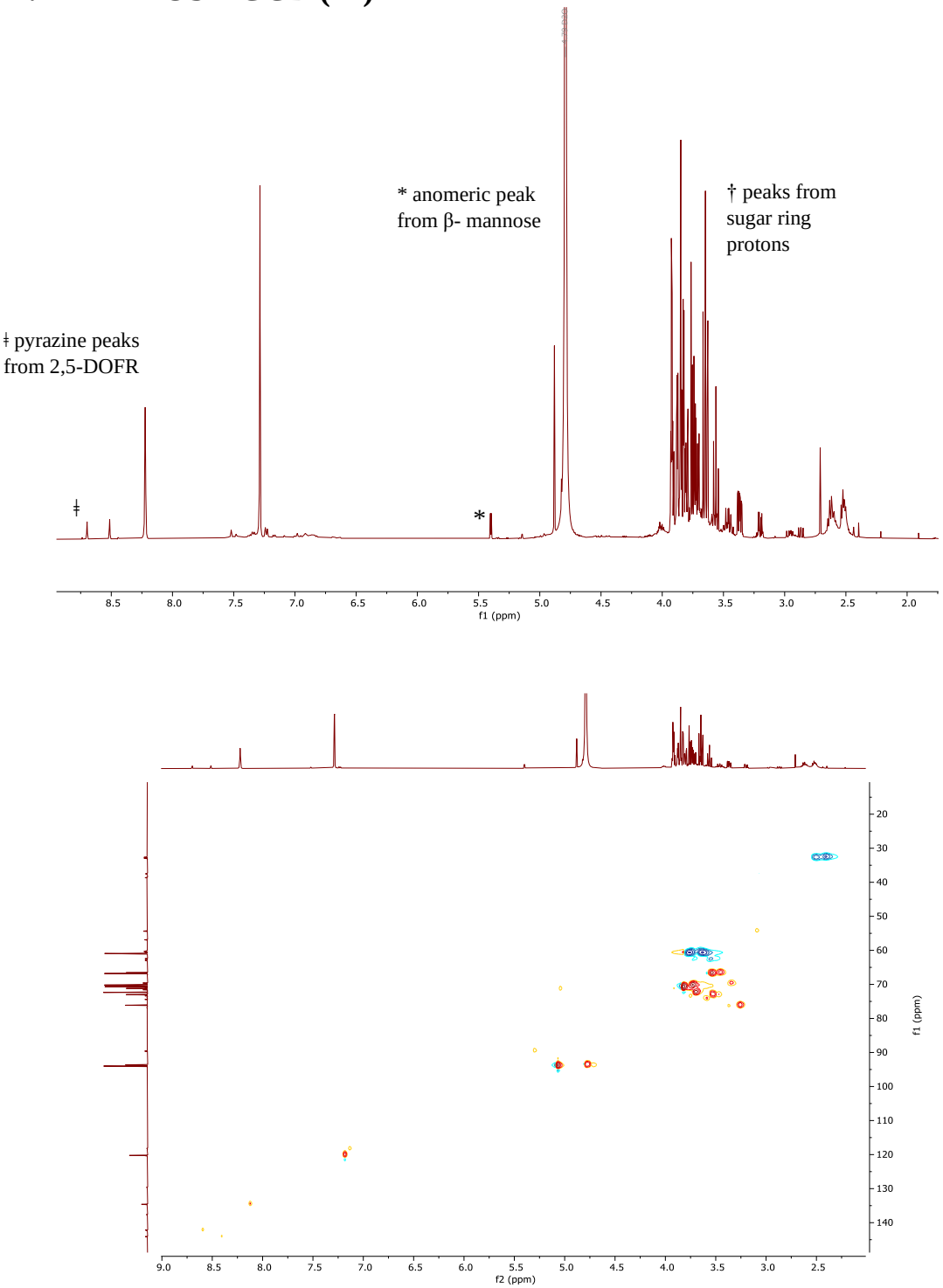

Figure S 21 ^{1}HNMR and HSQC in D_2O of GCDs functionalised with mannose **27**. As reported in Stephen A. Hill PhD thesis[328]

6.11.5 1,4-α-MANNOBIOSE-GCDS (28)

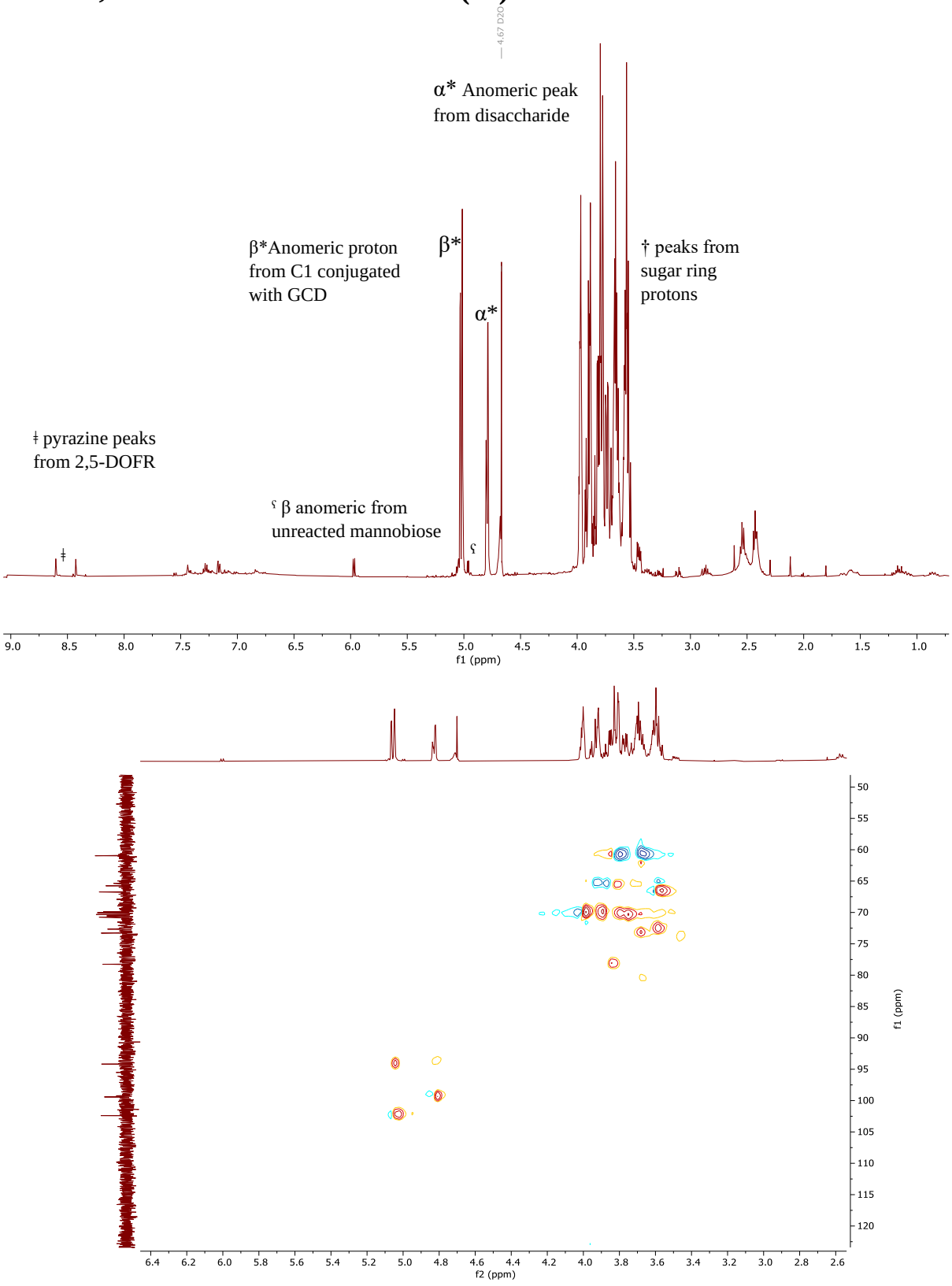

Figure S 22 ^{1}HNMR and HSQC in D_2O of GCDs functionalised with GCDs functionalised with mannobiose **28**

6.11.6 1,4-β-MANNOTRIOSE-GCDS (29)

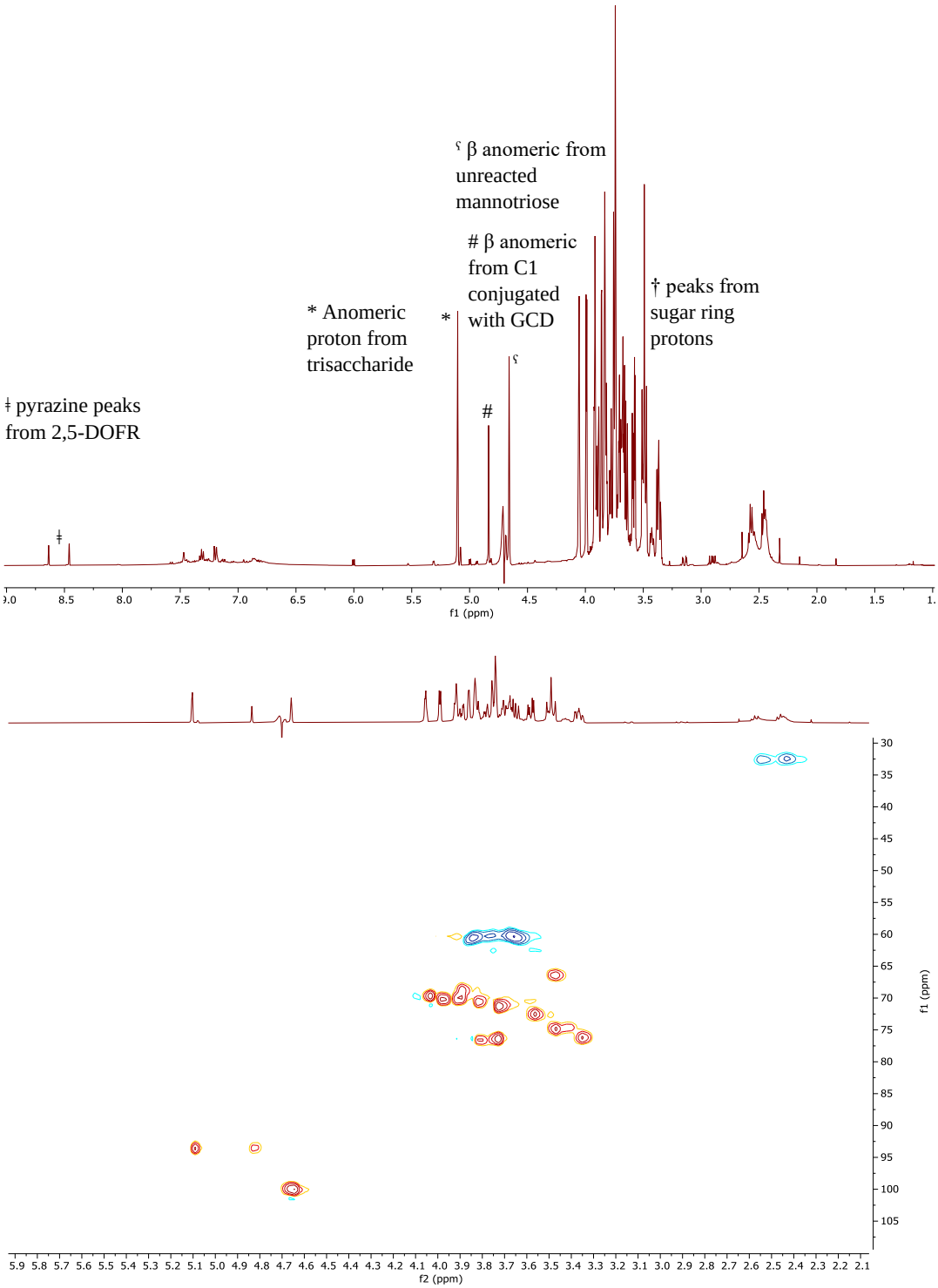

Figure S 23 ^{1}HNMR and HSQC in D_2O of GCDs functionalised with GCDs functionalised with 1,4 mannotriose **29**

6.11.7 1,3-α-1,4-α-MANNOTRIOSE-GCDS (30)

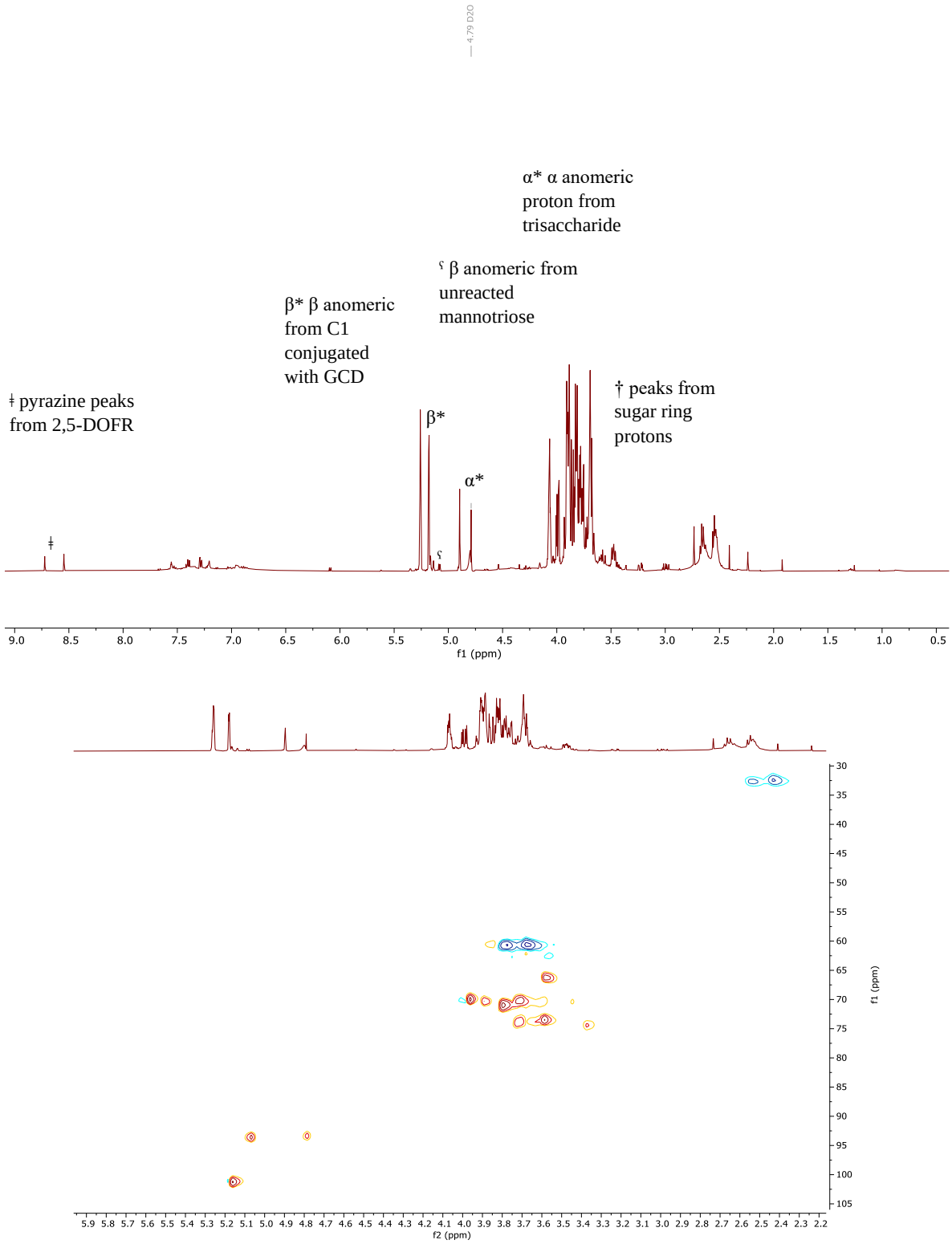

Figure S 24 ^{1}HNMR and HSQC in D_2O of GCDs functionalised with GCDs functionalised with 1,3 mannotriose **30**

6.11.8 – 1-(1,7-DIAMINOHEPTANE)-A/B-D-MANNOPYRANOSE (41)

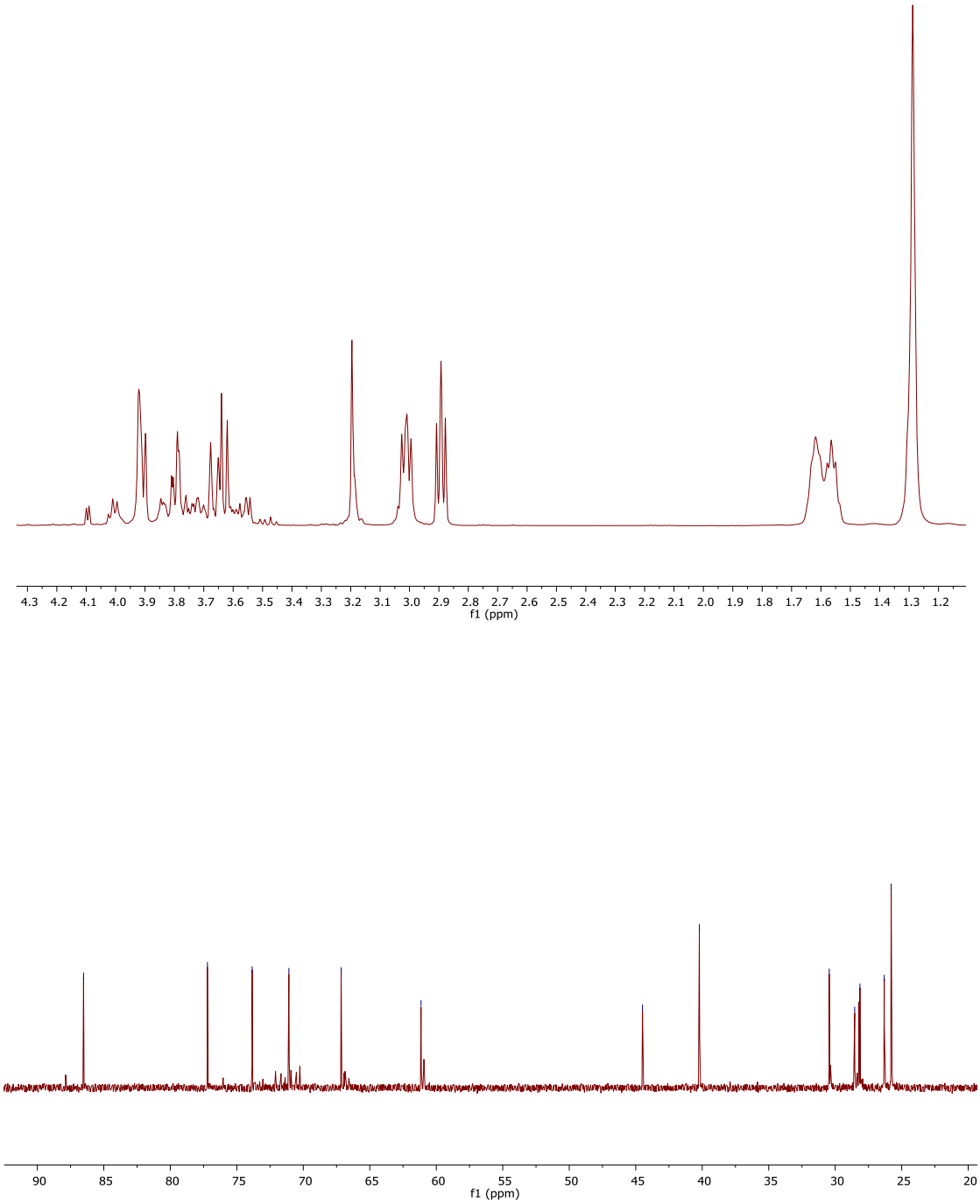

Figure S 25 ^{1}HNMR and ^{13}CNMR in $CDCl_3$ of seven carbon mannose ligand **41**

6.11.9 TTDDA LINKER (34)

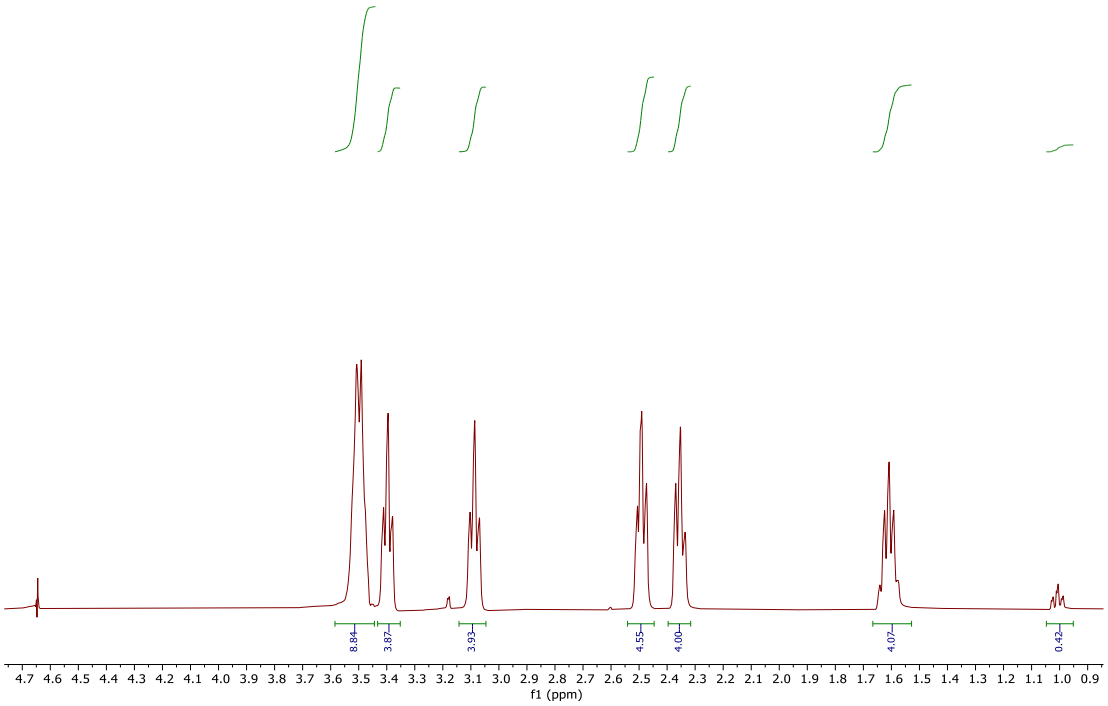

Figure S 26: ^{1}HNMR in D_2O spectrum of 4,20-dioxo-9,12,15-trioxa-5,19-diazatricosanedioic acid **34**

6.11.10 GCD-TTDDA LINKER (35)

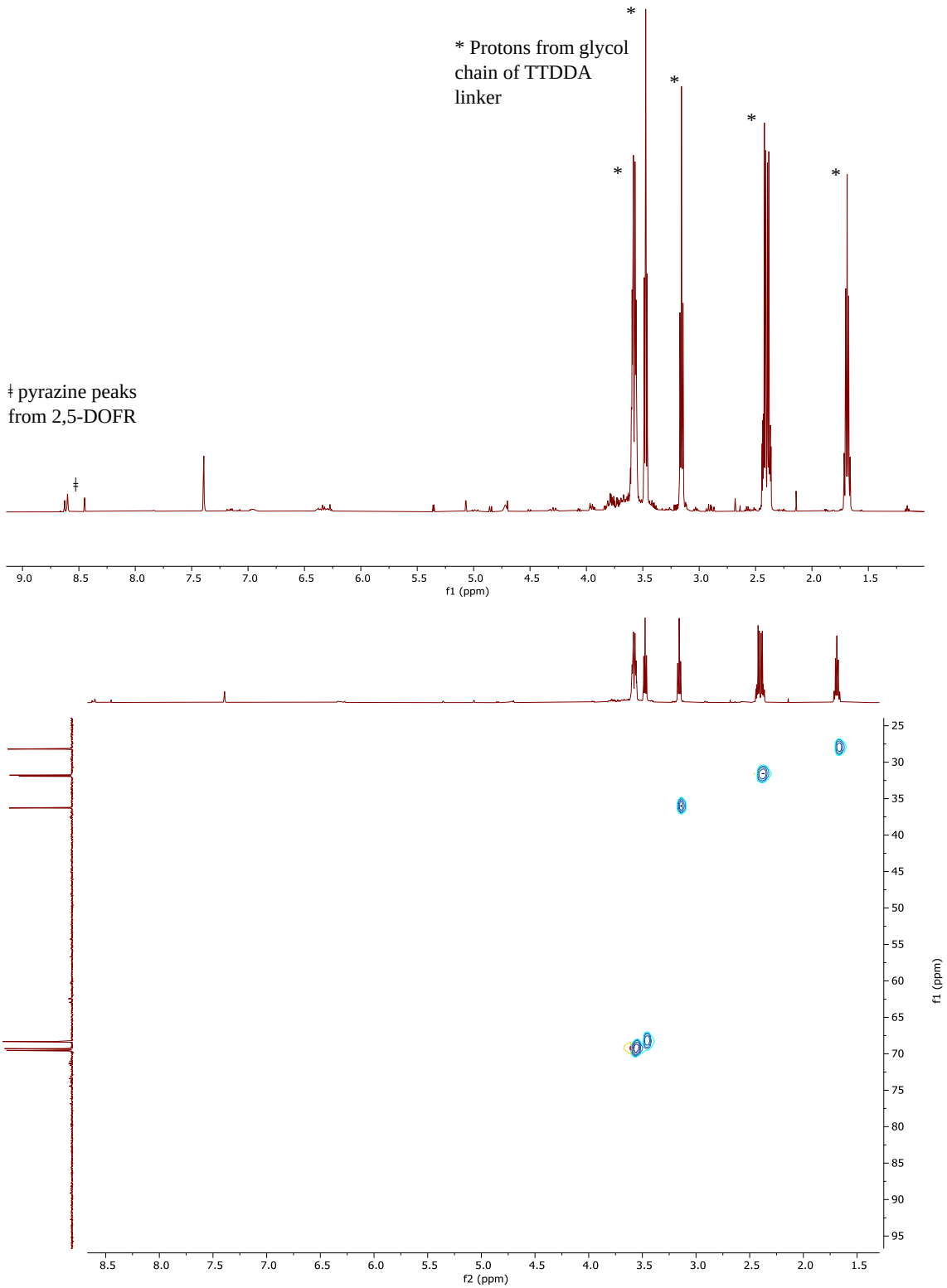

Figure S 27 ^{1}HNMR and HSQC in D_2O of GCDs functionalised with a TTDDA based linker **35**

6.11.11 GCD-TTDDA-MANNOSE (36)

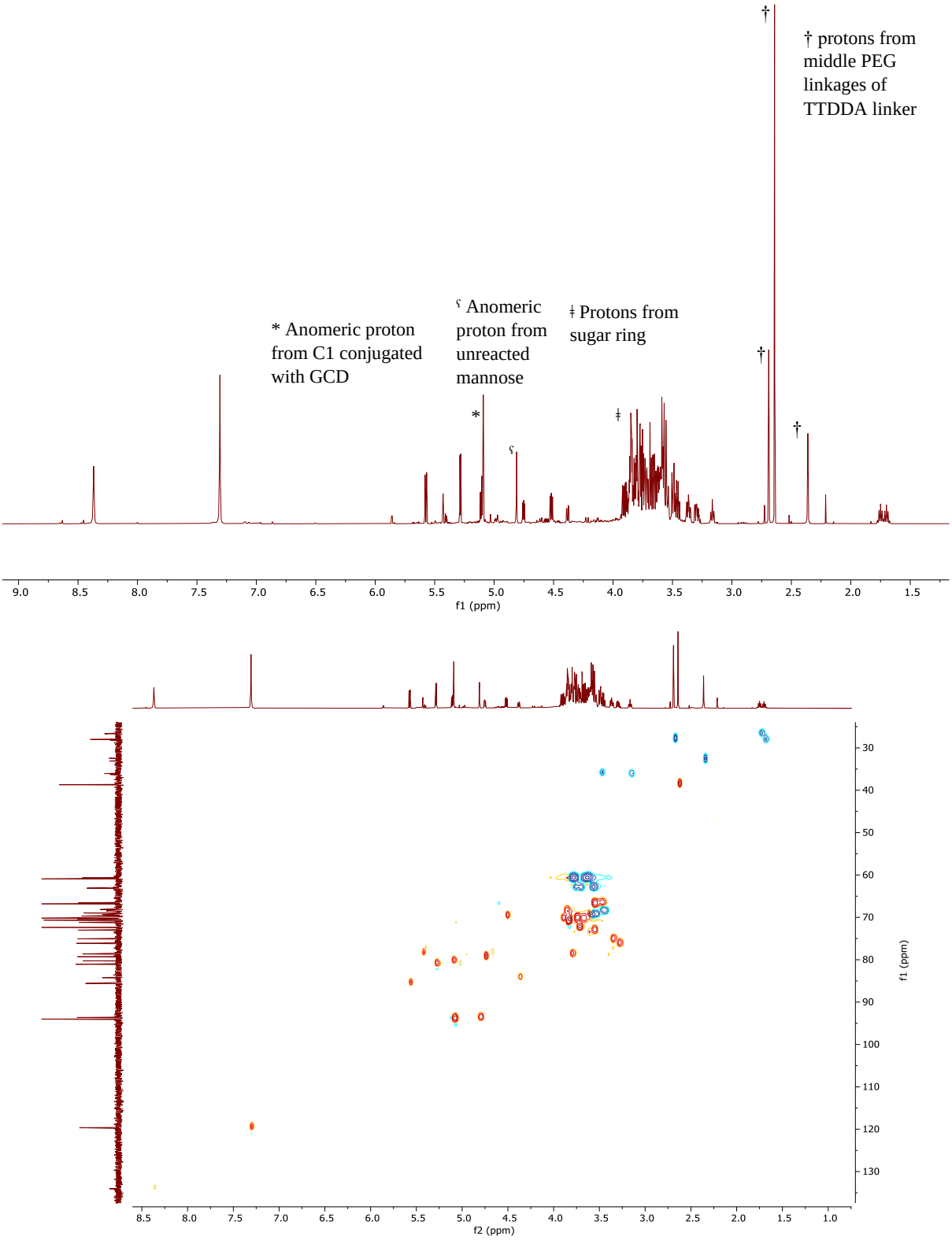

Figure S 28 ^{1}HNMR and HSQC in D_2O of TTDDA- GCDs functionalised with mannose **36**

6.11.12 TRIS{[2-(TERT-BUTOXYCARBONYL)ETHOXY]METHYL}METHYLAMINE (37)

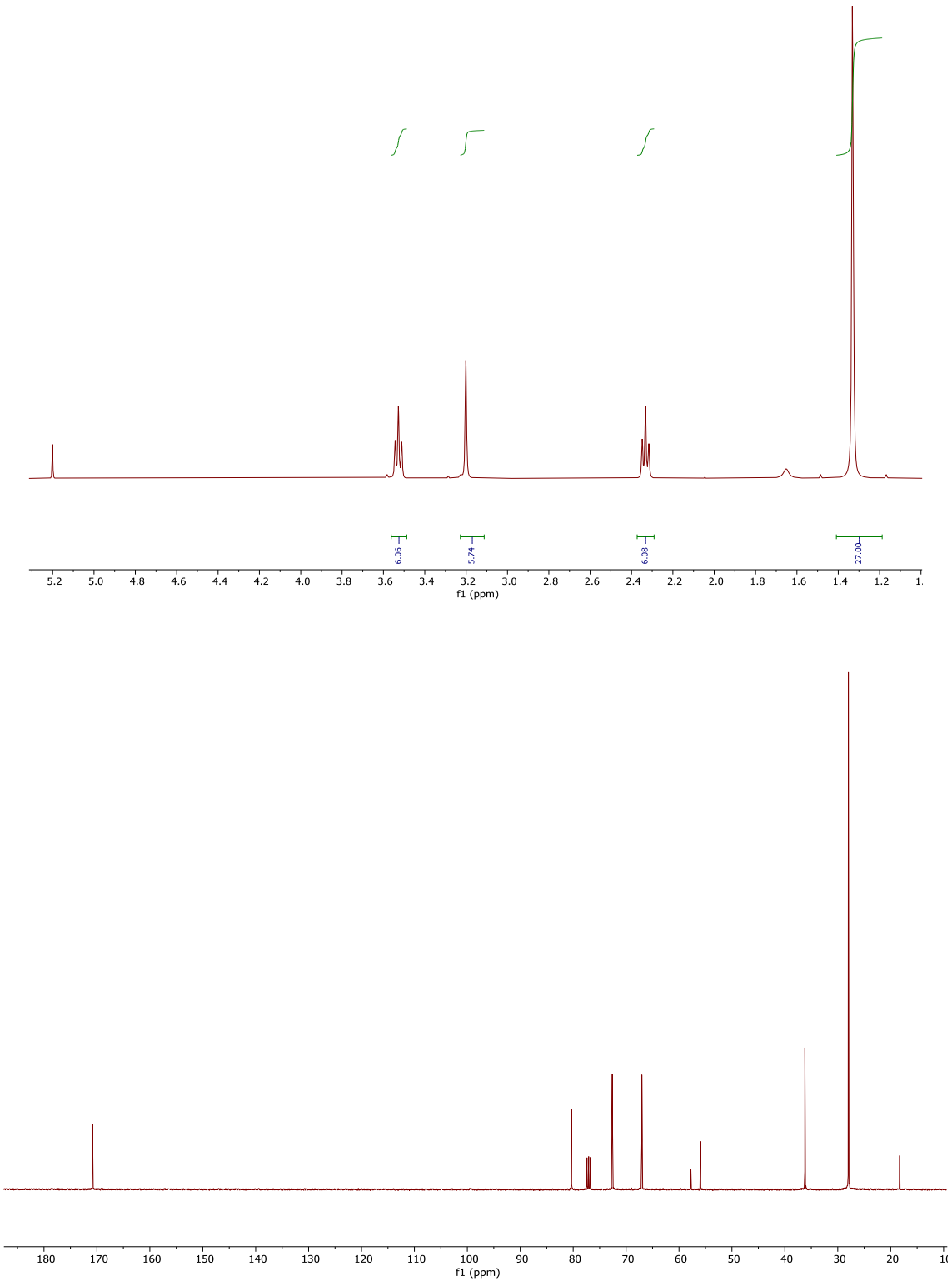

Figure S 29 ^{1}HNMR and ^{13}CNMR in $CDCl_3$ of Tris{[2-(tert-butoxycarbonyl)ethoxy]methyl}methylamine **37**

6.11.13 TRIS{[2-CARBOXYETHOXY]METHYL}METHYLAMINE (38)

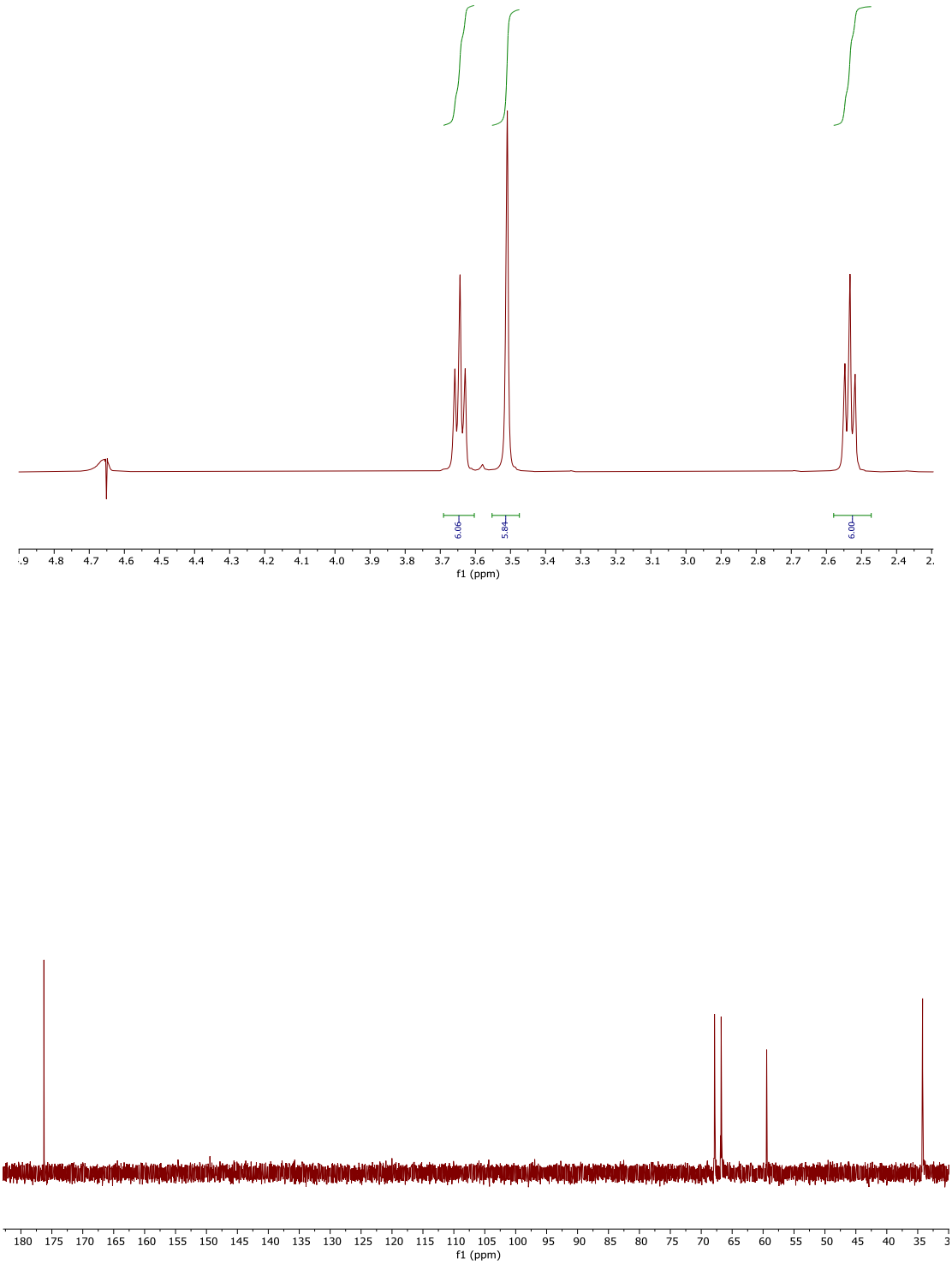

Figure S 30 ^{1}HNMR and ^{13}CNMR in D_2O of Tris{[2-carboxyethoxy]methyl}methylamine **38**

6.11.14 GCDS-DENDRIMER (39)

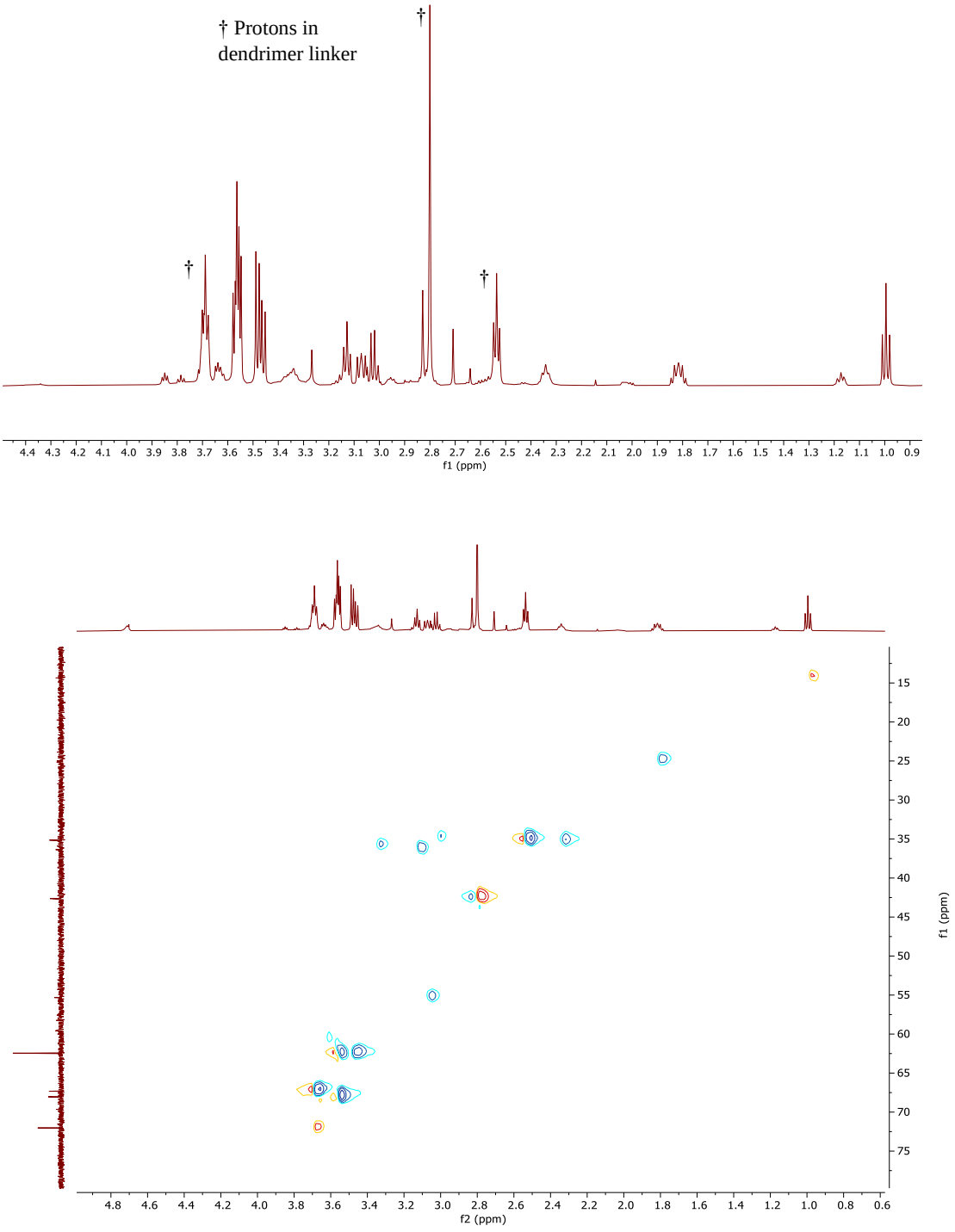

Figure S 31 ^{1}HNMR and HSQC in D_2O of GCDs functionalised with dendrimer **39**

6.11.15 GCD-DENDRIMER-MANNOSE (40)

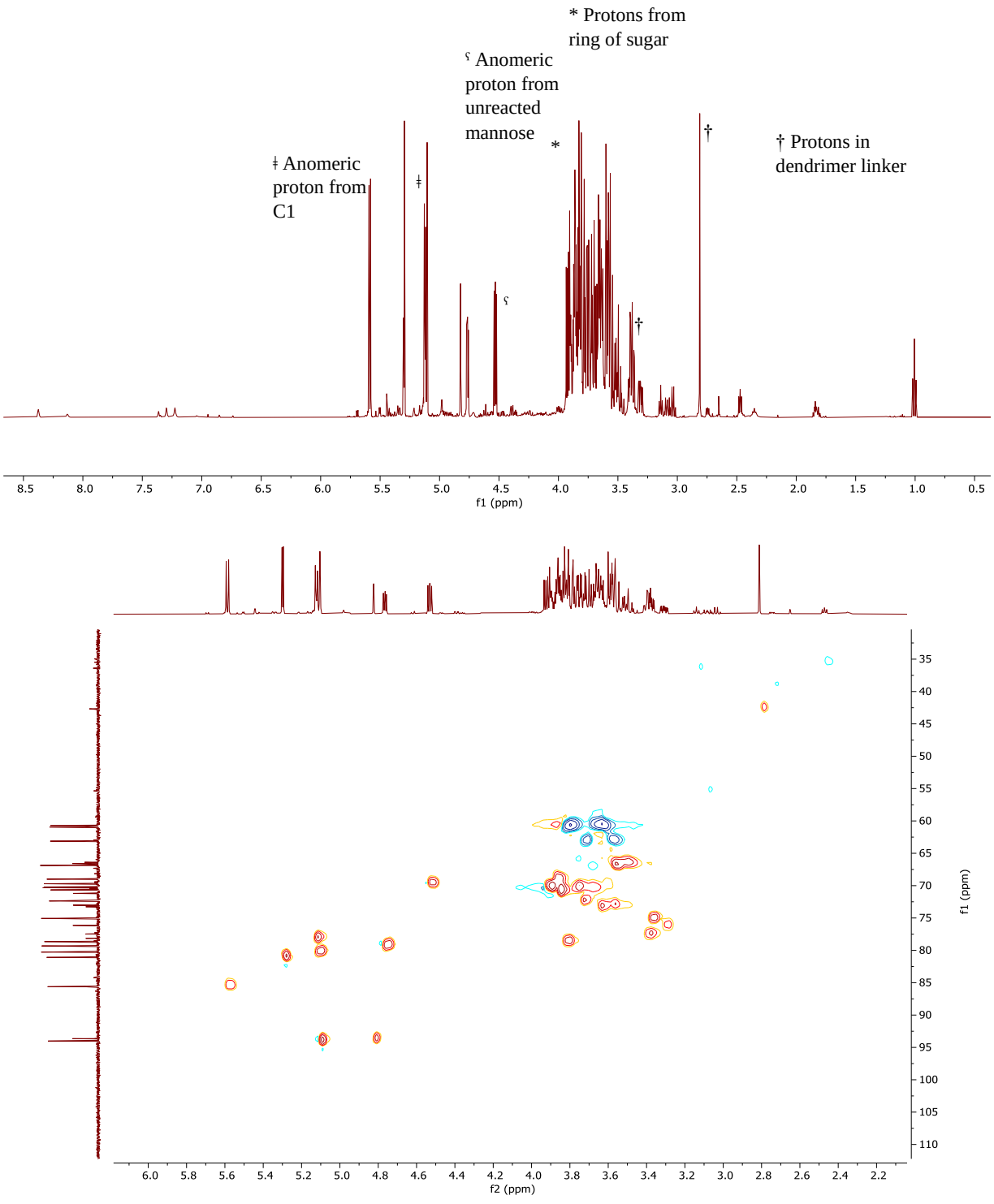

Figure S 32 ^{1}HNMR and HSQC in D_2O of dendrimer-GCDs functionalised with mannose **40**

6.11.16 (CD-10)-C7-MANNOSE (45)

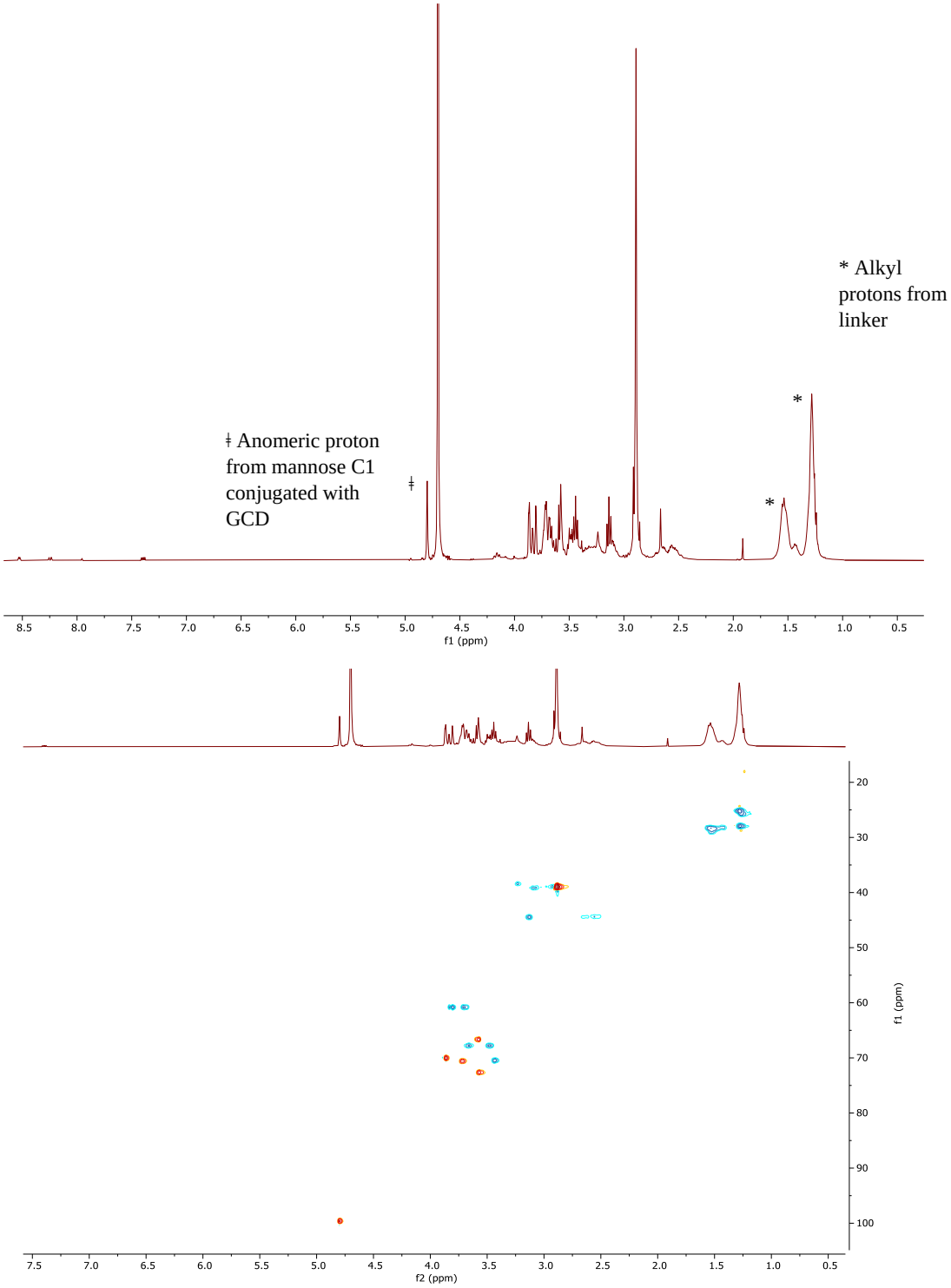

Figure S 33 ^{1}HNMR and HSQC in D_2O of **CD-10** functionalised with heptyl mannoside ligand, **45**. Synthesised and analysed by Francisco Javier Ramos Soriano[312]

6.11.16 (CD-10)-C7-GALACTOSE (46)

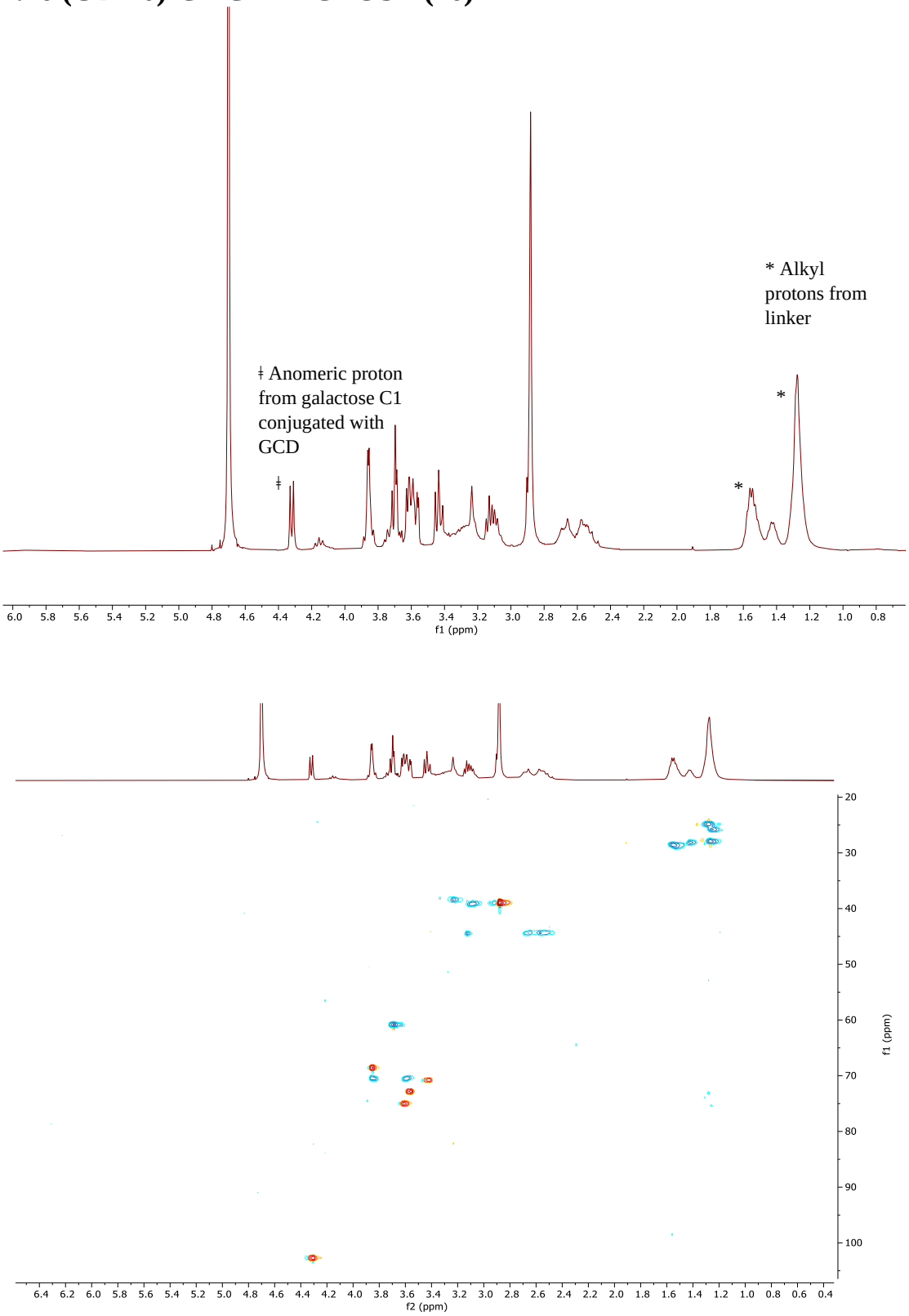

Figure S 34 ^{1}HNMR and HSQC in D_2O of **CD-10** functionalised with heptyl galactoside ligand, **46**. Synthesised and analysed by Francisco Javier Ramos Soriano[312]

6.11.17 (CD-10)-C3-MANNOSE (47)

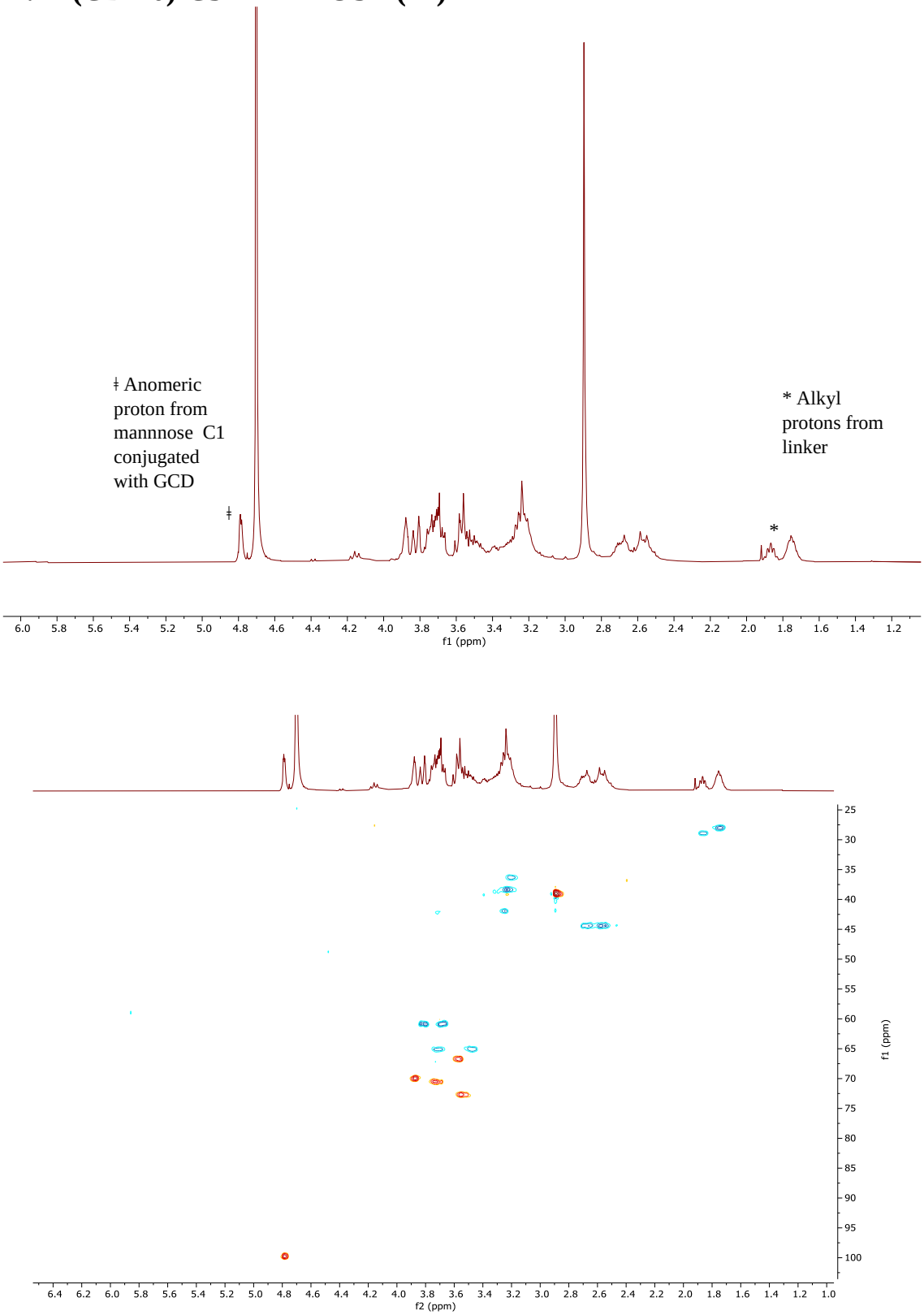

Figure S 35 ^{1}HNMR and HSQC in D_2O of **CD-10** functionalised with propyl mannoside ligand, **47**. Synthesised and analysed by Francisco Javier Ramos Soriano[312]

6.11.18 COMPARISON OF ^{1}HNMR SPECTRA OF GCDS AND PURIFIED GCDS

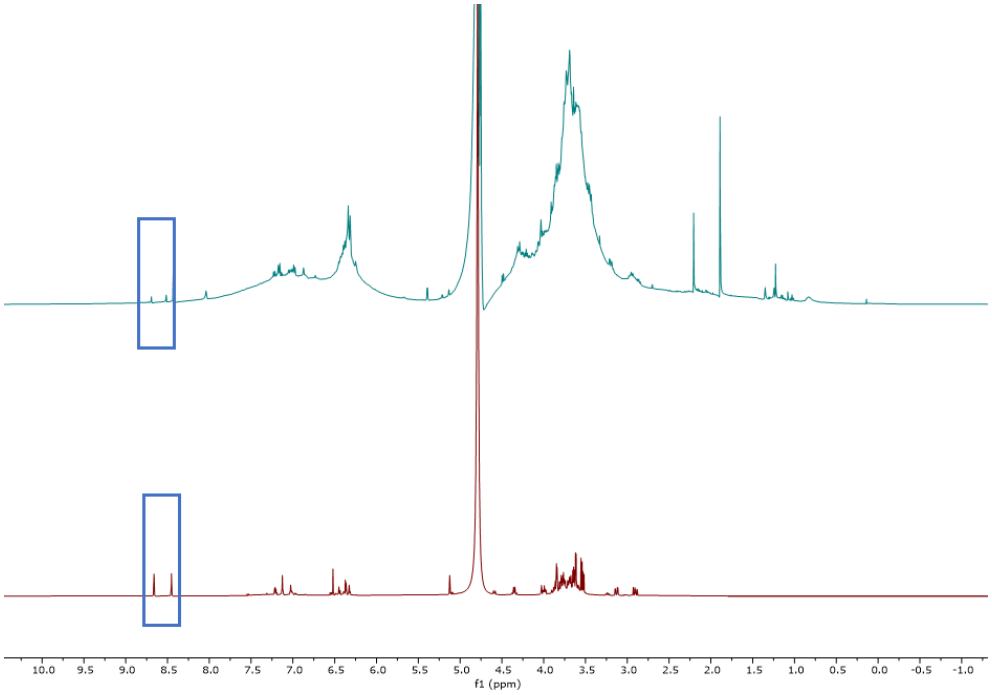

Figure S 36 Presat ^{1}HNMR of GCDs in D_2O (bottom red spectra) and GCDs purified by dialysis for 5 days (top green spectra). The two distinctive 2,5-DOFR peaks at ~ 8.5 ppm are highlighted by blue boxes

6.11.19 COMPARISON OF ^{1}NMR OF CD-4 PRE AND POST DIALYSIS

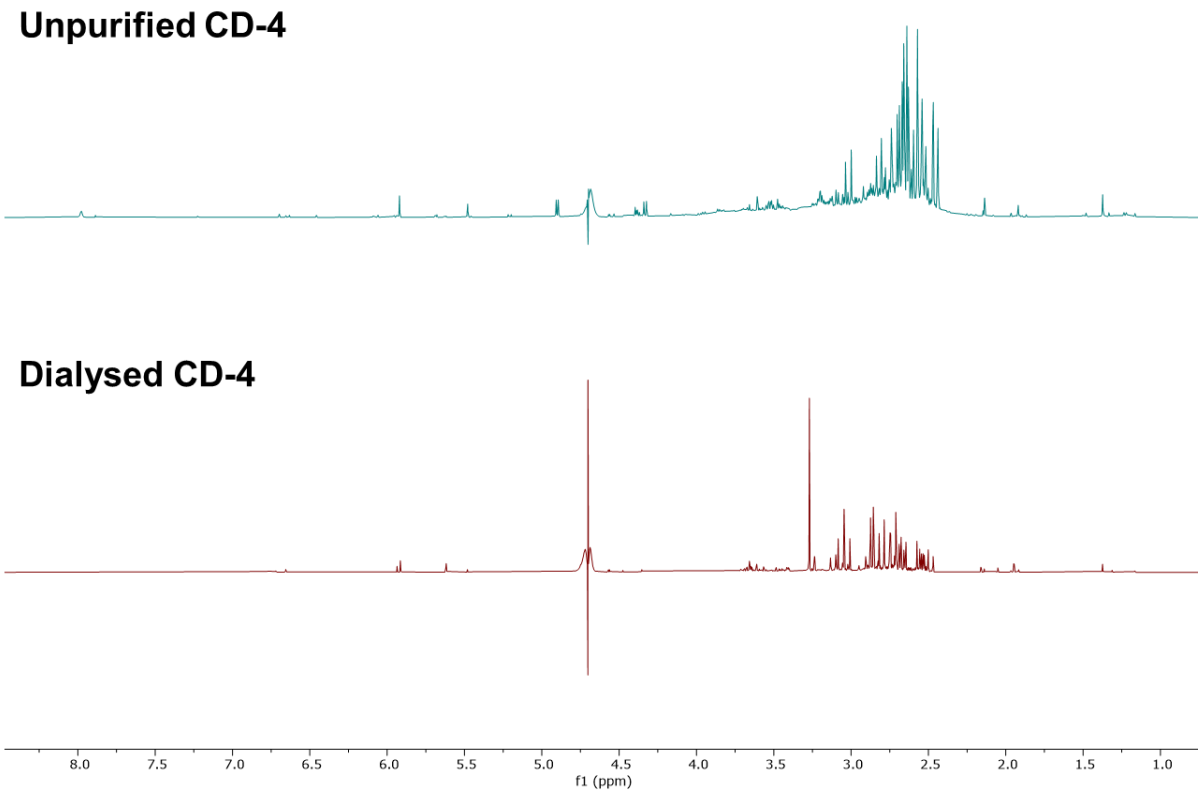

Figure S 37 ^{1}HNMR comparison of **CD-4** non-purified (top blue spectra) and after dialysis purification for 24 hours (bottom red spectra)

REFERENCES

1 C. Nathan and O. Cars, *N. Engl. J. Med.*, 2014, **371**, 1761–1763.

2 O. Cars, *Ups. J. Med. Sci.*, 2014, **119**, 209–214.

3 P. M. Hawkey, *BMJ*, 1998, **317**, 657–660.

4 C. L. Ventola, *P T a peer Rev. J. Formul. Manag.*, 2015, **40**, 277–83.

5 J. O'Neill, *Antimicrobial Resistance: Tackling a crisis for the health and wealth of nations*, 2014.

6 R. Coico, *Curr. Protoc. Microbiol.*, 2005, **00**, 3–4.

7 Z. Breijyeh, B. Jubeh and R. Karaman, *Molecules*, 2020, **25**, 1340–1348.

8 S. I. Miller, *MBio*, 2016, **7**, e01541-16.

9 L. Chiaradia, C. Lefebvre, J. Parra, J. Marcoux, O. Burlet-Schiltz, G. Etienne, M. Tropis and M. Daffé, *Sci. Rep.*, 2017, **7**, 12807.

10 H. C. Flemming and J. Wingender, *Nat. Rev. Microbiol.*, 2010, **8**, 623–633.

11 C. G. Roberts, *Am. J. Infect. Control*, 2013, **41**, S77–S80.

12 G. Ferreres, A. Bassegoda, J. Hoyo, J. Torrent-Burgués and T. Tzanov, *ACS Appl. Mater. Interfaces*, 2018, **10**, 40434–40442.

13 C. R. Lee, I. H. Cho, B. C. Jeong and S. H. Lee, *Int. J. Environ. Res. Public Health*, 2013, **10**, 4274–4305.

14 Z. Peng, D. Jin, H. B. Kim, C. W. Stratton, B. Wu, Y. W. Tang and X. Suna, *J. Clin. Microbiol.*, 2017, **55**, 1998–2008.

15 B. Aslam, W. Wang, M. I. Arshad, M. Khurshid, S. Muzammil, M. H. Rasool, M. A. Nisar, R. F. Alvi, M. A. Aslam, M. U. Qamar, M. K. F. Salamat and Z. Baloch, *Infect. Drug Resist.*, 2018, **11**, 1645–1658.

16 J. Davies, *Microbiologia*, 1996, **12**, 9–16.

17 L. J. V. Piddock, *Nat. Rev. Microbiol.*, 2006, **4**, 629–636.

18 C. Reading and M. Cole, *Antimicrob. Agents Chemother.*, 1977, **11**, 852–857.

19 P. J. Yeh, M. J. Hegreness, A. P. Aiden and R. Kishony, *Nat. Rev. Microbiol.*, 2009, **7**, 460–466.

20 C. T. Bergstrom, M. Lo and M. Lipsitch, *Proc. Natl. Acad. Sci. U. S. A.*, 2004, **101**, 13285–13290.

21 C. Ghosh, P. Sarkar, R. Issa and J. Haldar, *Trends Microbiol.*, 2019, **27**, 323–338.

22 C. Bebbington and G. Yarranton, *Curr. Opin. Biotechnol.*, 2008, **19**, 613–619.

23 C. Saylor, E. Dadachova and A. Casadevall, *Vaccine*, 2009, **27**, G38–G46.

24 E. Isolauri, *Am. J. Clin. Nutr.*, 2001, **73**, 1142S-1146S.

25 E. Isolauri, P. V. Kirjavainen and S. Salminen, *Gut*, 2002, **50**, iii54–iii59.

26 B. B. Lewis and E. G. Pamer, *Annu. Rev. Microbiol.*, 2017, **71**, 157–178.

27 J. M. T. Hamilton-Miller, *Int. J. Antimicrob. Agents*, 2003, **22**, 360–366.

28 A. G. Coffey, C. Daly and G. Fitzgerald, *Biotechnol. Adv.*, 1994, **12**, 625–633.

29 F. Driehuis, J. M. Wilkinson, Y. Jiang, I. Ogunade and A. T. Adesogan, *J. Dairy Sci.*, 2018, **101**, 4093–4110.

30 E. Tait, J. D. Perry, S. P. Stanforth and J. R. Dean, *TrAC - Trends Anal. Chem.*, 2014, **53**, 117–125.

31 J. D. Perry, *Clin. Microbiol. Rev.*, 2017, **30**, 449–479.

32 G. Funke and P. Funke-Kissling, *J. Clin. Microbiol.*, 2004, **42**, 4067–4071.

33 C. M. O'Hara, *Clin. Microbiol. Rev.*, 2005, **18**, 147–162.

34 P. Dixon, P. Davies, W. Hollingworth, M. Stoddart and A. MacGowan, *Eur. J. Clin. Microbiol. Infect. Dis.*, 2015, **34**, 863–876.

35 S. Angeletti, *J. Microbiol. Methods*, 2017, **138**, 20–29.

36 T. Y. Hou, C. Chiang-Ni and S. H. Teng, *J. Food Drug Anal.*, 2019, **27**, 404–414.

37 L. Ferreira, F. Sánchez-Juanes, M. González-Ávila, D. Cembrero-Fuciños, A. Herrero-Hernández, J. M. González-Buitrago and J. L. Muñoz-Bellido, *J. Clin. Microbiol.*, 2010, **48**, 2110–2115.

38 G. M. Pupo, R. Lan and P. R. Reeves, *Proc. Natl. Acad. Sci. U. S. A.*, 2000, **97**, 10567–10572.

39 L. Luo, W. Liu, B. Li, M. Li, D. Huang, L. Jing, H. Chen, J. Yang, J. Yue, F. Wang, H. Chu and Z. Zhang, *J. Clin. Microbiol.*, 2016, **54**, 2982–2989.

40 J. Rychert, *J. Infect.*, 2019, **2**, 1–5.

41 T. Mcmillen, Y. Tang, B. A. Brown-elliott, E. Iakhiaeva, R. Vasireddy and S. Vasireddy, *J. Clin. Microbiol.*, 2018, **56**, e00237-18.

42 N. Bhardwaj, S. K. Bhardwaj, M. K. Nayak, J. Mehta, K. H. Kim and A. Deep, *TrAC - Trends Anal. Chem.*, 2017, **97**, 120–135.

43 S. A. Barghouthi, *Indian J. Microbiol.*, 2011, **51**, 430–444.

44 A. Shahzad, G. Köhler, M. Knapp, E. Gaubitzer, M. Puchinger and M. Edetsberger, *J. Transl. Med.*, 2009, **7**, 99.

45 E. Engvall, *Med. Biol.*, 1977, **55**, 193–200.

46 H. E. Giana, L. Silveira, R. A. Zângaro and M. T. T. Pacheco, *J. Fluoresc.*, 2003, **13**, 489–493.

47 C. C. Lin, Y. C. Yeh, C. Y. Yang, C. L. Chen, G. F. Chen, C. C. Chen and Y. C. Wu, *J. Am. Chem. Soc.*, 2002, **124**, 3508–3509.

48 F. Lin, Y.-W. Bao and F.-G. Wu, *C*, 2019, **5**, 33–51.

49 K. Chitra and G. Annadurai, *J. Nanotechnol.*, 2013, **2013**, 1–7.

50 T. K. Mandal and N. Parvin, *J. Biomed. Nanotechnol.*, 2011, **7**, 846–848.

51 A. K. Sahoo, S. Sharma, A. Chattopadhyay and S. S. Ghosh, *Nanoscale*, 2012, **4**, 1688–1694.

52 S. Suherman, N. Audio Haryanto, E. Tri Wahyuni, M. Ilmi, K. Morita and Y. Oki, *Orient. J. Chem.*, 2019, **35**, 49–55.

53 S. Chandra, T. K. Mahto, A. R. Chowdhuri, B. Das and S. kumar Sahu, *Sensors Actuators, B*

Chem., 2017, **245**, 835–844.

54 J. Gao, D. Liu and Z. Wang, *Anal. Chem.*, 2010, **82**, 9240–9247.

55 N. Sharon and I. Ofek, *Crit. Rev. Food Sci. Nutr.*, 2002, **42**, 267–272.

56 B. K. Brandley and R. L. Schnaar, *J. Leukoc. Biol.*, 1986, **40**, 97–111.

57 S. Park, M. R. Lee and I. Shin, *Chem. Commun.*, 2008, **37**, 4389–4399.

58 T. R. Patel, T. M. D. Besong, M. Meier, K. McEleney, S. E. Harding, D. J. Winzor and J. Stetefeld, *Eur. Biophys. J.*, 2018, **47**, 751–759.

59 N. Sharon and I. Ofek, *Glycoconj. J.*, 2000, **17**, 659–664.

60 Y. C. Lee and R. T. Lee, *Acc. Chem. Res.*, 1995, **28**, 321–327.

61 F. S. Coulibaly and B. B. C. Youan, *Biosens. Bioelectron.*, 2014, **59**, 404–411.

62 L. Wang, G. Fang, L. Li and D. Cao, *Sensors Actuators, B Chem.*, 2016, **229**, 47–56.

63 J. Matsumoto, T. Shiragami, K. Hirakawa and M. Yasuda, *Int. J. Photoenergy*, 2015, **2015**, ID 148964.

64 T. M. Hooton and W. E. Stamm, *Infect. Dis. Clin. North Am.*, 1997, **11**, 551–581.

65 A. Ronald, *Disease-a-Month*, 2003, **49**, 71–82.

66 L. K. Mydock-McGrane, T. J. Hannan and J. W. Janetka, *Expert Opin. Drug Discov.*, 2017, **12**, 711–731.

67 J. Bouckaert, J. Berglund, M. Schembri, E. De Genst, L. Cools, M. Wuhrer, C. S. Hung, J. Pinkner, R. Slättegård, A. Zavialov, D. Choudhury, S. Langermann, S. J. Hultgren, L. Wyns, P. Klemm, S. Oscarson, S. D. Knight and H. De Greve, *Mol. Microbiol.*, 2005, **55**, 441–455.

68 G. Waksman and S. J. Hultgren, *Nat. Rev. Microbiol.*, 2009, **7**, 765–774.

69 A. Wellens, C. Garofalo, H. Nguyen, N. Van Gerven, R. Slättegard, J. P. Hernalsteens, L. Wyns, S. Oscarson, H. De Greve, S. Hultgren and J. Bouckaert, *PLoS One*, 2008, **3**, e-2040.

70 I. Ofek, D. Mirelman and N. Sharon, *Nature*, 1977, **265**, 623–625.

71 N. Firon, S. Ashkenazi, D. Mirelman, I. Ofek and N. Sharon, *Infect. Immun.*, 1987, **55**, 472–476.

72 J. R. Neeser, B. Koellreutter and P. Wuersch, *Infect. Immun.*, 1986, **52**, 428–436.

73 N. Firon, I. Ofek and N. Sharon, *Carbohydr. Res.*, 1983, **120**, 235–249.

74 N. Firon, I. Ofek and N. Sharon, *Biochem. Biophys. Res. Commun.*, 1982, **105**, 1426–1432.

75 C. S. Hung, J. Bouckaert, D. Hung, J. Pinkner, C. Widberg, A. DeFusco, C. G. Auguste, R. Strouse, S. Langermann, G. Waksman and S. J. Hultgren, *Mol. Microbiol.*, 2002, **44**, 903–915.

76 A. Wellens, M. Lahmann, M. Touaibia, J. Vaucher, S. Oscarson, R. Roy, H. Remaut and J. Bouckaert, *Biochemistry*, 2012, **51**, 4790–4799.

77 G. Roos, A. Wellens, M. Touaibia, N. Yamakawa, P. Geerlings, R. Roy, L. Wyns and J. Bouckaert, *ACS Med. Chem. Lett.*, 2013, **4**, 1085–1090.

78 Z. Han, J. S. Pinkner, B. Ford, R. Obermann, W. Nolan, S. A. Wildman, D. Hobbs, T. Ellenberger, C. K. Cusumano, S. J. Hultgren and J. W. Janetka, *J. Med. Chem.*, 2010, **53**, 4779–4792.

79 Yeeman K. Ramtohul, S. K. Da, Sc. Cadilhac, T. J. Reddy, L. Vaillancourt, M. Gallant, B. Liu, E. Dietrich, F. VALLEE, J. MARTEL and C. Poisson, 2013, WO/2013/134415.

80 L. Mydock-McGrane, Z. Cusumano, Z. Han, J. Binkley, M. Kostakioti, T. Hannan, J. S. Pinkner, R. Klein, V. Kalas, J. Crowley, N. P. Rath, S. J. Hultgren and J. W. Janetka, *J. Med. Chem.*, 2016, **59**, 9390–9408.

81 D. Alvarez Dorta, A. Sivignon, T. Chalopin, T. I. Dumych, G. Roos, R. O. Bilyy, D. Deniaud, E. M. Krammer, J. De Ruyck, M. F. Lensink, J. Bouckaert, N. Barnich and S. G. Gouin, *ChemBioChem*, 2016, **17**, 936–952.

82 X. Jiang, D. Abgottspon, S. Kleeb, S. Rabbani, M. Scharenberg, M. Wittwer, M. Haug, O. Schwardt and B. Ernst, *J. Med. Chem.*, 2012, **55**, 4700–4713.

83 S. G. Gouin, A. Wellens, J. Bouckaert and J. Kovensky, *ChemMedChem*, 2009, **4**, 749–755.

84 M. Almant, V. Moreau, J. Kovensky, J. Bouckaert and S. G. Gouin, *Chem. - A Eur. J.*, 2011, **17**, 10029–10038.

85 A. Sivignon, X. Yan, D. A. Dorta, R. Bonnet, J. Bouckaert, E. Fleury, J. Bernard, S. G. Gouin, A. Darfeuille-Michaud and N. Barnich, *MBio*, 2015, **6**, e01298-15.

86 P. Bojarová, R. R. Rosencrantz, L. Elling and V. Křen, *Chem. Soc. Rev.*, 2013, **42**, 4774–4797.

87 F. Compostella, O. Pitirollo, A. Silvestri and L. Polito, *Beilstein J. Org. Chem.*, 2017, **13**, 1008–1021.

88 L. T. Mai Hoa, T. T. Dung, T. M. Danh, N. H. Duc and D. M. Chien, *J. Phys. Conf. Ser.*, 2009, **187**, 012048.

89 M. Erdem, S. Yalcin and U. Gunduz, *Hum. Exp. Toxicol.*, 2017, **36**, 833–845.

90 V. Tsyalkovsky, R. Burtovyy, V. Klep, R. Lupitskyy, M. Motornov, S. Minko and I. Luzinov, *Langmuir*, 2010, **26**, 10684–10692.

91 J. A. Zamora-Justo, P. Abrica-González, G. R. Vázquez-Martínez, A. Muñoz-Diosdado, J. A. Balderas-López and M. Ibáñez-Hernández, *J. Nanomater.*, 2019, **2019**, 5982047.

92 A. M. Smith and S. Nie, *Analyst*, 2004, **129**, 672–677.

93 D. Sumanth Kumar, B. Jai Kumar and H. M. Mahesh, in *Synthesis of Inorganic Nanomaterials*, 2018, pp. 59–88.

94 K. P. Burris and C. N. Stewart, *Trends Food Sci. Technol.*, 2012, **28**, 143–152.

95 Y. Guo, I. Nehlmeier, E. Poole, C. Sakonsinsiri, N. Hondow, A. Brown, Q. Li, S. Li, J. Whitworth, Z. Li, A. Yu, R. Brydson, W. B. Turnbull, S. Pöhlmann and D. Zhou, *J. Am. Chem. Soc.*, 2017, **139**, 11833–11844.

96 D. Benito-Alifonso, S. Tremel, B. Hou, H. Lockyear, J. Mantell, D. J. Fermin, P. Verkade, M. Berry and M. C. Galan, *Angew. Chemie - Int. Ed.*, 2014, **53**, 810–814.

97 H. Yang, X. Jie, L. Wang, Y. Zhang, M. Wang and W. Wei, *Microchim. Acta*, 2018, **185**, 512.

98 A. M. Derfus, W. C. W. Chan and S. N. Bhatia, *Nano Lett.*, 2004, **4**, 11–18.

99 D. Ioannou and D. K. Griffin, *Nano Rev.*, 2010, **1**, 5117.

100 X. Xu, R. Ray, Y. Gu, H. J. Ploehn, L. Gearheart, K. Raker and W. A. Scrivens, *J. Am. Chem. Soc.*, 2004, **126**, 12736–12737.

101 Y. P. Sun, B. Zhou, Y. Lin, W. Wang, K. A. S. Fernando, P. Pathak, M. J. Meziani, B. A. Harruff, X. Wang, H. Wang, P. G. Luo, H. Yang, M. E. Kose, B. Chen, L. M. Veca and S. Y.

Xie, *J. Am. Chem. Soc.*, 2006, **128**, 7756–7757.

102 H. Liu, T. Ye and C. Mao, *Angew. Chemie - Int. Ed.*, 2007, **46**, 6473–6475.

103 Y. Qin, Y. Cheng, L. Jiang, X. Jin, M. Li, X. Luo, G. Liao, T. Wei and Q. Li, *ACS Sustain. Chem. Eng.*, 2015, **3**, 637–644.

104 Z. A. Qiao, Y. Wang, Y. Gao, H. Li, T. Dai, Y. Liu and Q. Huo, *Chem. Commun.*, 2010, **46**, 8812–8814.

105 X. Wang, Y. Feng, P. Dong and J. Huang, *Front. Chem.*, 2019, **7**, 671.

106 L. Li and T. Dong, *J. Mater. Chem. C*, 2018, **6**, 7944–7970.

107 J. Jiang, Y. He, S. Li and H. Cui, *Chem. Commun.*, 2012, **48**, 9634.

108 Q. Tang, W. Zhu, B. He and P. Yang, *ACS Nano*, 2017, **11**, 1540–1547.

109 S. Qu, X. Wang, Q. Lu, X. Liu and L. Wang, *Angew. Chemie - Int. Ed.*, 2012, **51**, 12215–12218.

110 A. Sciortino, A. Cannizzo and F. Messina, *C*, 2018, **4**, 67–102.

111 Y. Yang, D. Wu, S. Han, P. Hu and R. Liu, *Chem. Commun.*, 2013, **49**, 4920–4922.

112 B. Zhang, C. Y. Liu and Y. Liu, *Eur. J. Inorg. Chem.*, 2010, 4411–4414.

113 J. Zhu, X. Bai, J. Bai, G. Pan, Y. Zhu, Y. Zhai, H. Shao, X. Chen, B. Dong, H. Zhang and H. Song, *Nanotechnology*, , DOI:10.1088/1361-6528/aaa321.

114 S. Zhu, Q. Meng, L. Wang, J. Zhang, Y. Song, H. Jin, K. Zhang, H. Sun, H. Wang and B. Yang, *Angew. Chemie - Int. Ed.*, 2013, **52**, 3953–3957.

115 D. M. A. Crista, J. C. G. E. da Silva and L. P. da Silva, *Nanomaterials*, 2020, **10**, 1–15.

116 R. Ludmerczki, S. Mura, C. M. Carbonaro, I. M. Mandity, M. Carraro, N. Senes, S. Garroni, G. Granozzi, L. Calvillo, S. Marras, L. Malfatti and P. Innocenzi, *Chem. - A Eur. J.*, 2019, **25**, 11963–11974.

117 F. Wang, Z. Xie, H. Zhang, C. Y. Liu and Y. G. Zhang, *Adv. Funct. Mater.*, 2011, **21**, 1027–1031.

118 A. M. Schwenke, S. Hoeppener and U. S. Schubert, *Adv. Mater.*, 2015, **27**, 4113–4141.

119 M. L. Liu, B. Bin Chen, C. M. Li and C. Z. Huang, *Green Chem.*, 2019, **21**, 449–471.

120 H. Zhu, X. Wang, Y. Li, Z. Wang, F. Yang and X. Yang, *Chem. Commun.*, 2009, **34**, 5118–5120.

121 T. V. De Medeiros, J. Manioudakis, F. Noun, J. R. Macairan, F. Victoria and R. Naccache, *J. Mater. Chem. C*, 2019, **7**, 7175–7195.

122 Q. Hu, X. Gong, L. Liu and M. M. F. Choi, *J. Nanomater.*, 2017, **2017**, ID 1804178.

123 C. Y. Chen, Y. H. Tsai and C. W. Chang, *New J. Chem.*, 2019, **43**, 6153–6159.

124 H. Ding, X. H. Li, X. B. Chen, J. S. Wei, X. B. Li and H. M. Xiong, *J. Appl. Phys.*, 2020, **127**, 1101.

125 L. Shi, J. H. Yang, H. B. Zeng, Y. M. Chen, S. C. Yang, C. Wu, H. Zeng, O. Yoshihito and Q. Zhang, *Nanoscale*, 2016, **8**, 14374–14378.

126 J. B. Essner, J. A. Kist, L. Polo-parada and G. A. Baker, *Chem. Mater.*, 2018, **30**, 1878–1887.

127 G. Zuo, A. Xie, J. Li, T. Su, X. Pan and W. Dong, *J. Phys. Chem. C*, 2017, **121**, 26558–26565.

128 X. Miao, D. Qu, D. Yang, B. Nie, Y. Zhao, H. Fan and Z. Sun, *Adv. Mater.*, 2018, **30**, 1704740.

129 Y. Yang, J. Cui, M. Zheng, C. Hu, S. Tan, Y. Xiao, Q. Yang and Y. Liu, *Chem. Commun.*, 2012, **48**, 380–382.

130 S. Chandra, P. Patra, S. H. Pathan, S. Roy, S. Mitra, A. Layek, R. Bhar, P. Pramanik and A. Goswami, *J. Mater. Chem. B*, 2013, **1**, 2375–2382.

131 A. Ananthanarayanan, Y. Wang, P. Routh, M. A. Sk, A. Than, M. Lin, J. Zhang, J. Chen, H. Sun and P. Chen, *Nanoscale*, 2015, **7**, 8159–8165.

132 J. Manioudakis, F. Victoria, C. A. Thompson, L. Brown, M. Movsum, R. Lucifero and R. Naccache, *J. Mater. Chem. C*, 2019, **7**, 853–862.

133 S. Bhattacharyya, F. Ehrat, P. Urban, R. Teves, R. Wyrwich, M. Döblinger, J. Feldmann, A. S. Urban and J. K. Stolarczyk, *Nat. Commun.*, 2017, **8**, 1401.

134 W. Yang, H. Zhang, J. Lai, X. Peng, Y. Hu, W. Gu and L. Ye, *Carbon N. Y.*, 2018, **128**, 78–85.

135 A. C. Croce and G. Bottiroli, *Eur. J. Histochem.*, 2014, **58**, 320–337.

136 X. Zhu, H. Jin, C. Gao, R. Gui and Z. Wang, *Talanta*, 2017, **162**, 65–71.

137 H. Li, Y. Zhang, L. Wang, J. Tian and X. Sun, *Chem. Commun.*, 2011, **47**, 961–963.

138 F. Yan, Y. Jiang, X. Sun, Z. Bai, Y. Zhang and X. Zhou, *Microchim. Acta*, 2018, **185**, 1–34.

139 M. X. Gao, L. Yang, Y. Zheng, X. X. Yang, H. Y. Zou, J. Han, Z. X. Liu, Y. F. Li and C. Z. Huang, *Chem. - A Eur. J.*, 2017, **23**, 2171–2178.

140 S. Li, Z. Guo, R. Feng, Y. Zhang, W. Xue and Z. Liu, *RSC Adv.*, 2017, **7**, 4975–4982.

141 S. A. Hill, D. Benito-Alifonso, S. A. Davis, D. J. Morgan, M. Berry and M. C. Galan, *Sci. Rep.*, 2018, **8**, 12234.

142 R. Yang, X. Guo, L. Jia and Y. Zhang, *Microchim. Acta*, 2017, **184**, 1143–1150.

143 L. Chai, J. Zhou, H. Feng, C. Tang, Y. Huang and Z. Qian, *ACS Appl. Mater. Interfaces*, 2015, **7**, 23564–23574.

144 R. Wang, Y. Xu, T. Zhang and Y. Jiang, *Anal. Methods*, 2015, **7**, 1701–1706.

145 D. Zhong, Y. Zhuo, Y. Feng and X. Yang, *Biosens. Bioelectron.*, 2015, **74**, 546–553.

146 X. Lu, Z. Zhang, Q. Xia, M. Hou, C. Yan, Z. Chen, Y. Xu and R. Liu, *Mater. Sci. Eng. C*, 2018, **82**, 190–196.

147 T. A. Swift, D. Fagan, D. Benito-Alifonso, S. A. Hill, M. L. Yallop, T. A. A. Oliver, T. Lawson, M. C. Galan and H. M. Whitney, *New Phytol.*, 2021, **229**, 783–790.

148 C. I. Weng, H. T. Chang, C. H. Lin, Y. W. Shen, B. Unnikrishnan, Y. J. Li and C. C. Huang, *Biosens. Bioelectron.*, 2015, **68**, 1–6.

149 I. P. J. Lai, S. G. Harroun, S. Y. Chen, B. Unnikrishnan, Y. J. Li and C. C. Huang, *Sensors Actuators, B Chem.*, 2016, **228**, 465–470.

150 X. Y. Wong, A. Sena-Torralba, R. Álvarez-Diduk, K. Muthoosamy and A. Merkoçi, *ACS Nano*, 2020, **14**, 2585–2627.

151 K. O. Boakye-Yiadom, S. Kesse, Y. Opoku-Damoah, M. S. Filli, M. Aquib, M. M. B. Joelle, M. A. Farooq, R. Mavlyanova, F. Raza, R. Bavi and B. Wang, *Int. J. Pharm.*, 2019, **564**, 308–317.

152 X. W. Hua, Y. W. Bao and F. G. Wu, *ACS Appl. Mater. Interfaces*, 2018, **10**, 16924.

153 M. Zheng, Y. Li, S. Liu, W. Wang, Z. Xie and X. Jing, *ACS Appl. Mater. Interfaces*, 2016, **8**, 23533–23541.

154 C. Liu, P. Zhang, X. Zhai, F. Tian, W. Li, J. Yang, Y. Liu, H. Wang, W. Wang and W. Liu, *Biomaterials*, 2012, **33**, 3604–3613.

155 J. Xu, F. Zeng, H. Wu, C. Hu, C. Yu and S. Wu, *Small*, 2014, **10**, 3750–3760.

156 J. Tang, B. Kong, H. Wu, M. Xu, Y. Wang, Y. Wang, D. Zhao and G. Zheng, *Adv. Mater.*, 2013, **25**, 6569–6574.

157 J. Chen, L. Keltner, J. Christophersen, F. Zheng, M. Krouse, A. Singhal and S. S. Wang, *Cancer J.*, 2002, **8**, 154–163.

158 S. Sun, L. Zhang, K. Jiang, A. Wu and H. Lin, *Chem. Mater.*, 2016, **28**, 8659–8668.

159 H. Li, J. Huang, Y. Song, M. Zhang, H. Wang, F. Lu, H. Huang, Y. Liu, X. Dai, Z. Gu, Z. Yang, R. Zhou and Z. Kang, *ACS Appl. Mater. Interfaces*, 2018, **10**, 26936–26946.

160 S. Mitra, S. Chandra, D. Laha, P. Patra, N. Debnath, A. Pramanik, P. Pramanik and A. Goswami, *Mater. Res. Bull.*, 2012, **47**, 586–594.

161 A. Pramanik, S. Jones, F. Pedraza, A. Vangara, C. Sweet, M. S. Williams, V. Ruppa-Kasani, S. E. Risher, D. Sardar and P. C. Ray, *ACS Omega*, 2017, **2**, 554–562.

162 O. Moradlou, Z. Rabiei and N. Delavari, *J. Photochem. Photobiol. A Chem.*, 2019, **379**, 144–149.

163 J. Yang, X. Zhang, Y. H. Ma, G. Gao, X. Chen, H. R. Jia, Y. H. Li, Z. Chen and F. G. Wu, *ACS Appl. Mater. Interfaces*, 2016, **8**, 32170–32181.

164 X. Shao, W. Zhang, M. I. Umar, H. Y. Wong, Z. Seng, Y. Xie, Y. Zhang, L. Yang, C. K. Kwok and X. Deng, *MBio*, 2020, **11**, e02926-19.

165 L. M. Harris and C. J. Merrick, *PLoS Pathog.*, 2015, **11**, 1–15.

166 B. Alberts, A. Johnson, J. Lewis, D. Morgan, M. Raff, K. Roberts and P. Walter, in *Molecular Biology of the Cell*, 2015, p. 173.

167 L. A. Pray, *Nat. Educ.*, 2008, **1**, 100.

168 J. D. Watson and F. H. C. Crick, *Nature*, 1953, **171**, 737–738.

169 D. Svozil, J. Kalina, M. Omelka and B. Schneider, *Nucleic Acids Res.*, 2008, **36**, 3690–3706.

170 K. Hoogsteen, *Acta Crystallogr.*, 1963, **16**, 907–916.

171 J. L. Asensio, T. Brown and A. N. Lane, *Structure*, 1999, **7**, 1–11.

172 K. Gehring, J. L. Leroy and M. Guéron, *Nature*, 1993, **363**, 561–565.

173 H. A. Day, P. Pavlou and Z. A. E. Waller, *Bioorganic Med. Chem.*, 2014, **22**, 4407–4418.

174 M. GELLERT, M. N. LIPSETT and D. R. DAVIES, *Proc. Natl. Acad. Sci. U. S. A.*, 1962, **48**, 2013–2018.

175 I. Bang, *Biochem. Z.*, 1910, **26**, 293–311.

176 E. Henderson, C. C. Hardin, S. K. Walk, I. Tinoco and E. H. Blackburn, *Cell*, 1987, **51**, 899–908.

177 D. Sen and W. Gilbert, *Nature*, 1988, **334**, 364–366.

178 C. Kang, X. Zhang, R. Ratliff, R. Moyzis and A. Rich, *Nature*, 1992, **356**, 126–131.

179 G. Laughlan, A. I. H. Murchie, D. G. Norman, M. H. Moore, P. C. E. Moody, D. M. J. Lilley and B. Luisi, *Science (80-.).*, 1994, **265**, 520–524.

180 F. W. Smith and J. Feigon, *Nature*, 1992, **356**, 164–168.

181 Y. Wang and D. J. Patel, *Structure*, 1993, **1**, 263–282.

182 J. Bidzinska, G. Cimino-Reale, N. Zaffaroni and M. Folini, *Molecules*, 2013, **18**, 12368–12395.

183 S. Zhang, Y. Wu and W. Zhang, *ChemMedChem*, 2014, **9**, 899–911.

184 D. Bhattacharyya, G. M. Arachchilage and S. Basu, *Front. Chem.*, 2016, **4**, 38.

185 F. Dumetz and C. J. Merrick, *Molecules*, 2019, **24**, 1339.

186 J. Guillon, A. Cohen, R. N. Das, C. Boudot, N. M. Gueddouda, S. Moreau, L. Ronga, S. Savrimoutou, L. Basmaciyan, C. Tisnerat, S. Mestanier, S. Rubio, S. Amaziane, A. Dassonville-Klimpt, N. Azas, B. Courtioux, J. L. Mergny, C. Mullié and P. Sonnet, *Chem. Biol. Drug Des.*, 2018, **91**, 974–995.

187 V. Yadav, Hemansi, N. Kim, N. Tuteja and P. Yadav, *Front. Plant Sci.*, 2017, **8**, 1163.

188 E. Ruggiero and S. N. Richter, *Nucleic Acids Res.*, 2018, **46**, 3270–3283.

189 P. Majee, U. Shankar, S. Pasadi, K. Muniyappa, D. Nayak and A. Kumar, *Virus Res.*, 2020, **283**, 197960.

190 P. Majee, S. Kumar Mishra, N. Pandya, U. Shankar, S. Pasadi, K. Muniyappa, D. Nayak and A. Kumar, *Sci. Rep.*, 2020, **10**, 1477.

191 G. Marsico, V. S. Chambers, A. B. Sahakyan, P. McCauley, J. M. Boutell, M. Di Antonio and S. Balasubramanian, *Nucleic Acids Res.*, 2019, **47**, 3862–3874.

192 V. S. Chambers, G. Marsico, J. M. Boutell, M. Di Antonio, G. P. Smith and S. Balasubramanian, *Nat. Biotechnol.*, 2015, **33**, 877–881.

193 T. A. Brooks, S. Kendrick and L. Hurley, *FEBS J.*, 2010, **277**, 3459–3469.

194 A. Cammas and S. Millevoi, *Nucleic Acids Res.*, 2017, **45**, 1584–1595.

195 S. T. G. Street, D. N. Chin, G. J. Hollingworth, M. Berry, J. C. Morales and M. C. Galan, *Chem. - A Eur. J.*, 2017, **23**, 6953–6958.

196 S. Neidle, *Therapeutic applications of quadruplex nucleic acids*, Elsevier, London, 2012.

197 J. W. Shay and W. E. Wright, *FEBS Lett.*, 2010, **584**, 3819–3825.

198 J. W. Shay and S. Bacchetti, *Eur. J. Cancer*, 1997, **33**, 787–791.

199 A. M. Zahler, J. R. Williamson, T. R. Cech and D. M. Prescott, *Nature*, 1991, **350**, 718–720.

200 K. M. Burchett, Y. Yan and M. M. Ouellette, *PLoS One*, 2014, **9**, e85155.

201 Y. E. Yegorov, D. N. Chernov, S. S. Akimov, N. L. Bolsheva, A. A. Krayevsky and A. V. Zelenin, *FEBS Lett.*, 1996, **389**, 115–118.

202 D. Sun, B. Thompson, B. E. Cathers, M. Salazar, S. M. Kerwin, J. O. Trent, T. C. Jenkins, S. Neidle and L. H. Hurley, *J. Med. Chem.*, 1997, 40, 2113–2116.

203 S. Asamitsu, S. Obata, Z. Yu, T. Bando and H. Sugiyama, *Molecules*, 2019, **24**, 429.

204 A. R. Duarte, E. Cadoni, A. S. Ressurreição, R. Moreira and A. Paulo, *ChemMedChem*, 2018, **13**, 869–893.

205 J. Cuesta, M. Read and S. Neidle, *Mini-Reviews Med. Chem.*, 2012, **3**, 11–21.

206 D. Monchaud and M. P. Teulade-Fichou, *Org. Biomol. Chem.*, 2008, **6**, 627–636.

207 J. Dash, P. S. Shirude, S. T. D. Hsu and S. Balasubramanian, *J. Am. Chem. Soc.*, 2008, **130**, 15950–15956.

208 R. F. Pasternack, E. J. Gibbs, J. J. Villafranca and J. J. Villafranca, *Biochemistry*, 1983, **22**, 5409–5417.

209 R. T. Wheelhouse, D. Sun, H. Han, F. X. Han and L. H. Hurley, *J. Am. Chem. Soc.*, 1998, **120**, 3261–3262.

210 J. Ren and J. B. Chaires, *Biochemistry*, 1999, **38**, 16067–16075.

211 R. J. Harrison, J. Cuesta, G. Chessari, M. A. Read, S. K. Basra, A. P. Reszka, J. Morrell, S. M. Gowan, C. M. Incles, F. A. Tanious, W. D. Wilson, L. R. Kelland and S. Neidle, *J. Med. Chem.*, 2003, **46**, 4463–4476.

212 R. Rodriguez, S. Müller, J. A. Yeoman, C. Trentesaux, J. F. Riou and S. Balasubramanian, *J. Am. Chem. Soc.*, 2008, **130**, 15758–15759.

213 J. F. Moruno-Manchon, E. C. Koellhoffer, J. Gopakumar, S. Hambarde, N. Kim, L. D. McCullough and A. S. Tsvetkov, *Aging (Albany. NY).*, 2017, **9**, 1957–1970.

214 C. Lin and D. Yang, in *Methods in Molecular Biology*, 2017, vol. 1587, pp. 171–196.

215 S. Haider and S. Neidle, *Methods Mol. Biol.*, 2010, **608**, 17–37.

216 M. Bončina, Č. Podlipnik, I. Piantanida, J. Eilmes, M. P. Teulade-Fichou, G. Vesnaver and J. Lah, *Nucleic Acids Res.*, 2015, **43**, 10376–10386.

217 B. Ranjbar and P. Gill, *Chem. Biol. Drug Des.*, 2009, **74**, 101–120.

218 A. Randazzo, G. P. Spada and M. W. Da Silva, *Top. Curr. Chem.*, 2013, **330**, 67–86.

219 D. Shrestha, A. Jenei, P. Nagy, G. Vereb and J. Szöllősi, *Int. J. Mol. Sci.*, 2015, **16**, 6718–6756.

220 G. A. Jones and D. S. Bradshaw, *Front. Phys.*, 2019, **7**, 100.

221 R. B. Sekar and A. Periasamy, *J. Cell Biol.*, 2003, **160**, 629–633.

222 J. L. Mergny and J. C. Maurizot, *ChemBioChem*, 2001, **2**, 124–132.

223 J. L. Mergny, L. Lacroix, M. P. Teulade-Fichou, C. Hounsou, L. Guittat, M. Hoarau, P. B. Arimondo, J. P. Vigneron, J. M. Lehn, J. F. Riou, T. Garestier and C. Hélène, *Proc. Natl. Acad. Sci. U. S. A.*, 2001, **98**, 3062–3067.

224 P. Rawal, V. B. R. Kummarasetti, J. Ravindran, N. Kumar, K. Halder, R. Sharma, M. Mukerji, S. K. Das and S. Chowdhury, *Genome Res.*, 2006, **16**, 644–655.

225 N. Beaume, R. Pathak, V. K. Yadav, S. Kota, H. S. Misra, H. K. Gautam and S. Chowdhury, *Nucleic Acids Res.*, 2013, **41**, 76–89.

226 N. Jain, S. K. Mishra, U. Shankar, A. Jaiswal, T. K. Sharma, P. Kodgire and A. Kumar, *Genomics*, 2020, **112**, 4863–4874.

227 U. Shankar, N. Jain, S. K. Mishra, T. K. Sharma and A. Kumar, *Front. Microbiol.*, 2020, **11**, 1269.

228 L. A. Cahoon and H. S. Seifert, *Science (80-.).*, 2009, **325**, 764–767.

229 Z. A. E. Waller, B. J. Pinchbeck, B. S. Buguth, T. G. Meadows, D. J. Richardson and A. J. Gates, *Chem. Commun.*, 2016, **52**, 13511–13514.

230 O. I. Kaplan, B. Berber, N. Hekim and O. Doluca, *Nucleic Acids Res.*, 2016, **44**, 9083–9095.

231 I. T. Holder and J. S. Hartig, *Chem. Biol.*, 2014, **21**, 1511–1521.

232 X. Wu and N. Maizels, *Nucleic Acids Res.*, 2001, **29**, 1765–1771.

233 J. L. Li, R. J. Harrison, A. P. Reszka, R. M. Brosh, V. A. Bohr, S. Neidle and I. D. Hickson, *Biochemistry*, 2001, **40**, 15194–15202.

234 R. S. Thakur, A. Desingu, S. Basavaraju, S. Subramanya, D. N. Rao and G. Nagaraju, *J. Biol. Chem.*, 2014, **289**, 25112–25136.

235 S. K. Mishra, U. Shankar, N. Jain, K. Sikri, J. S. Tyagi, T. K. Sharma, J. L. Mergny and A. Kumar, *Mol. Ther. - Nucleic Acids*, 2019, **16**, 698–706.

236 R. Perrone, E. Lavezzo, E. Riello, R. Manganelli, G. Palù, S. Toppo, R. Provvedi and S. N. Richter, *Sci. Rep.*, 2017, **7**, 5743.

237 S. A. Hill, S. Sheikh, Q. Zhang, L. Sueiro Ballesteros, A. Herman, S. A. Davis, D. J. Morgan, M. Berry, D. Benito-Alifonso and M. C. Galan, *Nanoscale Adv.*, 2019, **1**, 2840–2846.

238 S. A. Hill, D. Benito-Alifonso, D. J. Morgan, S. A. Davis, M. Berry and M. C. Galan, *Nanoscale*, 2016, **8**, 18630–18634.

239 C. I. Weng, H. T. Chang, C. H. Lin, Y. W. Shen, B. Unnikrishnan, Y. J. Li and C. C. Huang, *Biosens. Bioelectron.*, 2015, **68**, 1–6.

240 B. Mukhopadhyay, M. B. Martins, R. Karamanska, D. A. Russell and R. A. Field, *Tetrahedron Lett.*, 2009, **50**, 886–889.

241 I. L. Gunsolus, D. Hu, C. Mihai, S. E. Lohse, C. S. Lee, M. D. Torelli, R. J. Hamers, C. J. Murhpy, G. Orr and C. L. Haynes, *Analyst*, 2014, **139**, 3174–3178.

242 A. J. Hobro and N. I. Smith, *Vib. Spectrosc.*, 2017, **91**, 31–45.

243 L. Paavilainen, Å. Edvinsson, A. Asplund, S. Hober, C. Kampf, F. Pontén and K. Wester, *J. Histochem. Cytochem.*, 2010, **58**, 237–246.

244 Y. Chao and T. Zhang, *Appl. Microbiol. Biotechnol.*, 2011, **92**, 381–392.

245 S. Ravikumar, R. Surekha and R. Thavarajah, *J. Dr. NTR Univ. Heal. Sci.*, 2014, **3**, 1.

246 R. T. Borlinghaus and C. Kappel, *Nat. Methods*, 2016, **13**, i–iii.

247 J. M. Wood, *J. Gen. Physiol.*, 2015, **145**, 381–388.

248 J. Schindelin, I. Arganda-Carreras, E. Frise, V. Kaynig, M. Longair, T. Pietzsch, S. Preibisch, C. Rueden, S. Saalfeld, B. Schmid, J. Y. Tinevez, D. J. White, V. Hartenstein, K. Eliceiri, P. Tomancak and A. Cardona, *Nat. Methods*, 2012, **9**, 676–682.

249 K. Wojcik and J. W. Dobrucki, *Cytom. Part A*, 2008, **73**, 555–562.

250 H. Ding, S. B. Yu, J. S. Wei and H. M. Xiong, *ACS Nano*, 2016, **10**, 484–491.

251 S. Wu, X. Dai, F. Shilong, M. Zhu, X. Shen, K. Zhang and S. Li, *Food Sci. Biotechnol.*, 2018, **27**, 1–7.

252 Y. Hrynets, A. Bhattacherjee, M. Ndagijimana, D. J. Hincapie Martinez and M. Betti, *J. Agric. Food Chem.*, 2016, **64**, 3266–3275.

253 M. Zhao, M. M. Araújo, S. Dal, S. Sigrist, M. Bergaentzlé, D. Ramanitrahasimbola, C. Andrianjara and E. Marchioni, *J. Chromatogr. A*, 2016, **1473**, 66–75.

254 A. Bhattacherjee, Y. Hrynets and M. Betti, *Food Chem.*, 2019, **271**, 354–361.

255 M. J. Meziani, X. Dong, L. Zhu, L. P. Jones, G. E. Lecroy, F. Yang, S. Wang, P. Wang, Y. Zhao, L. Yang, R. A. Tripp and Y. P. Sun, *ACS Appl. Mater. Interfaces*, 2016, **8**, 10761–10766.

256 R. Jijie, A. Barras, J. Bouckaert, N. Dumitrascu, S. Szunerits and R. Boukherroub, *Colloids Surfaces B Biointerfaces*, 2018, **170**, 347–354.

257 Z. Pang, R. Raudonis, B. R. Glick, T. J. Lin and Z. Cheng, *Biotechnol. Adv.*, 2019, **37**, 177–192.

258 T. Dai, M. S. Vrahas, C. K. Murray and M. R. Hamblin, *Expert Rev. Anti. Infect. Ther.*, 2012, **10**, 185–195.

259 B. Li, Y. Qiu, H. Shi and H. Yin, *Analyst*, 2016, **141**, 3059–3067.

260 M. D. Rolfe, C. J. Rice, S. Lucchini, C. Pin, A. Thompson, A. D. S. Cameron, M. Alston, M. F. Stringer, R. P. Betts, J. Baranyi, M. W. Peck and J. C. D. Hinton, *J. Bacteriol.*, 2012, **194**, 686–701.

261 O. Fridman, A. Goldberg, I. Ronin, N. Shoresh and N. Q. Balaban, *Nature*, 2014, **513**, 418–421.

262 A. Zhu, J. B. Huang, A. Clark, R. Romero and H. R. Petty, *Carbohydr. Res.*, 2007, **342**, 2745–2749.

263 A. Bhattacherjee, Y. Hrynets and M. Betti, *J. Agric. Food Chem.*, 2016, **64**, 8530–8539.

264 D. Fuentealba, M. Galvez, E. Alarcón, E. Lissi and E. Silva, *Photochem. Photobiol.*, 2007, **83**, 563–569.

265 Y. Okano, H. Masaki and H. Sakurai, *J. Dermatol. Sci.*, 2001, **27**, 11–18.

266 H. Masaki, Y. Okano and H. Sakurai, *Biochim. Biophys. Acta - Gen. Subj.*, 1999, **1428**, 45–56.

267 A. De La Rochette, I. Birlouez-Aragon, E. Silva and P. Morlière, *Biochim. Biophys. Acta - Gen. Subj.*, 2003, **1621**, 235–241.

268 M. Merchat, G. Bertolini, P. Giacomini, A. Villanueva and G. Jori, *J. Photochem. Photobiol. B Biol.*, 1996, **32**, 153–157.

269 Y. Matsumoto, K. Hayama, S. Sakakihara, K. Nishino, H. Noji, R. Iino and A. Yamaguchi, *PLoS One*, 2011, **6**, e18547.

270 M. Toyofuku, N. Nomura and L. Eberl, *Nat. Rev. Microbiol.*, 2019, **17**, 13–24.

271 C. Muheim, H. Götzke, A. U. Eriksson, S. Lindberg, I. Lauritsen, M. H. H. Nørholm and D. O. Daley, *Sci. Rep.*, 2017, **7**, 17629.

272 A. Liu, L. Tran, E. Becket, K. Lee, L. Chinn, E. Park, K. Tran and J. H. Miller, *Antimicrob. Agents Chemother.*, 2010, **54**, 1393–1403.

273 X. Bao, Y. Yuan, J. Chen, B. Zhang, D. Li, D. Zhou, P. Jing, G. Xu, Y. Wang, K. Holá, D. Shen, C. Wu, L. Song, C. Liu, R. Zbořil and S. Qu, *Light Sci. Appl.*, 2018, **7**, 2047–7538.

274 F. C. Fang, *MBio*, 2011, **2**, e00141-11.

275 Q. Wang and M.-H. Zou, *Methods Mol Biol.*, 2018, **1732**, 507–517.

276 A. Schmidt, K. Kochanowski, S. Vedelaar, E. Ahrné, B. Volkmer, L. Callipo, K. Knoops, M. Bauer, R. Aebersold and M. Heinemann, *Nat. Biotechnol.*, 2016, **34**, 104–110.

277 M. Kuroda, H. Kuroda, T. Oshima, F. Takeuchi, H. Mori and K. Hiramatsu, *Mol. Microbiol.*, 2003, **49**, 807–821.

278 S. Utaida, P. M. Dunman, D. Macapagal, E. Murphy, S. J. Projan, V. K. Singh, R. K. Jayaswal and B. J. Wilkinson, *Microbiology*, 2003, **149**, 2719–2732.

279 F. McAleese, S. W. Wu, K. Sieradzki, P. Dunman, E. Murphy, S. Projan and A. Tomasz, *J. Bacteriol.*, 2006, **188**, 1120–1133.

280 A. Muthaiyan, J. A. Silverman, R. K. Jayaswal and B. J. Wilkinson, *Antimicrob. Agents Chemother.*, 2008, **52**, 980–990.

281 M. Kostakioti, M. Hadjifrangiskou and S. J. Hultgren, *Cold Spring Harb. Perspect. Med.*, 2013, **3**, a010306.

282 J. L. del Pozo, M. S. Rouse and R. Patel, *Int. J. Artif. Organs*, 2008, **31**, 786–795.

283 G. A. O'Toole, *J. Vis. Exp.*, 2010, **47**, 2437.

284 B. Unnikrishnan, R. S. Wu, S. C. Wei, C. C. Huang and H. T. Chang, *ACS Omega*, 2020, **5**, 11248–11261.

285 G. Ramachandraiah, N. R. Chandra, A. Surolia and M. Vijayan, *Glycobiology*, 2003, **13**, 765–775.

286 K. Ohlsen, T. A. Oelschlaeger, J. Hacker and A. S. Khan, *Top. Curr. Chem.*, 2009, **288**, 109–120.

287 B. A. Hendrickson, J. Guo, R. Laughlin, Y. Chen and J. C. Alverdy, *Infect. Immun.*, 1999, **67**, 745–753.

288 D. Abgottspon, G. Rölli, L. Hosch, A. Steinhuber, X. Jiang, O. Schwardt, B. Cutting, M. Smiesko, U. Jenal, B. Ernst and A. Trampuz, *J. Microbiol. Methods*, 2010, **82**, 249–255.

289 D. Vetter and M. A. Gallop, *Bioconjug. Chem.*, 1995, **6**, 316–318.

290 M. Bejugam and S. L. Flitsch, *Org. Lett.*, 2004, **3**, 6–9.

291 L. M. Likhosherstov, O. S. Novikova and V. N. Shibaev, *Dokl. Chem.*, 2002, **383**, 89–92.

292 S. Sheikh, *Univ. Bristol*, 2020, Thesis.

293 K. Abstiens, M. Gregoritza and A. M. Goepferich, *ACS Appl. Mater. Interfaces*, 2019, **11**, 1311–1320.

294 D. Aldakov, M. T. Sajjad, V. Ivanova, A. K. Bansal, J. Park, P. Reiss and I. D. W. Samuel, *J. Mater. Chem. A*, 2015, **3**, 19050–19060.

295 C. H. Kapadia, S. Tian, J. L. Perry, J. C. Luft and J. M. Desimone, *ACS Omega*, 2019, **4**, 5547–5555.

296 R. Atav, in *Waterproof and Water Repellent Textiles and Clothing*, 2018, pp. 191–214.

297 S. G. Stahlhut, V. Tchesnokova, C. Struve, S. J. Weissman, S. Chattopadhyay, O. Yakovenko, P. Aprikian, E. V. Sokurenko and K. A. Krogfelt, *J. Bacteriol.*, 2009, **191**, 6592–6601.

298 D. Avichezer and N. Gilboa-Garber, *FEBS Lett.*, 1987, **216**, 62–66.

299 S. Qu, X. Liu, X. Guo, M. Chu, L. Zhang and D. Shen, *Adv. Funct. Mater.*, 2014, **24**, 2689–2695.

300 W. U. Khan, D. Wang, W. Zhang, Z. Tang, X. Ma, X. Ding, S. Du and Y. Wang, *Sci. Rep.*, 2017, **7**, 14866.

301 T. Yu, H. Wang, C. Guo, Y. Zhai, J. Yang and J. Yuan, *R. Soc. Open Sci.*, 2018, **5**, 180245.

302 Q. Liu, N. Zhang, H. Shi, W. Ji, X. Guo, W. Yuan and Q. Hu, *New J. Chem.*, 2018, **42**, 3097–3101.

303 Y. Jiao, X. Gong, H. Han, Y. Gao, W. Lu, Y. Liu, M. Xian, S. Shuang and C. Dong, *Anal. Chim. Acta*, 2018, **1042**, 125–132.

304 Z. L. Wu, M. X. Gao, T. T. Wang, X. Y. Wan, L. L. Zheng and C. Z. Huang, *Nanoscale*, 2014, **6**, 3868–3874.

305 E. F. C. Simões, J. M. M. Leitão and J. C. G. E. da Silva, *Microchim. Acta*, 2016, **183**, 1769–1777.

306 R. Sendão, M. del V. M. de Yuso, M. Algarra, J. C. G. Esteves da Silva and L. Pinto da Silva, *J. Clean. Prod.*, 2020, **254**, 120080.

307 W. Kasprzyk, T. Świergosz, S. Bednarz, K. Walas, N. V. Bashmakova and D. Bogdał, *Nanoscale*, 2018, **10**, 13889–13894.

308 J. Stetefeld, S. A. McKenna and T. R. Patel, *Biophys. Rev.*, 2016, **8**, 409–427.

309 T. G. Millan, Unpublished work.

310 P. Senthil Kumar, K. Grace Pavithra and M. Naushad, in *Nanomaterials for Solar Cell Applications*, 2019, pp. 97–124.

311 I. Kalograiaki, M. Abellán-Flos, L. Á. Fernández, M. Menéndez, S. P. Vincent and D. Solís, *Anal. Chem.*, 2018, **90**, 12314–12321.

312 F. J. R. Soriano, Unpublished work.

313 C. M. A. Caipang and C. C. Lazado, in *Mucosal Health in Aquaculture*, 2015, pp. 211–272.

314 D. Yang, in *Methods in Molecular Biology*, 2019, vol. 2035, pp. 1–24.

315 D. Bhartiya, V. Chawla, S. Ghosh, R. Shankar and N. Kumar, *Genomics*, 2016, **108**, 224–231.

316 M. P. O'Hagan, P. Peñalver, R. S. L. Gibson, J. C. Morales and M. C. Galan, *Chem. - A Eur. J.*, 2020, **26**, 6224–6233.

317 W. M. Kirby, G. M. Yoshihara, K. S. Sundsted and J. H. Warren, *Antibiot. Annu.*, 1956, 892–897.

318 A. W. Bauer, D. M. Perry and W. M. M. Kirby, *A.M.A Arch. Intern. Med.*, 1959, **104**, 208–216.

319 M. D. A. W. Bauer, M.D., W. M. M. Kirby, M.D., J. C. Sherris, M.D., M. Turck, *Am. J. Clin. Pathol.*, 1966, **45**, 493–496.

320 J. H. Jorgensen and J. D. Turnidge, in *Manual of Clinical Microbiology*, 2015, pp. 1253–1273.

321 B. Zhou, Y. Geng, C. Liu, H. Miao, Y. Ren, N. Xu, X. Shi, Y. You, T. Lee and G. Zhu, *Sci. Rep.*, 2018, **8**, 2366.

322 P. L. Weiden, W. Epstein and S. G. Schultz, *J. Gen. Physiol.*, 1967, **50**, 1641–1661.

323 M. Pai, M. A. Behr, D. Dowdy, K. Dheda, M. Divangahi, C. C. Boehme, A. Ginsberg, S. Swaminathan, M. Spigelman, H. Getahun, D. Menzies and M. Raviglione, *Nat. Rev. Dis. Prim.*, 2016, **2**, 16076.

324 N. Sattarahmady, M. Rezaie-Yazdi, G. H. Tondro and N. Akbari, *J. Photochem. Photobiol. B Biol.*, 2017, **166**, 323–332.

325 R. Knoblauch and C. D. Geddes, *Materials (Basel).*, 2020, **13**, 4004.

326 D. Zhong, Y. Zhuo, Y. Feng and X. Yang, *Biosens. Bioelectron.*, , DOI:10.1016/j.bios.2015.07.015.

327 W. U. Khan, D. Wang, W. Zhang, Z. Tang, X. Ma, X. Ding, S. Du and Y. Wang, *Sci. Rep.*, 2017, **7**, 14866.

328 S. A. Hill, 2017, PhD Thesis, University of Bristol.

329 S. Hill and M. C. Galan, *Beilstein J. Org. Chem.*, 2017, **13**, 675–693.

330 C. M. Cardona and R. E. Gawley, *J. Org. Chem.*, 2002, **67**, 1411–1413.

331 RStudio, 2020, Integrated Development for R. RStudio, PBC, Boston.

332 H. Mi, D. Ebert, A. Muruganujan, C. Mills, L. P. Albou, T. Mushayamaha and P. D. Thomas, *Nucleic Acids Res.*, 2021, **49**, D394–D403.

333 A. De Cian, L. Guittat, M. Kaiser, B. Saccà, S. Amrane, A. Bourdoncle, P. Alberti, M. P. Teulade-Fichou, L. Lacroix and J. L. Mergny, *Methods*, 2007, **42**, 183–195.

APPENDIX 1: G4 LIGANDS

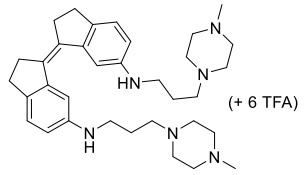

L1

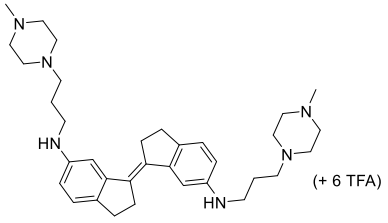

L2

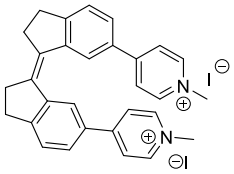

L3

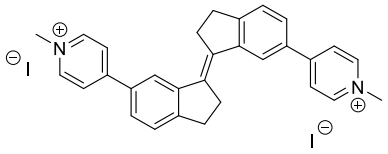

L4

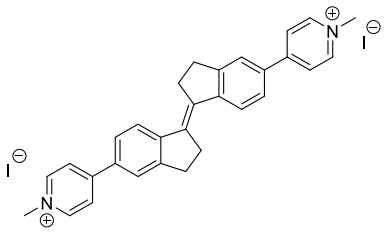

L5

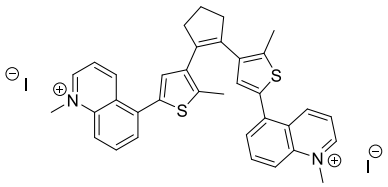

L6

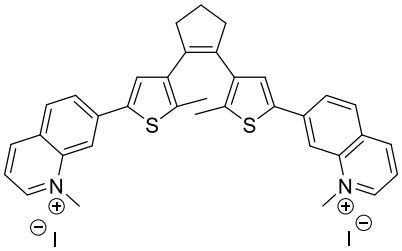

L7

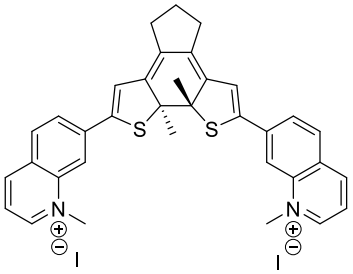

L8

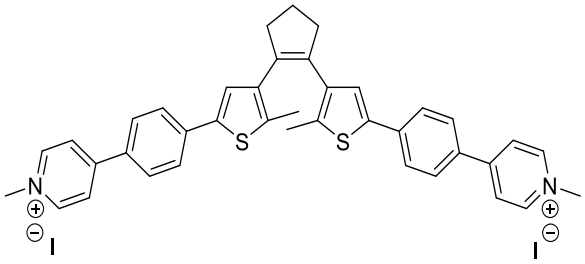

L9

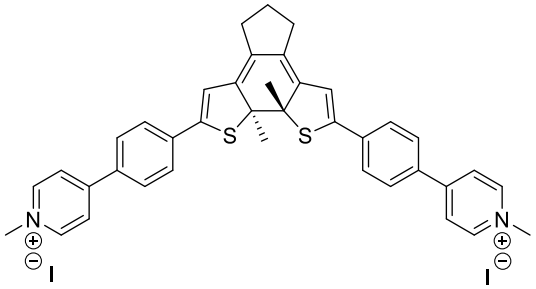

L10

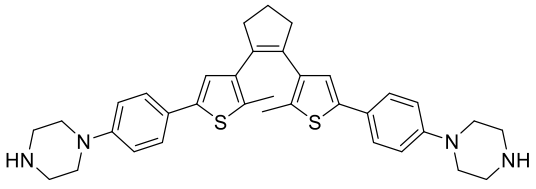

L11

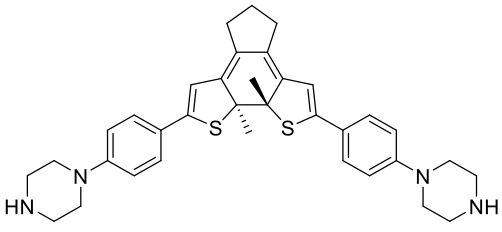

L12

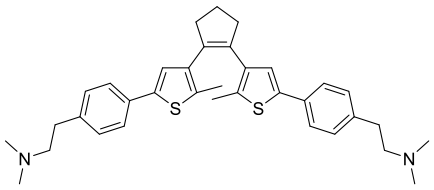

L13

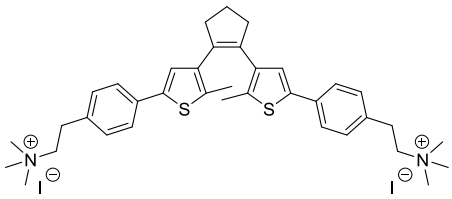

L14

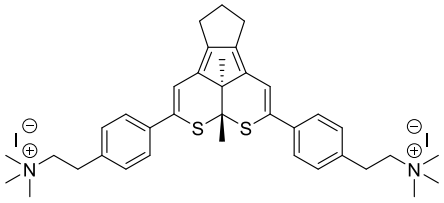

L15

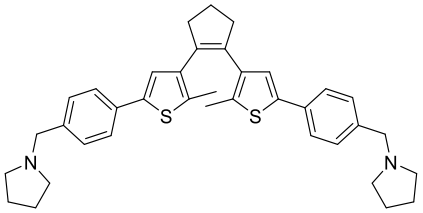

L16

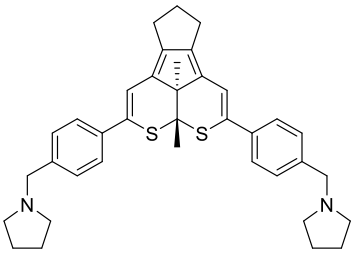

L17

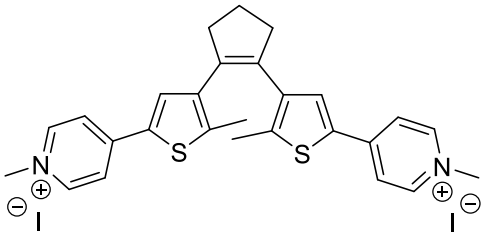

L18

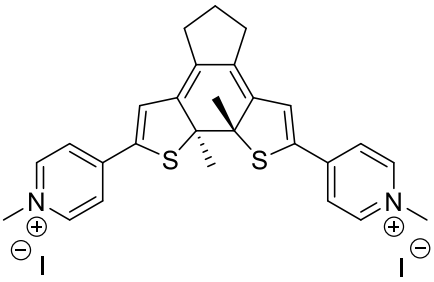

L19

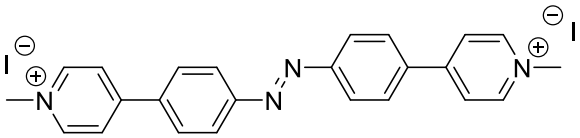

L20

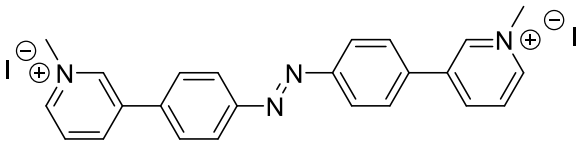

L21

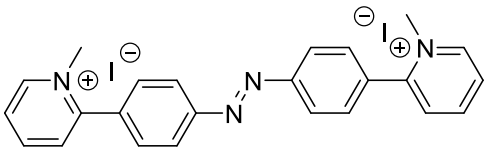

L22

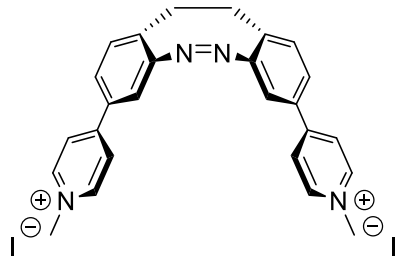

L23

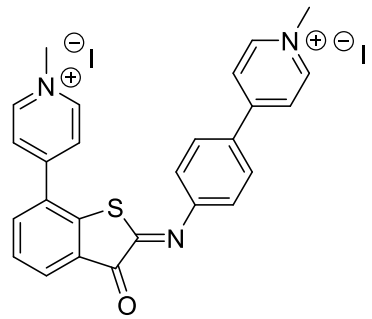

L24

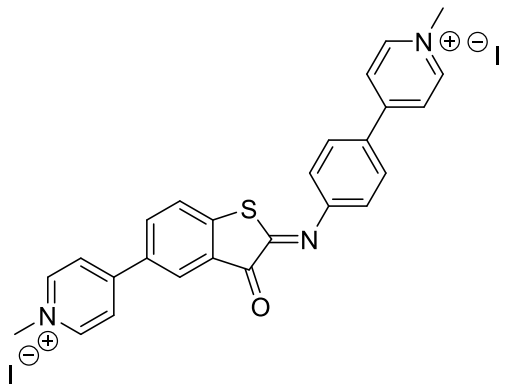

L25

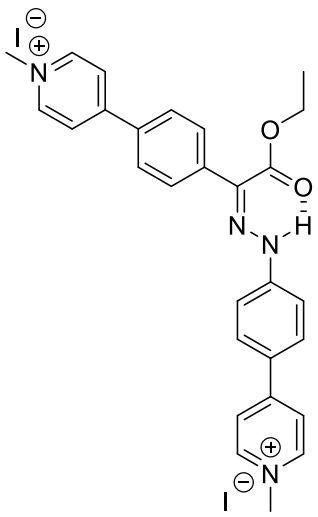

L26